Alma Mater Studiorum – Università di Bologna

DIPARTIMENTO DI FISICA E ASTRONOMIA
Corso di Dottorato di Ricerca in Astronomia
CICLO XXV

THE GASEOUS HALO OF THE MILKY WAY

Dottorando
Antonino Marasco

Relatore
Chiar.mo Prof. F. Fraternali

Coordinatore
Chiar.mo Prof. L. Moscardini

Esame finale anno 2013

SCUOLA DI DOTTORATO IN SCIENZE MATEMATICHE, FISICHE E ASTRONOMICHE
Settore Concorsuale: 02/C1 – Astronomia, Astrofisica, Fisica della Terra e dei Pianeti
Settore Scientifico-Disciplinare: FIS/05 – Astronomia e Astrofisica

Contents

Chapter 1

Introduction

In recent years, sensitive observations have revealed that the gas in disc galaxies is not solely confined to a thin disc, but extends for several kiloparsecs into the halo region, building up multiphase layers that we refer to as *gaseous halos*. These structures are thought to be produced by the circulation of gas from a disc to the surrounding environment and/or vice-versa. The study of gaseous halos is of fundamental importance to understand galaxy evolution, as this latter depends dramatically on how galaxy discs interact with the environment in which they live.

This Thesis is devoted to the study of the closest to us of these structures: the gaseous halo of the Milky Way. In this Introduction, we discuss the main observational properties of the gaseous halos of nearby disc galaxies (Section 1.1) and of the Milky Way (Section 1.2), and we also address possible interpretations for their origin. The importance of gaseous halos in the evolution of discs is discussed in Section 1.3. In Section 1.4 we introduce the model of the galactic fountain, that will be used in Chapters 3 and 5 to describe the gaseous halo of the Milky Way. Finally, Section 1.5 describes the aims of this work and its organisation.

In the following, we use without distinction the terms *halo gas* and *extraplanar gas* to refer to these gaseous environments.

1.1 Gaseous halos in disc galaxies

1.1.1 Cold phase

The cold phase ($T \lesssim 10^4$ K) of the halo gas is directly probed by the 21-cm emission line of neutral hydrogen (H I), and is the best studied. Sensitive H I observations have revealed that about 5−10% of the total H I content of nearby spiral galaxies is located outside the thin disc in structures extending typically up to a few kpc from the midplane (e.g. Fraternali 2010). These structures are called H I *thick discs*, by

analogy with the stellar component, or HI halos. The left panel of Fig. 1.1 shows the striking case of NGC 891, an edge-on galaxy with an exceptionally massive HI thick disc that contains $\sim 30\%$ of the total mass of neutral hydrogen (Oosterloo et al. 2007). The edge-on inclination of this galaxy favours the study of rotational motions: Oosterloo et al. (2007) found that the extraplanar HI rotates more slowly than the gas in the thin disc, and its velocity decreases with increasing vertical distance from the midplane. The right panel of Fig. 1.1 shows the HI rotation curves derived at different heights from the disc of NGC 891. Similar 'lagging' HI halos have been found also in other galaxies, like NGC 2403 (Fraternali et al. 2002), NGC 6503 (Greisen et al. 2009) and the Milky Way itself (Levine et al. 2008, and Chapter 2 of this Thesis).

Galaxies seen at inclination angle different from edge-on offer the opportunity to study non-circular motions of the extraplanar gas. In these cases, a careful modelling of the position-velocity distribution of the HI emission is needed to disentangle between the disc and the halo components. These models have shown that HI thick discs appear to inflow radially towards the galaxy centre (Fraternali et al. 2002). Also, motions perpendicular to the disc are present (Boomsma et al. 2005). Similar models are adopted in Chapter 2 to study the properties of the Galactic HI halo.

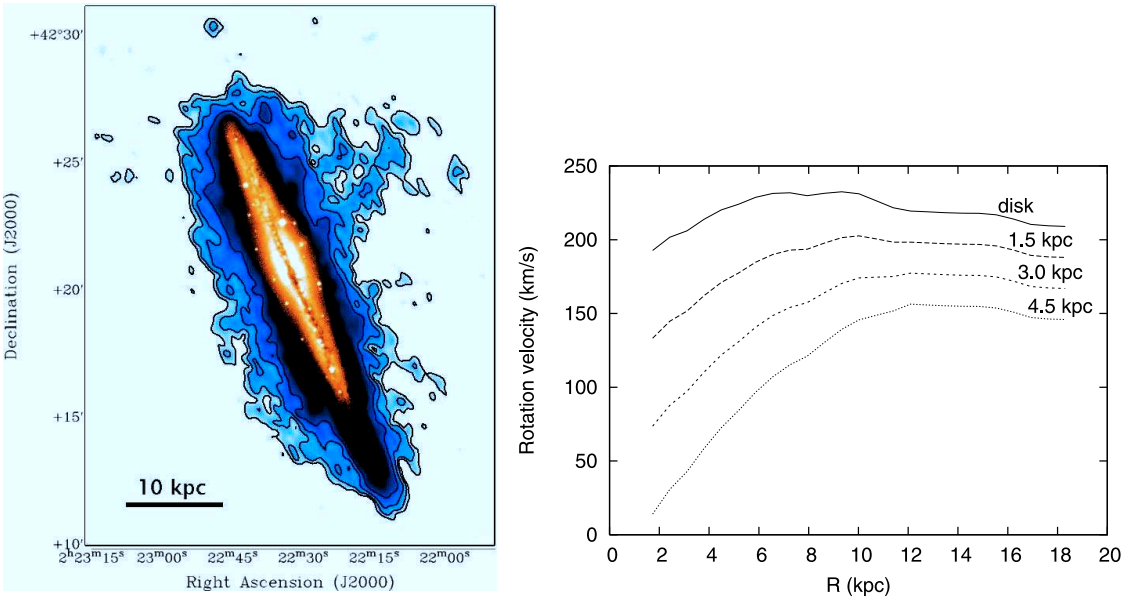

Figure 1.1: The massive, extended, slow-rotating HI halo of NGC 891. *Left panel*: total HI map (blue + contours) overlaid on the optical image (orange) (from Fraternali 2009). *Right panel*: rotation curves at different heights from the midplane (from Oosterloo et al. 2007).

The origin of the extraplanar HI is rather uncertain, and both internal and external processes can contribute to build up this layer. The disc-like kinematics of HI halos points towards an internal origin. Stellar feedback (i.e. clustering of supernova explosions) injects thermal and mechanical energy on the surrounding gas. This gas is ejected outside the disc into the halo region, travels through the halo and

eventually falls back to the disc producing a cycle of gas that goes under the name of *galactic fountain* (Shapiro and Field 1976). In the classical view (e.g. Bregman 1980), supernova-heated gas arises above the disc in a hot phase at temperatures of $\sim 10^6$ K, forming a 'dynamic hot corona' around the galaxy. Neutral clouds can condense from this corona via thermal instability, producing a rain of cold clumps towards the disc. Subsequent studies, like those performed by Melioli et al. (2008, 2009) with 3D hydrodynamical simulations, have shown that the gas ejected from the disc tends to have much lower temperatures ($\sim 10^5$ K) and can cool very rapidly. This gas can reach typical heights of ~ 2 kpc above the disc and then falls back in the form of cold dense clouds and filaments. There is strong evidence that a large fraction of the extraplanar H I is built up by the galactic fountain. Galaxies with unusually large star formation rates (SFRs) show more massive H I halos, as in the case of NGC 891. Prominent H I clouds at anomalous velocities are found near regions of the disc where H I is depleted and massive young stars are present (Kamphuis et al. 1991; Pidopryhora et al. 2007; Boomsma et al. 2008). Finally, galactic fountain models are very successful in reproducing the H I data, we discuss this extensively in Chapter 3.

In spite of the success of the galactic fountain, some fraction of the extraplanar H I could have an external origin. This is supported by the presence of some counterrotating H I clouds, which are not consistent with having an internal origin (e.g., Oosterloo et al. 2007). A possibility is that this gas is built by material stripped from satellites and currently accreting onto the main galaxies. H I observations in the local Universe have revealed that minor merger events are rather common, as $\sim 25\%$ of disc galaxies, including the Milky Way itself (Section 1.2), show signs of an ongoing interaction (Sancisi et al. 2008). Another explanation could be that halo H I are produced by 'cosmological' accretion of pristine gas that permeates the intergalactic space (e.g. Kereš et al. 2005; Kaufmann et al. 2006). Further details on these processes are given is Section 1.3.

Finally, we point out that hydrostatic, baroclinic models of H I halos have been discarded on theoretical grounds because, in order to reproduce the observed scale-height and rotational gradient, the gas temperature should be of $\sim 10^5$ K (Barnabè et al. 2006), much above the typical H I temperature. More generally, stationary models of H I halos can not reproduce the detailed kinematics of the H I thick discs (Marinacci et al. 2010b).

1.1.2 Warm-hot phase

Emission in Hα and other optical lines is commonly observed around disc galaxies, probing the existence of diffuse ionised gas (DIG) layers at temperatures of $\sim 10^4$ K. These structures are located in the lower halo, extending on average $1-2$ kpc from the discs (Hoopes et al. 1999). Several pieces of evidence indicate that these layers are simply the ionised counterpart of the H I thick discs. Galaxies with larger SFRs

show more prominent DIG layers (Rossa and Dettmar 2003) and the kinematics of this ionised gas is consistent with that of the H I halo, showing both a lagging rotation (Heald et al. 2006, 2007) and non-circular motions (Fraternali et al. 2004). Thus, the photoionisation of extraplanar H I from bright stars in the disc is the most likely explanation for the DIG layers.

Besides the DIG, galaxies appear to be surrounded by a much more extended ionised medium. Highly ionised atomic species, O VI *in primis*, are observed in absorption towards AGNs out to a distance of half a Mpc from galaxies (Wakker and Savage 2009). This indicates the presence of ionised material in the intergalactic space at temperatures around 10^5 K. This warm-hot intergalactic medium (WHIM) is though to permeate the space between galaxies, and probably constitutes a large fraction of the so-called 'missing baryons' (Section 1.1.3). It is unlikely that the absorption features located at large distances from galaxy discs are produced by a 'normal' feedback activity from the hosting galaxy. UV background photoionisation, shock-heating of cosmological filaments, strong outflows by galactic superwinds are more viable possibilities (Stocke et al. 2006). Another possible explanation is that these features are produced in the interstellar medium of very faint dwarf galaxies, or by the interaction between these latter and the circumgalactic medium (Tumlinson et al. 2005).

1.1.3 Coronal phase

Arguments based on the primordial nucleosynthesis (Pagel 1997) and on the anisotropy of the cosmic microwave background (Spergel et al. 2007) indicate unambiguously that the baryon content of the Universe exceeds the amount of visible matter in galaxies and galaxy clusters by a factor of about 10. Therefore, most of the baryons are expected to be located in the intergalactic space. A fraction around 30 per cent of these missing baryons may be associated to the local Lyα forest (Penton et al. 2004), while the rest is still missing and probably comprises the WHIM, as mentioned in Section 1.1.2; assuming a constant ratio between dark and visible matter, the WHIM is expected to reach high densities in regions where the potential wells are deeper. Thus, spiral galaxies, like more massive structures such as galaxy clusters, should be embedded in massive atmospheres of plasma at about the virial temperature, called *coronae*.

In rich galaxy clusters, these coronae are commonly observed through their free-free X-ray emission (Sarazin 2009). The structures have temperatures close to the clusters' virial temperature ($\sim 10^{7-8}$ K) and contain roughly the theoretical fraction of baryonic matter. In contrast, there is no definitive evidence for coronae around field or group disc-galaxies that contain the expected amount of baryons. Cosmological coronae of Milky-Way-like galaxies should have temperatures of a few 10^6 K and should extend out to a few hundred kiloparsecs from the galaxy centres (Fukugita and Peebles 2006). Because of their temperature, these structures should be emit-

ting in the soft X-ray band (0.5−2 keV), but their surface brightness is close to the sensitivity of the current generation of instruments (Bregman 2007). Fig. 1.2 shows the synthetic X-ray emission around a disc galaxy drown from the GIMIC suite of N-body + smoothed-particle hydrodynamics (SPH) simulations (Crain et al. 2009, 2010).

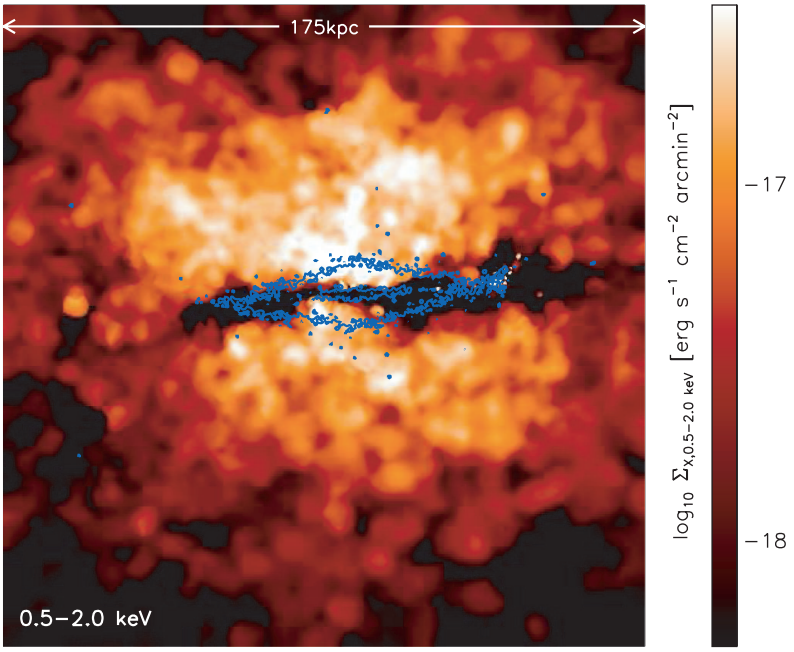

Figure 1.2: Cosmological corona of a simulated disc galaxy at redshift 0, drawn from the GIMIC suite of N-body + SPH simulations (Crain et al. 2009). Background color represents the X-ray surface brightness of the corona, while the overlapped blue contours trace the expected K-band surface density of the galaxy (from Crain et al. 2010).

Coronae of large disc galaxies are expected to be extended, dense and massive. In the giant spirals NGC 1961 and UGC 12591, X-ray emission has been detected out to more than 50 kpc from the centre (Anderson and Bregman 2011; Dai et al. 2012), indicating the presence of hot gas possibly accounting for $10 - 30\%$ of the missing baryons associated to these galaxies. Coronae are expected to be made of pristine material. Hodges-Kluck and Bregman (2012) modelled the diffuse X-ray emission in the inner $\sim 10\,\mathrm{kpc}$ around NGC 891, and obtained a best fit using a single gas component with a metallicity of $0.1\,Z_{\odot}$, in agreement with the theoretical expectation. Indirect probes for the presence of a cosmological corona around our Galaxy are discussed in Section 1.2.3.

1.2
The case of the Milky Way

1.2.1 Cold phase

In our Galaxy, the cold phase of the halo has been largely probed by isolated H I complexes at line-of-sight velocities inconsistent with those expected from the disc rotation (e.g. Oort 1966, 1970; van Woerden et al. 1985; Wakker and van Woerden 1997). Depending on their velocity, these objects are divided in *High-Velocity Clouds* (HVCs) and *Intermediate-Velocity Clouds* (IVCs).

HVCs are defined as H I clouds whose velocities in the local standard of rest deviate by more than $\sim 90\,\mathrm{km\,s^{-1}}$ from the speed predicted by a differentially rotating thin disc (Wakker 1991, and Section 2.2.1). An all-sky map of these complexes is shown in the top panel of Fig. 1.3. Recent works (e.g. Wakker et al. 2007, 2008) have revealed that HVCs are located at $\sim 10\,\mathrm{kpc}$ from the Sun ($\sim 6-7\,\mathrm{kpc}$ above the disc) and their metallicity is between 0.1 and 0.4 solar, which supports the idea of an external origin. For this reason, HVCs are regarded as the main evidence of an ongoing extragalactic accretion of cold gas onto the Galaxy disc (see also Section 1.3). However, the nature of these complexes is still poorly understood. It is possible that HVCs originate from gas that has been stripped from satellites of the Local Group (e.g. Putman et al. 2004), or that they are produced in the outskirt of the Galactic corona, as a consequence of perturbations exerted by the WHIM (Kereš and Hernquist 2009). Finally, HVCs can form inside warm filaments of gas that connect the Milky Way with the intergalactic medium, as suggested by the hydrodynamical cosmological simulations of Fernández et al. (2012).

IVCs are H I systems whose velocities in the local standard of rest deviate by $35 - 90\,\mathrm{km\,s^{-1}}$ from the speed predicted by a differentially rotating thin disc (van Woerden et al. 2004). The bottom panel of Fig. 1.3 gives an all-sky view of these complexes. These objects have metallicities close to the solar value and a disc-like kinematics, which suggests that they have been probably ejected from the Galactic disc by supernova feedback. However, IVCs are local features: they are placed at about $1-2\,\mathrm{kpc}$ from the Sun, and their total H I mass is of the order of $10^6\,\mathrm{M_\odot}$ (van Woerden et al. 2004).

Besides these large complexes at anomalous velocities, diffuse H I emission has been observed by Lockman (1984) in the lower halo of the inner Galaxy, between 4 and 8 kpc from the Galactic centre. This 'Lockman layer' has a scale height of $\sim 500\,\mathrm{pc}$, much larger than that of the H I thin disc ($\sim 150\,\mathrm{pc}$, e.g. Kalberla et al. 2007). Lockman (2002) confirmed that this layer is built up by single clouds with typical H I masses of $50\,\mathrm{M_\odot}$, and there is evidence for a slower rotation of this medium with respect to the thin disc (Levine et al. 2008). All these pieces of evidence support the idea that an H I thick disc, similar to that observed in external

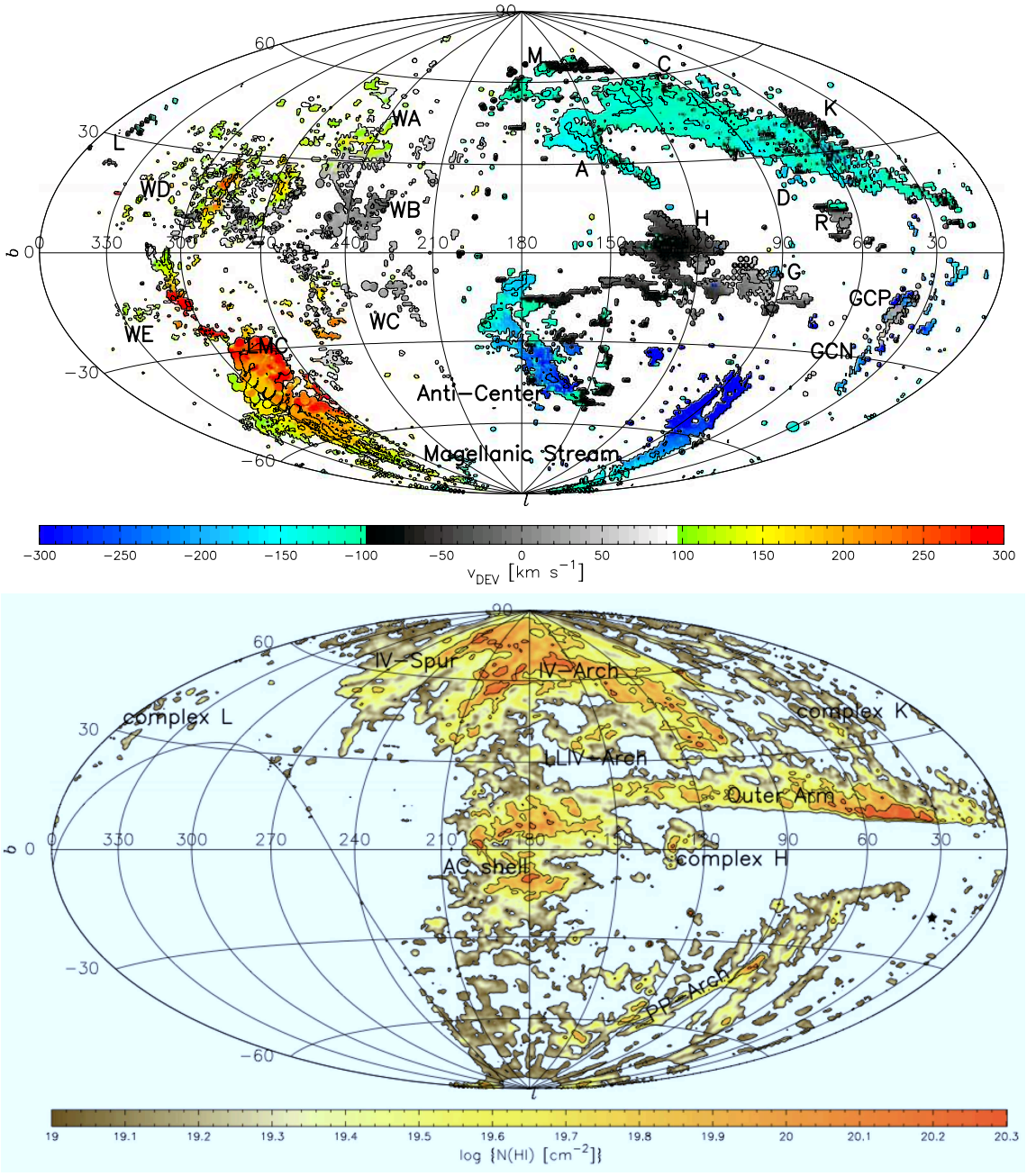

Figure 1.3: The High and the Intermediate-Velocity Clouds of the Milky Way. *Top panel*: Aitoff projection all-sky map of the HVCs, based on the Hulsbosch and Wakker (1988) and Morras et al. (2000) dataset. Contours at 2 and $20{\times}10^{18}\,\mathrm{cm}^{-2}$ in H I column density. Colors code deviation velocities v_{DEV} (see Section 2.2.1). Grey clouds have $|v_{\mathrm{LSR}}| > 90\,\mathrm{km\,s}^{-1}$ but $|v_{\mathrm{DEV}}| < 90\,\mathrm{km\,s}^{-1}$. From van Woerden et al. (2004). *Bottom panel*: Aitoff projection all-sky map of the IVCs, based on the Leiden-Dwingeloo Survey (Hartmann and Burton 1997). Contours at 1, 5 and $12 \times 10^{19}\,\mathrm{cm}^{-2}$ in H I column density. The IVC complex IV-WA is not shown. From van Woerden et al. (2004).

galaxies (Section 1.1.1), may be present in the Milky Way as well. We discuss this topic further in Chapter 2.

1.2.2 Warm-hot phase

The presence of diffuse ionised gas at temperature $\sim 10^4$ K extending up to ~ 1 kpc above the Galactic disc is classically probed by pulsar dispersion measurements from globular clusters, and constitutes the so-called 'Reynolds' layer' (e.g. Reynolds 1991). This is the equivalent of the DIG layers that are observed in external galaxies (Section 1.1.2). Stellar feedback plays an important role in building up this component, as suggested by the large quantities of ionised gas visible in Hα in the Cassiopeia and Ophiuchus superbubbles (Reynolds et al. 2001; Pidopryhora et al. 2007).

The advent of modern ultraviolet spectrographs, like the Far Ultraviolet Spectroscopic Explorer (FUSE), the Space Telescope Imaging Spectrograph (STIS) and the Cosmic Origins Spectrograph (COS), have unveiled the presence of ionised material at higher temperatures. The discovery of high-ion (Si II, Si III, Si IV, C III, C IV, O VI) absorption features towards background sources shows that gas at $2 < T < 30 \times 10^4$ K is widespread in the Galactic halo (e.g. Collins et al. 2003; Sembach et al. 2003; Savage et al. 2003; Shull et al. 2009; Lehner et al. 2012). Fig. 1.4 shows the all-sky velocity map for the O VI absorption features (circles) detected by Sembach et al. (2003).

The origin of these features is not clear, and may depend on their distance from the Galaxy, which is in most cases unknown. For absorbers at several tens or hundreds of kpc from the disc, explanations similar to those discussed for the warm-hot gas around external galaxies (Section 1.1.2) are probably valid. In some cases, absorption lines have been detected towards halo stars, indicating that at least a subsample of these features are located within ~ 15 kpc from the Sun (Zsargó et al. 2003; Lehner and Howk 2011). It has been argued that these 'local' features belongs to the ionised envelope that surrounds the classical HVCs, which is visible in Hα (e.g. Putman et al. 2003). This hypothesis is supported by the idea that HVCs form within large filaments of warm gas, as discussed in Section 1.2.1. In Chapter 5 we present an alternative picture in which these warm-hot absorbers originate from the interaction between galactic fountain clouds and the hot corona of the Milky Way.

1.2.3 Coronal phase

The existence of a Galactic hot corona was originally hypothesised by Spitzer (1956) as a medium to provide pressure confinement to the HVCs, which would otherwise evaporate on timescales of a few tens of Myr. Spitzer suggested that HVCs must be embedded in a hot plasma at the typical temperature of 10^6 K and electron density of $\simeq 5 \times 10^{-4}$ cm^{-3}. About 50 years later, observations of O VII absorption

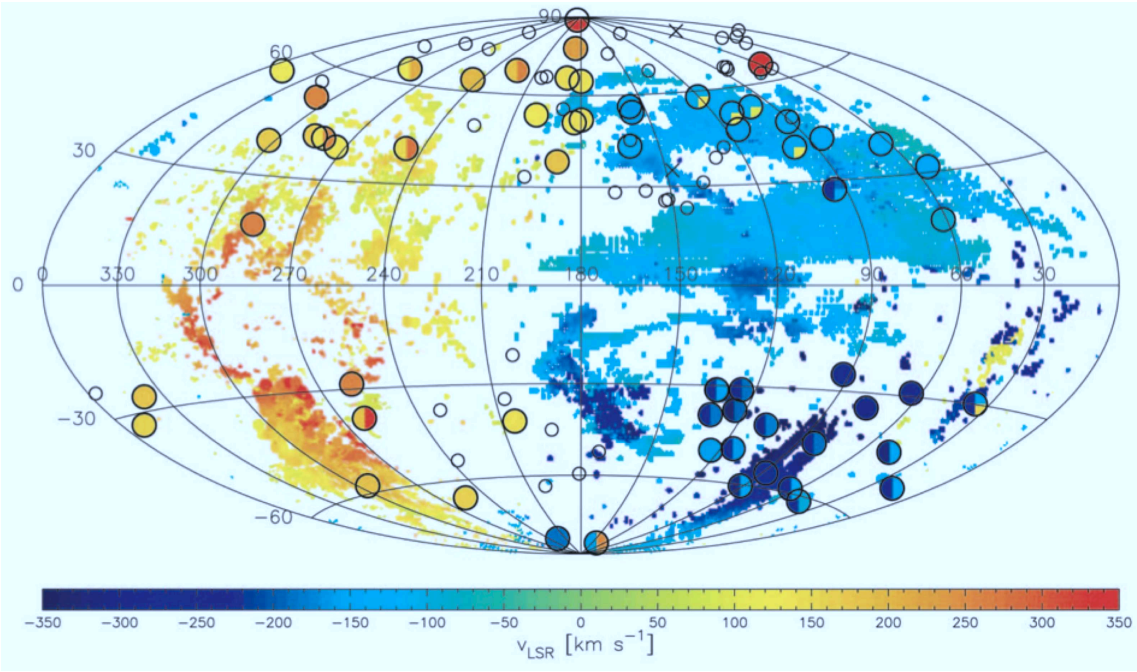

Figure 1.4: All-sky map of the high-velocity O VI absorption features detected by Sembach et al. (2003) (large filled circles, color-coded accordingly to their $v_{\rm LOS}$), probing the warm-hot phase of the Galactic halo. Small open circles represent non-detections. Background colors represent the mean $v_{\rm LOS}$ of the classical HVCs (from Sembach et al. 2003).

lines, probing material at temperature of $\sim 10^6$ K, still did not succeed to provide a definitive evidence for an extended hot medium around the Milky Way (Bregman and Lloyd-Davies 2007; Yao et al. 2008). Despite the lack of direct observational probes, there are several indirect pieces of evidence of its existence. The head-tail structure observed in several compact HVCs (Putman et al. 2011) can be easily explained by ram-pressure stripping exerted by the coronal medium onto these clouds (left panel of Fig. 1.5). Also, N-body+SPH simulations suggest that the stream of cold gas trailing the Magellanic Clouds, the so-called Magellanic Stream (top panel of Fig. 1.3), can not be explained without considering a diffuse ionised medium permeating the space around the Galaxy up to ~ 50 kpc from the disc (Mastropietro et al. 2005). At larger distances, the most striking evidence is constituted by the spatial segregation between H I-rich and H I-depleted satellites in the Local Group (e.g. Grcevich and Putman 2009), with respect to the Milky Way and M31 (Fig. 1.5, right panel).

1.3 Gaseous halos and gas accretion

A long standing problem in galaxy evolution is how star-forming galaxies like the Milky Way acquire their gas from the surrounding environment. The Galaxy is forming stars at a rate of $1-3\,{\rm M}_\odot\,{\rm yr}^{-1}$ (Chomiuk and Povich 2011) and would con-

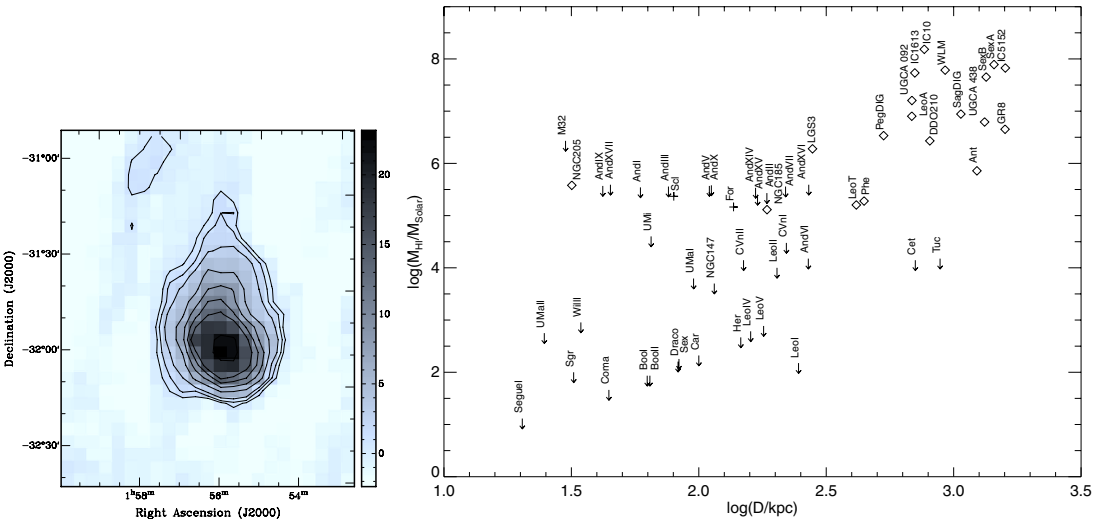

Figure 1.5: Two indirect pieces of evidence for the presence of a hot corona around the Galaxy. *Left panel*: head-tail structure of a compact Galactic HVC, indicating the presence of an ongoing interaction with a diffuse medium (from Putman et al. 2011). *Right panel*: H I mass vs. distance to the centre of the Milky Way or M31 (whichever is closer) for the dwarf galaxies of the Local Group. Satellites closer to the Milky Way or M31 are gas depleted, indicating an interaction with a denser diffuse medium. Downward arrows indicate upper limits, plus signs are ambiguous detections, diamonds indicate confident detections (from Grcevich and Putman 2009).

sequently consume its current stock of gas ($\sim 5.3 \times 10^9\,\mathrm{M}_\odot$, Binney and Merrifield 1998) in a few Gyrs. Studies of the solar neighborhood indicate that the star formation rate of the Milky Way has decreased only by a factor $2-3$ over the last 10 Gyr (e.g. Twarog 1980; Aumer and Binney 2009). The fact that our Galaxy kept forming its stellar disc at a roughly constant rate on cosmological timescales implies that its gaseous content gets continuously replenished. Also, chemical evolution models requires gas accretion of pristine material to account for the metallicity distribution of stars in the solar neighborhood (e.g. Chiappini et al. 1997). More in general, there are indications that at any time star-forming galaxies must have accreted extragalactic material at a rate proportional to their star formation rate (Hopkins et al. 2008; Fraternali and Tomassetti 2012).

In the local Universe, minor mergers and HVCs are the main candidates for accretion of cold gas onto galaxy discs. However, observations indicate that the accretion rate provided by these systems is largely insufficient to mach the galaxy SFRs. In external galaxies, minor mergers seem to account only for 0.1–0.2 $\mathrm{M}_\odot\,\mathrm{yr}^{-1}$, which is $\sim 10\%$ of the accretion required (Sancisi et al. 2008; Fraternali 2010). In the Milky Way, the situation is similar. The most recent estimate of accretion rate from HVCs gives a value of $\sim 0.08\,\mathrm{M}_\odot\,\mathrm{yr}^{-1}$ (Putman et al. 2012), and an upper limit to the gas accretion rate provided by the Magellanic Stream is $\sim 0.16\,\mathrm{M}_\odot\,\mathrm{yr}^{-1}$ (see Chapter 6).

An alternative possibility is that gas accretion manifests itself mostly as ionised gas. As discussed in Sections 1.1.2 and 1.2.2, UV absorption lines of high-ions are

commonly seen around galaxies, probing the presence of highly ionised material in the circumgalactic medium. After converting the measured ion column densities to a total gas mass, both Shull et al. (2009) and Lehner and Howk (2011) inferred accretion rates of ionised material onto the disc of the Milky Way of $\sim 1\,\mathrm{M}_\odot\,\mathrm{yr}^{-1}$. These results are in qualitative agreement with the adaptive mesh refinement (AMR) simulations of Joung et al. (2012) which suggest that, at the present epoch, the gas acquired by Milky-Way-like galaxies is organised in filamentary structure of warm-hot ($T \sim 10^{5-6}\,\mathrm{K}$) material.

In the last ten years, cosmological simulations in ΛCDM framework have shown that there are two main 'modes' by which galaxies acquire gas from the intergalactic medium. In dark matter halos with mass below a given threshold ($\sim 10^{11.4}\,\mathrm{M}_\odot$ in Kereš et al. 2005), the so-called 'cold mode' accretion dominates. In this mode, cold filaments of gas flowing through the cosmic web are able to reach the centres of the halos feeding the central galaxies without being shock-heated during their inflow. In structures above the mass threshold, gas accretion occurs instead in a 'hot mode', analogous to the classical scenario of galaxy formation proposed by White and Rees (1978). In this case, filaments are no longer able to reach the central object as they get shock-heated to the halo's virial temperature, building up an extended, diffuse corona of gas in hydrostatic equilibrium around the host galaxy. Because of the hierarchical formation of structures predicted by ΛCDM, the mass threshold that separates the two modes corresponds to a threshold in redshift: the high-redshift Universe ($z \sim 3$–4) is dominated by small structures in which galaxies accrete gas via the cold mode, whereas at lower redshift, when large structures have been formed, the hot mode becomes dominant. For a Milky-Way-like galaxy, the passage from the cold to the hot mode must have occurred at about $z \simeq 1$ (Kereš et al. 2009b).

Cosmological coronae can constitute a virtually infinite reservoir of gas to feed star formation. However, a recurring question is how these media can cool and accrete onto the host galaxies. It has been argued that cooling can occur spontaneously via thermal instability, producing ubiquitous clumps of cold gas in the coronal medium (e.g. Maller and Bullock 2004). However, deep H I surveys of galaxy groups systematically failed to find isolated floating clouds with H I masses $\gtrsim 10^6\,\mathrm{M}_\odot$ without optical counterparts at large distances from the host galaxies (e.g. Pisano et al. 2007; Chynoweth et al. 2009). Also, analytical calculations suggest that, in a corona stratified in a galactic potential, the combination of buoyancy and thermal conduction can efficiently suppress the growth of thermal perturbations (Binney et al. 2009; Nipoti 2010).

In N-body + SPH simulations, systems of cold clumps at large distances from Milky-Way-like simulated galaxies are commonly seen (Peek et al. 2008; Kaufmann et al. 2009). These clumps, when falling onto the disc, form a spinning medium with properties similar to those of the extraplanar H I (Kaufmann et al. 2006). In the last years, however, it became clear that the formation of clumps in these simulations is an artifact due to over-cooling problems of the SPH method. Indeed, AMR cosmological simulations do not show spontaneous cooling of the corona (e.g.

Joung et al. 2012), and this result is now confirmed also by state-of-the-art SPH simulations that adopt a more accurate treatment of the phase mixing (Hobbs et al. 2013). Therefore, the question of how the cosmological corona can cool and feed the galaxy disc remains open.

1.4 A model of galactic fountain

As mentioned in Section 1.1.1, several pieces of evidence suggest that H I halos are mainly built up by the galactic fountain cycle, i.e., a continuous flow of gas from the disc to the halo and back produced by stellar feedback. Fraternali and Binney (2006, hereafter FB06) developed a dynamical model of the galactic fountain and applied it to two nearby galaxies, NGC 891 and NGC 2403, known to have a substantial amount of extraplanar H I. In their model, particles - representing H I clouds - are ejected from the disc, and their orbits are followed until they return back to the midplane. The number of particles ejected at each radius is proportional to the local star formation rate density. The approach is purely ballistic, since particles move in a given gravitational potential and hydrodynamical effects are not taken into account. The output of the model is an artificial datacube (i.e., H I column density as a function of angular position and line-of-sight velocity) that can be directly compared to 21-cm observations. The parameters of the model (e.g. ejection angles and velocities) are derived by fitting the H I datacubes of the forementioned galaxies. FB06 found that their best-fit model reproduced very well the vertical distribution of the extraplanar H I of both galaxies, but could not account for the exact vertical lag in rotational velocity found in NGC 891 (Oosterloo et al. 2007) and for the radial inflow observed in NGC 2403 (Fraternali et al. 2002).

Fraternali and Binney (2008, hereafter FB08) modified their model by considering that fountain cloud particles, during their orbits, interact with a diffuse ambient gas having angular momentum lower than that of the disc. They assumed that this interaction produces accretion of the diffuse gas onto the fountain clouds at an exponential rate. The material harvested from the ambient gas by fountain cloud particles is then accreted onto the disc when the clouds return. Since gas particles must share their angular momentum with the ambient medium, they suffer a substantial decrease in their rotational speed. They also acquire an inward radial motion during the descending part of their orbits. The magnitude of this mass accretion is a free parameter of the model, and is derived, as in the previous case, by fitting the model to the H I datacubes of the two external galaxies. FB08 found an intriguing result: the amount of gas accretion required to reproduce the H I observations of NGC 891 and NGC 2403 is very similar to their respective current star formation rates. In FB08, the nature of the ambient medium with what the fountain clouds interact is not specified. They considered the cosmological corona but concluded

that accretion from such a medium should not take place, because its cooling time should exceed the time required for the coronal gas to flow past the fountain cloud.

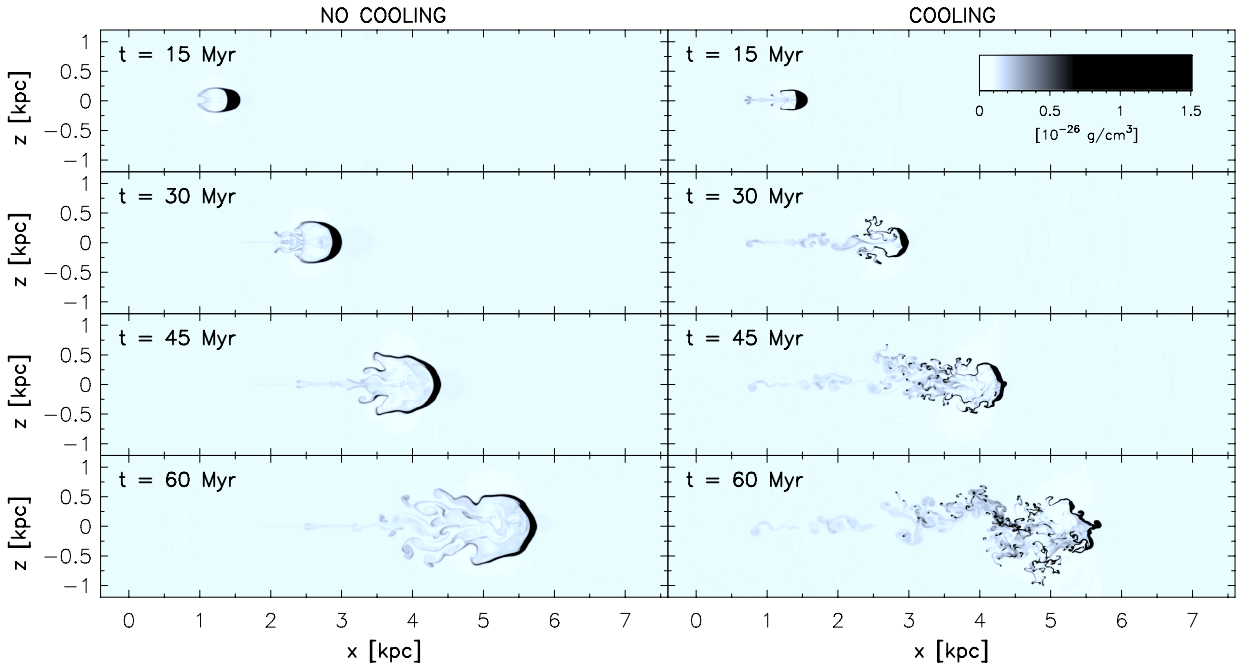

Figure 1.6: Density snapshots from the simulations of cloud-corona interaction of Marinacci et al. (2011) with and without radiative cooling (right-hand and left-hand panels respectively). The time at which the snapshots have been taken is indicated in each panel. The initial relative velocity between the cloud and the corona is $100\,\mathrm{km\,s^{-1}}$. The initial position of the cloud centre is $x = 0$ (from Marinacci et al. 2011).

Marinacci et al. (2010a) and Marinacci et al. (2011) investigated in more detail the interaction between fountain clouds and the cosmological corona by simulating clouds of cold ($10^4\,\mathrm{K}$) gas at solar metallicity traveling through a homogeneous medium with a temperature of $2\times10^6\,\mathrm{K}$ and a metallicity of $0.1\,Z_\odot$. They found that, as the cloud moves through the coronal medium, the Kelvin-Helmholtz instability develops. This produces a turbulent wake behind the cold gas in which material stripped from the cloud mixes with the ambient hot gas, increasing the metallicity of the latter and thus decreasing its cooling time. As a result, the amount of warm and cold gas in the cloud's wake increases exponentially with time, to the detriment of the coronal gas: i.e., the galactic fountain triggers the cooling of the cosmological corona, as the FB08 model required. Fig. 1.6 shows four density snapshots at different times of the simulation of Marinacci et al. (2011) with (right panels) and without (left panels) radiative cooling. When radiative cooling is switched on, the cloud gets more fragmented and condensation of coronal gas manifests itself as dense cloudlets located in the cloud's wake. These features are not present in the adiabatic run. Moreover, as the cloud moves through the corona, the cold and the hot phases exchange momentum with each other. The efficiency of this mass and momentum transfer depends critically on the relative velocity between the two gas

phases. Marinacci et al. (2011) found that the corona ceases to acquire momentum when the relative velocity between the two phases drops below $\sim 75\,\mathrm{km\,s^{-1}}$, because condensation immediately recaptures the momentum gained by the hot phase. The existence of this velocity threshold suggests that the corona must spin, at least in the regions closer to the Galaxy, but with a velocity $75-100\,\mathrm{km\,s^{-1}}$ lower than that of the disc.

These results are the starting point for our model of the galactic fountain of the Milky Way (Chapters 3 and 5).

1.5 This Thesis

This Thesis is a study of the gaseous halo of the Milky Way carried out via the modelling of the available H I and absorption-line data. We show that galactic fountain models can reproduce the fundamental properties of the different phases of this gas layer, and provide a consistent picture of how star-forming discs are connected to the extragalactic environment. In Chapter 2 we focus on the fundamental properties of the neutral hydrogen component of the halo. We use simple kinematical models to fit the 21-cm emission at anomalous velocities detected in the Leiden-Argentine-Bonn (LAB Kalberla et al. 2005) Survey, and we derive the mass, the scale-height, and the global kinematics of this component. We show that the total H I mass of this layer ($\sim 3\times10^8\,\mathrm{M_\odot}$) is much larger than the sum of the single IVCs and HVCs, and that most of this gas has a fountain-like kinematics. In Chapter 3 we use an improved version of the galactic fountain model of FB08, that takes into account the interaction with a spinning hot corona, to fit the anomalous H I emission in the LAB data. For a proper choice of the fountain parameters, the model can nicely reproduce the position-velocity distribution of the H I halo. Models that take into account the interaction between fountain clouds and the Galactic corona perform much better and predict a global accretion of coronal gas onto the Galactic disc at a rate of a few $\mathrm{M_\odot\,yr^{-1}}$. In Chapter 4 we analyze the gaseous halos of two different synthetic disc galaxy, including a Milky-Way-like spiral, as resulting from recent N-body + SPH simulations. We show that the H I halo properties of these objects are different from those of real galaxies, and vary significantly depending on how stellar feedback is implemented and on the resolution of the simulation. In Chapter 5 we extend the dynamical model described in Chapter 3 to the warm-hot component of the gaseous halo, showing that most of the high-ion UV absorption features detected towards background sources are consistent with being produced by the interaction between the fountain clouds and the Galactic corona. In Chapter 6 we discuss the results obtained and draw our conclusions.

Chapter 2

Global properties of the Galactic HI halo

2.1 Introduction

In the last decade, sensitive H I observations have revealed that neutral hydrogen of nearby disc galaxies is not confined to a thin disc, but a significant fraction of it ($\sim 5-10\%$) extends for a few kiloparsecs into the halo region (Fraternali et al. 2002; Boomsma et al. 2005; Oosterloo et al. 2007; Fraternali 2010). These H I layers have kinematics similar to that of the disc H I (Fraternali et al. 2002), but with some peculiar properties: a) they rotate more slowly (Oosterloo et al. 2007); b) they show vertical motions (Boomsma et al. 2005); c) they have a global inflow (Fraternali et al. 2002). Galactic fountains (Shapiro and Field 1976; Bregman 1980; Fraternali and Binney 2006) and extra-galactic accretion (Oort 1970; Kaufmann et al. 2006; Kereš and Hernquist 2009) are considered the main processes that contribute to create these media.

In the case of the Milky Way, the study of the extraplanar H I is particularly arduous because of the inside view, which makes it difficult to disentangle between a disc and a halo component. High and Intermediate-Velocity Clouds (HVCs and IVCs, Wakker and van Woerden 1997) have long been regarded as the main evidence for the presence of an H I medium above the disc. Studies of absorption lines in the UV spectra of background targets have revealed that the HVCs are located in the halo region at distances of ~ 10 kpc from the Sun (van Woerden et al. 2004; Wakker et al. 2007, 2008, e.g.), and have a metallicity of $\sim 0.2\,Z_\odot$ (e.g. Tripp et al. 2003, for complex C), which suggests an external origin for these objects. In contrast, the IVCs (H I clouds with a lower anomalous velocities) seem to constitute a different population: their metallicity is higher ($\sim 1\,Z_\odot$) and their kinematics more closely follow the Galactic rotation, so these clouds have been regarded as possible Galactic fountain objects (Wakker 2001). However, classical IVCs are placed at 1–2 kpc from the Sun (van Woerden et al. 2004) thus they can not be representative for the whole gas layer produced by the Galactic fountain mechanism.

HVCs and IVCs are not the only observable H I features of the Galactic halo. A large amount of diffuse H I emission has been found by Lockman (1984) in the lower halo regions of the inner Galaxy. This 'Lockman layer' extends to about 1 kpc above the disc and shows signs of a rotational lag similar to that found in the H I thick discs of external galaxies (Levine et al. 2008). Also, ionised hydrogen at temperature of about 10^4 K is present up to ~ 1 kpc above the disc and constitutes the so-called 'Reynolds layer' (Reynolds et al. 1973; Reynolds 1991). This component is the analogous of the DIG layers visible in Hα in external star-forming galaxies (Section 1.1.2) and is presumably built up by photo-ionised gas ejected from the disc by stellar feedback. Signs of an ongoing galactic fountain in the Milky Way are visible in the Ophiucus superbubble, a large structure of neutral and ionised hydrogen located in the proximity of a young stellar cluster and extending up to $\sim$3.4 kpc above the disc (Pidopryhora et al. 2007).

The most comprehensive attempt to describe the H I halo of the Milky Way as a global structure has been that of Kalberla and Dedes (2008, hereafter KD08), who derived the whole Galactic H I distribution via a spatial reconstruction of the Leiden-Argentine-Bonn (LAB, Kalberla et al. 2005) H I Survey dataset. The de-projection of the data relies sensitively on the rotation curve assumed, which has been derived by modelling the Galactic dark matter halo (Kalberla et al. 2007) under the assumption that gravity dominates the dynamics of the gas everywhere. KD08 found that $\sim 10\%$ of the Galactic H I is located outside the disc and is highly turbulent. In contrast, the classical HVCs and IVCs account only for $< 1\%$ of the total H I mass (e.g. Putman et al. 2012) of the Milky Way, indicating that these complexes are probably only the 'tip of the iceberg' of a much massive and extended extraplanar H I component.

In this Chapter we study the global H I component that surrounds the disc of our Galaxy. We make no assumption about the dynamical state of this gas[1], but simply derive its global properties directly from the data. Section 2.2 describes how we model the halo emission and explains the effect of the various kinematical parameters. In Section 2.3 we derive the vertical rotational gradient in the inner halo, and in Section 2.4 we estimate the kinematical parameter of the Galactic halo. A discussion of the physical interpretation of these parameters follows in Section 2.5.

The results of this Chapter have been published in paper form in Marasco and Fraternali (2011).

[1] A dynamical description of the Galactic H I halo will be given in Chapter 3

2.2 Modelling the H I halo

The neutral hydrogen of disc galaxies is commonly studied using three-dimensional data, also known as 'datacubes', representing the H I emission as a function of the angular position in the sky and the velocity along the line of sight. In order to study the global properties of the Galactic H I halo, the LAB Survey (Kalberla et al. 2005) represents the best available dataset in terms of resolution (0.6°), sensitivity (rms noise $\simeq 0.08\,\mathrm{K}$ in brightness temperature), spatial and kinematic coverage (all-sky at $-450 < v_{\mathrm{LSR}} < 400\,\mathrm{km\,s^{-1}}$).

Here, we assume that the Galactic H I emission is caused by two distinct components: the disc and the halo. The physical and kinematical properties of the first are assumed to be known (Section 2.2.1). In contrast, the halo properties are not known and its distribution and kinematics have to be derived by fitting a number of free parameters. We model the Galactic H I emission by building artificial datacubes (or 'modelcubes') with the same resolution and total flux as the LAB dataset, and we compare them with the latter.

Below we use two coordinate systems. The first is the Galactic coordinate system, where l is the Galactic longitude, b the Galactic latitude, and v_{LOS} is the velocity along the line of sight. The second is a cylindrical system centred at the Galactic Centre, where R is galactocentric radius, ϕ is the azimuthal angle (set to 0° at $l = 0°$) and z is the height from the mid-plane.

2.2.1 Removing the H I disc emission

In order to better visualise the extraplanar H I emission of the Milky Way, we first remove the emission associated with the disc by applying the standard technique that makes use of the *deviation velocity* (Wakker 1991). For a fixed (l, b) pair, the deviation velocity v_{DEV} is the difference between the observed v_{LOS} and the highest velocity predicted by a disc model. It depends on the rotation curve and on the adopted disc geometry. We assume circular orbits and a flat rotation curve, independent of z, with rotation velocity $v_\phi(R, z) = v_\odot = 220\,\mathrm{km\,s^{-1}}$. For the disc geometry we use the flared disc described in KD08, with the scale-height given by $h_{\mathrm{s}}(R) = h_\odot e^{(R - \mathrm{R}_\odot)/R_{\mathrm{f}}}$, where $h_\odot = 0.15\,\mathrm{kpc}$ and $R_{\mathrm{f}} = 9.8\,\mathrm{kpc}$. The $h_{\mathrm{s}}(R)$ holds for $R > 5\,\mathrm{kpc}$ and it is constant for inner radii.

The line-of-sight velocity of a cloud at a distance d from the Sun in a generic direction (l, b) is given by

$$v_{\mathrm{LOS}}(l, b, d) = \left(v_\phi(R, z) \frac{\mathrm{R}_\odot}{R} - v_\odot \right) \sin(l) \cos(b)\,, \tag{2.1}$$

where $\mathrm{R}_\odot = 8.5\,\mathrm{kpc}$ is the distance of the Sun from the Galactic Centre. The maximum and the minimum values of eq. (2.1) (the 'envelope' of v_{LOS}) have to be

determined by varying d in the range $[0, d_{\rm max}]$, where $d_{\rm max}$ is $d(R_{\rm max}, z_{\rm max})$. We assume $R_{\rm max} = 35\,{\rm kpc}$ (as in KD08) and $z_{\rm max}$ is chosen to be $7 \times h_{\rm s}(R)$, i.e. about 1 kpc in the central parts. With these assumptions the envelope is large, ensuring that the disc emission is completely removed. Given this envelope, $v_{\rm DEV}$ can be easily estimated for any (l, b); in agreement with the literature (van Woerden et al. 2004), we cut out data points at $|v_{\rm DEV}| < 35\,{\rm km\,s^{-1}}$. We also remove the H I emission of the Outer Arm region (a distant and bright spiral arm that belongs to the warp; Habing 1966), the Magellanic Clouds, the Magellanic Stream and external galaxies. These latter are easily recognizable in the LAB data as tiny stripes of H I emission elongated by more than $100\,{\rm km\,s^{-1}}$ in the velocity axis. Notably, the geometrical parameters used to describe the shape of the disc weakly affect the deviation-velocity calculation. For example, assuming a disc with no flare and 2 kpc of thickness gives an envelope of $v_{\rm LOS}$ very similar to the one above. The same is valid if we adopt a more realistic rotation curve (see Appendix A) instead of a constant rotation velocity.

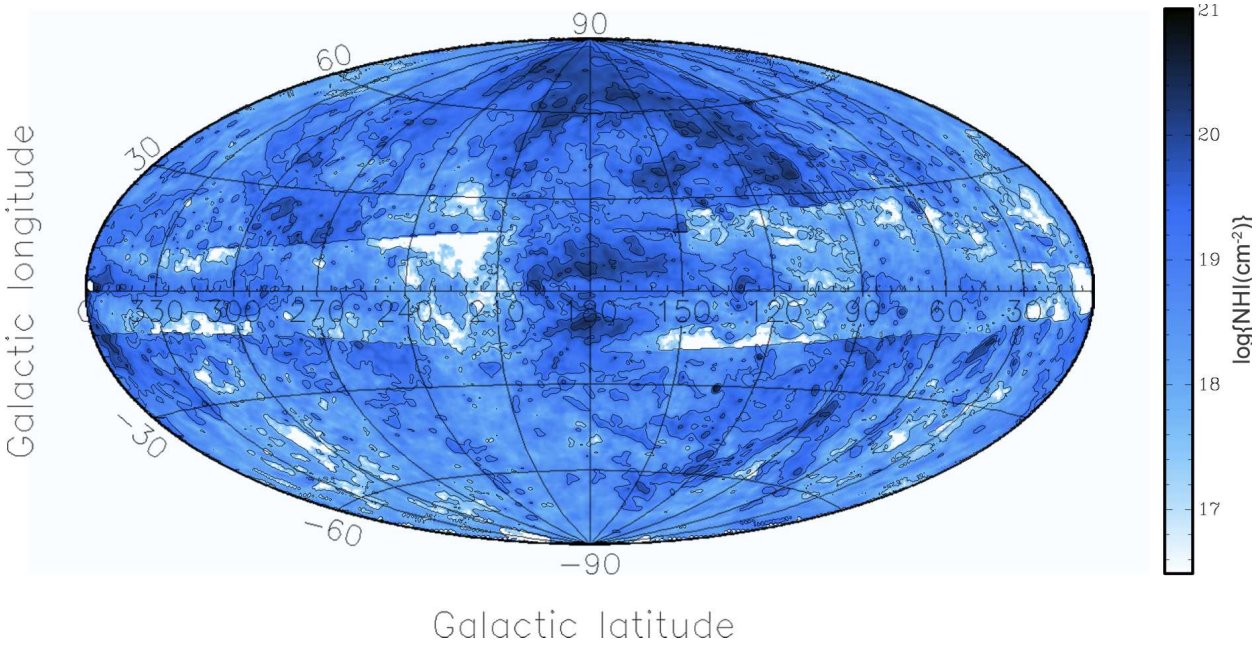

Figure 2.1: All-sky map of the H I halo of the Milky Way: velocity integrated H I map obtained from the LAB Survey after removing the disc emission, the Magellanic Clouds and Stream and the Outer Arm. The sharp edges close to the mid-plane are artefacts of the disc removal. The dataset has been smoothed to 1° resolution. Contour levels are 0.5, 10, 50 and $120 \times 10^{18}\,{\rm cm^{-2}}$ in column density.

Figure 2.1 shows the resulting velocity-integrated H I emission obtained after the disc exclusion. All the H I emission in Fig. 2.1 is incompatible with a thin disc in differential rotation. Some HVCs and IVCs can be recognised in this map, and they appear to be embedded in a diffuse extended medium. This medium is visible in almost any direction of the sky and is the main subject of our investigation.

2.2.2 The H I halo distribution and kinematics

We model the H I halo of the Milky Way assuming a density distribution $\rho(R, z)$ analogous to that used by Oosterloo et al. (2007) for the nearby galaxy NGC 891, described by the formula

$$\rho(R,z) = \rho_0 \left(1 + \frac{R}{R_\mathrm{g}}\right)^{\gamma} \exp\left(-\frac{R}{R_\mathrm{g}}\right) \mathrm{sech}^2\left(\frac{z}{h_\mathrm{g}}\right) , \tag{2.2}$$

where $R_\mathrm{g} = 1.61\,\mathrm{kpc}$ and $\gamma = 4.87$, as recently estimated by Marinacci et al. (2010b). For a given kinematics, the only parameter that critically influences the resulting modelcube is the scale-height, while the scale-radius R_g has a minor effect. Therefore we set h_g as a free parameter, and we fix R_g and γ to the above values. Furthermore, we set the central density ρ_0 so that the total flux of the model equals the flux of the LAB data, once the disc emission has been excluded.

We model the kinematics of the halo using three parameters:

1. the vertical gradient of rotation velocity $dv_\phi/d|z|$, so that $v_\phi(z) = v_\odot + |z| \times dv_\phi/d|z|$ for every R;
2. the velocity along the z-direction v_z, assumed to be positive if the gas is escaping from the disc;
3. the velocity along the R-direction v_R, assumed to be positive if the gas is moving to larger radii.

At first, we assume that these parameters do not depend on R and z. The resulting velocity field $\mathbf{v} = (v_R, v_\phi, v_z)$ has to be projected along the line of sight to obtain v_LOS:

$$v_\mathrm{LOS}(l,b,d) = v_R \left(\frac{R^2 + d^2 - \mathrm{R}_\odot^2 - z^2}{2\,R\,d}\right) + v_z \sin(b) + \\ + \left(\frac{\mathrm{R}_\odot}{R} v_\phi - v_\odot\right) \sin(l)\cos(b) , \tag{2.3}$$

where d is the heliocentric distance. Given $\rho(R, z)$ and $\mathbf{v}(R, z)$, the H I column density $N_\mathrm{HI}(l, b, v)$ or the brightness temperature $T_\mathrm{B}(l, b, v)$ can be easily derived. We also include an isotropic velocity dispersion of $20\,\mathrm{km\,s^{-1}}$ (see Oosterloo et al. 2007) for the H I halo, spreading the computed components $N_\mathrm{HI}(l, b, v)$ over the neighbouring channels.

2.2.3 Toy models

To understand the effects of the different kinematic parameters on the modelcubes we first build some 'toy' models with straightforward kinematics. For simplicity we set the H I halo scale-height to 2 kpc and its mass to $5 \times 10^8\,\mathrm{M}_\odot$. We remove the

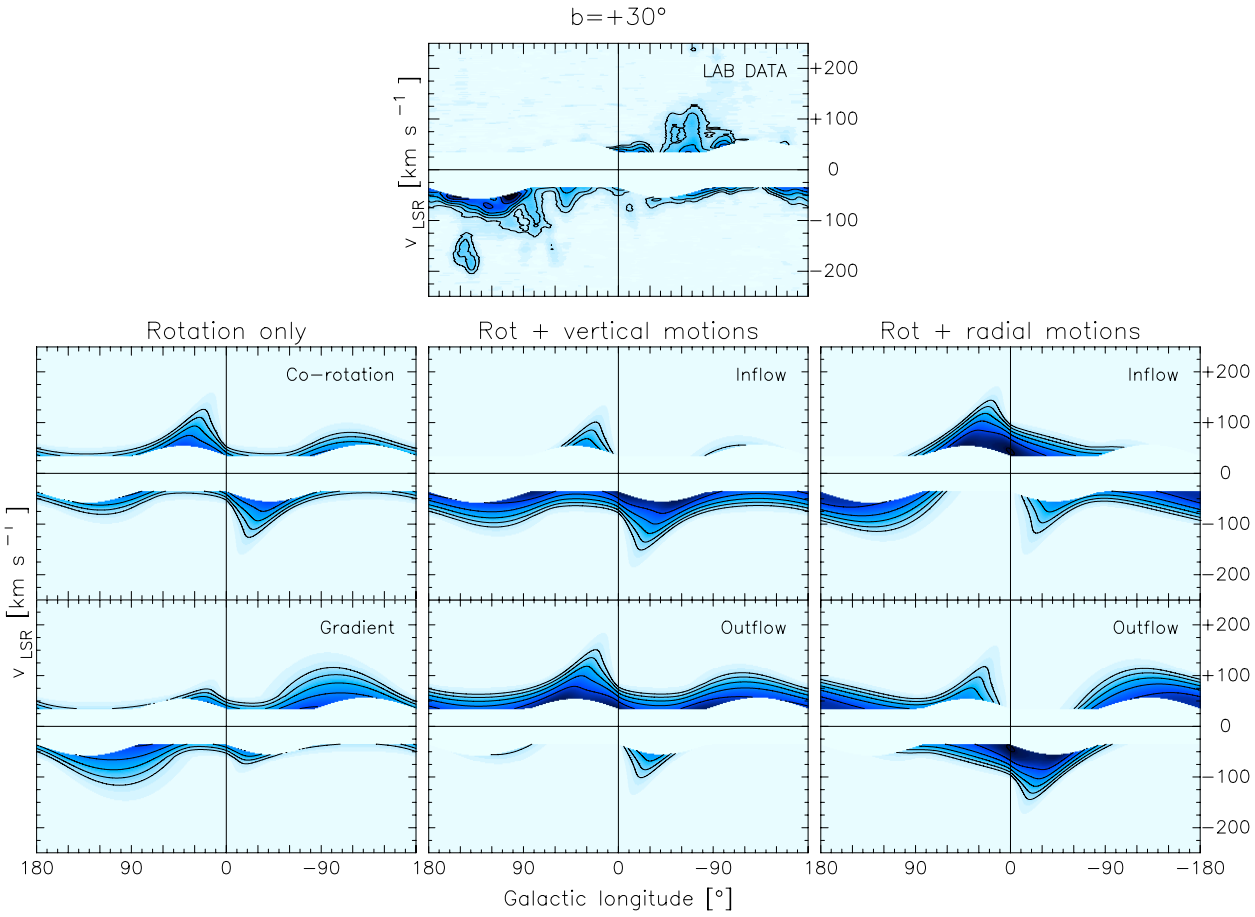

Figure 2.2: $l-v$ slices at $b = 30°$ for the LAB dataset (top panel) and for six different halo models. *Left panels*: halo corotating with the disc (top) and rotating with a vertical lag $dv_\phi/d|z| = -20\,\mathrm{km\,s^{-1}\ kpc^{-1}}$ (bottom); *central panels*: halo corotating with vertical motions $v_z = -50\,\mathrm{km\,s^{-1}}$ (top) and $v_z = +50\,\mathrm{km\,s^{-1}}$ (bottom); *right panels*: halo corotating with radial motions $v_R = -50\,\mathrm{km\,s^{-1}}$ (top) and $v_R = +50\,\mathrm{km\,s^{-1}}$ (bottom). Regions with $|v_{\mathrm{DEV}}| < 35\,\mathrm{km\,s^{-1}}$ have been excluded. All the cubes have been smoothed to 8° resolution. Contour levels are 40, 80, 160, 320, 640 and 1280 mK in brightness temperature.

disc emission as discussed in 2.2.1. Figure 2.2 shows the longitude-velocity slice $(l-v)$ at the galactic latitude $b = 30°$ for the LAB data for six different models. As anticipated, the data panel shows that a large fraction of H I emission still remains after the disc cut in v_{DEV} (white region at low velocities) .

A halo with the same kinematics as the disc (centre left panel) poorly reproduces the data: in this model the inner halo regions ($l \in [0°, 90°]$ at $v_{\mathrm{LOS}} > 0$ - the 'receding' quadrant QI, and $l \in [-90°, 0°]$ at $v_{\mathrm{LOS}} < 0$ - the 'approaching' quadrant QIV) show 'horn-like' structures because of the fast rotation of the gas, whilst in the data these structures are absent. Also, the regions related to the external halo ($l \in [0, 180°]$ at $v_{\mathrm{LOS}} < 0$ and $l \in [-180, 0°]$ at $v_{\mathrm{LOS}} > 0$) do not reach the same v_{LOS} of the data. Adding a vertical lag in the halo rotation (bottom left panel) improves the comparison with the data: the horns disappear thanks to the lower rotation, while the external halo reaches higher velocities along the line of sight. This comparison

suggests that the H I halo of the Galaxy does not corotate with the disc.

A vertical motion (central panels) globally shifts the halo emission to negative $v_{\rm LOS}$ for $v_z<0$ or to positive $v_{\rm LOS}$ for $v_z>0$, because the gas is approaching the line of sight with an additional velocity $v_z\sin(b)$ for any fixed b. This motion is not visible at low latitudes, but dominates at the highest ones. The high-latitude emission in the LAB data occurs mostly at $v_{\rm LOS}<0$, suggesting a global vertical infall of the gas, as already pointed out by the analysis of the HVCs and IVCs kinematics (Bajaja et al. 1987). A global vertical outflow from the disc is excluded.

The effects of radial motions (right panels) are not easily foreseen because of the off-centred position of the Sun with respect to the rotation axis. Obviously around the anti-centre region ($l=180°$) the emission is shifted towards negative (for $v_R<0$) or positive (for $v_R>0$) velocities, because the gas is almost directly approaching the Sun or receding from it. Around the Galactic Centre the $l-v$ profile is globally 'deformed' (with respect to the corotating case) towards positive velocities for $v_R>0$ and towards negative ones for $v_R<0$.

This qualitative analysis suggests that the H I halo of the Milky Way has two kinematical properties: lagging rotation and global infall. In principle we could quantify the various velocity components by comparing our models with the data. But these models were built by assuming a value for the scale-height of the H I halo, and this is a critical assumption because there is a *degeneracy* between the vertical rotational gradient and the halo scale-height indeed. Because of projection effects, halving $h_{\rm g}$ and doubling $dv_\phi/d|z|$ (or vice versa) distributes the emission over the channels in similar ways at the high latitudes. As an example, Fig. 2.3 shows the $l-v$ slice at $b=45°$ for two halo models with circular rotation: the first with $h_{\rm g}=2\,$kpc and $dv_\phi/d|z|=-20\,{\rm km\,s^{-1}\ kpc^{-1}}$, the second with $h_{\rm g}=0.5\,$kpc and $dv_\phi/d|z|=-80\,{\rm km\,s^{-1}\ kpc^{-1}}$. The total fluxes of the models were normalised to the same value. Evidently the first model is almost indistinguishable from the second even if the parameters used differ significantly.

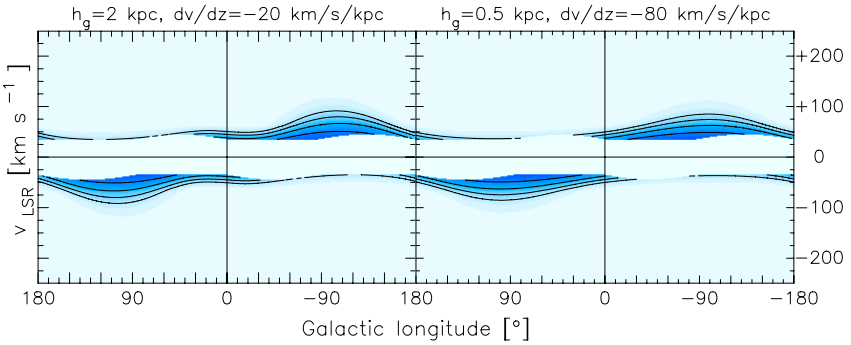

Figure 2.3: Effect of the gradient-thickness degeneracy: the $l-v$ slices at $b=45°$ for the two different rotating halo models are almost indistinguishable. The disc emission has been excluded and the cubes have been smoothed to 8° resolution. Contour levels are 40, 80, 160, 320, 640 and 1280 mK in brightness temperature.

Since at high latitudes we are not able to distinguish between a strongly lagging

thin halo and a weakly lagging thick halo, we need an independent measurement for either $h_{\rm g}$ or $dv_\phi/d|z|$. We tried to estimate $h_{\rm g}$ from the emission along b in the H I velocity-integrated maps (which do not depend on the kinematics), but we found that this method is also degenerate. Consequently, we search for an independent measurement of the velocity gradient.

2.3 The rotation velocity gradient in the inner Galaxy

2.3.1 Method of tangent-point

The classical method to estimate the mid-plane rotation curve in the inner Galaxy (inside the solar circle) is that of the *tangent-point*: if the gas is in circular rotation without turbulent motions, the highest velocity measured in the profile (the 'terminal velocity' $v_{\rm ter}$) for any direction l is the line-of-sight velocity of the ring at the tangent-point radius $R_{\rm tan} = {\rm R}_\odot|\sin(l)|$ (the 'tangent velocity' $v_{\rm tan}$). Therefore, using eq. (2.1) for $b = 0^\circ$ we have $v_\phi(R_{\rm tan}, 0) = |v_{\rm ter} + v_\odot \sin(l)|$. Turbulent motions smear the H I line profiles, so $v_{\rm ter}$ is actually lower than the highest measurable velocity and it has to be searched for in the wings of the profiles using some assumptions. Some authors used a brightness temperature threshold (Malhotra 1995), others chose values related to the first peak in the spectrum (Kerr 1962, 1964) or to the integral of the profile past this peak (Shane and Bieger-Smith 1966). Levine et al. (2008) used a more complex approach based on the fitting of the whole line profile around the tangent velocity (Celnik et al. 1979). In Appendix A we present a novel approach, based on an iterative fitting algorithm.

All those methods that make use of the end-line peak in the spectra - including both that of Levine et al. (2008) and that described in Appendix A - are not applicable at high latitudes since this peak is too faint to be detected because of the falloff in the H I density at high z. Thus, we adopt a different approach, which is often used for the external galaxies: we assume a certain velocity dispersion for the gas, and performe a Gaussian fit to the emission falloff for each line profile, leaving the amplitude and the mean ($v_{\rm ter}$) of the Gaussian as free parameters. This method gives similar results as most of the approaches described above if applied in the mid-plane, but it also has the advantage to be suitable at different latitudes (see below). In exchange, it requires a higher signal-to-noise (S/N) ratio compared to other approaches, because it uses only the last points at low brightness temperature for each spectrum. To improve the S/N we smooth the cubes: tests performed on the toy models (Section 2.3.2) showed that after smoothing to $3^\circ - 4^\circ$ this approach works well for values of S/N typical of the LAB data.

To estimate the inner velocity gradient of the Milky Way we applied the tangent-point method outside the mid-plane. For any (l, b) in the inner Galaxy, the tangent

point is at $R_{\rm tan} = {\rm R}_\odot |\sin(l)|$ and $z_{\rm tan} = {\rm R}_\odot \cos(l)\tan(b)$. However, if the gas is not exactly in corotation at any height from the plane, $v_{\rm ter}$ is no longer equal to $v_{\rm tan}$. For example, in a lagging halo for any $b \neq 0^\circ$ the highest velocity emission comes from a region closer to us than the tangent point, and if we use the method described, we would assign to $v_\phi(R_{\rm tan}, z_{\rm tan})$ a value valid for a lower z: basically we would overestimate v_ϕ. The question is whether this *geometric bias* forbids the derivation of $v_\phi(R,z)$, or if there is a window in the (R,z)-space where this effect is negligible and therefore

$$v_\phi(R_{\rm tan}, z_{\rm tan}) \simeq \left| \frac{v_{\rm ter}}{\cos(b)} + v_\odot \sin(l) \right| . \qquad (2.4)$$

We check this by builing 3D models in Section 2.3.2, finding that it is feasible to estimate the rotation up to a few kiloparsecs from the mid-plane.

2.3.2 Testing the method

We apply the tangent-point method to different models to verify that a) in the presence of moderate gradients, the geometrical bias produces negligible errors and dv_ϕ/dz can be correctly derived; b) different density distributions weakly affect the estimate of the gradient. We build two modelcubes with the same H I halo mass ($5 \times 10^8\,{\rm M}_\odot$) and the same kinematics: $v_\phi(R,0) = 220\,{\rm km\,s^{-1}}$ and $dv_\phi/d|z| = -20\,{\rm km\,s^{-1}\ kpc^{-1}}$. In the first (model A) the H I density distribution follows eq. (2.2), in the second (model B) the halo density decreases exponentially as $|z|$ increases and is constant in R (see insets in Fig. 2.4). The vertical scale-height is 2 kpc for both models. We add a velocity dispersion of $20\,{\rm km\,s^{-1}}$ for the halo gas.

We apply the method described in Section 2.3.1 to both models, calculating $v_\phi(R,z)$ for $|z| < 6$ kpc using the input H I velocity dispersion as the sigma of the Gaussian for fitting the profiles. Without noise we are able to perform fits using components with an arbitrary low $T_{\rm B}$, taking into account only the dispersion falloff of the lines. In this ideal case the resulting velocity fields of both models are perfectly reconstructed for $1 < R < 5$ kpc and $1 < z < 4$ kpc. Outside this window the geometric bias (see 2.3.1) is no longer negligible.

We add a Gaussian noise to our models, with a dispersion of 50 mK ($1\sigma_{\rm rms}$ of the Hanning-smoothed release of the LAB dataset), and we perform the fits using only the components with $T_{\rm B} > 2.5\sigma_{\rm rms} = 125$ mK: the velocity field is unsatisfactory for model B, showing that a higher S/N is required. To improve the S/N, we smooth the modelcubes to 4° and perform another Hanning smoothing: this brings the average $1\sigma_{\rm rms}$ to 5 mK and the threshold of the fit to 12.5 mK. We re-perform the fits by averaging all profiles within the new beam and using only independent points, finding that for any fixed R between 2 and 5 kpc the $v_\phi(z)$ curve can be fitted with a straight line that agrees well with the input slope. We average $v_\phi(z)$ over a range of R in order to improve the statistics on the single measurements, at 4° of resolution there are about three independent points for $3.5 < R < 5.5$ kpc.

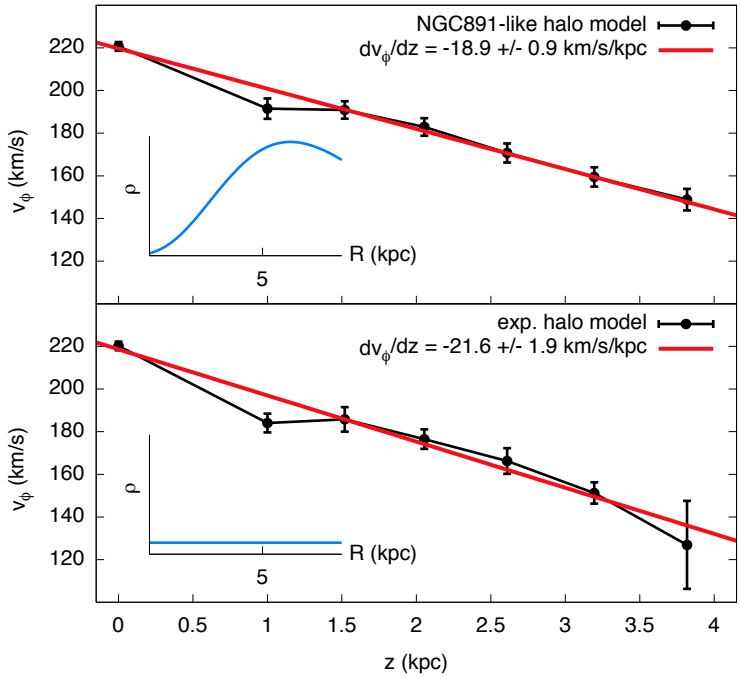

Figure 2.4: Rotation velocity $v_\phi(z)$ (black points) averaged in the region $3.5 < R < 5.5\,\mathrm{kpc}$ computed with the tangent point method for the model A (top panel) and B (bottom panel). The red thick line is the linear fit. The insets show the radial density distribution from $R = 0$ to $\mathrm{R}_\odot$.

Figure 2.4 shows the R-averaged $v_\phi(z)$ curve derived for the two models with the method described. We also included a point for the mid-plane. We assumed that the error on the single measurement $v_\phi(z)$ is given by the squared sum of three terms: a) the rms of the $v_\phi(z)$ distribution over $3.5 < R < 5.5\,\mathrm{kpc}$; b) the maximum statistical error on the Gaussian fits computed in this distribution; c) a 'base' error of $4\,\mathrm{km\,s^{-1}}$ that takes into account uncertainties in the gas velocity dispersion. Fitting the points with a straight line we obtain $dv_\phi/d|z| = -18.9 \pm 0.9\,\mathrm{km\,s^{-1}\ kpc^{-1}}$ for model A and $-21.6 \pm 1.9\,\mathrm{km\,s^{-1}\ kpc^{-1}}$ for model B, in good agreement with the input gradient. We tested this method further by varying the vertical scale-height of model A from 0.75 kpc to 3 kpc, obtaining similar results. Our method depends weakly on the density distribution, so we can proceed to apply it to the LAB data.

2.3.3 Application to the data

The H I distribution in the Milky Way is neither exactly axisymmetric nor b-symmetric. Therefore we derive four $v_\phi(z)$ curves in the inner Galaxy ($R < \mathrm{R}_\odot$), one for each quadrant (QI and QIV, see Section 2.2.3) and for the positive and the negative latitudes separately. We use the LAB dataset smoothed both spatially (4°) and in velocity (Hanning), averaging the profiles within the new beam and using only the independent points. The threshold used is $2.5 \times 6\,\mathrm{mK}$ for QI and $2.5 \times 4\,\mathrm{mK}$ for QIV, since the noises in regions at positive and negative declinations slightly differ. We

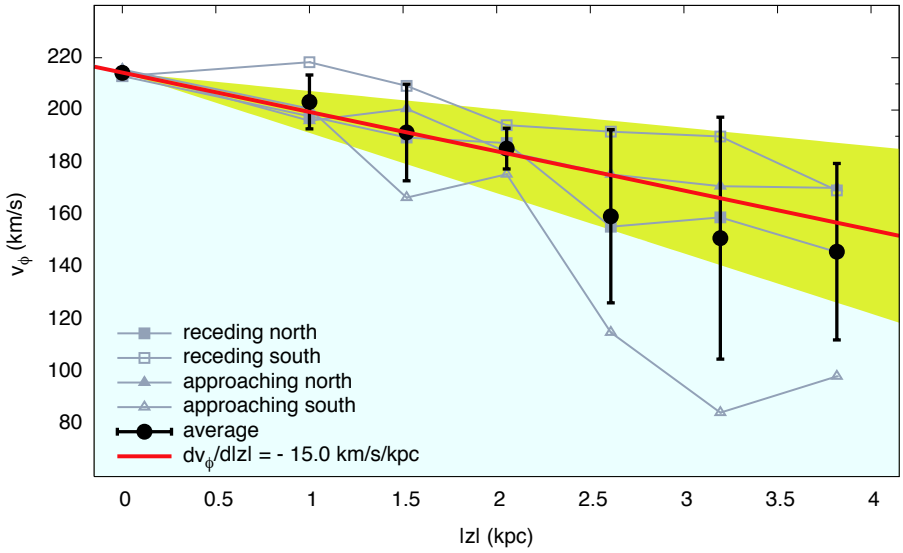

Figure 2.5: Vertical rotational gradient in the inner Milky Way. *Thin lines*: rotation velocity $v_\phi(z)$ averaged in the region $3.5 < R < 5.5$ kpc derived with the LAB dataset using the tangent point method. Each curve stands for a different region. Error bars are not shown. *Black points*: average $v_\phi(z)$ curve. *Thick red line*: linear fit to the average curve. The yellow region stands for the 2σ error on the gradient ($1\sigma = 4\,\mathrm{km\,s^{-1}\ kpc^{-1}}$).

assume a velocity dispersion of $20\,\mathrm{km\,s^{-1}}$ for the halo gas. This value was estimated for NGC 891 by Oosterloo et al. (2007). In the Milky Way, Ford et al. (2008) found a cloud-to-cloud velocity dispersion of $18\,\mathrm{km\,s^{-1}}$ for the H I emission in the lower halo regions. The errors on the single fits are derived as described in Section 2.3.2.

We find that in the LAB Survey the statistical mean of the noise is not zero, but is instead systematically around +10 mK. In the full resolution dataset the $2.5\sigma_{\mathrm{rms}}$ threshold is well above these values, but after a 4° smoothing has been applied, it comes to be of the same order. The nature of this emission is not clear, and systematic errors at this low level in the LAB Survey may exist (P. Kalberla, private communication). We consider this emission spurious and re-set the noise zero point, channel by channel, by subtracting the average value estimated in regions not contaminated by the Galactic emission. This is equivalent to using a threshold higher than 2.5σ and different for each channel map for our fit.

Figure 2.5 shows the four R-averaged $v_\phi(z)$ curves derived for each quadrant and also the mean curve and its linear fit. We added two points belonging to the mid-plane, one for QI and one for QIV, averaged in $3.5 < R < 5.5$ kpc. The method used to derive the rotation velocity in the mid-plane $v_\phi(R, 0)$ is described in Appendix A. The linear fit gives $-15\,\mathrm{km\,s^{-1}\ kpc^{-1}}$ for the average vertical falloff in the rotation velocity. We estimate an error of $4\,\mathrm{km\,s^{-1}\ kpc^{-1}}$ obtained using as a constraint the point at $z = 2$ kpc; the shaded area in Fig. 2.5 shows the 2σ confidence level.

If vertical and radial motions are present, they may affect the calculation of $v_\phi(z)$, because non-circular motions modify the shape of the $l-v$ distribution (Section 2.2.3). We check this by adding a vertical infall ($v_z = -40\,\mathrm{km\,s^{-1}}$) and a radial inflow ($v_R = -30\,\mathrm{km\,s^{-1}}$) to our models and re-estimating $v_\phi(z)$. We find that in

the presence of these motions the gradient would be overestimated in the QI regions and underestimated in the QIV regions. However, the overall effect is inside the error bar of our gradient estimate, and we can neglect it.

Recently it was pointed out that the velocity of the solar circle $v_\odot$ could be significantly higher than the standard value of $220\,\mathrm{km\,s^{-1}}$ (Reid et al. 2009; McMillan 2011). We note that the value of $v_\odot$ has no impact on our gradient estimate. Equation 2.4 states that changing $v_\odot$ would shift the rotation velocity up or down at a certain longitude (i.e. at a certain R) for any z. For instance, in Fig. 2.5 all points would be vertically shifted by the same amount, with no consequences for the fitted slope.

Finally, we point out that the implicit assumption behind the method used is that in the regions investigated the gas is dense enough to show a significant emission. Testing the method with very different density distributions and scale-heights (Section 2.3.2) gave comforting results. If however an unusually deep depletion of H I were present in the inner Galactic regions, our gradient would be overestimated.

2.4 Results

In the previous Section we derived the inner rotational gradient of the Milky Way H I halo. We proceed now to estimate the remaining three free parameters of the halo: the vertical scale height (h_g), the vertical component (v_z) of the global motion and the radial one (v_R). The rotation curve adopted is similar to that derived in Appendix A. Given the inapplicability of the tangent-point method we cannot derive the rotation velocity for $R > \mathrm{R}_\odot$. Thus we assume that a) the mid-plane rotation curve remains flat beyond $\mathrm{R}_\odot$; b) the rotational gradient, derived for $3.5 < R < 5.5\,\mathrm{kpc}$, is the same ($-15\,\mathrm{km\,s^{-1}\ kpc^{-1}}$) at each radius.

2.4.1 Minimization of residuals

We build a series of models with different combinations of the three parameters (h_g, v_z, v_R) and search for the values that minimise the differences with the data. We explore the following ranges: from $-100\,\mathrm{km\,s^{-1}}$ to $0\,\mathrm{km\,s^{-1}}$ in steps of $10\,\mathrm{km\,s^{-1}}$ for v_z, from $-50\,\mathrm{km\,s^{-1}}$ to $50\,\mathrm{km\,s^{-1}}$ in steps of $10\,\mathrm{km\,s^{-1}}$ for v_R, from 0.5 kpc to 4 kpc in steps of 0.25 kpc for $h_\mathrm{g}(R)$. We exclude a positive range for v_z because the data clearly do not show a systematic shift of the emission towards the positive velocities. For each model the total flux computed in the halo region is normalised to the observed halo flux by multiplying each $T_\mathrm{B}(l, b, v_\mathrm{LOS})$ for an appropriate factor, and because $T_\mathrm{B} \propto N_\mathrm{HI} \propto M_\mathrm{HI}^\mathrm{halo}$ this is a correction to the H I halo mass. The resulting halo masses above 2 disc scale-heights for different models vary from $0.5 \times 10^8\,\mathrm{M_\odot}$ to $9 \times 10^8\,\mathrm{M_\odot}$.

Table 2.1: Global parameters of the H I halo of the Milky Way, from our best halo model (see text).

H I mass	$3.2^{+1.0}_{-0.9} \times 10^8$	$M_\odot$
Scale-height (h_g)[a]	$1.6^{+0.6}_{-0.4}$	kpc
Rotational gradient ($dv_\phi/d\|z\|$)	-15^{+4}_{-4}	$km\,s^{-1}\,kpc^{-1}$
Vertical velocity (v_z)	-20^{+5}_{-7}	$km\,s^{-1}$
Radial velocity (v_R)	-30^{+7}_{-5}	$km\,s^{-1}$

[a] obtained using a $sech^2$ formula (see eq. 2.2)

For each model we compute the difference with the LAB datacube pixel by pixel, and sum these values with a $\cos(b)$ weight-factor to take into account the projection effects. We use both a quadratic sum and an absolute sum, obtaining little differences. The sums are extended to all components with the exception of the regions occupied by the disc emission ($|v_{DEV}| < 35\,km\,s^{-1}$) and by a) the Magellanic Stream; b) the Leading Arm; c) the GCP complex (or 'Smith Cloud'; Smith 1963), which is an isolated cloud with an anomalous kinematics (Lockman et al. 2008); d) the Outer Arm (see Section 2.2.1); e) the external galaxies. We also disregard components with $|v_{LOS}| > 250\,km\,s^{-1}$, because at these velocities only some isolated very high-velocity clouds contribute to the emission, and obviously our models do not attempt to reproduce these features. Furthermore, we exclude the QI and QIV regions for $|b| < 50°$ (the 'horn-like' structure, see Section 2.2.3), because their emission - for a fixed density distribution - gives information mainly on $dv_\phi/d|z|$, which has already been set.

2.4.2 The best model

We find that the kinematical parameters that minimise the differences between the models and the data are $v_z = -20\,km\,s^{-1}$, $v_R = -30\,km\,s^{-1}$. For the vertical scale-height we obtain 1.75 kpc computing the residuals using the squared sum and 1.5 kpc using the absolute sum, thus we set $h_g = 1.6$ kpc. The H I halo mass above 2 disc scale-heights (see Section 2.2.1) is $3.2 \times 10^8\,M_\odot$. Table 2.1 summarises the parameters of the best halo model and their errors. These latter are obtained by searching for 'acceptable models' around the best set of parameters. Note that the H I halo mass reported corresponds to $5-10\%$ of the total Galactic H I.

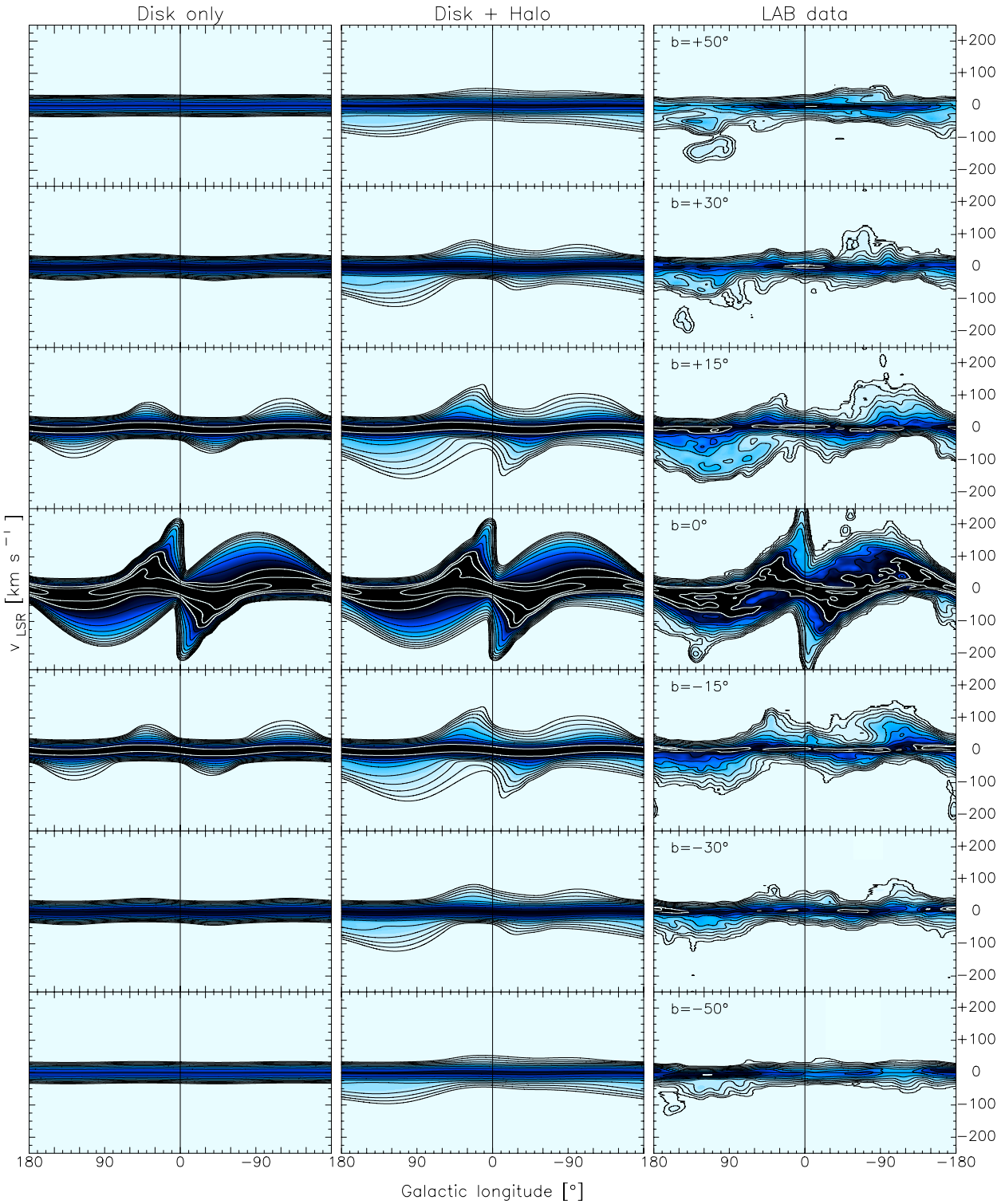

Figure 2.6: $l-v$ slices at 7 different latitudes indicated at the top left corners of the rightmost plots. *First column*: the H I disc model; *second column*: H I disc + best halo model; *third column*: the LAB data. Each cube is smoothed to 8° resolution. Contour levels in brightness temperature range from 0.04 K to 81.92 K scaling by a factor 2. The Magellanic Clouds, the Magellanic Stream and the Leading Arm have been removed.

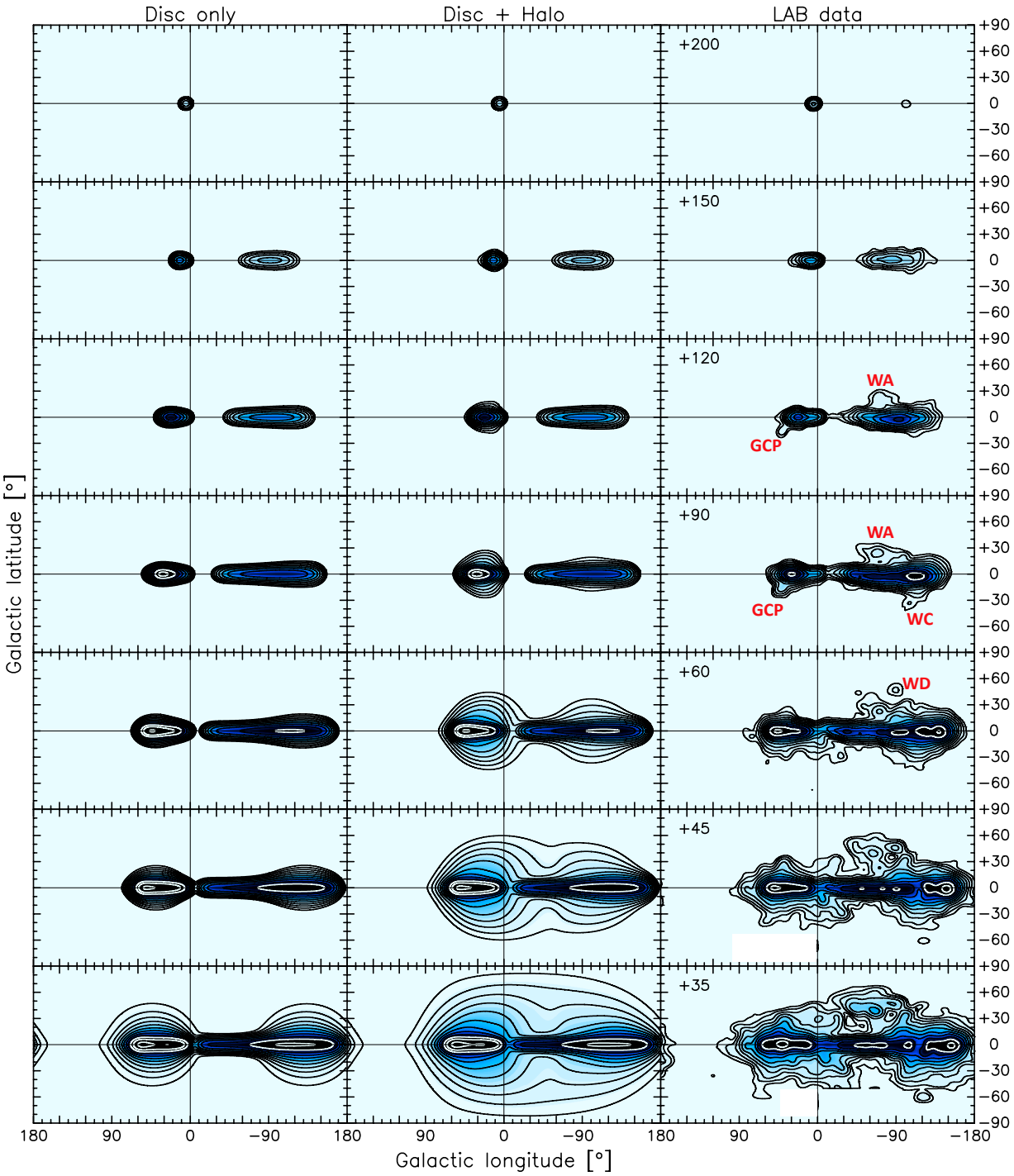

Figure 2.7: Channel maps at 14 different velocities indicated (in $\mathrm{km\,s^{-1}}$) at the top left corners (for $v_{\mathrm{LOS}} > 0$) or at the bottom right corner (for $v_{\mathrm{LOS}} < 0$) of the rightmost plots. *First column*: the H I disc model; *second column*: H I disc + best halo model; *third column*: the LAB data. Each cube is smoothed to 8° resolution. Contour levels in brightness temperature range from 0.04 K to 81.92 K scaling by a factor 2. The classical HVCs are labelled in red. The Magellanic Clouds, the Magellanic Stream and the Leading Arm have been removed.

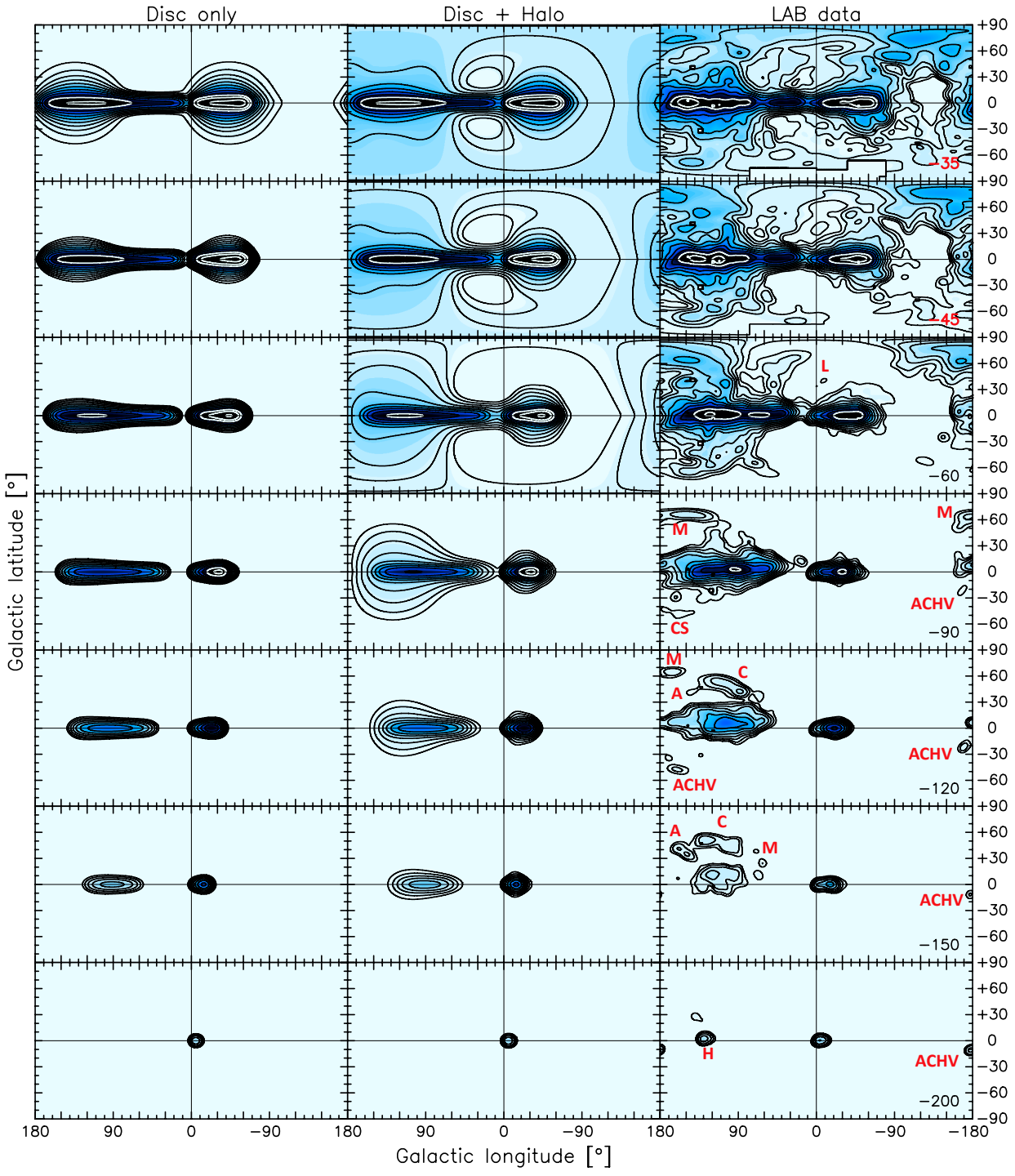

Figure 2.7 (Continued)

Figure 2.6 shows seven representative $l-v$ slices at various latitudes for three cubes: a model with only the H I disc component, a model with both (disc + best halo) components, and the data. The H I distribution in the disc is modelled as reported in KD08, but we used the rotation curve found in Appendix A (thick lines in Fig. 2.9), we added an isotropic velocity dispersion of $10\,\mathrm{km\,s^{-1}}$ and we included an exponential decrease in density for $R<4.75\,\mathrm{kpc}$. We did not include the warp (but see Section 2.4.3). The comparison between models and data clearly highlights how the H I disc emission alone fails to reproduce the observations, especially at the intermediate latitudes ($b=\pm15^\circ$ and $b=\pm30^\circ$). Instead, adding the halo component allows us to reproduce most of the H I features at low brightness temperature ($T_\mathrm{B}\lesssim 0.5\,\mathrm{K}$), especially those coming from the external regions ($0^\circ<l<180^\circ$ at $v_\mathrm{LOS}<0$, and $-180^\circ<l<0^\circ$ at $v_\mathrm{LOS}>0$) at latitudes $|b|\geq15^\circ$. The inner regions (QI and QIV) appear to reach velocities higher than the data: this can be interpreted as evidence of a steeper gradient in the innermost regions - as found by Oosterloo et al. (2007) for NGC 891 - or of a depletion of H I in these areas (see next Section). Also, the LAB data show asymmetries between the positive and the negative latitudes that we cannot reproduce with our symmetric models.

Figure 2.7 shows fourteen representative channel maps at different v_LOS for the disc model, the disc+halo model and the LAB data. It is evident that the disc alone can not explain the low level emission occurring at the intermediate velocities ($|v_\mathrm{LOS}|\leq 90\,\mathrm{km\,s^{-1}}$), which is instead nicely reproduced when the H I halo is taken into account. Channel maps at $|v_\mathrm{LOS}|\leq 60\,\mathrm{km\,s^{-1}}$ in the LAB data show that this low level emission occurs preferentially at negative velocities, where most of the IVCs are located. This effect is present also in our halo model, and is caused by the global inflow of the extraplanar H I towards the disc.

In order to estimate the impact of the local H I emission on the parameters of our model we perform the following test. We consider three models, each one excluding a different part of the halo: in model #1 we consider only the inner halo by excluding the H I emission at $R>8\,\mathrm{kpc}$, in model #2 we add the local gas by excluding the emission at $R>9\,\mathrm{kpc}$, in model #3 we exclude the H I at $R<9\,\mathrm{kpc}$ in order to take into account only the outer emission. For each model we perform the analysis described in Section 2.4.1. We find that the best parameters for model #2 are the same as those of Table 2.1, while those of model #1 and #3 slightly differ: we obtain ($v_z=-25\,\mathrm{km\,s^{-1}}, v_R=-30\,\mathrm{km\,s^{-1}}, h_\mathrm{g}=1.1\,\mathrm{kpc}$) for the first and ($v_z=-15\,\mathrm{km\,s^{-1}}, v_R=-20\,\mathrm{km\,s^{-1}}, h_\mathrm{g}=1.6\,\mathrm{kpc}$) for the latter. These values are all consistent within the errors with those of Table 2.1, and we can conclude that our results are generally true.

To understand if a variation of the parameters R_g and γ (see eq. 2.2) affects our results, we build four new models. In two of them we keep $\gamma=4.87$ and use $R_\mathrm{g}=2.4\,\mathrm{kpc}$ and $R_\mathrm{g}=1.1\,\mathrm{kpc}$, while in the other two we keep $R_\mathrm{g}=1.61\,\mathrm{kpc}$ and use $\gamma=2$ and $\gamma=8$. For each model we re-perform the minimization of the residuals, finding that in all cases the best parameters are consistent within the errors with those of Table 2.1. Finally, we investigate the impact of $v_\odot$ on the residuals by

re-building all models using $v_\odot = 250\,\mathrm{km\,s^{-1}}$ for both the mid-plane rotation and the velocity projections, obtaining no variation from the above best-fit parameters.

2.4.3 Further refinements

We consider the effect of a Galactic warp. Following Levine et al. (2006), we model the offset of the mid-plane z_0 from the plane $z=0$ with the formula

$$z_0(R,\phi) = W_0(R) + W_1(R)\sin(\phi - \phi_1(R)) + W_2(R)\sin(2\phi - \phi_2(R)) \ , \qquad (2.5)$$

where the dependencies on R of the three amplitudes W_i and the two phases ϕ_j have been taken from Kalberla et al. (2007, Fig. 16 and Fig. 17 therein). We consider the warp only for $R > \mathrm{R}_\odot$, and we set $W_2(R) = 0\,\mathrm{kpc}$ for $R < 16\,\mathrm{kpc}$. Under the assumption that the H I halo stratifies like the H I disc, we include the warp in our models just substituting the density computed in (R,z) with that computed in $(R, z-z_0)$ for both the disc and the halo distribution. The halo rotation curve $v_\phi(R,z)$ is also substituted with $v_\phi(R, z-z_0)$. This cannot be considered a full treatment of the warp effect, because we use eq. (2.3) to compute the line-of-sight velocity and we assume that the orbits are circular. However, the mid-plane significantly deviates from the $z=0$ plane only at large radii ($R > 15\,\mathrm{kpc}$) and around $\phi \sim 80°$, which makes the contribution of the halo emission in the warp region negligible.

Figure 2.8 shows the two $l-v$ plots at $b = \pm 15°$ for the data (rightmost panels) compared with a disc-only model (left column) and a disc+halo model, both with the inclusion of the warp. The warp is very asymmetric and mostly visible at positive latitudes for $l = 90°$. In this region - the Outer Arm zone - the H I emission is deformed towards negative velocities and the warp model reproduces the data

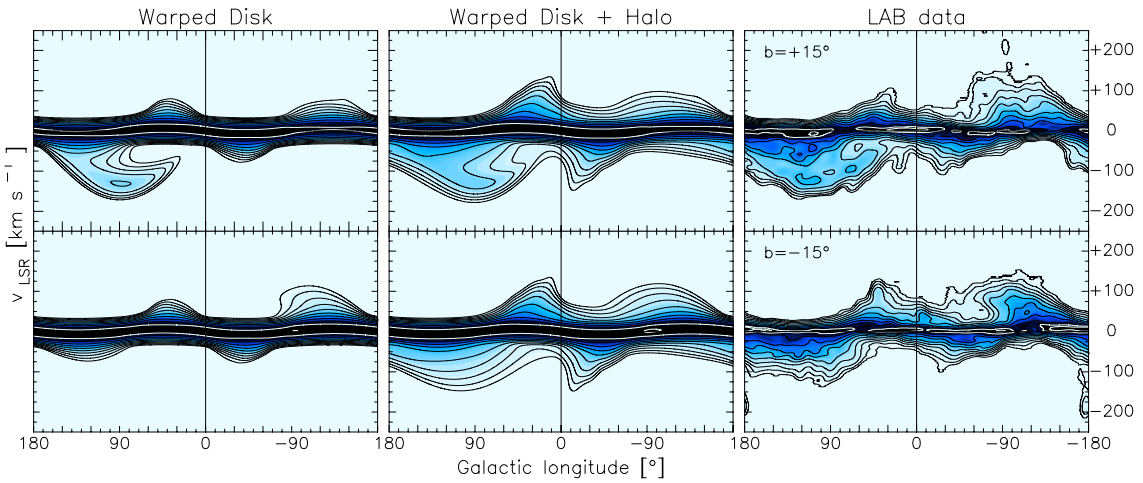

Figure 2.8: $l-v$ slices at $b = +15°$ (top) and $b = -15°$ (bottom). *First column*: the warped H I disc model; *second column*: the warped best model (H I disc + halo); *third column*: the LAB data. Each cube is smoothed to 8° resolution. Contour levels in brightness temperature range from 0.04 K to 81.92 K scaling by a factor 2.

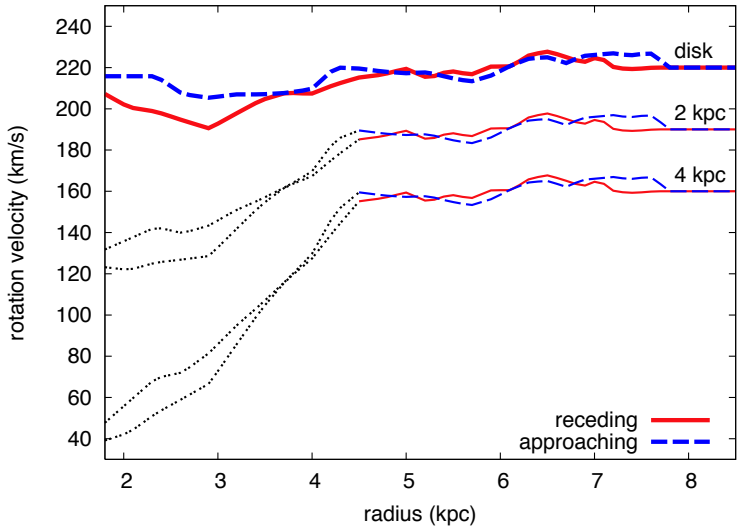

Figure 2.9: Rotation curves as a function of the height from the Milky Way mid-plane used in the modelling. The thick lines on top stand for the mid-plane rotation. *Red solid lines*: receding curves; *blue dashed lines*: approaching curves; *black dotted lines*: rotation velocities assumed for the 'shallow rise' model at $R < 4.5$ kpc. For $R > 7.7$ kpc we assumed that the curves are flat.

significantly better. At higher latitudes the effect of the warp is negligible and the other $l - v$ diagrams in Fig. 2.6 remain unchanged. Clearly, the inclusion of a warp does not significantly affect our results for the H I halo.

In order to reproduce the emission related to the inner regions (QI and QIV) we consider two effects separately. The first is the inclusion of a radial dependence for the rotational gradient in the inner halo. We assume that for $R < 4.5$ kpc the magnitude of the rotational lag increases linearly each kiloparsec by 10 km s^{-1} kpc^{-1}. The effect of this 'shallow rising' rotation curve (dotted curves in Fig. 2.9) is to lower $v_{\rm LOS}$ in the inner halo, reducing the 'horns' (see Section 2.2.3) in the $l-v$ diagrams. Figure 2.10 shows that this effect is not sufficient, since the $l-v$ profiles obtained for this model (second column) differ only slightly from the one with a constant vertical velocity gradient (first column).

As a second attempt we reduce the halo thickness in inner regions. We assume that the vertical scale-height of the H I halo decreases linearly for $R < {\rm R}_\odot$, vanishing at the Galactic Centre. Figure 2.10 shows a model with this thin inner halo (third column) and constant rotational gradient of -15 km s^{-1} kpc^{-1}. This model reproduces fairly well the H I emission in these regions of the datacube.

We conclude that the scale-height of the H I halo of the Milky Way inside ${\rm R}_\odot$ is likely to be lower that our average value of 1.6 kpc, the rotational gradient may also be steeper than 15 km s^{-1} kpc^{-1} in the inner parts. It is difficult to separate these two effects in our analysis. For instance, given the degeneracy between dv_ϕ/dz and $h_{\rm g}$ (Section 2.2.3), a non-constant gradient with R would imply a corresponding variation of the vertical scale-height. Both a decreasing scale-height and an increasing gradient in the inner parts are consistent with a Galactic fountain origin for the Milky Way halo, as we show in the next Chapter (Sections 3.4.1 and 3.4.2).

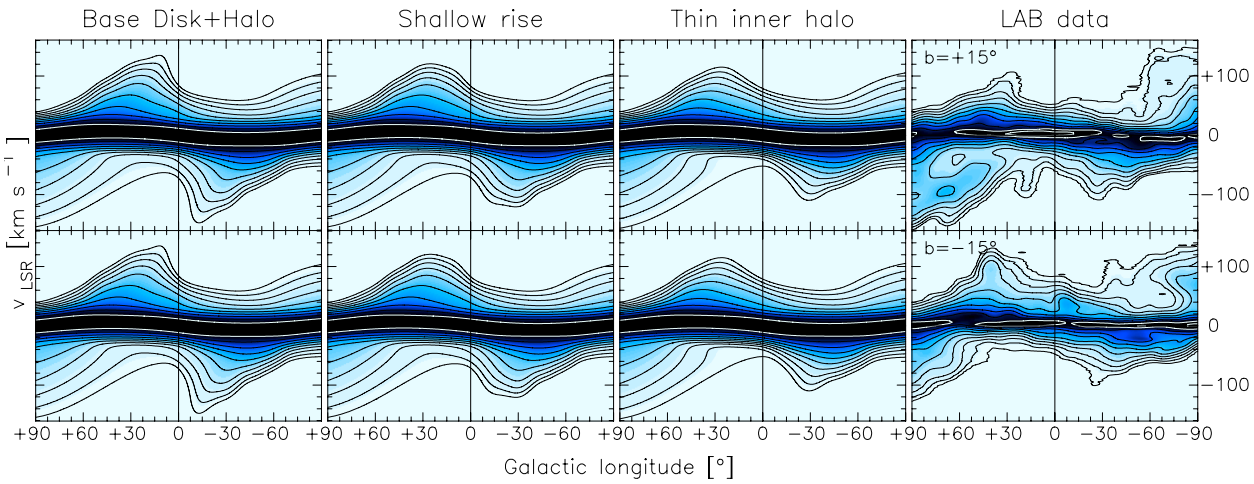

Figure 2.10: $l-v$ slices at $b=+15°$ (top) and $b=-15°$ (bottom) at longitudes $-90° < l < 90°$. *First column*: the best model shown in Fig. 2.6; *second column*: the model refined including a radial dependence of $dv_\phi/d|z|$ for $R < 4.5$ kpc; *third column*: the model refined including a linear decrease of the halo thickness for $R < \mathrm{R}_\odot$; *fourth column*: the LAB data. Each cube is smoothed to 8° resolution. Contour levels in brightness temperature from 0.04 K to 81.92 K scaling by a factor 2.

2.5 Discussion

In the previous Sections we have estimated the global properties of the Milky Way H I halo by building 3D models and comparing them with the LAB Survey dataset. We found that the Galactic H I halo can be globally described by the following average kinematical parameters: $dv_\phi/d|z| = -15 \pm 4\,\mathrm{km\,s^{-1}\ kpc^{-1}}$, $v_z = -20^{+5}_{-7}\,\mathrm{km\,s^{-1}}$ and $v_R = -30^{+7}_{-5}\,\mathrm{km\,s^{-1}}$ (Section 2.4.2). Below we discuss the obtained results.

2.5.1 Physical interpretation

Fraternali and Binney (2006) successfully reproduced the vertical gaseous distribution of NGC 891 and NGC 2403 by modelling the halo as a continuous flow of non-interacting galactic fountain clouds moving ballistically in the galactic potential (see also Collins et al. 2002; Heald et al. 2007). However, they were forced to include interactions of these clouds with the environment in order to reproduce the vertical rotational lag (Fraternali and Binney 2008): in this scenario the fountain clouds accrete gas from an ambient medium with a low angular momentum with respect to the galactic disc. This process slows down the rotation of the Galactic fountain clouds and produces gas accretion towards the disc. Hydrodynamical simulations show that the Galactic corona could be the reservoir of this accreting gas (Marinacci et al. 2010a). The typical orbits of this 'accreting Galactic fountain' differ from those of a fountain without accretion for the presence of inward radial motions

(Fig. 6 in Fraternali and Binney 2008), which indeed were observed in the H I halo of NGC 2403 (Fraternali et al. 2002). In Section 2.4.2 we showed that the H I halo of the Milky Way has global vertical and radial motions of inflow, and in Section 2.3.3 we estimated a vertical lag equal to the one found in NGC 891. These results suggest that the dynamical interpretation given for the gaseous halo of NGC 891 is suitable for the Milky Way halo as well.

The vertical inflow motion estimated ($v_z < 0$) can be explained supposing that the Galactic fountain gas is initially ionised for a certain part of the rising orbit, becoming visible in H I only after recombination. If one considers a typical fountain orbit where the gas is ejected vertically from the disc with an ejection velocity $v_{\rm kick}$ and a vertical velocity that decreases roughly linearly with time (Fig. 6 in Fraternali and Binney 2008), to have an average vertical velocity $\overline{v_z} < 0$ the gas should be ionised for a fraction $-2\,\overline{v_z}/v_{\rm kick}$ of the rising orbit. This fraction is around $50-70\%$ for the vertical velocity derived in Section 2.4.2 ($-20^{+5}_{-7}\,{\rm km\,s^{-1}}$) and for typical ejection velocities of $60-80\,{\rm km\,s^{-1}}$.

The negative value of v_R in the halo is more difficult to interpret. Note that in the context of a phase-change fountain, $v_R < 0$ does not imply a net inflow for the whole gaseous halo, but only for the neutral descending clouds. For each cloud, this inward motion would be roughly balanced by an outward motion during the first part of the orbit, when the gas is ionised. A ballistic non-interacting fountain cloud may have some negative v_R, but only at the very end of its orbit (Fraternali and Binney 2006). It seems therefore more likely that such a high value of v_R is produced by the loss of angular momentum due to gas accretion hypothesised by Fraternali and Binney (2008). In order to fully understand these effect, one requires a full dynamical modelling of the halo, which is the subject of Chapter 3.

2.5.2 Relation to previous works

Lockman (1984) found that in the lower halo regions of the inner Galaxy a large amount of H I is present. He estimated that this medium has a vertical scale-height of 500 pc approximately constant for $4 < R < 8\,{\rm kpc}$. Moreover, Lockman (2002) confirmed that the diffuse H I emission in these areas is organised into discrete clouds (see also Ford et al. 2008). In Section 2.4.2 we found that all the acceptable models have larger scale-heights. The difference can be explained as follows: a) our average scale-height is derived using the emission from the entire halo while it seems that in the innermost regions of the Galaxy the halo is thinner (Section 2.4.2 and 2.4.3); b) Lockman derived the position (R, z) of the emission at the tangent point assuming co-rotation for the halo gas, and he pointed out that in the case of a lagging halo the amount of H I would be underestimated.

Levine et al. (2008) were the first to derive a value for the vertical falloff in the Galactic rotation velocity using a direct approach. They applied the tangent point method to both the VLA Galactic Plane Survey (Stil et al. 2006) and Southern

Galactic Plane Survey (McClure-Griffiths et al. 2005) dataset to derive the inner rotation curves up to $|z| = 100$ pc. The method used to determine the tangent velocity was based on fitting the whole profile around $v_{\rm ter}$ (see Section 2.3.1) using a form derived by Celnik et al. (1979). They found an average lag of $-22 \pm 6\,{\rm km\,s^{-1}\ kpc^{-1}}$, in broad agreement with our estimate obtained in the halo region for $1 < |z| < 4$ kpc. With the resolution and the S/N of the LAB data we cannot determine the rotation curve for $|z| \lesssim 1$ kpc, thus a direct comparison with the work of Levine et al. is not possible.

A local value for the vertical rotational gradient was derived by Pidopryhora et al. (2007) in a small region (the 'plume') above the Ophiuchus superbubble. Assuming that the feature is located at the tangent point, they found a lag of $-27\,{\rm km\,s^{-1}}$ with respect to the corotation at position $R = 4$ kpc, $z = 3.4$ kpc. This means an average gradient of $-8\,{\rm km\,s^{-1}\ kpc^{-1}}$ at that radius. In the same region we measured a gradient of roughly a factor 2 steeper (see receding northern curve in Fig. 2.5). In the LAB data smoothed at 4°, the Ophiucus superbubble is not visible and we are likely measuring the average velocity of the surrounding region where the superbubble is expanding.

In the attempt to reconstruct the spatial H I distribution by a 3D de-projection of the LAB data, rotation curves at several heights from the mid-plane were derived by Kalberla et al. (2007) using a theoretical approach, previously adopted by Levine et al. (2006). They modelled the Galactic dark matter distribution so that the resulting rotation curve (obtained assuming that the gravity dominates the gas dynamics everywhere) gives hydrostatic H I distribution whose properties (e.g. the flaring) are consistent with the dark halo itself. The curves obtained (Fig. 9 in Kalberla et al. 2007) differ from those we derived (Fig. 2.9), specifically the vertical lag at $R = 4.5$ averaged for $1 < |z| < 4$ kpc is around $-22\,{\rm km\,s^{-1}\ kpc^{-1}}$ and it decreases as R increases. Our approach does not rely on any assumption about the dynamical state of the system, because we simply derive the best model that reproduces the observations. We point out that if the H I halo is produced by Galactic fountains interacting with the environment (see Section 2.5.1), assuming that the dynamics of the gas is dominated by gravity is not necessarily a good description of the system (Fraternali and Binney 2008). Marinacci et al. (2010b) also showed that for NGC 891 a hydrostatic model does not satisfactorily reproduce the data.

Finally, KD08 analysed the Galactic H I model derived in Kalberla et al. (2007). They found that $\sim 10\%$ of the H I is not related to the disc, in agreement with our estimate for the H I halo mass (Section 2.4.2).

2.5.3 HVCs and IVCs

Intermediate and High-Velocity Clouds are regarded as the main evidence for the presence of a gaseous halo in our Galaxy, and it is important to understand how they fit with the results of this Chapter. Even if the emission of these objects dominates

the H I flux in regions outside the H I disc, at low column densities the sky is basically filled with neutral hydrogen emission (Fig. 2.1).

Distance estimates for the IVCs show that they are a local phenomenon (van Woerden et al. 2004, and references therein), and their disc-like metallicities and kinematics suggest a Galactic fountain origin. In this Chapter we showed that these clouds are embedded in a diffuse halo, which shares the same kinematics. The emission of this gaseous component (IVCs + diffuse H I) is reproduced by our model. This suggests that the whole H I halo is made up of IVC-like objects, most of which are at large distances and thus unresolved. If these clouds had typical H I masses of $\sim 10^{4-5}\,\mathrm{M}_\odot$, the H I halo would contain several thousand such objects.

Recent studies on HVCs established that these complexes have higher distances and heights from the plane and lower metallicities than IVCs (Wakker et al. 2007, 2008). The H I emission of these systems is indicated in the rightmost panels of Fig. 2.7. Clearly, our best-fit model of disc+halo (middle panels of Fig. 2.7) is unable to reproduce the H I emission of most of the HVCs, which implies that the halo parameters derived in this Chapter (Table 2.1) are not representative of their properties. This suggests that the nature and origin of these clouds are different from those of the halo described here. There are special cases such as the the well-known complexes C and A, visible in Fig. 2.7 at $v_{\mathrm{LOS}} = -120$ and $-150\,\mathrm{km\,s^{-1}}$. Although separated from the 'normal' halo gas, these clouds appear in a location that is not completely peculiar. They follow the trend of the halo emission, but at a more extreme velocity. A recent study puts complex C at $\sim 7-8\,\mathrm{kpc}$ above the mid-plane (Thom et al. 2008). Interestingly, its projected velocity is not very different from what one would derive by extrapolating our vertical rotational gradient at these heights.

2.5.4 Comparison with external galaxies

The properties of the Galactic H I halo derived here are similar to those of external galaxies. The vertical rotational gradient estimated in Section 2.3.3 is the same as the one found by Oosterloo et al. (2007) for NGC 891; inward radial motions of $10-20\,\mathrm{km\,s^{-1}}$ have been found by Fraternali et al. (2002) in the H I halo of NGC 2403; Boomsma et al. (2008) showed the presence of vertical motions for halo gas clouds in NGC 6946. The halo H I mass derived for the Milky Way is also consistent with the values estimated in other galaxies (see Fraternali 2010). However, we notice that the techniques used to separate the halo gas from the disc gas are very different and a direct comparison is difficult. Nevertheless, it is clear that a remarkably massive halo like that detected in NGC 891 ($1.2\times10^9\,\mathrm{M}_\odot$, 30% of the total H I) is not present in the Milky Way and it is perhaps fair to say at this point that NGC 891 constitutes an extreme case.

A recurring question is whether or not the anomalous H I clouds observed around external galaxies are of the same nature as the galactic IVCs and HVCs. If all ha-

los are made up of clouds with properties similar to the IVCs, then they would be unresolved in external galaxies and appear like a smooth medium, as observed. Observations of external galaxies also show the presence of very massive clouds ($\sim 10^7\,M_\odot$) such as the filaments of NGC 891 (Oosterloo et al. 2007) and NGC 2403 (Fraternali et al. 2002). These clouds have properties similar to those of large Galactic HVCs, like complex C. They have the same masses (the H I mass of complex C is $\sim 5 \times 10^6\,M_\odot$, Thom et al. 2008) and they show comparable kinematics. For instance the filament in NGC 2403 follows the general kinematic pattern of the halo gas, but at a more extreme velocity. This is analogous to what has been described in Section 2.5.3 for complex C. In external galaxies, clouds are also detected at large distances and/or very anomalous velocities: e.g. the 'forbidden' clouds in NGC 2403 (Fraternali et al. 2002), the so-called counter-rotating clouds (see Fraternali 2010) and the clouds surrounding M 31 at tens of kpc from the disc (Thilker et al. 2004). Very massive and very anomalous clouds are not consistent with a Galactic fountain origin. They are more likely to be gas falling into these galaxies for the first time either from satellites or directly from the intergalactic medium, although the latter mechanism is not clearly understood (Binney et al. 2009). All things considered, they are similar to the Galactic HVCs.

2.6 Conclusions

Our Galaxy offers the unique opportunity to study an H I halo from two different perspectives: on the one hand one may analyse the single bright anomalous clouds - the HVCs and IVCs - which populate the extraplanar regions, on the other hand one may consider the halo as a global component and analyse its global parameters. In this Chapter we have adopted the latter approach.

We modelled the extraplanar H I of the Milky Way and compared its emission to the Leiden-Argentine-Bonn Survey. Using the tangent-point method we estimated the vertical gradient in the rotation velocity. The main results can be summarised as follows:

1. the Milky Way has a halo of neutral gas with an H I mass of $3.2^{+1.0}_{-0.9} \times 10^8\,M_\odot$ ($\sim 5-10\%$ of the total H I mass) and an average vertical scale-height (sech^2 formula) of $1.6^{+0.6}_{-0.4}$ kpc, which seems to be decreasing in the innermost regions.

2. The H I halo has a global vertical lag in rotation velocity. We measured the magnitude of this lag in the region $3.5 < R < 5.5$ kpc and $1 < |z| < 4$ kpc, obtaining an average value of $-15 \pm 4\,\mathrm{km\,s^{-1}\ kpc^{-1}}$.

3. We detected a global inflow motion in both the vertical ($-20^{+5}_{-7}\,\mathrm{km\,s^{-1}}$) and the radial ($-30^{+7}_{-5}\,\mathrm{km\,s^{-1}}$) directions.

4. The H I halo is likely to have been generated by supernova explosions, which create a galactic fountain. If a single fountain cloud has properties similar to the local IVCs, then the halo should contain thousands of these objects.

5. The properties of the Milky Way H I halo are broadly similar to those derived in external galaxies.

Chapter 3

A dynamical model for the Galactic HI halo

3.1 Introduction

As discussed in Section 1.1.3, current cosmological models suggest that disc galaxies in the local Universe are embedded in pressure-supported structures of plasma at the virial temperature called *coronae*. These media should typically extend to a few hundred kiloparsecs from galaxy centres (Fukugita and Peebles 2006) and contain a large fraction of the so-called 'missing baryons'. The observational quest for these coronae is ongoing (Bregman 2007), and there is some debate as to whether the observational constraints are compatible with the cosmological predictions or not (Rasmussen et al. 2009; Anderson and Bregman 2010, 2011; Hodges-Kluck and Bregman 2012). Cosmological coronae would constitute a virtually infinite source of gas to feed star formation in Milky-Way-like galaxies, but there is no general consensus on how these media can cool from the virial temperature and accrete gas onto the discs.

If disc galaxies are embedded in cosmological coronae, the two media are expected to interact with each other. This interaction is enhanced by the onset of a galactic fountain. Fraternali and Binney (2006, 2008, hereafter FB06, FB08) built models of galactic fountains with and without interaction with the surrounding environment, and applied them to two nearby galaxies: NGC 891 and NGC 2403. They found that the kinematics of the extraplanar gas – rotational lag with respect to the disc and global inflow – could only be explained once *accretion* from the corona onto the fountain clouds was included. Moreover, the accretion rate required to explain the observed kinematics turned out to be very close to the star formation rates (SFR) of these galaxies. Despite these successes, the mechanism by which coronal gas should cool and accrete onto a fountain cloud remained unclear until Marinacci et al. (2010a, 2011) studied the interaction between these two media using hydrodynamical

simulations. They found that as the cloud moves, gas is stripped off it and mixed with the much hotter coronal gas. If the metallicity and density of the mixed gas are high enough, radiative cooling is fast and a consistent fraction of this mixture can cool to $\sim 10^4$ K within a dynamical time. Then the gradually eroding H I cloud trails a wake of warm and cold gas behind it, and the total mass of H I increases with time, just as the models of FB08 required.

Inspired by these works, in this Chapter we build a model of the galactic fountain and apply it to the H I halo of the Milky Way. As in Chapter 2, our approach consists of deriving modelcubes of H I emission and comparing them with the datacube of the LAB Survey (Kalberla et al. 2005). In Section 3.2 we describe the model we will be using, which is an updated version of that described in FB08, and explain how we evaluate the fit between a modelcube and the datacube of the LAB survey. In Section 3.3.1 we investigate whether the H I thick disc of the Milky Way can be produced by a pure galactic fountain. Then in Section 3.3.2 we present evidence that this fountain in fact interacts with the ambient coronal gas. In Section 3.4 we use our model to infer the large-scale structure of the Galaxy's H I halo, and argue that there is a fundamental distinction between High-Velocity Clouds (HVCs), which have an extragalactic origin, and Intermediate-Velocity Clouds (IVCs), which are dominated by fountain gas. In Section 3.5 we show that our model's parameter values are remarkably consistent with results from earlier studies of (a) small-scale hydrodynamical simulations of turbulent mixing (i.e. Marinacci et al.'s works), and (b) analysis of data for external galaxies. Section 3.6 sums up.

The results of this Chapter have been published in paper form in Marasco et al. (2012).

3.2 The model

We set up a galactic fountain model for the Milky Way by integrating orbits of gas clouds in the Galactic potential. The latter has been constructed using the standard decomposition into a bulge, stellar and gaseous discs, and a dark-matter halo. The physical parameters and functional forms for the various components have been taken from Binney and Tremaine (2008, Model II, p. 113).

The clouds are ejected from the disc into the halo, and we follow their trajectories until they return to the disc as described in FB06. The probability of ejection at speed v and angle θ with respect to the vertical direction is

$$P(v,\theta) \propto \exp\left(-\frac{v^2}{2h_{\rm v}^2\cos^{2\Gamma}\theta}\right), \tag{3.1}$$

where $h_{\rm v}$ is a characteristic velocity and Γ is a constant that determines the extent to which clouds are ejected perpendicular to the disc. Here we treat $h_{\rm v}$ as a free parameter but adopt $\Gamma = 5$ from FB06 – such a large value of Γ implies strong

collimation of ejecta towards the normal to the plane. The integration is performed in the (R, z) plane and then spread through the Galaxy by assuming azimuthal symmetry. The number of clouds ejected as a function of radius is proportional to the SFR density at that radius (see Section 3.2.2). Other parameters and properties of the model are as described in FB06 except for some updates to the model that are specified in the following subsections.

3.2.1 Phase-change

We follow the orbits of gas that leaves the disc at relatively low temperatures ($\lesssim 10^4$ K) after being swept up in the expansion of a superbubble that is powered by multiple supernova explosions. The virial-temperature gas filling the bubble is presumed to contain negligible mass and to merge with the pre-existing coronal gas. In the Milky Way, emission from the H I halo occurs mainly at negative line-of-sight velocities (van Woerden et al. 1985). This observation suggests that the neutral gas is seen mainly as it descends to the plane, so a significant fraction of the ejected gas must be ionised, and indeed from our best kinematic models of the Galactic halo (Chapter 2) we estimated that the rising clouds are ~ 60 per cent ionised. If we are to compare our models with the LAB survey of neutral gas, we have to find a way to estimate the fraction of a cloud's orbit that is ionised.

FB06 built models with and without phase-change, the latter having the whole trajectory 'visible' as H I gas, the former only the descending part. Here we refine this treatment as follows. We assume that a cloud ejected from the disc with a kick velocity $v_{\rm kick}$ will become visible (i.e. neutral) only when

$$v_z(t) < v_{z,0}(1 - f_{\rm ion}), \tag{3.2}$$

where v_z is the vertical component of the cloud's velocity, $v_{z,0} = v_{\rm kick} \times \cos\theta$ and $0 \leq f_{\rm ion} \leq 1$ is a free parameter that regulates the "visibility" of the cloud. If $f_{\rm ion} = 1$, the fountain cloud is neutral only for negative values of v_z (i.e. in the descending part of the orbit), while if $f_{\rm ion} = 0$, the cloud will always be visible. We infer the correct value of $f_{\rm ion}$ from the datacube (see Sections 3.3.1 and 3.3.2).

3.2.2 Star-Formation Law

We assume that the strength of the supernova feedback, i.e. the number of gas clouds ejected per surface element, is proportional to the local SFR. Given that our model is axisymmetric, we require an estimate of the SFR as a function of R. In FB06 and FB08 that was estimated from the surface density of neutral plus molecular gas using the Schmidt-Kennicutt law (Schmidt 1959; Kennicutt 1998). The SFR was then set to zero beyond a certain cut-off radius. Here, we refine this procedure as follows. We use a sample of galaxies with known radial trends of gas surface density

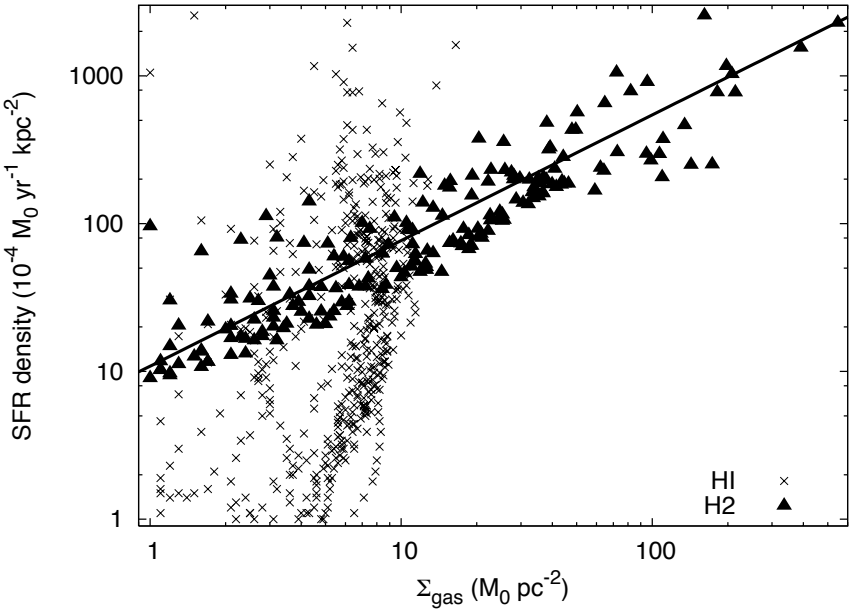

Figure 3.1: Star formation rate densities vs gas surface densities, both for molecular gas (filled triangles) and neutral atomic gas (crosses); from the sample of nearby galaxies studied by Leroy et al. (2008). The points come from an azimuthal averages at different radii over the galactic discs of 17 galaxies. The curve shows the power law fit described in the text.

and SFR density and derive a star-formation law for molecular gas. We then use this law to obtain the Milky Way's SFR as a function of R from the axisymmetrised surface density of molecular gas given in Binney and Merrifield (1998).

Fig. 3.1 is a plot of SFR density versus the molecular gas density. The filled triangles show data points for galaxies in the sample of Leroy et al. (2008) that have stellar masses above $10^9\,\mathrm{M}_\odot$. Each point refers to an azimuthal average at a given radius. The scatter in the relation between gas density and SFR is remarkably small considering that the points come from very different galaxies. We fitted these points with a power law of the form:

$$\Sigma_{\mathrm{SFR}} = A \left(\frac{\Sigma_{\mathrm{H_2}}}{\mathrm{M}_\odot\,\mathrm{pc}^{-2}} \right)^N , \tag{3.3}$$

where Σ_{SFR} and $\Sigma_{\mathrm{H_2}}$ are, respectively, the SFR and the molecular gas density. We found

$$\begin{aligned} A &= 10.8 \pm 2.3 \times 10^{-4}\,\mathrm{M}_\odot\,\mathrm{yr}^{-1}\,\mathrm{kpc}^{-2} \\ N &= 0.85 \pm 0.04\ . \end{aligned} \tag{3.4}$$

The slope of this relation is very different from the standard Schmidt-Kennicutt law, mainly because we are considering only molecular gas (see also Krumholz et al. 2011). Including H I would increase the slope to about $1.3-1.4$, however the average H I surface density correlates very little with the SFR density – see the grey crosses in Fig. 3.1 and Kennicutt et al. (2007). Therefore, given that the distribution of molecular gas in the disc of the Milky Way is known reliably, we prefer to obtain

the SFR density from equation (3.3). Our results do not depend strongly on the SF law.

3.2.3 Supernova-driven gas accretion

The pure galactic fountain model described above is modified to include interaction with the coronal gas according to FB08. We assume that the main mechanism at work is that described by Marinacci et al. (2010a): the Kelvin-Helmholtz instability generates a turbulent wake behind each cloud in which material stripped from the cloud mixes with coronal gas, enhancing the metallicity and the density of the latter and substantially decreasing its cooling time. As a consequence, part of the corona condenses into the wake and the mass of 'cold' gas increases. The combined mass of cold gas in the cloud and in the wake grows with distance along the cloud's path through the halo very much as proposed by FB08. We demonstrate this quantitatively in Section 3.5.1.

Condensation in the wake modifies the kinematics of the cold gas in a way that depends on the kinematics of the corona. The latter is not known a priori, but must be strongly influenced by this interaction because the portion of the corona that interacts with fountain clouds does not contain much mass, and the interaction has been taking place throughout the disc's lifetime. FB08 considered the effect of the drag between the clouds and the corona and concluded that, if there were no exchange of gas between the clouds and the corona, ram pressure would force the corona to corotation with the cold gas in a time shorter than the fountain's dynamical time. In reality much of the coronal gas that acquires momentum from a fountain cloud subsequently condenses in the cloud's wake, so the momentum that is transferred to the coronal gas is in the end not lost by the whole body of cool gas. Marinacci et al. (2011) studied the transfer of momentum between fountain clouds and the corona in hydrodynamical simulations and found that there is a net transfer of momentum to the corona until the speed at which the clouds move through the corona falls to $50 - 100\,\mathrm{km\,s^{-1}}$, depending on the physical properties of the system. Below this threshold speed, net momentum transfer to the corona ceases as a result of coronal gas cooling in the cloud's wake. In view of the short timescale on which ram-pressure can change the rotation rate of the corona, it is natural to assume that the corona has reached the velocity at which all the angular momentum imparted by ram pressure is subsequently recovered through condensation of coronal gas in the wake. Thus we assume that the rotation velocity of the corona is

$$v_\phi(R,z) = \sqrt{R\frac{\partial\Phi(R,z)}{\partial R}} - v_{\mathrm{lag}}, \tag{3.5}$$

where $\Phi(R,z)$ is the potential of the Galaxy and $v_{\mathrm{lag}} = 75\,\mathrm{km\,s^{-1}}$ is the (constant) velocity offset between clouds and corona at which condensation recaptures angular momentum transferred by ram pressure.

Following the prescription of FB08, the mass of cold gas (cloud+wake) associated with any cloud increases as

$$\dot{m} = \alpha m, \tag{3.6}$$

where α is the condensation rate, while the combined effect of condensation and drag decreases the velocity centroid of the cold gas at a rate (FB08)

$$\dot{v} = -\left(\alpha + \frac{1}{t_{\rm drag}\,(1 + t/t_{\rm drag})}\right)(v - v_\phi) \tag{3.7}$$

where $t_{\rm drag}$ is the time at which the relative velocity between the cold gas and the corona halves due to the drag only. Since $t_{\rm drag} \propto |v - v_\phi|^{-1} \sim v_{\rm lag}^{-1}$, the drag efficiency decreases as the kinematics of the corona approaches that of the disc. We assumed a constant value for $t_{\rm drag}$ of 800 Myr, according to the results of Marinacci et al. (2011) for $|v - v_\phi| = 75\,{\rm km\,s^{-1}}$ (see Section 3.5.1), and we fitted the parameter α. As we see below (Section 3.3.2), in order to reproduce the data we need $\alpha > 1/t_{\rm drag}$, i.e. the condensation is the dominant process at work, while the drag plays only a secondary role. Note that fixing $t_{\rm drag}$ at 800 Myr implies that we are considering clouds with masses and sizes similar to those of Marinacci et al.'s simulations ($M_{\rm HI} \sim 10^4\,{\rm M_\odot}, R \sim 100\,{\rm pc}$).

3.2.4 Comparison with the data

The comparison between the models and the data is performed as in Chapter 2 by building modelcubes that resemble the LAB datacube. After each timestep of the integration, the positions and velocities of the particles are projected along the line of sight of an observer located in the mid-plane of the Galaxy, at a radius $\rm R_\odot = 8.5\,kpc$, and moving at a circular speed $v_\odot = 220\,{\rm km\,s^{-1}}$. Using the same gas density for each cloud, we construct from these positions and velocities an artificial datacube. The artificial datacube is smoothed to 8° resolution and then compared with the LAB datacube at the same resolution. The comparison is performed only in the portion of $(l, b, v_{\rm LOS})$ space to which the thin disc should not contribute. Following Wakker (1991), we use the *deviation velocity* $v_{\rm DEV}$ to identify this region. We model the footprint of the thin disc as described in Chapter 2 and exclude data with $|v_{\rm DEV}| < 35\,{\rm km\,s^{-1}}$. We also exclude the H I emission of the Magellanic Clouds and Stream, the Stream's Leading Arm, the GCP complex, the Outer Arm and all external galaxies. In the following we refer to the surviving part of $(l, b, v_{\rm LOS})$ space as the *halo region*. The total model flux in the halo region is normalized to the corresponding LAB flux. This step fixes the mass of the H I halo.

Although the quantitative comparison between models and data is done only in the halo region, in all the plots of this Chapter a thin disc has been added for presentation purposes. This disc has a density profile taken from Binney and Merrifield (1998) and a scale-height taken from Kalberla et al. (2007). The velocity

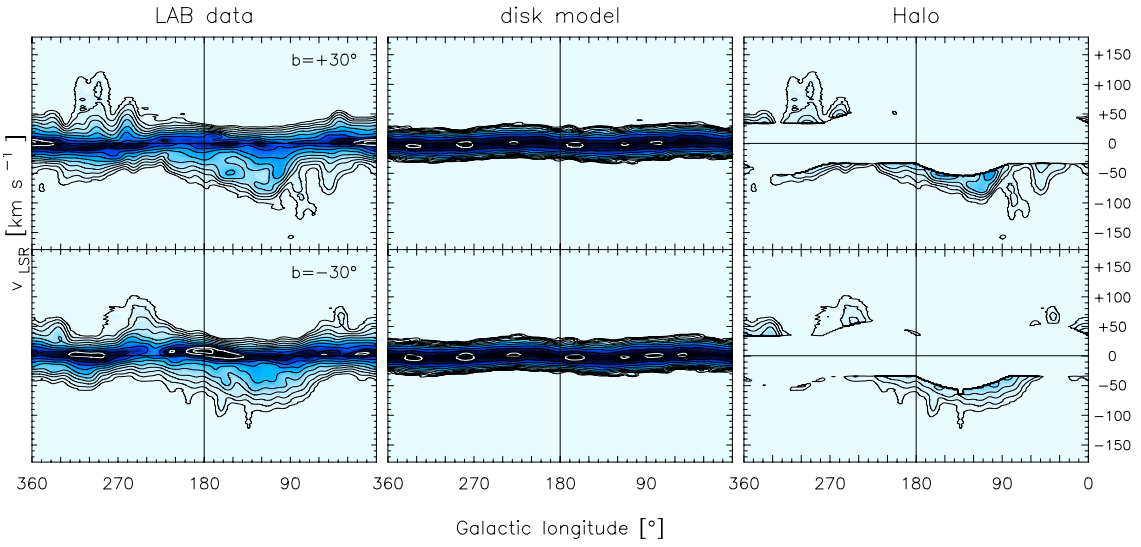

Figure 3.2: Longitude-velocity diagrams at latitudes ±30° above and below the mid-plane of the Galaxy. *Left panels*: LAB survey. *Middle panel*: disc model used throughout this Chapter. *Right panel*: LAB survey after the region of the disc has been removed, the remaining emission is used to compared our models with the data. Each cube is smoothed to 8° resolution. Contour levels in brightness temperature range from 0.04 K to 81.92 K scaling by a factor 2.

dispersion decreases linearly from 12 km s^{-1} in the Galactic centre to 6 km s^{-1} at $R_\odot$ (see Appendix A), and it remains constant at larger radii.

The leftmost column of Fig. 3.2 shows two longitude-velocity $(l-v)$ plots at latitudes ±30° extracted from the LAB survey. The middle column of the same figure shows our model disc and the rightmost column shows the emission in the halo region of the LAB datacube. All the plots are centered at the anti-centre ($l=180°$). Note that our cut is rather conservative and there should be no contamination from disc emission in the halo region. Further details on the separation between the H I disc and the halo can be found in Section 2.2.1.

In the application of the model to external galaxies, the fountain clouds have been modelled as point particles because individual clouds, with typical sizes ~ 100 pc, were unresolved in the data (FB06). In the Milky Way nearby clouds and their wakes will be resolved, so we have to check at each time step whether the combined emission of a cloud and its wake is resolved at the angular resolution of the data. If the emission is resolved, we spread the flux in a circular region around its centre. The flux density is assumed to decrease Gaussianly with distance from the centre, with FWHM equal to the apparent size of the cloud and its wake. Given that the data are used at 8° resolution, a cloud and its wake are resolved only if their distance is smaller than $700 \times \frac{D_{\rm cl}}{100\,{\rm pc}}$ pc, where $D_{\rm cl}$ is the system's lengthscale. According to the simulations of Marinacci et al. (2010a), turbulent wakes have sizes of $1-2$ kpc, so they will be resolved out to distances of about 10 kpc. The pattern of emission from a cloud and its wake is quite elongated, having axis ratio ~ 0.5, but the long axis of the emission is randomly orientated, so our circular Gaussian smoothing should provide an adequate representation of the total emission from an ensemble of clouds.

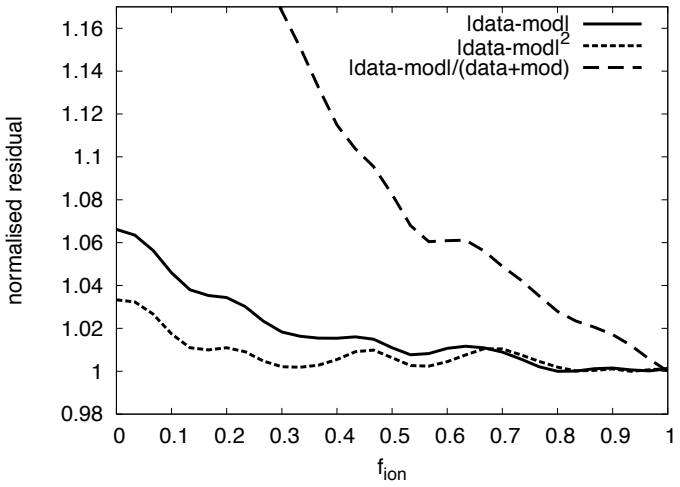

Figure 3.3: Residuals between models and data as a function of $f_{\rm ion}$ for the pure galactic fountain with $h_{\rm v} = 70\,{\rm km\,s^{-1}}$, evaluated using absolute differences (*solid line*), squared differences (*short-dashed line*) and weighted differences (*long-dashed lines*). All residuals have been divided by their respective minimum.

We tested the effect of resolution by increasing $D_{\rm cl}$ up to 2 kpc and found that the modelcube looked just like a smoothed version of that produced with smaller values of $D_{\rm cl}$. In the following we use models with small clouds, $D_{\rm cl} = 200\,{\rm pc}$, for which the modelcube can be computed significantly more quickly.

Once we have a modelcube at the same resolution and with the same total flux as the LAB datacube, we compare them quantitatively by calculating the residuals between them. This calculation is performed by adding up the differences between the models and the data, pixel by pixel, in the halo region. We use absolute differences, squared differences and also weighted residuals, i.e. |data−model| divided by (data+model). The residuals are calculated for a set of models with different input parameters such as the kick velocities $h_{\rm v}$ of the fountain clouds, and the model with the smallest residuals is our "best model". In the following Section we describe our best pure fountain model and our best fountain + condensation model, showing that the latter provides a better description of the Galaxy's H I data.

3.3 Results

3.3.1 A pure galactic fountain

In a pure galactic fountain, the angular momentum of clouds is constant and trajectories depend only on the characteristic kick velocity $h_{\rm v}$ of the clouds. However, the shape of the modelcube is also affected by the ionised fraction $f_{\rm ion}$, which has to be treated as a freely variable parameter.

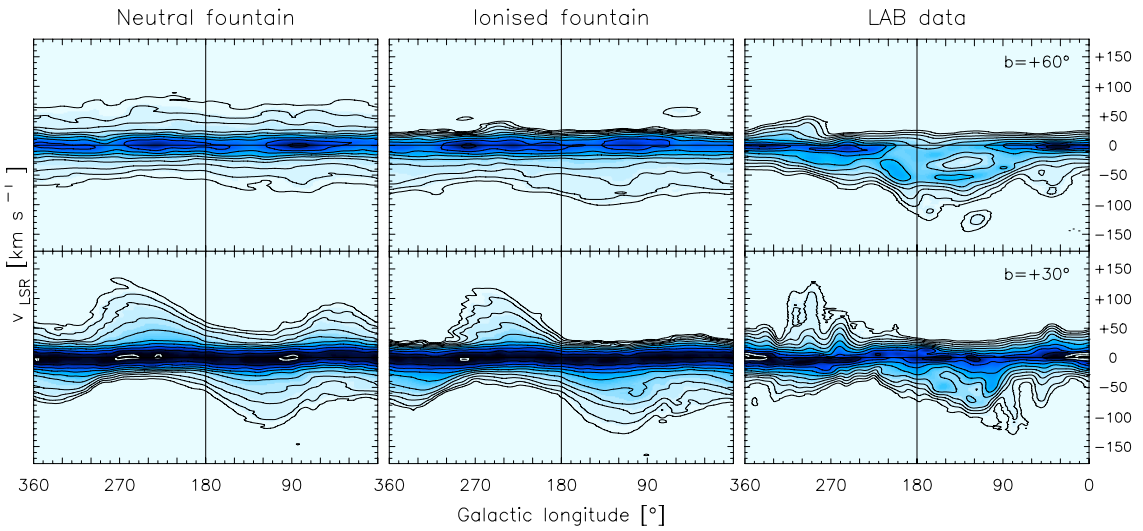

Figure 3.4: Longitude-velocity (l–v) diagrams at $b=60°$ (top panels) and $b=30°$ (bottom panels). *First column*: pure fountain model without phase-change ($f_{\rm ion}=0$); *second column*: best pure fountain model ($f_{\rm ion}=1$); *third column*: the LAB data. Each cube is smoothed to 8° resolution. Contour levels in brightness temperature range from 0.04 K to 81.92 K scaling by a factor 2.

We have calculated the residuals for $h_{\rm v}$ in the range $(30,120)\,{\rm km\,s^{-1}}$ and $f_{\rm ion}$ between 0 and 1. The weighted and non-weighted residuals give different results but the confidence contours overlap for $h_{\rm v}\simeq 70\,{\rm km\,s^{-1}}$ and $f_{\rm ion}=1$. In Fig. 3.3 we show the normalized residuals as a function of $f_{\rm ion}$ for $h_{\rm v}=70\,{\rm km\,s^{-1}}$. Clearly the differences between models and data decrease as $f_{\rm ion}$ approaches 1, regardless of the method of comparison. The mass of the H I halo derived for this model is $M_{\rm halo}=5.2\times10^8\,{\rm M}_\odot$. Here and below the halo masses are estimated by excluding fountain clouds at $|z|<0.4\,{\rm kpc}$, which is roughly the blowout height of a superbubble (see Spitoni et al. 2008). Taking into account also clouds at heights $0.2<|z|<0.4\,{\rm kpc}$, the H I halo mass would become $M_{\rm halo}=7.2\times10^8\,{\rm M}_\odot$.

Fig. 3.4 shows two representative $l-v$ diagrams (centred on the anticentre) at latitudes $b=60°$ and $b=30°$ for: the best pure galactic fountain model (middle column); the same model without phase-change (left column); the data (right column). The difference between the two models is striking, especially at higher latitudes. The l–v plots for the neutral ($f_{\rm ion}=0$) fountain are rather symmetric with respect to the zero velocity line. In the ionised fountain by contrast, the gas appears systematically located at negative velocities. This effect is a consequence of clouds of the ionised fountain being visible only as they fall back to the disc. The data clearly display this preference for more negative than positive velocities. The leftmost column in Fig. 3.7 shows additional $l-v$ diagrams for the best pure fountain model. This model fives a fairly good description of the data, as the most prominent features are reproduced.

Table 3.1: Best galactic fountain models for the Milky Way.

Parameters	Units	Model		
		Neutral (pure)	Ionised (pure)	With corona condensation
h_v	($\mathrm{km\,s^{-1}}$)	70[b]	70	70
$\mathrm{M_{HI}}$ [a]	($\mathrm{M_\odot}$)	4.6×10^8	5.2×10^8	2.7×10^8
$\mathrm{M_{HI+HII}}$ [a]	($\mathrm{M_\odot}$)	4.6×10^8	10.4×10^8	3.0×10^8
f_{ion}		0.0[b]	1.0	0.3
α	($\mathrm{Gyr^{-1}}$)	0.0[b]	0.0[b]	6.3
$\mathrm{M_{accr}}$	($\mathrm{M_\odot\,yr^{-1}}$)	0.0	0.0	1.6
Residual[c]		1.60	1.48	1.26

[a] estimated above 400 pc from the plane; [b] fixed; [c] calculated as absolute differences, the closer to 1 the better the fit.

3.3.2 Including the condensation of the corona

The best pure fountain model described above is extreme in that it requires the full ionisation of ejected clouds and a large mass of the gaseous halo (see Table 3.1). Moreover there are several locations in the artificial datacube where the model systematically fails to reproduce the data in detail. The arrows in Fig. 3.7 indicate such regions. In these regions radial motions are important. For instance filled arrows show the region around the anticentre, $150^\circ < l < 250^\circ$, where the data, almost at every latitude, have a broader distribution in velocity than the pure fountain model. Gas in this region is flowing towards the centre of the Galaxy from beyond the Solar circle. In a pure galactic fountain, orbits seldom move in this way (FB06) and independently of the ionised fraction they do not produce much emission in the marked region. This is clearly visible in Fig. 3.5, which shows some representative orbits for our model of the galactic fountain: gas particles in a pure fountain (red curves) tend to move outwards.

We now show that including the interaction between clouds and the corona as described in Section 3.2.3 substantially improves this situation. The interaction is parametrised by the specific condensation rate α. The larger α is, the faster gas condenses from the corona, the greater the rotational lag of the H I, and the more prominent is inward radial motion of H I (blue curves in Fig. 3.5).

Now the residuals between the data and the models are minimised by varying three parameters ($h_{\mathrm{v}}, f_{\mathrm{ion}}, \alpha$). We assume that condensation and drag are suppressed close to the Galactic plane ($|z| < 0.4\,\mathrm{kpc}$). A full analysis of this three-dimensional parameter space would be too expensive computationally, so we explore only the space (α,f_{ion}) and fix the kick velocities at three values: $h_{\mathrm{v}} = 60$, 70 and $80\,\mathrm{km\,s^{-1}}$. For each value of h_{v} we build a map of the residuals between models and data by varying the other parameters in the ranges $0 < f_{\mathrm{ion}} < 1$ and $-3 < \log(\alpha/\,\mathrm{Gyr^{-1}}) < -1.67$ with a step of 0.033 in both directions. This map is then smoothed to the

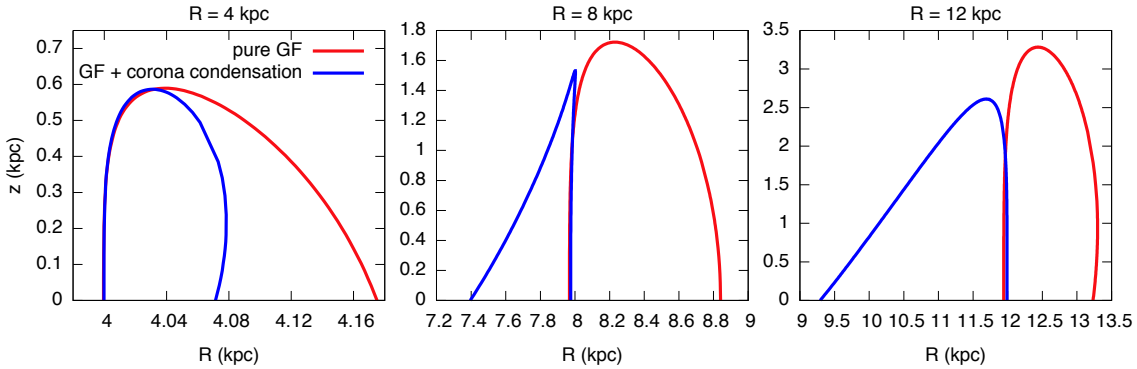

Figure 3.5: Trajectories on the meridional plane (R, z) for fountain particles ejected from the disc at three different radii (indicated on top of each panel) in our model of the galactic fountain. *Red* curves represent orbits for the pure fountain model, while *blue* curves represents orbits for the fountain model with coronal condensation ($\alpha = 6.3\,\mathrm{Gyr}^{-1}$). The direction of the ejection is perpendicular to the plane and v_{kick} is fixed at $70\,\mathrm{km\,s}^{-1}$.

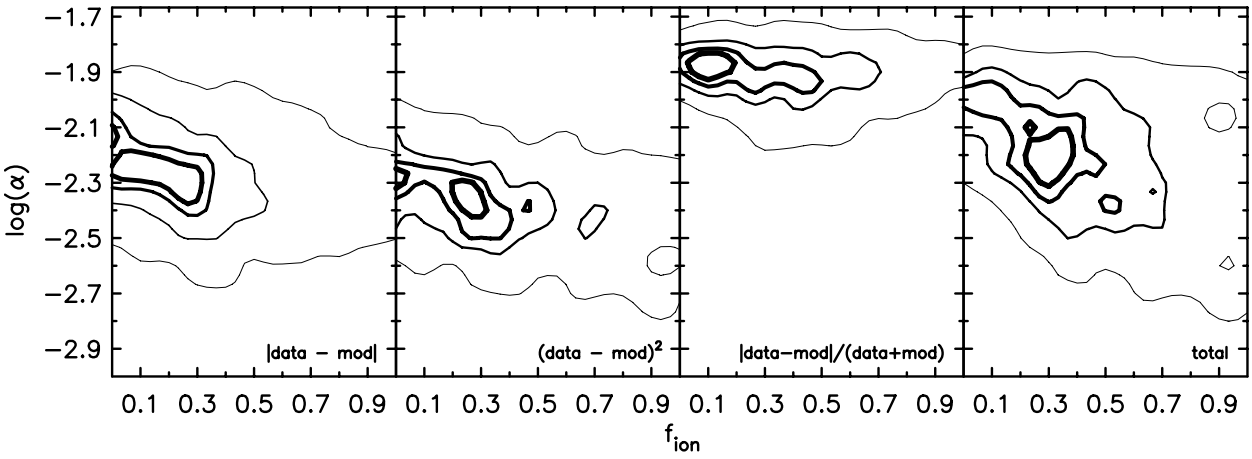

Figure 3.6: Contour plots of residuals between models with corona condensation and data evaluated in the parameter space $(\log(\alpha), f_{\mathrm{ion}})$ for $h_{\mathrm{v}} = 70\,\mathrm{km\,s}^{-1}$. Different panels compare models and data in different ways, as labelled. In each panel all values have been divided by the respective minimum. The fourth panel is the sum of the previous three, divided by the resulting minimum. Contour levels at $1.005, 1.01, 1.02, 1.05$.

resolution of 0.1×0.1 in order to minimise the stochastic effects due to the probability distribution function (eq. 3.1) used to build our models. As in the case of a pure fountain, different residuals give different results. Regardless of α and f_{ion}, absolute and squared differences have lower values for $h_{\mathrm{v}} = 80\,\mathrm{km\,s}^{-1}$, while relative residuals favour $h_{\mathrm{v}} = 60\,\mathrm{km\,s}^{-1}$. Hence we set our kick velocity in the middle and focus on models with $h_{\mathrm{v}} = 70\,\mathrm{km\,s}^{-1}$.

The first three panels in Fig. 3.6 show the residual maps obtained with $h_{\mathrm{v}} = 70\,\mathrm{km\,s}^{-1}$ for different types of residuals. In each panel all values are divided by the respective minimum, thus they are dimensionless and ≥ 1. Combining these three panels we obtain the fourth (rightmost) panel, which is the sum of the previous three divided by the resulting minimum, which occurs at $f_{\mathrm{ion}} = 0.3$ and $\log(\alpha) = -2.2$ (so $\alpha = 6.3\,\mathrm{Gyr}^{-1}$). For this best model the mass of the H I halo is $2.7 \times 10^8\,\mathrm{M}_\odot$. Table

3.1 lists these parameters.

The middle column of Fig. 3.7 shows that the model with coronal condensation reproduces the emission near the anticentre better than the pure fountain model. The open arrows (latitudes $b = \pm 30°$) indicate other regions where the inclusion of coronal condensation improves the fit to the data. These are regions in which H I is flowing out from the inner disc, and the pure fountain provides too much emission.

The superiority of our model with corona condensation with respect to the pure fountain is also evident in some of the channel maps shown in Fig. 3.8. In particular, at velocities of $+45\,\mathrm{km\,s^{-1}}$ and $+35\,\mathrm{km\,s^{-1}}$ the model without condensation underestimates the amount of emission at longitudes $l < 90°$, which is instead significant in both the other model and in the LAB data. The opposite happens at $v_{\mathrm{LSR}} = -60\,\mathrm{km\,s^{-1}}$ for latitudes $l > 270°$, where the pure model shows an evident excess of H I emission which is not visible in the other panels. These discrepancies are due to the combination of the global radial outflow and the strong vertical infall predicted by our best pure fountain model. Note that the H I blobs at anomalous positions visible in the pure fountain at $v_{\mathrm{LOS}} = +35, +60\,\mathrm{km\,s^{-1}}$ are due to the stochastic nature of our models. Neither of the two models can reproduce the emission of the HVCs, with the exception perhaps of complexes WA, WC and WD, which however have velocities close to the IVC regime. We discuss in more detail the relation between our model and the HVCs/IVCs in Section 3.4.4.

For our best-fitting value of α, the condensation rate of coronal gas into the clouds' wakes is $\dot{M} = 1.6\,\mathrm{M_\odot\,yr^{-1}}$. Correcting this value for the He content increases the condensation rate to $2.3\,\mathrm{M_\odot\,yr^{-1}}$. This value is remarkably close to the Galaxy's SFR, which we assume to be in the range $1{-}3\,\mathrm{M_\odot\,yr^{-1}}$ (Chomiuk and Povich 2011). We consider it highly significant that $\dot{M}$ deduced from an H I survey should agree so well with that required to sustain the SFR, which is obtained without reference to H I.

The exact value of the condensation rate $\dot{M}$ depends on several factors. An important parameter is the value of v_{lag} (eq. 3.5), which regulates the rotation of the corona and therefore the efficiency of both the drag ($t_{\mathrm{drag}} \propto v_{\mathrm{lag}}^{-1}$) and the condensation (Marinacci et al. 2011). However, experiments show that the dependence of $\dot{M}$ on the adopted value of v_{lag} is not too strong: ($v_{\mathrm{lag}} = 50\,\mathrm{km\,s^{-1}}$, $t_{\mathrm{drag}} = 1200\,\mathrm{Myr}$) yields $\dot{M} = 2.8\,\mathrm{M_\odot\,yr^{-1}}$ ($3.9\,\mathrm{M_\odot\,yr^{-1}}$ when corrected for He), while ($v_{\mathrm{lag}} = 100\,\mathrm{km\,s^{-1}}$, $t_{\mathrm{drag}} = 600\,\mathrm{Myr}$) yields $\dot{M} = 1.0\,\mathrm{M_\odot\,yr^{-1}}$ ($1.4\,\mathrm{M_\odot\,yr^{-1}}$ when corrected for He). It is interesting to note that $\dot{M}$ depends very little on the criterion used to minimise the residuals. Although the three criteria yield rather different values for the best-fitting α (see Fig. 3.6), $\dot{M}$ only varies between 1.5 and $1.7\,\mathrm{M_\odot\,yr^{-1}}$ given that the halo masses also vary between the three models.

Our parametrisation assumes that α is spatially constant. Fortunately, the density of the corona should not vary too much in the regions where the interaction with the fountain is efficient (Marinacci et al. 2011), so spatial variation of α is not expected to give significantly different results.

On the whole, the dynamical modelling of the Galactic H I halo performed in

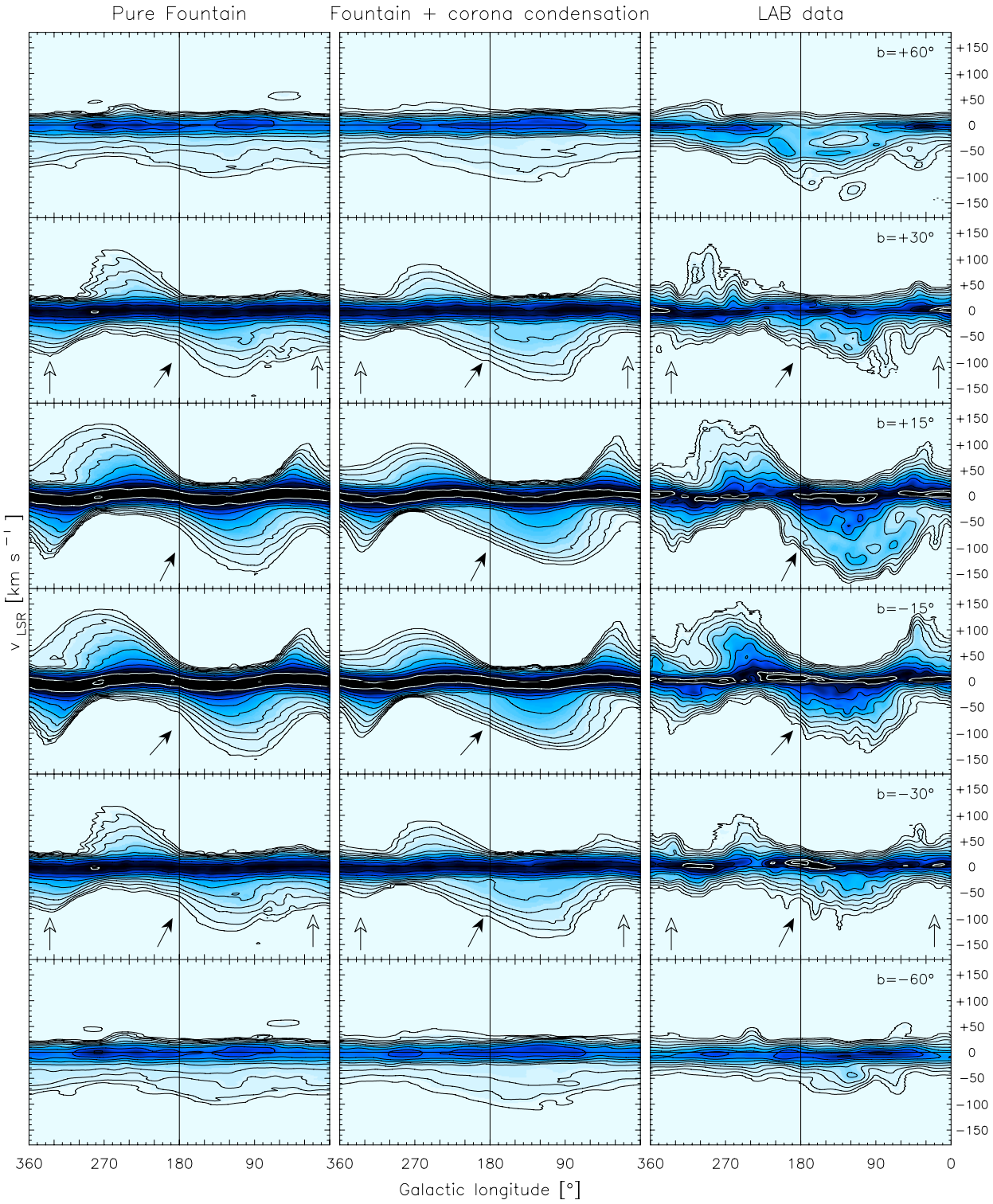

Figure 3.7: $l-v$ slices at 6 different latitudes indicated at the top right corner of the rightmost plots. *First column*: best pure Galactic fountain; *second column*: best fountain with condensation of the corona; *third column*: the LAB data. Each cube is smoothed to 8° resolution. Contour levels in brightness temperature range from 0.04 K to 81.92 K scaling by a factor 2. The arrows show regions where radial motions are present and the model with coronal condensation reproduces the data better than the pure fountain model, see text.

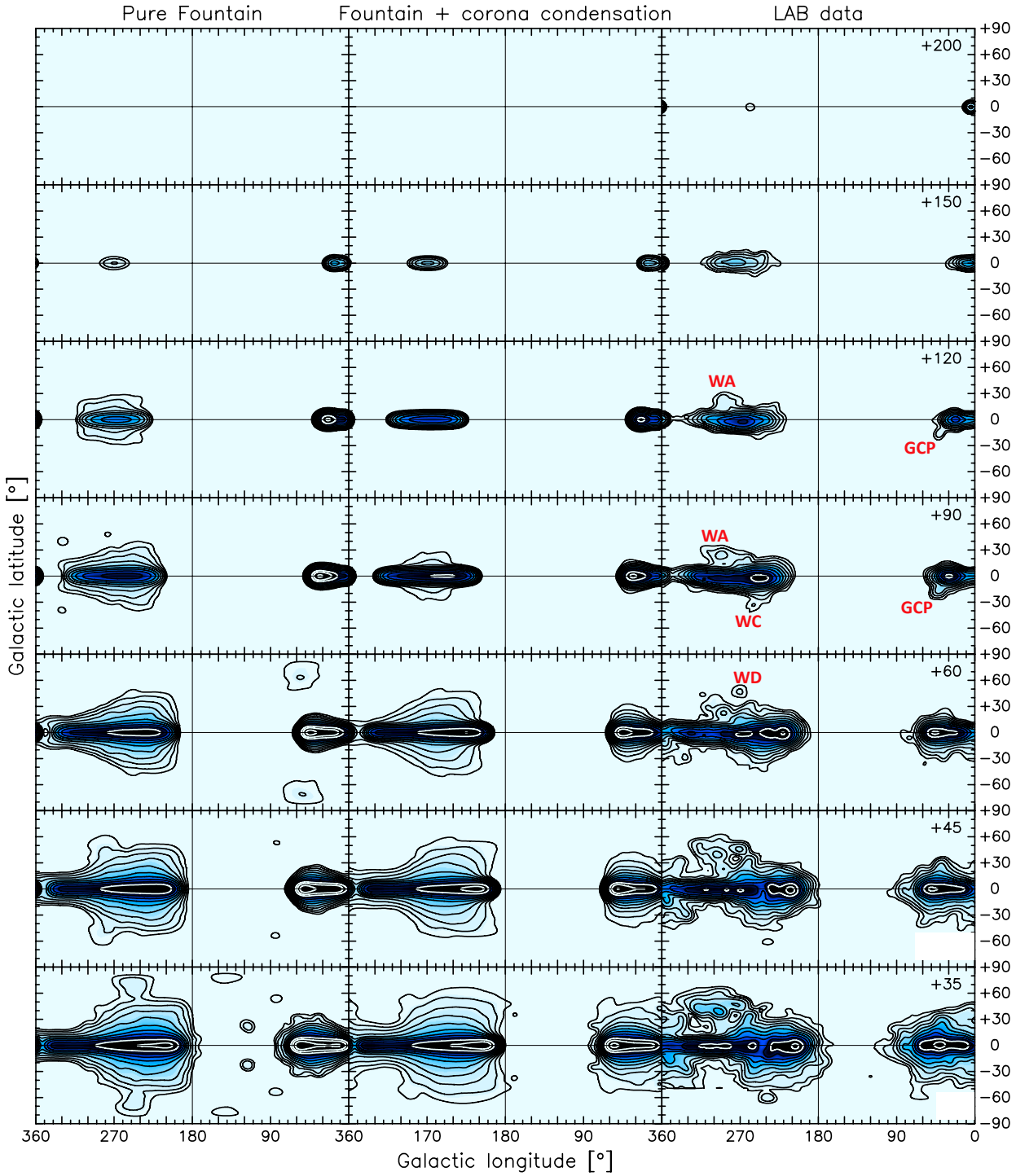

Figure 3.8: Channel maps at 14 different velocities indicated at the top right corners (for $v_{\rm LOS} > 0$) or at the bottom left corner (for $v_{\rm LOS} < 0$) of the rightmost plots. *First column*: best pure Galactic fountain; *second column*: best fountain with condensation of the corona; *third column*: the LAB data. Each cube is smoothed to 8° resolution. Contour levels in brightness temperature range from 0.04 K to 81.92 K scaling by a factor 2. The classical HVCs are labelled. The Magellanic Clouds, the Magellanic Stream and the Leading Arm have been removed.

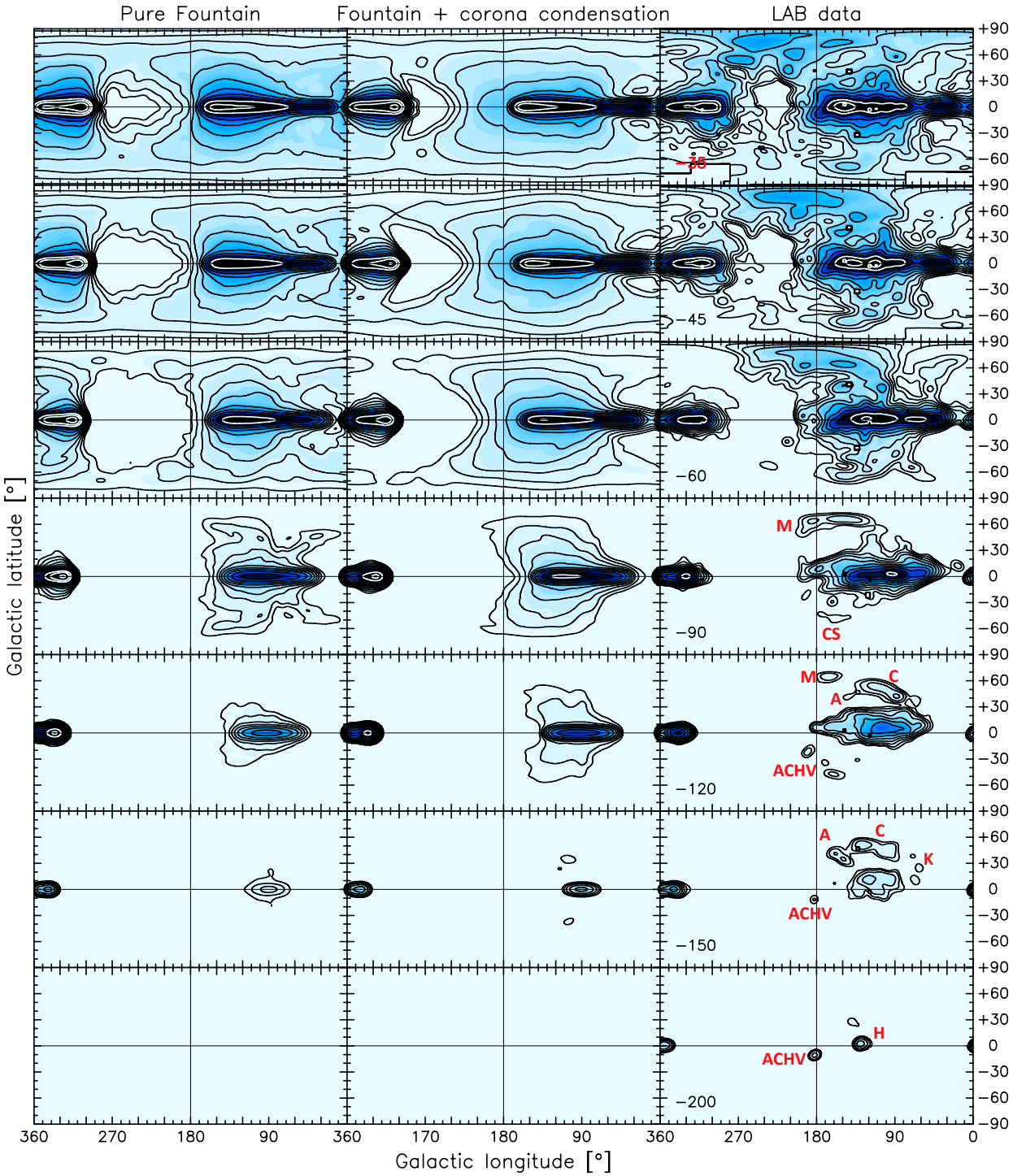

Figure 3.8 (Continued)

this work is a success. The results are consistent with the conclusions drew from the kinematic model in Chapter 2. We found negative values for both the average vertical and the radial velocities of the halo material, and deduced that ejected clouds must be partially ionised (but in a fraction larger than our current determination). Our dynamical analysis identifies these properties as arising from the sharing of angular momentum with gas accreted from the lagging corona. Finally, our Galactic fountain is dynamically sustainable. It requires a rate of kinetic-energy injection equal to $6.2 \times 10^{39}\mathrm{erg\,s^{-1}}$, which with a supernova rate $\mathrm{SNR} = 0.03\,\mathrm{M_\odot\,yr^{-1}}$ and an energy per supernova of 1×10^{51}erg corresponds to an efficiency of about 0.7%.

3.4 Properties of the Galactic H I layer

Now that we have a model that reproduces all the main features of the LAB datacube, we can investigate in detail the physical properties of the Galaxy's extraplanar H I layer.

3.4.1 Rotation versus height

Fig. 3.9 shows the rotation curve of the Galaxy's extraplanar gas at different distances from the plane as a function of R. These values were derived from our best model by simply taking the weighted mean of the azimuthal components of the velocities of the particles at different heights. As expected, the halo gas is lagging the rotation of the disc (thick curve), whose rotational speed has been taken equal to the circular velocity in the assumed gravitational potential. Roughly 50% of this lag is due to gravity (FB06) whilst the other half is produced by a combination of the interaction with the corona and the phase-change. At $\mathrm{R_\odot}$ the gradient is about $-14.3 \pm 1.1\,\mathrm{km\,s^{-1}\ kpc^{-1}}$ in excellent agreement with the average value derived in Section 2.3.3 for the inner regions of the Milky Way ($-15 \pm 4\,\mathrm{km\,s^{-1}\ kpc^{-1}}$), which also coincides with the value derived for NGC 891 by Oosterloo et al. (2007). Note that the disc rotation curve in the inner $3-4$ kpc is uncertain due to the presence of the Galactic bar.

3.4.2 Thickness of the H I layer

A second fundamental property of the Galaxy's H I halo is its thickness. To obtain it we fitted the vertical density profiles in our models at different radii with exponential functions. Fig. 3.10 shows the (exponential) scaleheight of the H I halo of our best model as a function of R.

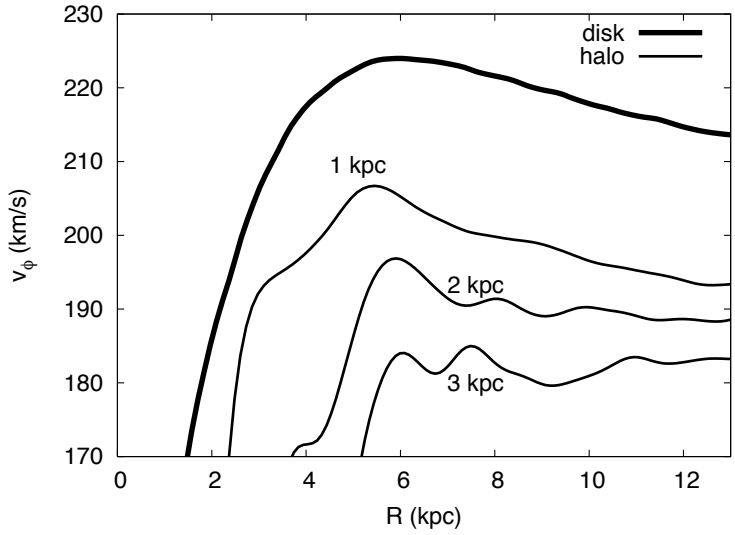

Figure 3.9: Rotational velocities for the H I layer of the Milky Way at different heights from the plane (thin lines), compared to the disc rotation curve (thick line). The velocities are derived from our best fountain model with condensation of the corona by taking the weighted average of v_ϕ at that (R, z) location.

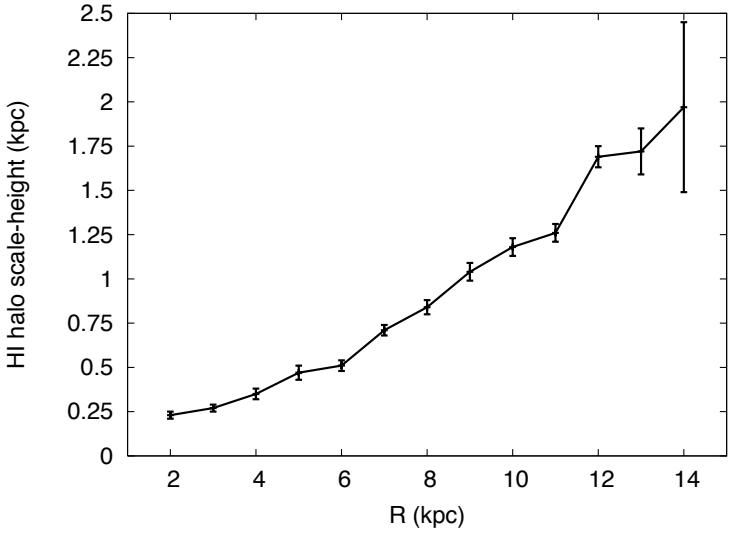

Figure 3.10: Scale-height as a function of R for our best halo model including condensation of the coronal gas.

The thickness increases with R because the gravitational restoring force to the plane diminishes outwards (FB06 and Fig. 3.5). The halo density decreases abruptly for $R > 14$ kpc, so its thickness cannot be reliably determined at larger radii. The shape of the scaleheight as a function of R is partially due to the assumption of our model that the kick velocity $h_{\rm v}$ does not change with radius (for a discussion see FB06). In the inner Galaxy there has long been evidence for a population of H I clouds extending up to ~ 1 kpc above the midplane (Lockman 1984, 2002; Ford et al. 2010). In Chapter 2 we assumed a constant thickness for the halo and derived a value of 1.6 kpc using a sech^2 formula, which corresponds to $\sim$ 800 pc for an

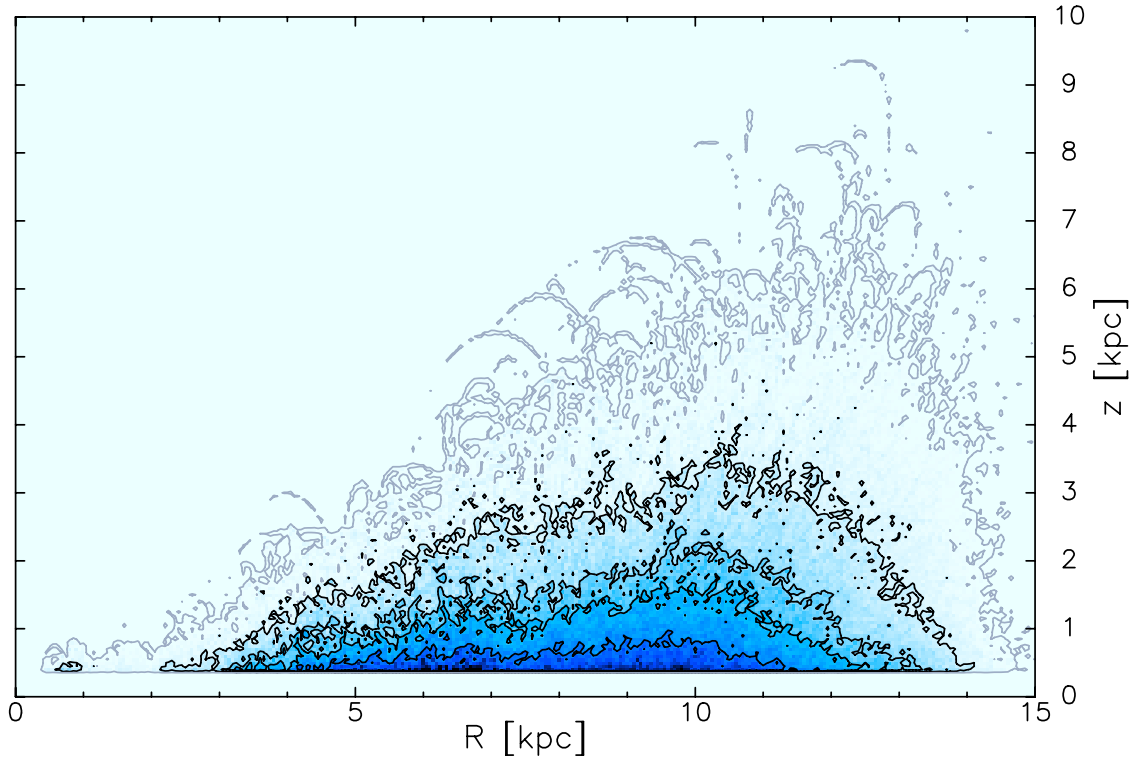

Figure 3.11: H I particle density $n_{\rm HI}(R,z)$ for our best halo model including condensation of the coronal gas. Black contours are at 1, 3, 5 and $10\times10^{-3}\,{\rm cm}^{-3}$ from the outermost to the innermost. The outer grey contour is at $10^{-4}\,{\rm cm}^{-3}$. Regions at $z<400\,{\rm pc}$ are not shown.

exponential function. This value agrees well with the average of the scaleheights plotted in Fig. 3.10.

Fig. 3.11 shows the H I density on the meridional plane (R,z) for our best halo model including corona condensation. The thickness of the H I layer increases clearly with R, implying a toroidal shape for the three-dimensional distribution of cold gas. Fig. 3.10 indicates that the halo H I in the Milky Way is mostly located within a distance of $3-4\,{\rm kpc}$ from the disc. Interestingly, however, fountain cloud particles above that height are present in the model and produce a faint layer that extends vertically up to $\sim10\,{\rm kpc}$ (grey contour in Fig. 3.11). This layer is probably built by particles in the high-velocity tail of the $v_{\rm kick}$ distribution. To test this, we built a model with corona condensation by considering a constant kick velocity of $70\,{\rm km\,s}^{-1}$ for all the particles, finding that in this case no clouds are located beyond 3.7 kpc from the disc. The average H I density above $z\sim3.5\,{\rm kpc}$ from the disc drops below $10^{-3}\,{\rm cm}^{-3}$ (outermost black contour in Fig. 3.11), value that can be taken as representative for the coronal gas (e.g. Fukugita and Peebles 2006; Heitsch and Putman 2009; Marinacci et al. 2010a). This would suggest that cold fountain clouds above 3.5 kpc from the disc must be rare. These considerations indicate that virtually all the cold gas ejected in the halo of the Milky Way by stellar feedback is likely to be located within a few kpc from the disc.

Kalberla et al. (2007) studied the vertical structure of the Galaxy's H I layer on

the assumption that the layer is in hydrostatic equilibrium. Using this assumption, they inferred that while at $R_\odot$ the H I layer extends only a few hundred parsecs from the plane, at $R \simeq 35\,\mathrm{kpc}$ the vertical structure of the H I layer can be fitted by a Gaussian distribution with scale height 2.5 kpc. Thus they deduced a very extended H I layer with strong flaring. They also inferred the existence of a massive ring of dark matter between $R = 13$ and 18.5 kpc. The assumption of hydrostatic equilibrium leads, however, to models that fail to match the data correctly (see Barnabè et al. 2006; Marinacci et al. 2010b). If Kalberla et al. (2007) had used the prediction of a fountain model for the distribution of H I near $R_\odot$ rather than a model based on hydrostatic equilibrium, they would have come to different conclusions regarding the radii responsible for each quantity of emission in the LAB datacube. Consequently, the distribution of the matter and the structure of the H I flare in the Milky Way should be re-derived. While this topic merits further work, our comparisons of the fountain model with the data yield no compelling evidence for substantial flaring of the H I layer much beyond $R \sim 15\,\mathrm{kpc}$.

3.4.3 Accretion and circulation of gas

Infall of metal-poor gas to the star-forming disc is an essential ingredient of current models of the Galaxy's chemical evolution (e.g. Chiappini et al. 2001; Schönrich and Binney 2009). The predictions of such models depend to a significant extent on the radial profile of the infall, but hitherto there has been no credible way of determining this profile. The prediction of our model for this profile is shown in Fig. 3.12 (bottom panel). The curve shows the pristine gas that, condensing from the corona onto the fountain cloud wakes, follows the cloud trajectories back to the disc. The shape of the accretion profile is due to the variation of the mass outflow and the orbital time with radius. At $R \lesssim 3\,\mathrm{kpc}$ the specific accretion rate essentially vanishes because the orbits of the fountain clouds are confined within few hundred of parsecs from the disc (see Fig. 3.10). It then rises to a peak at $R \simeq 9\,\mathrm{kpc}$ as in this region both the orbital time and the star formation are sufficiently high. At $R > 9\,\mathrm{kpc}$ the accretion rate falls again due to the low level of star formation at these radii, and drops to about zero beyond $R = 13\,\mathrm{kpc}$. The integral of this curve over the disc surface gives a global accretion rate of $\dot{M} = 1.6\,\mathrm{M_\odot\,yr^{-1}}$. Note that the peak in the accretion rate lies well beyond the peak in the Milky Way's SFR, which occurs around $R = 4\,\mathrm{kpc}$. This implies the need for a redistribution of gas in the disc, the study of which is beyond the scope of the present Thesis (but see for instance Schönrich and Binney 2009; Spitoni and Matteucci 2011; Bilitewski and Schönrich 2012).

The top panel of Fig. 3.12 shows the net flow (H I+H II) as function of R, obtained as the difference between the rate at which gas arrives at a given radius and the rate at which supernovae eject gas from that radius. The net flow profile differs from the accretion profile because fountain clouds do not fall back onto the disc at the same radius they are ejected from, as shown in Fig. 3.5. As R increases, the trajectories

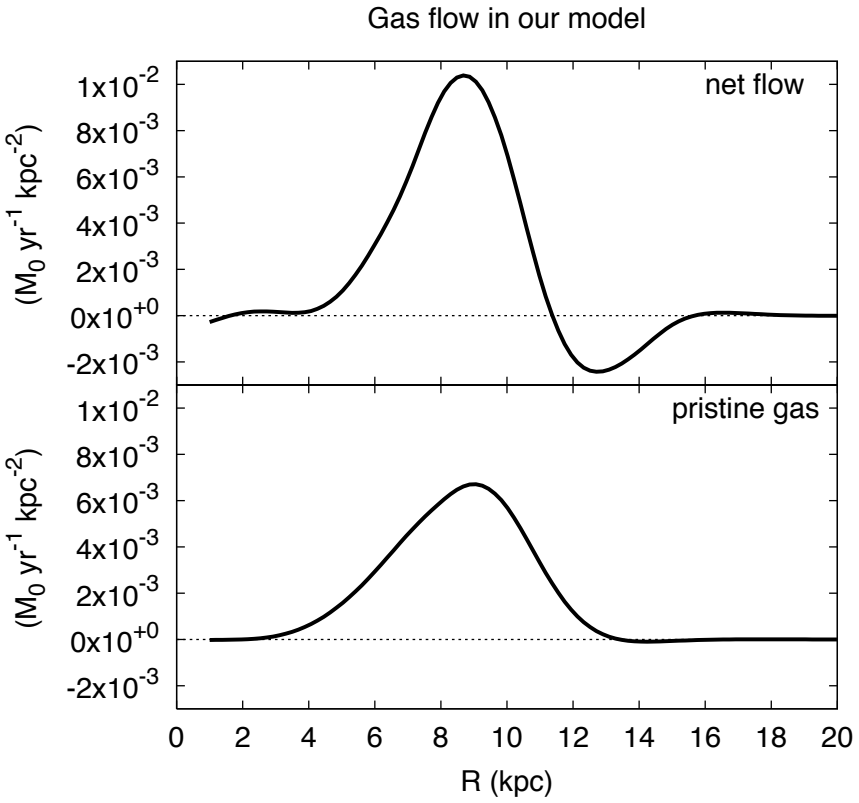

Figure 3.12: Hydrogen flow as function of R predicted by our best model with condensation of the corona. Inflows (outflows) are represented by positive (negative) values. *Top panel*: net flow (inflow − outflow) produced by the Galactic fountain. *Bottom panel*: accretion of pristine gas from the corona onto the disc. The global accretion rate is $1.6\,\mathrm{M}_\odot\,\mathrm{yr}^{-1}$.

of fountain clouds start to get an inward component because of the interaction with the corona, thus clouds land at smaller and smaller radii. In particular, most of the clouds ejected at $11 < R < 15\,\mathrm{kpc}$ fall back onto the disc at $6 < R < 11\,\mathrm{kpc}$ (rightmost panel of Fig. 3.5). As a consequence, a 'draining region' forms at $11 < R < 15\,\mathrm{kpc}$, while inside this annulus the amount of gas falling onto the disc significantly exceeds the outflowing counterpart: about 70% of this inflow comes from the condensation of the corona, the remaining part is due to the described gas circulation. On the whole, the fountain circulation contributes to 76% of the halo mass, while the accreted gas is 24%. This latter is similar to that derived by FB08 for NGC 891 and NGC 2403 ($\sim 10 - 20\%$).

3.4.4 HVCs and IVCs

At large line-of-sight velocities the H I emission in the halo region of our Galaxy is dominated by the HVCs, the emission from which lies in rather isolated outlying regions of the (l, b, v) space delimited by $|v_{\mathrm{DEV}}| > 90\,\mathrm{km\,s}^{-1}$ (van Woerden et al. 2004). The upper panels in Fig. 3.13 compare the emission predicted by our best model (left panel) near $v_{\mathrm{LSR}} = -144\,\mathrm{km\,s}^{-1}$ with what is actually observed. In the

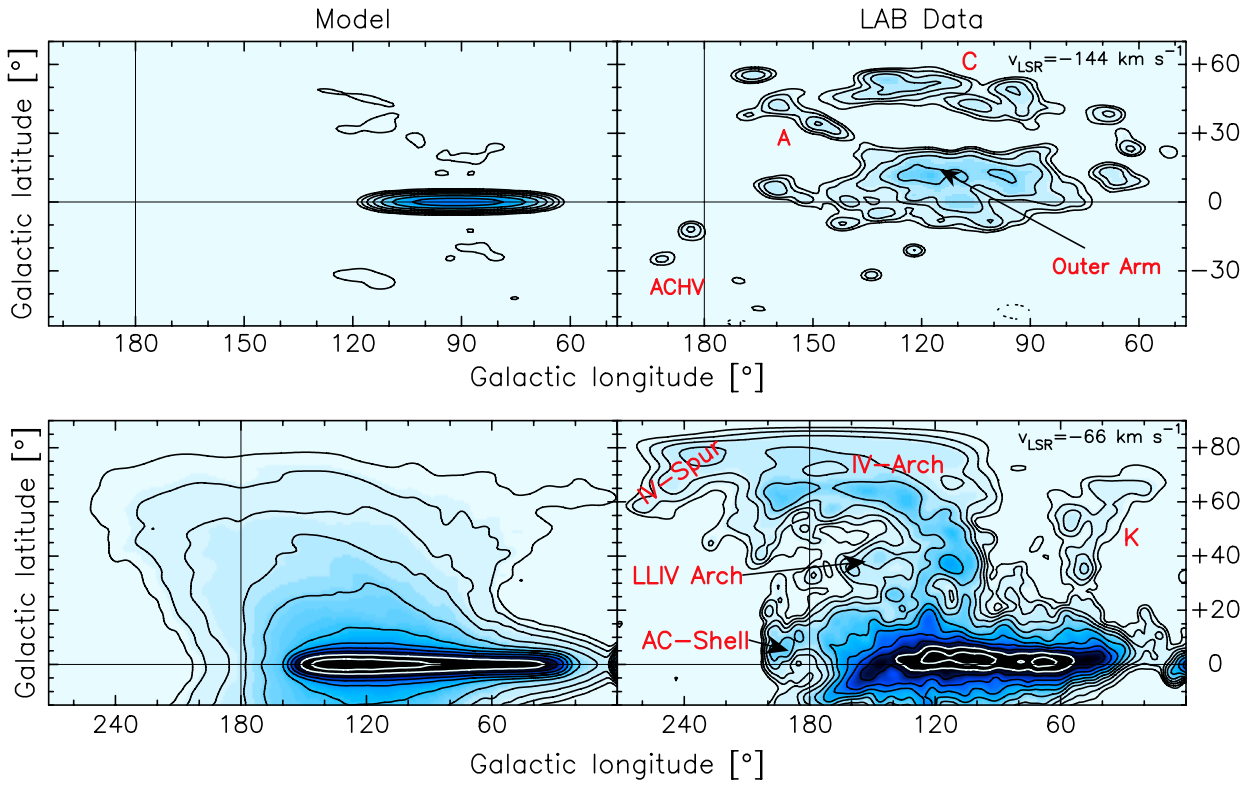

Figure 3.13: Channel maps at $v_{\rm LSR} = -144\,{\rm km\,s^{-1}}$ (top) and $v_{\rm LSR} = -66\,{\rm km\,s^{-1}}$ (bottom) for our best model with coronal condensation (left panels) and the LAB data (right panels). Both model and data are smoothed to 4° resolution. Contour levels in brightness temperature range from 0.04 K to 81.92 K scaling by a factor 2. Some of the high and intermediate-velocity complexes are labelled (see text).

data, three main islands of emission are apparent. At $b > 30°$ we see Complexes A and C, which have no real counterparts in the model. Similarly emission at $l \gtrsim 180°$ associated with the Anticentre High-Velocity Cloud (ACHV) has no counterpart in the model. The same is valid for other HVCs like complexes H and GCP, as shown in Fig. 3.8. It is well known that the metallicity of most HVCs, in particular Complexes A and C is much lower than that of gas in the disc, which strongly suggests that they come from outside the Galaxy (see Wakker 2001). Moreover, assuming a distance of 10 kpc for both Complexes A and C (van Woerden et al. 2004; Thom et al. 2008) gives for these objects heights from the midplane of $6 - 8$ kpc. To produce emission so far from the plane, we would need a kick velocity $h_{\rm v} \gtrsim 150\,{\rm km\,s^{-1}}$ (see also Section 5.4.3). A model with $h_{\rm v}$ so large completely fails to reproduce the data globally. In summary, HVCs such as Complexes A and C are almost certainly extragalactic in origin and our model is quite correct not to reproduce them. The rate at which the Galaxy accretes gas from infalling HVCs is $\sim 0.08\,{\rm M_\odot\,yr^{-1}}$ (Putman et al. 2012), an order of magnitude lower than our estimate of the rate of accretion via the fountain + corona condensation mechanism.

The main body of emission in the upper right panel of Fig. 3.13 forms a large island that straddles the plane. Its summit lies at $(l, b) = (120°, 15°)$ and is labelled

"Outer Arm". This feature is thought to arise from the warp of the H I disc. Our model (left panel) does not include a warp in the disc, so apart from two horns of very faint emission either side of the plane, its emission is confined in a thin region around the plane.

The lower panels of Fig. 3.13 show predicted (left) and observed (right) emission at much lower heliocentric velocities ($v_{\rm LSR} \simeq -66\,{\rm km\,s^{-1}}$) than the upper panel. At such Intermediate Velocities (IVCs are classically defined to be at $35\,{\rm km\,s^{-1}} < |v_{\rm DEV}| < 90\,{\rm km\,s^{-1}}$) the model is seen to reproduce the global structure of the data very well, as already shown in Fig. 3.13. Moreover, some of the IVCs that contribute to this emission have been shown to have a distance from the Sun of $\lesssim 3\,{\rm kpc}$ and disc-like metallicities (van Woerden et al. 2004), consistent with their being fountain clouds. In the lower-right panel of Fig. 3.13 several IVCs are visible (IV-Arch, IV-Spur, LLIV-Arch, AC-Shell, Complex K), mainly at positive latitudes. The emission of our model is smoother than the data, but apart from that it is consistent with the location of all the IVCs.

The classical IVCs shown in the lower right panel of Fig. 3.13 must be just the most conspicuous members of a large population of IVCs that collectively comprise the H I halo, as already discussed in Section 2.5.3. By assuming azimuthal symmetry, our model suppresses much of the noise inherent in observing a population of discrete clouds. In principle one could hope with a more sophisticated model to reproduce the statistical properties of this noise, but there is no particular merit in reproducing individual IVCs, which will just be the chance, and ephemeral, products of individual bursts of star formation.

If IVCs contain a mixture of metal-rich gas ejected from the disc and gas condensed from the rather metal-poor corona, the metallicities of these clouds should be intermediate between those of the disc and corona. Since the fraction of accreted material is only $\sim 24\%$ of the whole halo mass, the IVCs should be somewhat more metal-poor than the disc.

3.5 Discussion

3.5.1 Analytic approximation vs hydrodynamical simulations

In Section 3.2.3 we pointed out that our assumption of exponential growth of the mass of the cold gas is qualitatively similar to that observed by Marinacci et al. (2010a) in their hydrodynamical simulations of cold clouds travelling through a hot medium. Here we show that this agreement is quantitatively sound.

The points in the left panel of Fig. 3.14 show the mass of coronal gas that has $T < 3 \times 10^4\,{\rm K}$ in the simulations of Marinacci et al. (2011); the units are fractions of the initial mass of the cloud. The curve shows the mass accreted by a particle that

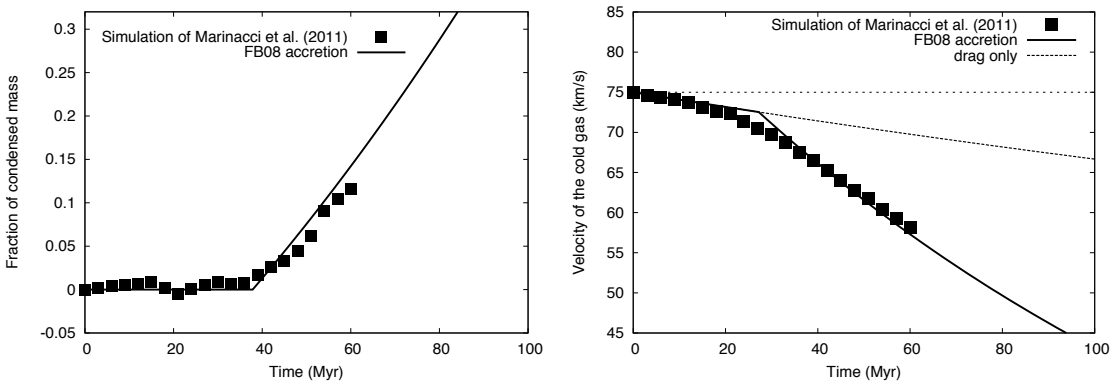

Figure 3.14: *Left panel:* The square points show the mass of coronal gas that condensed into the cloud wake as a function of time extracted from the simulations of Marinacci et al. (2011). *Right panel:* The square points show the velocity centroid of cold gas in the simulations of Marinacci et al. (2011), the dashed curve shows the prediction in case of drag ($t_{\rm drag} = 800\,{\rm Myr}$) without condensation. In each panel the solid curves show the predictions of the inelastic collision+drag recipe used in this work (equation 3.7).

after 38 Myr starts to accrete according to equation (3.6) with the growth rate set to the value, $\alpha = 6.3\,{\rm Gyr}^{-1}$, determined by our fits to the LAB datacube (Table 3.1). The fit in Fig. 3.14 between the curve and the data points from Marinacci et al. (2010a) is excellent. We interpret the delay by 38 Myr before accretion starts as the time required for cold gas from the cloud to mix with the coronal gas plus the time required for the coronal gas to cool to $T < 3 \times 10^4\,{\rm K}$.

The points in the right panel of Fig. 3.14 show the velocity of the cold-gas centroid in the simulations of Marinacci et al. (2011). The dashed line shows the evolution of the velocity if the cloud were a rigid body that experienced hydrodynamical drag as described in FB06 with $t_{\rm drag} = 800\,{\rm Myr}$. This line fits the data from Marinacci et al. (2011) well until $t \simeq 20\,{\rm Myr}$. At later times the full thick curve shows the prediction for the combined effects of drag and condensation, obtained from equation (3.7) using again $\alpha = 6.3\,{\rm Gyr}^{-1}$. The required condensation rate is very similar than that predicted by the simulations.

It is remarkable that detailed hydrodynamical simulations yield a value of the accretion rate α that agrees so well with the value we obtained by fitting the H I datacube because the only connection between these two determinations is the underlying physics of turbulence. It is true that to obtain the agreement we did have to choose a value for the delay between the start of a hydrodynamical simulation and the onset of effective cooling. *Some* delay is inevitable because the hydrodynamical simulations start with unrealistically spherical clouds and no wake. More realistic initial conditions for the dynamics of gas expelled from the disc by a superbubble would yield a time shorter than $30 - 40\,{\rm Myr}$ for steady accretion to become established.

The simulations of Marinacci et al. (2011) last only 60 Myr; new simulations that also include gravity (Marinacci et al. 2012) show that the cold gas (cloud + wake) falls back to the disc in rather coherent structures with sizes of $1 - 1.5\,{\rm kpc}$

and after times larger than 60 Myr and comparable to the ballistic travel times.

While our choice of temperature threshold at $T = 3 \times 10^4\,\mathrm{K}$ for gas to become visible as H I is somewhat arbitrary, experimenting with different temperature thresholds we found that the trends of mass and velocity are perfectly comparable with the one shown here (F. Marinacci, private communication).

In conclusion, the analytical treatment of an *inelastic collision* between fountain particles and ambient gas proposed by FB08 and adopted here is quantitatively supported by the numerical simulations of Marinacci et al. (2011). The system of cloud + turbulent-wake accretes mass and looses specific momentum in the way predicted by the analytical formula. Remarkably the rate at which this process occurs in the simulations is the same as the rate we estimated by fitting models to the LAB survey data.

3.5.2 Comparison to other galaxies

FB06 and FB08 applied the model discussed here to two external galaxies, the MW-like NGC 891, and the M33-like NGC 2403. For the former the kick velocities necessary to reproduce the data were in the range $70 - 90\,\mathrm{km\,s^{-1}}$ depending on the shape of the potential and the extent and type of gas accretion considered. For NGC 2403 the data could be reproduced with values of the initial kick velocity from $75\,\mathrm{km\,s^{-1}}$ down to about $50\,\mathrm{km\,s^{-1}}$. Thus the value of $70\,\mathrm{km\,s^{-1}}$ that minimises the residuals in the Milky Way is fully consistent with those needed to produced the H I halos of other galaxies. As discussed in FB06, these velocities are also consistent with hydrodynamical simulations of superbubble expansion (e.g. Mac Low et al. 1989).

The accretion parameters α estimated by FB08 for NGC 891 and NGC 2403 are a factor $3 - 7$ lower than that found here for the Milky Way. This would imply shorter timescales for the condensation of the ambient gas in the Milky Way. However, the value of α is linked to the rotational velocity assumed for the corona where it interacts with the fountain. FB08 assumed that the fountain gas interacted with a *static* ambient medium, which maximised the effect of the process. Had we considered such a configuration for our corona we would have found a condensation parameter $\alpha = 2.5\,\mathrm{Gyr^{-1}}$. In this case $t_{\mathrm{drag}} \sim 300\,\mathrm{Myr}$, which implies that the drag slightly dominates over the condensation. However, as explained in Section 3.2.3, a static (non-rotating) corona is not a realistic possibility.

3.5.3 Comparison with the kinematic model

It is interesting to compare the best-fit fountain models (with and without coronal condensation) with the optimised kinematic model described in Chapter 2. Fig. 3.15 shows the $l-v$ diagrams at two representative latitudes for our best-fit kinematic

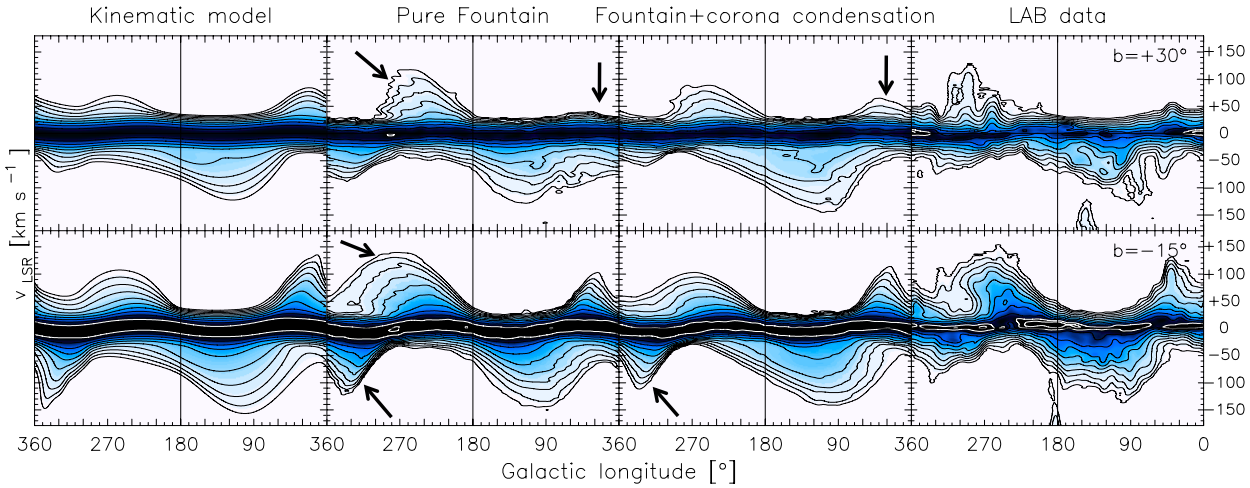

Figure 3.15: Comparison between the H I halo predicted by different models. $l-v$ slices at two representative latitudes (+30° on top, and −15° on bottom) for the best kinematic model derived in Chapter 2 (*first column*), the best pure Galactic fountain (*second column*), the best fountain with condensation of the corona (*third column*), and the LAB data (*last column*). The arrows show regions where the galactic fountain models reproduce the data better than the kinematic model. Contour levels in brightness temperature range from 0.04 K to 81.92 K scaling by a factor 2.

model (first column), the best-fit pure fountain model (second column), the best-fit fountain model with condensation of the corona (third column), and compare them with the $l-v$ diagrams of the LAB data (last column). The weighted-difference residuals (see Section 3.2.4) indicate that the pure fountain model provides a better description of the data with respect to the kinematic model. At latitude $b = -15°$ the superiority of the former is clear at $l > 270°$ (arrows). At latitude $b = +30°$, the superiority is clear at $l \sim 270°$ and $l \sim 30°$ (arrows). The kinematic model was built under the assumption that the scaleheight and kinematic parameters of the halo (rotation velocity gradient, vertical and radial velocities) are independent of radius. Although the assumption is restrictive, the model has been fitted to the data by freely varying these quantities, regardless of their dynamical plausibility. The fact that a dynamical model with only two free parameters fits the data better is remarkable, and strongly supports the idea that the H I halo of the Milky Way is produced by supernova feedback from the Galactic disc. There are only minor differences between the l–v diagram of our fountain model with corona condensation and those predicted by the best kinematic model, which indicates that we have kept the fundamental properties of the Milky Way's extraplanar gas. The main discrepancies between the two models arise in the regions closer to the Galactic Centre, at $l < 90°$ and $l > 270°$, where the dynamical model shows less prominent 'horn-like' structures (see Section 2.4.3), in better agreement with the data. This is due to the fact that, in the dynamical model, the thickness of the extraplanar layer decreases when approaching the Galactic Centre, as we have shown in Section 3.4.2.

3.6
Summary and concluding remarks

In this Chapter we have investigated the extent to which the Galaxy's H I datacube can be understood using a model of the extraplanar H I that emerged from observations of external galaxies such as NGC 891 and NGC 2403. In this model, clouds of relatively cool gas are ejected from the plane by supernova-driven superbubbles and subsequently orbit over the disc on near ballistic trajectories whilst weakly interacting with the virial-temperature coronal gas through which they move. The interaction with the coronal gas is through a combination of ram-pressure drag and accretion of gas that cools in the cloud's wake. As a result of this accretion, more gas returns to the plane than left it.

In light of recent developments, we modified the model slightly before applying it to the Galaxy. The principal modifications were (a) to allow for rotation of the corona, and (b) to change the rule for determining the SFR from one based on total gas density to one based on the density of molecular gas alone. Neither modification arises from a desire to fit data for the Galaxy better; (a) reflects an improved understanding of the hydrodynamics of cloud-corona interaction, and (b) arises from better data for external galaxies.

Our model has three adjustable parameters, the characteristic velocity of cloud ejection $h_{\rm v}$, the specific accretion rate of clouds α, and a dimensionless parameter $f_{\rm ion}$, which determines where along its trajectory the cloud's gas, which is initially photoionised, becomes visible as H I. To fit the data we require $h_{\rm v} \simeq 70\,{\rm km\,s^{-1}}$, regardless of the assumptions we make about the values of α and $f_{\rm ion}$.

At high Galactic latitudes, the observations show a clear bias towards negative velocities, and from this fact it follows that $f_{\rm ion}$ has to be larger than zero. If we set $\alpha = 0$, thus excluding accretion from the corona, we obtain a reasonable fit to the data with $f_{\rm ion} = 1$, so clouds become neutral only when they start to move back towards the plane.

Permitting α to be non-zero yields fits to the data that are improved in small but significant ways. In particular, with $\alpha > 0$, more emission is predicted at negative velocities at low latitudes and $l = 180°$. Also less emission is predicted at negative velocities and $|l| \simeq \pm 10°$ and $|b| \simeq 30°$. Both these changes arise from an increase in the extent of global inflow of the H I, and they improve the fit to the data. Moreover, with $\alpha \neq 0$ the optimum value of $f_{\rm ion}$ is reduced from unity to 0.3, so clouds become neutral about 30 percent of the way to their highest point above the plane. Our best-fitting model has $\alpha = 6.3\,{\rm Gyr^{-1}}$, which implies that $1.6\,{\rm M_\odot\,yr^{-1}}$ of hydrogen is accreted from the corona. Including the He content, this value rises to $2.3\,{\rm M_\odot\,yr^{-1}}$. This accretion rate is in excellent agreement with estimates of the accretion rate required to sustain the Galaxy's current rate of star formation without depleting its rather meagre stock of interstellar gas.

Unfortunately, two problems prevent us from tightly constraining the value of α.

The first is that it is inferred from some quite subtle features in the H I datacube. The second is that the optimum value of α depends on the value adopted for $v_{\rm lag}$, the equilibrium difference in the rotation velocities of the H I halo and the corona. When $v_{\rm lag}$ is raised to $100\,{\rm km\,s^{-1}}$, the optimum value of α decreases to $4.0\,{\rm Gyr^{-1}}$, which corresponds to an accretion rate of $1.0\,{\rm M_\odot\,yr^{-1}}$ ($1.4\,{\rm M_\odot\,yr^{-1}}$ including the He content).

Fig. 3.13 illustrates how successfully the model simulates H I emission at Intermediate Velocities – the simulation is probably as perfect as it can be without reproducing individual superbubbles. By contrast, the model does not reproduce emission at High Velocities, presumably because HVCs are extragalactic in origin.

We find remarkable agreement between the optimum values of the model's parameters and the values found in earlier work. In particular, our value of $h_{\rm v}$ lies within the ranges of values found for NGC 891 and NGC 2403, and although our value for α is higher than that found for NGC 891, this difference can be traced to different assumptions regarding the rotation of the corona here and in the work of FB08 on NGC 891. Our value of α does beautifully reproduce the results of a simulation by Marinacci et al. (2011) of the hydrodynamics of cloud-corona interaction. Our value $dv_\phi/dz \simeq -14.3\,{\rm km\,s^{-1}\,kpc^{-1}}$ for the vertical gradient of the halo's mean-streaming velocity agrees perfectly with the value ($\sim -15\,{\rm km\,s^{-1}\,kpc^{-1}}$) determined for NGC 891. These quantitative agreements between studies that use either radically different methodologies or data inspires confidence that our underlying physical picture is correct.

If we accept the fundamental soundness of the model, we can from it infer the three-dimensional structure of the H I halo, which is otherwise unknown. We find that the halo contains $\sim 3.0\times10^8\,{\rm M_\odot}$ of gas, of which $2.7\times10^8\,{\rm M_\odot}$ is neutral, in agreement with the value of $3.2^{+1.0}_{-0.9}\times10^8\,{\rm M_\odot}$ estimated in Chapter 2. Its vertical scaleheight increases roughly linearly with radius from $\sim 250\,{\rm pc}$ at $R = 3\,{\rm kpc}$ to $2\,{\rm kpc}$ at $R = 14\,{\rm kpc}$. At larger radii the scaleheight falls along with the local SFR. This H I halo is neither in hydrostatic equilibrium nor strictly in circular rotation: an analysis of the data that is nevertheless based on the assumption of hydrostatic equilibrium and circular motion will yield a misleading structure for the H I disc, especially the flare. This structure will in turn lead to false conclusions about the distribution of matter required to gravitationally confine the H I disc (see Sect. 3.4.2). The rate per unit area at which the halo deposits coronal gas on the disc increases roughly linearly from near zero at $R = 3\,{\rm kpc}$ to a peak at $R = 9\,{\rm kpc}$ and then falls roughly linearly to near zero at $R = 13\,{\rm kpc}$. Models of the chemical evolution of the disc need the accretion profile as an input, and it will be interesting to discover how the predictions of such models change when the present accretion profile is adopted.

Chapter 4

Extra-planar HI in simulated disc galaxies

4.1 Introduction

Numerical simulations constitute a fundamental tool to study the formation and the evolution of a large variety of astrophysical objects. They are widely used to investigate processes at very different scales, from stars and protoplanetary systems to cosmology. The last 20 years have seen the development of a plethora of numerical codes, which differ primarly in how they solve the equations for gravity and hydrodynamics. In this Chapter, we analyse hydrodynamical simulations of disc galaxies and compare them with H I observations. We consider simulations of two different classes: cosmological and non-cosmological.

Cosmological simulations, usually carried out in the context of the standard ΛCDM scenario, follow the evolution of a large box of the Universe *ab initio* down to a certain redshift. In the past, they have been extensively used to study the formation and the evolution of structures in the Universe using only dark matter; a well-known example is the Millennium Simulation (Springel et al. 2005). However, recent improvements in computational power allowed to increase dramatically the mass resolution and to follow self-consistently the evolution of both dark matter and baryons. These cosmological hydrodynamical simulations revealed that the classical picture of galaxy formation via cooling and condensation of shock-heated plasma at the virial temperature (White and Rees 1978) is valid at low redshift ($z < 1-2$) and for massive halos ($M_{\rm halo} \gtrsim 10^{11.4}\,{\rm M}_\odot$), while galaxies at high redshift build up their gas content via streams of 'cold' gas that penetrate the dark matter halos without passing through a hot phase (Kereš et al. 2005; Dekel and Birnboim 2006; Kereš et al. 2009b; Crain et al. 2009). Feedback mechanisms from stars and AGNs also seem to be crucial in regulating the details of galaxy evolution and are considered the key to reproduce the observed properties of galaxies in the local Universe (e.g. Kereš et al. 2009a; Schaye et al. 2010).

In contrast to the above, non-cosmological simulations follow the evolution of a

single object (a galaxy or a cluster of galaxies) in a closed-box framework, assuming an initial distribution of gas, stars and dark matter. These simulations are very useful to investigate the physics at galactic scales. They have been widely used in the last decade to interpret the secular evolution of discs (Debattista et al. 2006; Combes 2008), to study the role of stellar feedback (Dalla Vecchia and Schaye 2008, 2012), and to understand the effect of major and minor mergers on the morphology and the dynamics of galaxies (Villalobos and Helmi 2009; Bois et al. 2011).

In this Chapter, we present the analysis of two simulated disc galaxies as resulting from two different runs: a galaxy similar to the Milky Way evolved in isolation (non-cosmological), and a large and massive disc galaxy selected from a cosmological run evolved down to redshift $z = 0$. Both simulations have been performed by the group of Joop Schaye (Leiden University) with the N-body + smoothed-particle hydrodynamics (SPH) code GADGET (Springel et al. 2001; Springel 2005), modified to implement two distinct treatments of the stellar feedback (Dalla Vecchia and Schaye 2008, 2012). Specifically, the cosmological run has been extracted from the GIMIC simulations presented by Crain et al. (2009). From both simulations we derive morphology, mass distribution and kinematics of the various mass components, focussing in particular on the cold neutral gas. We discuss the properties of the extraplanar H I of the simulated galaxies and the role of stellar feedback in shaping their gas layer. Finally, we compare the properties of these objects with those of two similar galaxies: the Milky Way itself for the isolated run, and the large spiral UGC 5253 for the cosmological run. Throughout this Chapter, we use the term *thick disc* to indicate the layer of gas located at a few kpc from the midplane and produced by supernova feedback. With the term *halo* we refer instead to material at larger distances.

The Chapter is organised as follows. In Section 4.2 we describe the approach used to analyse the outputs of the simulations. In Section 4.3 and 4.4 we present the results for the isolated and the cosmological simulation respectively, as well as the comparison with the observations. In Section 4.5 we discuss our results. Our conclusions are presented in Section 4.6.

4.2 Method

The output of a N-body+SPH simulation is a collection of gas, star and dark-matter particles at a given epoch. We refer to this collection with the term *snapshot*. The standard approach that we adopt to analyze these snapshots is to use all the available information on the particles (i.e., mass, density, position and velocity) to determine properties like the mass distribution, the rotation curve at different heights from the midplane and the inflow/outflow of the gas surrounding the disc. Then, these properties are compared with those derived from real data.

In addition, we use here the same approach employed in the previous Chapters, that consists in reducing all the information on the neutral gas in the snapshot into a modelcube of H I emission that can be compared with datacubes of real galaxies. This method provides a direct comparison between simulations and observations, but it necessarily implies a loss of information because of the passage from a 6D phase-space (vector positions and velocities) to a 3D observable-space (angles and line-of-sight velocities). On the other hand, it allows to take into account all the observational uncertainties, such as resolution and projection effects. We adopted this method to compare the H I properties of the simulated galaxies with those of real galaxies in Sections 4.3.3 and 4.4.2.

4.2.1 The snapshots

Two different versions of each simulated galaxy are available, depending on how the stellar feedback is implemented. Details on stellar feedback are given in Section 4.2.2. Altogether, we analysed four different snapshots:

- *mwK*: simulation of an isolated Milky-Way-like galaxy, starting from ad-hoc dark-matter, stellar and gaseous distributions. The galaxy evolves for 250 Myr. Photoionisation from UV background and collisional ionisation are included in post-processing. The stellar feedback is kinetic (see Section 4.2.2).
- *mwT*: as *mwK*, but the stellar feedback is thermal (see Section 4.2.2).
- *cosmoK*: box containing a galaxy extracted from a cosmological simulation evolved down to $z = 0$. Photoionisation from UV background and collisional ionisation are included in post-processing. The stellar feedback is kinetic.
- *cosmoT*: as *cosmoK*, but the stellar feedback is thermal.

The main properties of these snapshot are reported in Table 4.1. Note that in the isolated galaxy the mass resolution is considerably higher because of the smaller box and the shorter evolution time. Unfortunately, information on dark matter particles were available only for *cosmoK*.

4.2.2 Stellar feedback recipes

In the simulations analyzed, the star formation recipe adopted is pressure dependent and it is tuned to reproduce the observed Kennicutt-Schmidt law, as discussed in Dalla Vecchia and Schaye (2008). Stellar feedback from SNe is implemented following two different recipes:

- *kinetic feedback*: in this approach, 40% of the energy released by a SN explosion (assumed to be $1.8 \times 10^{48}\,\mathrm{erg\,M_\odot^{-1}}$) is transferred to the surrounding

Table 4.1: Main properties of the snapshots analysed. The vertical line divides isolated (on the left) and cosmological (on the right) simulations. Masses and lengths are in physical units instead of the usual co-moving units. Information on dark matter particles are available only for the *cosmoK* simulation.

Simulation	*mwK*	*mwT*	*cosmoK*	*cosmoT*	
Time	0.25	0.25	13.6	13.6	Gyr
Box size	0.30	0.30	3.01	3.01	Mpc
Feedback	kinetic	thermal	kinetic	thermal	
$\Gamma_{\rm UVB}$ [a]	8.34×10^{-14}	8.34×10^{-14}	8.34×10^{-14}	8.34×10^{-14}	$\rm s^{-1}$
$\overline{\sigma}_{\nu\,\rm HI}$ [b]	3.27×10^{-18}	3.27×10^{-18}	3.27×10^{-18}	3.27×10^{-18}	$\rm cm^2$
n. gas particles	203580	204993	2056764	1790459	
Total gas mass	1.4×10^{10}	1.4×10^{10}	5.0×10^{11}	4.3×10^{11}	$\rm M_\odot$
Total $\rm H_2$ mass[c]	4.1×10^{9}	3.7×10^{9}	2.2×10^{8}	1.8×10^{7}	$\rm M_\odot$
Total H I mass	4.2×10^{9}	4.7×10^{9}	1.8×10^{10}	1.1×10^{10}	$\rm M_\odot$
Total H II mass	2.5×10^{9}	2.3×10^{9}	3.6×10^{11}	3.1×10^{11}	$\rm M_\odot$
$\langle m_{\rm gas} \rangle$ [d]	7.0×10^{4}	7.0×10^{4}	2.4×10^{5}	2.4×10^{5}	$\rm M_\odot$
$\langle \lambda_{\rm gas} \rangle$ [e]	0.5	0.5	1.7	1.7	kpc
n. star particles	31714	30301	166898	56867	
Total stellar mass	2.2×10^{9}	2.1×10^{9}	3.4×10^{10}	1.1×10^{10}	$\rm M_\odot$
n. DM particles	n.a.	n.a.	2232996	n.a.	
Total DM mass	n.a.	n.a.	2.46×10^{12}	n.a.	$\rm M_\odot$

[a] hydrogen photoionisation rate in the UV background model adopted

[b] H I cross section for ionising photons in the UV background model adopted

[c] evaluated by deriving the $\rm H_2$ fraction from eq. (4.1)

[d] median mass of gas particles

[e] median smoothing length of gas particles

gas particles as kinetic energy. Each particle has a chance to be scattered in a random direction with an average kick velocity of $\sim 600\,\rm km\,s^{-1}$. Since the scattered particles are usually located inside the thin disc, hydrodynamical interactions can decelerate them very efficiently, thus the net speed of the outflowing material is about $50-100\,\rm km\,s^{-1}$. All the details on kinetic feedback are presented and discussed in Dalla Vecchia and Schaye (2008).

- *thermal feedback*: in this case, the energy is transferred to the surrounding gas particles as thermal energy. Each particle has a chance to increase its temperature by $\sim 10^{7.5}\,\rm K$. Such large value is required in order to avoid strong radiative losses that would make the feedback inefficient. With this recipe radiative cooling does not need to artificially switched off after the energy injection to avoid overcooling effects, as done is similar treatments (e.g. Stinson et al. 2006). The details on thermal feedback are presented and

discussed in Dalla Vecchia and Schaye (2012).

As we show in Sections 4.3 and 4.4, the two feedback recipes give similar results in the case of the isolated simulation, but they affect very significantly the morphology and the mass distribution of the galaxy simulated in the ΛCDM framework.

4.2.3 Gas fractions

For each particle i of the snapshot the position $\mathbf{x_i}$, the velocity $\mathbf{v_i}$ and the mass m_i are known. Gas and star particles have also their own *smoothing length* λ_i that defines the region of influence of a particle over its neighborhoods in the SPH calculations. The smoothing length decreases in the regions where particles crowd, making these areas better resolved in the simulation. For gas particles additional information are available, including temperature T_i, density ρ_i and H I fraction $f_{\mathrm{HI},i}$. We use $X = 0.75$ as the universal hydrogen abundance, hence the hydrogen mass of a generic i-th particle is $m_i X$ while the remaining mass $m_i(1 - X)$ is considered a mixture of Helium and metals. The hydrogen mass must be split into ionised (H II), neutral (H I) and molecular (H_2) fraction.

The H I fraction $f_{\mathrm{HI},i}$ is evaluated according to ionisation balance calculations, which take into account recombination, collisional ionisation and photo-ionisation processes. In particular, radiative transfer calculations are performed via the code TRAPHIC (Pawlik and Schaye 2008), which simulates photon packets as 'virtual' particles that travel at the speed of light and can be absorbed or emitted by ordinary gas particles. The extragalactic UV background is simulated as additional photon packets coming from the boundaries of the simulated box, and is set accordingly to the model of Haardt and Madau (2001). The main parameters of the UV background model used in the simulations are listed in Table 4.1. Further details on the radiative transfer calculations can be found in Rahmati et al. (2012).

Unlike the H I, the formation and the evolution of molecular hydrogen is not followed in the simulations. However, assuming that the molecular-to-atomic hydrogen ratio is determined by hydrostatic pressure alone (Blitz and Rosolowsky 2006), the H_2 fraction for the i-th gas particle can be estimated *a posteriori* following the recipe of Altay et al. (2011):

$$f_{\mathrm{H2},i} = \left[1 + 24.535 \left(10 \times (1+z)^3 h^2 \frac{\rho_i}{m_h}\right)^{-1.2267}\right]^{-1} \tag{4.1}$$

where z is the redshift of the snapshot, h is the Hubble parameter and m_h is the proton mass. Eq. 4.1 is used for gas particles that are considered to be star-forming at redshift z; f_{H2} is set to zero for particles that are not forming stars. The isolated galaxy is assumed to be at $z = 0$. Once removed the molecular fraction, we use the parameter $f_{\mathrm{HI},i}$ to split the remaining hydrogen mass into neutral ($f_{\mathrm{HI},i}$) and ionised ($1 - f_{\mathrm{HI},i}$).

4.2.4 From the snapshots to the modelcubes

In a N-body+SPH simulation, the classical way to evaluate any scalar quantity f in a given spatial position $\mathbf{x}$ is

$$f(\mathbf{x}) = \sum_{i=1}^{N} f_i \frac{m_i}{\rho_i} W(\mathbf{x_i} - \mathbf{x}, \lambda_i) \tag{4.2}$$

where N is the number of particles and W is a weight function that depends on the distance between $\mathbf{x}$ and the i-th particle and on the smoothing length of this latter. Note that W has the dimensions of a length^{-3}. If we use eq. (4.2) to derive the density field we simply obtain

$$\rho(\mathbf{x}) = \sum_{i=1}^{N} m_i W(\mathbf{x_i} - \mathbf{x}, \lambda_i), \tag{4.3}$$

which shows that $\rho(\mathbf{x})$ is obtained by spreading the mass of each particle over a volume that depends on the weight function. We assume that W is a 3D Gaussian function with FWHM equal to λ_i, thus each particle is approximated by a spherical blob of size $\sim \lambda_i$. Hence, we are assuming implicitly that the spatial resolution of the simulation is given by the smoothing length, and thus increases from the innermost region of the galaxy to the outside.

We consider a cube of coordinates (x, y, z), where z is the direction along the line of sight and the xy plane is the plane of the sky. On that plane, a surface density map $\Sigma(x, y)$ will be given by integrating eq. (4.3) in the z-direction. In the particular case of a gaussian weight function, we have

$$\Sigma(x, y) = \sum_{i=1}^{N} m_i g(x_i - x, \lambda_i) g(y_i - y, \lambda_i) \tag{4.4}$$

where $g(a, b)$ is a gaussian function centered in a with FWHM equal to b. We make extensive use of these maps in Section 4.4 to show the morphology of the various components (H I, H II, stars and dark matter) in the cosmological simulations *cosmoK* and *cosmoT*.

Assuming an optically thin regime for the neutral hydrogen, a modelcube is obtained by spreading the H I 21-cm line "emission" produced by each particles in the (x, y, v_z) space. We assume that each particle i is a cloud with internal velocity dispersion $\sigma_{v,i}$ given only by its thermal energy, neglecting any internal turbulence. In the optically thin regime, an H I brightness temperature (T_B) of 1 K corresponds to an H I column density $N_\mathrm{HI} = 1.82 \times 10^{18}\,\mathrm{cm}^{-2}$ integrated over a velocity range of $1\,\mathrm{km\,s}^{-1}$. Thus the H I brightness temperature in the (x, y, v_z) space will be given by

$$T_\mathrm{B}(x, y, v_z)[\mathrm{K}] = \frac{1}{1.82 \times 10^{18}} \sum_{i=1}^{N} \frac{m_{\mathrm{HI},i}}{m_\mathrm{p}}\, g(x_i - x, \lambda_i) g(y_i - y, \lambda_i) g(v_{z,i} - v_z, 2.35\sigma_{v,i}) \tag{4.5}$$

$m_{\mathrm{HI},i}$ is the H I mass of the i-th particle, m_{p} is the mass of the proton and $\sigma_{v,i} = \sqrt{k_B T_i / m_{\mathrm{p}}}$. These modelcubes are used in Sections 4.3.3 and 4.4.2 to compare the simulated H I emission in the snapshots with H I observations of real galaxies.

4.2.5 Tilted ring fit

In observed disc galaxies, the gas kinematics is usually inferred by fitting a so-called *tilted ring model* to the velocity field. In this approach, the galaxy is considered axisymmetric and its velocity field is assumed to be decomposable in a series of rings, each with a given centre, inclination, position-angle and rotation velocity. Determining the correct orientation of each ring with respect to the line of sight is very important to infer the rotation curve of the galaxy. In simulated galaxies, instead, the fit can be done directly on the 3D distribution of gas particles, and the kinematics and the rotation curve can be inferred using the vector velocity of the particles. In the following we describe the approach we use to fit a tilted ring model to the simulated galaxies.

First, we define the exact centre $\mathbf{x_c}$ and the systemic velocity $\mathbf{v_c}$ of the galaxy as follows. A first approximation for these quantities is given by the barycenter and the mass-weighted velocity of the stellar component evaluated using the whole snapshot. Then we re-derive these quantities iteratively, using boxes of progressively decreasing size centered around the previous value of $\mathbf{x_c}$, until we converged to the true centre. We prefer to use the stellar component because it is considerably more regular than the gaseous and the dark matter component (see Fig. 4.9).

After the spatial and the kinematic centres are fixed, the following method is adopted to re-project the galaxy to an arbitrary inclination angle. First, we search for a rotation of the coordinate system around the x and y axis that produces a face-on projection of the galaxy. Then, a further rotation ω_x around the x axis gives the desired inclined view. The face-on view is obtained by analysing the line-of-sight velocity distribution of the stellar component: the more the inclination approaches face-on, the more the distribution will crowd around $0\,\mathrm{km\,s^{-1}}$. In principle one could also look at the projected size of the total stellar map, but if the galaxy is bulge-dominated (like *cosmoK*) this approach gives less satisfactory results.

In the presence of a warp, the H I gas will not lie on one plane. In order to derive a map for the 'midplane' (i.e., the average displacement of the H I from the plane $z = 0$) and for the thickness of the H I distribution, we project the galaxy face-on and use eq. (4.3) to build a 3D map for the H I density distribution. Then we fit all the z-profiles of this modelcube - that are perpendicular to the galactic plane - with a series of Gaussian functions. Thus, for each position (x, y) in the plane of the sky, the mean of this fit represents the midplane, while the dispersion of the fit is the (gaussian) local scale-height of the H I. Finally, we fit the tilted ring model to the midplane map. We consider a series of rings with different radii; each ring is fitted to the midplane map using the inclination axis, the inclination angle and

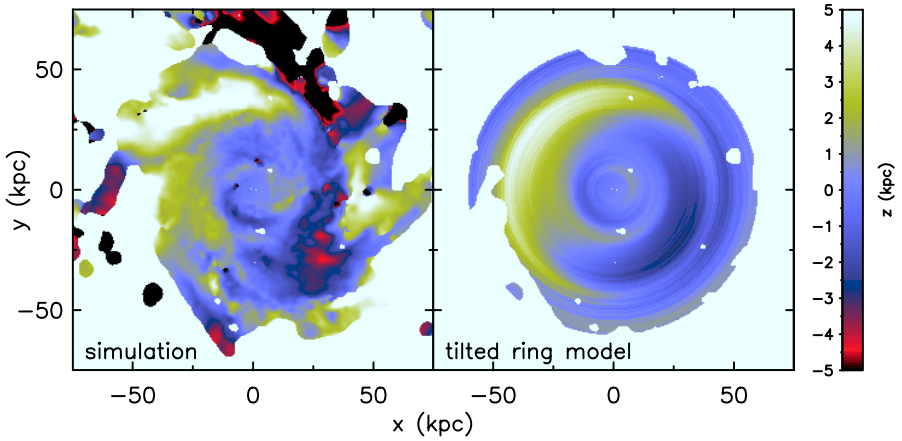

Figure 4.1: *Left panel:* map of the displacement of the midplane from $z = 0$ for the simulated galaxy *cosmoK*; *right panel:* synthetic map as resulting from our tilted ring fit.

the height of the ring centre with respect to the rotation axis as free parameters. Fig. 4.1 shows the results of this procedure for the simulated galaxy *cosmoK*: the left panel shows the midplane map derived with the Gaussian fit to the H I density distribution, while the right panel shows the axi-symmetric midplane model derived with our tilted ring fit.

We use our tilted ring model to evaluate the kinematical and the physical properties of the simulated galaxies as a function of R. Our results are discussed in the following sections.

4.3 Results for the isolated runs

Here, we present the results for the Milky-Way-like galaxy evolved for 250 Myr in a closed-box framework. At the beginning of the simulation, all the gas is already stratified in a thin disc which is embedded in a dark matter halo. A hot atmosphere (galactic corona) is not present. The initial conditions are set to produce a gaseous mass and kinematics similar to those of our Galaxy. During the evolution, stars form and stellar feedback injects energy in the surrounding environment.

4.3.1 Morphology

Fig. 4.2 and 4.3 show the total maps of the H I (top panels) and the H II gas (bottom panels) for the simulations *mwK* and *mwT* respectively. The different panels show the galaxy seen from different inclination angles (45°, 0° and 90° from left to right). The panels on the left show the whole simulated box, while the others focus on the gaseous disc. The outermost contour in the H I maps is at column density of $10^{19}\,\mathrm{cm}^{-2}$, which approximately corresponds to the current detection limit of deep

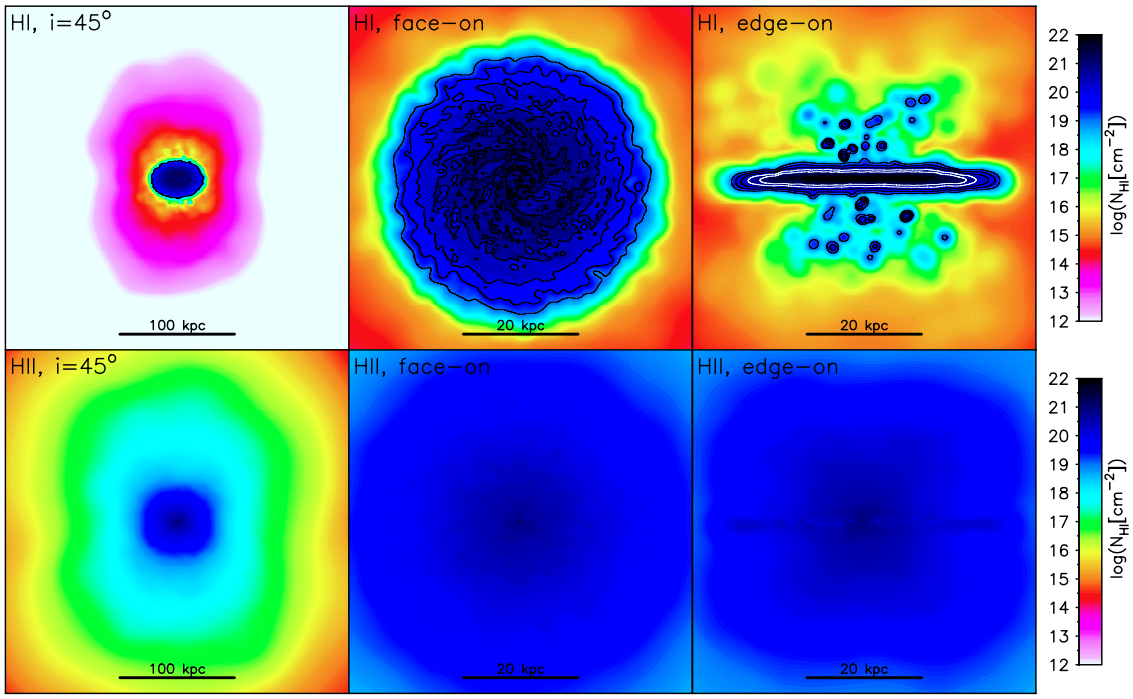

Figure 4.2: Gas surface density maps for the isolated simulation with kinetic feedback. H I is shown in the *top row*, H II in the *bottom row*. Different panels show different area coverages and inclination angles, as indicated on top of each panel. The first contour in the H I map is at $10^{19}\,\mathrm{cm}^{-2}$. The face-on and the edge-on maps show additional contours at $10^{19.5}$, 10^{20}, $10^{20.5}$ and $10^{21}\,\mathrm{cm}^{-2}$.

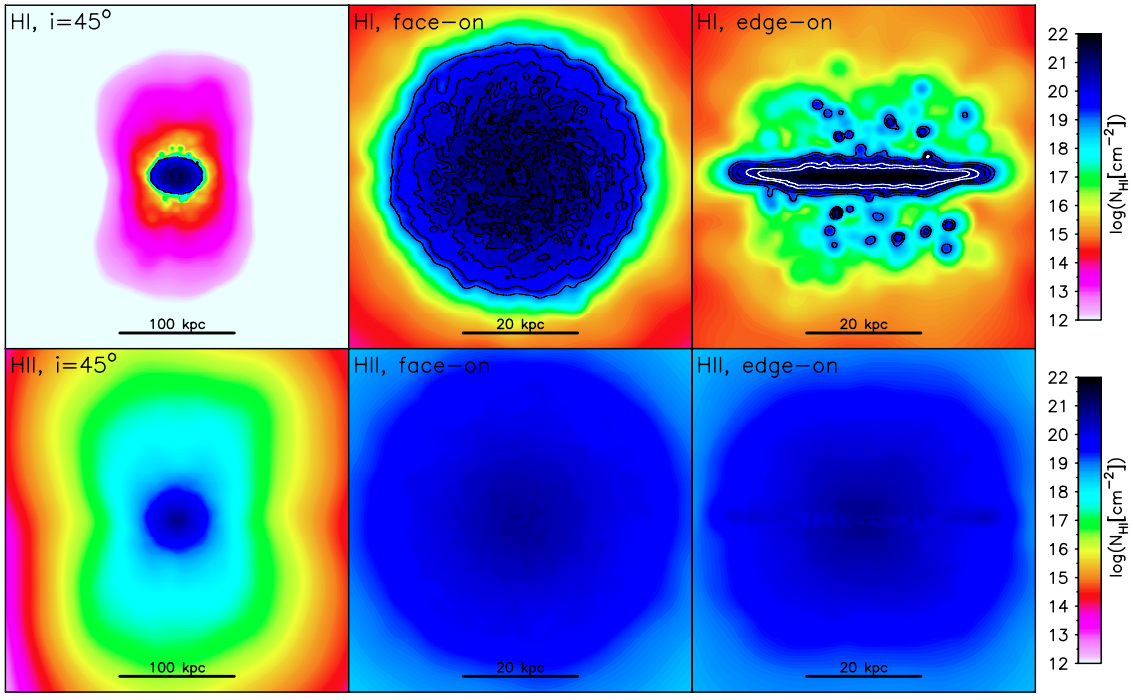

Figure 4.3: As in figure 4.2, but for the isolated simulation with thermal feedback.

H I observations (e.g. Oosterloo et al. 2007). The face-on maps show that the H I

disc is extended $\sim 25\,\mathrm{kpc}$ in radius, consistently with that of our Galaxy. The H I scale-height is $\sim 0.4\,\mathrm{kpc}$. Spiral arms are clearly visible in the inner 10 kpc but, for larger radii, the disc is rather smooth and not-warped. This is due to two reasons: a) the galaxy did not experience any merger events during its evolution; b) the dark matter distribution is spherical and dominates the dynamics of the system (see Section 4.3.2). An asymmetric warp is instead present in the H I disc of our Galaxy (e.g. Levine et al. 2006). The stellar disc is not shown in Fig. 4.2 and 4.3 because, due to the short evolution, it is only partially formed and the total stellar mass is very small (see table 4.1). A stellar bulge or bar is not present.

The edge-on maps in Fig. 4.2 and 4.3 show that a consistent amount of gas, mostly ionised, is located outside the disc of the simulated galaxy. Since the initial conditions do not account for the presence of a corona, the stellar feedback is responsible for the whole extra planar emission of neutral and ionised gas. The H II gas that surrounds the disc and fills the whole simulated box is built up completely by particles ejected from the disc via SN feedback. Thermal instability produces the fragmentation and the cooling of this medium, that partially falls back to the disc in the form of small H I clumps, especially visible in the edge-on projection at column densities larger than $10^{19}\,\mathrm{cm}^{-2}$. These cold clumps are located up to $10-15\,\mathrm{kpc}$ above the disc and have a typical H I mass of $10^5\,\mathrm{M}_\odot$. This mass is similar to that of the Intermediate-Velocity Clouds (IVCs) of the Milky Way, which however are confined to a few kpc from the Sun (van Woerden et al. 2004). The location of these clumps is instead more similar to that of the High-Velocity Clouds (HVCs) of the Milky Way that, as we saw in the previous Chapters, are likely to have an external origin. In the simulation with kinetic feedback, the total H I mass above 3 scale-heights from the disc is $8\times10^7\,\mathrm{M}_\odot$. About 3/4 of this medium ($6\times10^7\,\mathrm{M}_\odot$) is located in a smooth thick disc extended up to $\sim 5\,\mathrm{kpc}$ above the midplane, the remaining fraction ($2\times10^7\,\mathrm{M}_\odot$) is made of cold clumps floating at larger distances. In *mwT*, the H I above the disc is $1.6\times10^8\,\mathrm{M}_\odot$, and only $\sim 10\%$ of this layer is made of clumps. Thus thermal feedback produces a thicker and much smoother disc of neutral gas. This is also apparent from the thickness of the H I disc shown in the edge-on maps of Figs. 4.2 and 4.3. As we have shown in Chapters 2 and 3, the Milky Way has an extended H I thick-disc produced by stellar feedback with a mass of $\sim 3\times10^8\,\mathrm{M}_\odot$, which is likely to be made up of IVC-like clouds confined within a few kpc from the disc.

From a morphological point of view, only minor differences are visible between the kinetic and the thermal run. In Section 4.4 we show that the two feedback mechanisms produce very different results in the cosmological runs. This suggests that the two recipes shape the galaxy similarly only on short timescales.

4.3.2 Mass distribution and kinematics

The mass distribution and the H I kinematics are derived for both *mwK* and *mwT* using the technique described in Section 4.2.5. The radial separation between the various rings is 0.5 kpc. For each ring, we evaluated the surface densities of the different components (H I, H II, H_2 and stars) and the rotation curve. This latter is derived by considered only particles within 1 kpc from the plane.

The top panels of Fig. 4.4 show the surface density profiles for the various components of *mwK* (left panel) and *mwT* (middle panel), and compare them with those of Milky Way (right panel). The H I and the H_2 surface densities of our Galaxy have been taken from Binney and Merrifield (1998), while the stellar and the dark matter distributions are from the Galactic mass model of Sofue et al. (2009). In the simulated galaxies, the baryonic surface density for $R<7$ kpc is dominated by H_2, while the stellar component, which closely follows the molecular gas, is less important. Both these facts are due to the short evolution time of the runs: in the inner region, there is still a large amount of molecular gas available for future star formation. In the mass model considered, the total stellar mass of our Galaxy is $8.3 \times 10^{10}\,M_\odot$, which is almost 40 times larger than that of the simulated galaxy. On the other hand, the H I distribution resembles cloasely that of the Milky Way.

The bottom panels of Fig. 4.4 compare the H I rotation curve of the simulated galaxies with that of the Milky Way. This latter has been taken from Sofue et al. (2009). The contribute of the different components to the total rotation curve is also shown; the gas component of the Milky Way is not considered in Sofue et al. (2009). Since information on dark matter particles are not available for the isolated simulations, the contribution of this component to the kinematics of *mwK* and *mwT* has been set to match the total rotation curve. Note that in Sofue et al. (2009) the fiducial value of the circular velocity at the solar radius is $v_\odot = 200\,\mathrm{km\,s^{-1}}$ and not $220\,\mathrm{km\,s^{-1}}$ as we assume throughout this Thesis. A conversion to a different $v_\odot$ is possible but not straightforward because it affects the mass distribution and we preferred to leave it to its original value. Only minor differences are visible between the kinematics of the two simulated galaxies. The rotation curves of both *mwK* and *mwT* are flat at the value of $\sim 220\,\mathrm{km\,s^{-1}}$. The main difference is that in our Galaxy, at least accordingly to the mass model considered, the kinematics is everywhere dominated by the baryonic matter, while gas and stars in *mwK* and *mwT* account only for a negligible fraction of the total circular velocity. The rotation curve of these simulated objects are totally dominated by dark matter.

Figure 4.5 shows the rotation curve for the simulated galaxies at different heights from the plane, derived by increasing the height of each ring from its original position. Remarkably, in both *mwK* and *mwT* the gas above the disc is clearly rotating slower and slower as the height from the midplane increases. This kinematics is produced spontaneously when gaseous thick disc is built up by particles ejected from the thin disc (see also our dynamical model in Chapter 3). The magnitude of this lag at

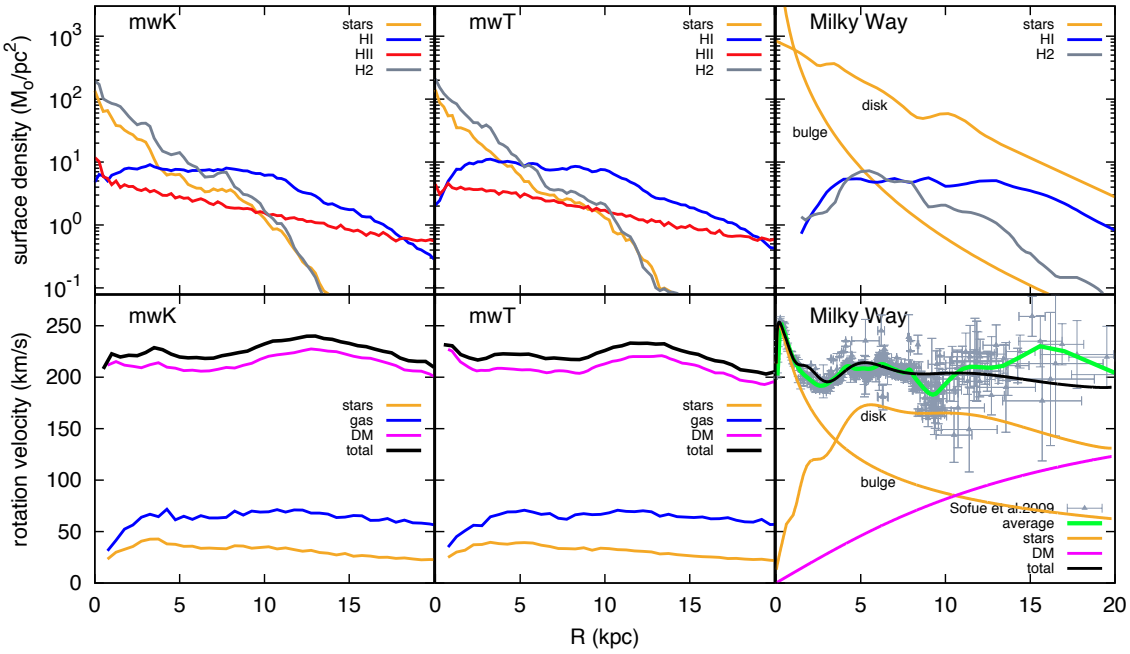

Figure 4.4: *Top panels:* surface density profiles of the various components for the simulated galaxies *mwK* (*left*) and *mwT* (*middle*), compared with that of the Milky Way (*right*). *Bottom panels*: H I rotation curve and contribution of the various component to the circular velocity for the same galaxies. The H I and the H_2 surface densities of the Milky Way are taken from Binney and Merrifield (1998), while the surface densities of the other components and the kinematics are from Sofue et al. (2009). The green line shows the average rotation curve of the Milky Way, obtained by approximating the data of Sofue et al. (2009) with a Bezier curve.

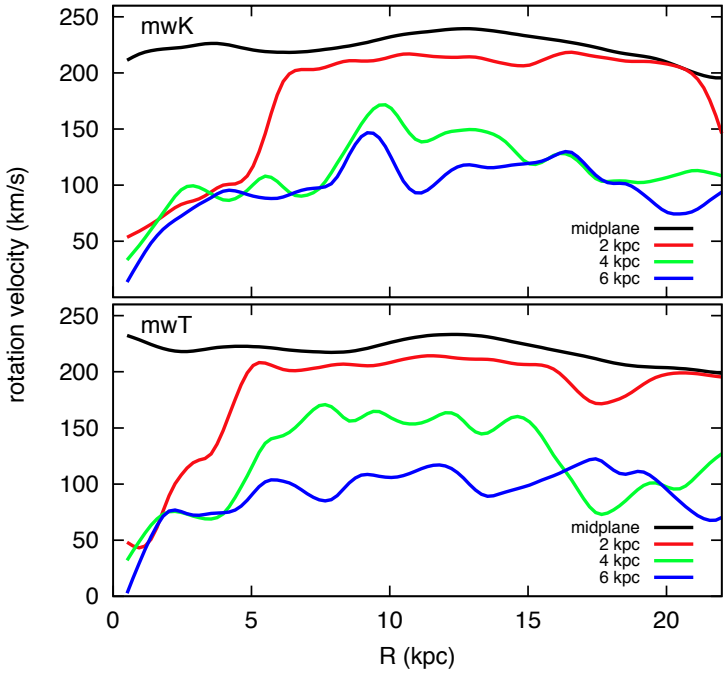

Figure 4.5: Rotation curves at different height from the midplane for the simulated galaxies *mwK* (*top panel*) and *mwT* (*bottom panel*). Rings with less than 10 particles have been excluded.

$R = 10\,\mathrm{kpc}$ is $\frac{dv_\phi}{dz} \simeq 18\,\mathrm{km\,s^{-1}\ kpc^{-1}}$ but it increases for $R < 5\,\mathrm{kpc}$, consistently with that observed for the extraplanar H I of the Milky Way (Chapter 2) and of external galaxies (Oosterloo et al. 2007).

4.3.3 Comparison with the LAB data

In the previous Chapters, we had made extensively use of the LAB Survey 21-cm data (Kalberla et al. 2005) to compare our models with the H I emission in the Milky Way. Here, we adopt the same approach. We use a modified version of eq. (4.5) to build modelcubes for the H I component in the simulations *mwK* and *mwT*, we project them for an inside view and compare them with the LAB data. As in the previous Chapters, we adopt the Galactic coordinate system (l,b) ($l = 0°$ points at the Galactic centre).

The inner projection of the simulations is obtained by placing the observer in the disc at a given space position $\mathbf{x_0}$, where $|\mathbf{x}_0| = 8.5\,\mathrm{kpc}$ is the distance between the observer and the galactic centre. A pseudo-local standard of rest (pLSR) has been defined by averaging the kinematics of all the star particles within 1 kpc from this position, obtaining the local velocity vector $\mathbf{v_0}$. This large volume is needed to determine a robust measure for the average motion. For the generic i-th gas particle, the line-of-sight velocity with respect to this pLSR is given by

$$\widetilde{v}_i = \frac{(\mathbf{x_i} - \mathbf{x_0}) \cdot (\mathbf{v_i} - \mathbf{v_0})}{|\mathbf{x_i} - \mathbf{x_0}|}\,. \tag{4.6}$$

If b_i is latitude of the particle, the angular resolution in the b direction will be $\sigma_{b,i} = \lambda_i/d_i$, while that in the l direction will be $\sigma_{l,i} = \sigma_{b,i}/\cos(b_i)$. Finally, the H I brightness temperature for an optically thin regime can be derived similarly to eq. (4.5) as

$$T_\mathrm{B}(l,b,\widetilde{v})[\mathrm{K}] = \frac{1}{1.82\times10^{18}} \sum_{i=1}^{N} \frac{m_{\mathrm{HI},i}}{m_\mathrm{p}} g(l_i - l, \sigma_{l,i})\, g(b_i - b, \sigma_{b,i})\, g(\widetilde{v}_i - \widetilde{v}, 2.35\sigma_{v,i}). \tag{4.7}$$

Fig. 4.6 compares seven different longitude-velocity (l–v) diagrams obtained for the simulated galaxies *mwK* (left panels) and *mwT* (middle panels) with those of the LAB data smoothed to 8° of resolution (right panels). The H I emission extracted from the simulated galaxies reproduce the Milky Way data qualitatively well, especially when kinetic feedback is used. The emission in the simulated cubes is more spread in the velocity direction with respect to the data, and this effect is very prominent in the thermal run. It is interesting to investigate the origin of this spread further. Fig. 4.7 shows the H I velocity dispersion profile for both *mwK* and *mwT*, evaluated using our tilted ring model by considering the motion of the particles inside 1 kpc from the midplane. We compare this with the H I velocity dispersion derived in the inner disc of the Galaxy (see Appendix A), we point out that this latter is consistent with that of a typical nearby disc galaxy (e.g. Boomsma

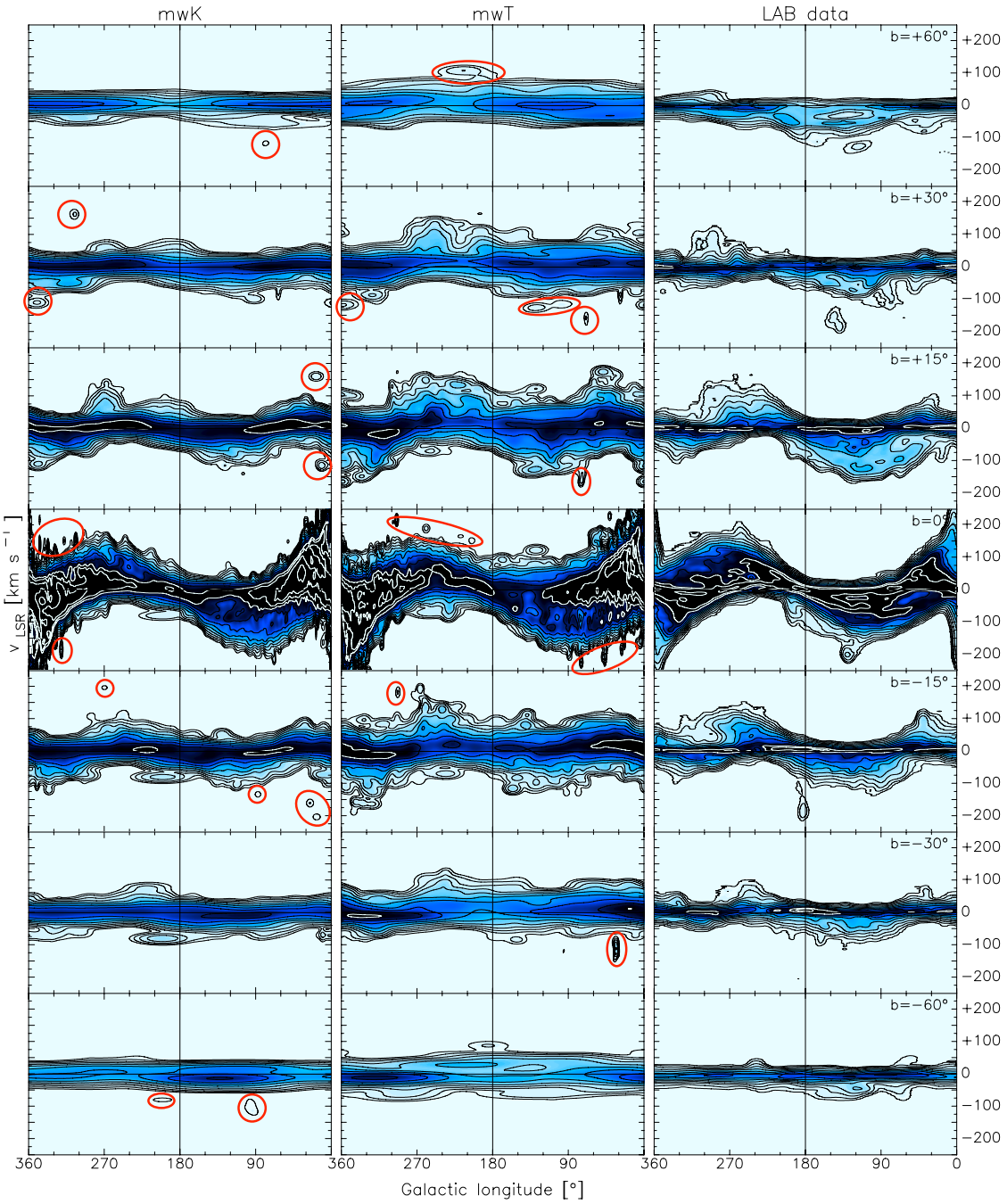

Figure 4.6: Longitude-velocity diagrams of H I at 7 different latitude - as indicated at the top right corner of the rightmost plot - for the simulated galaxies *mwK* (*left column*) and *mwT* (*middle column*), and for the LAB data (*right column*). These latter have been smoothed to 8° of resolution. Contour levels in brightness temperature range from 0.04 to 81.92 K scaling by a factor 2. Red circles show the locations of H I emission at very anomalous velocities in the simulations.

et al. 2008). Clearly, simulations overestimate the amount of turbulence in the disc by a factor $2-3$. Since the galaxy is isolated, it would be tempting to conclude that such a large velocity dispersion is exclusively due to stellar feedback, but actually mass resolution may play an important role. Nevertheless, it seems unlikely that the discrepancies between the two simulated cubes are solely due to a difference of $5-10\,\mathrm{km\,s^{-1}}$ in the H I velocity dispersion, and it is possible that the larger mass and size of the thick H I disc in the thermal run, when combined with the poor resolution (i.e., larger smoothing lengths), can produce some spurious effects in the modelcube.

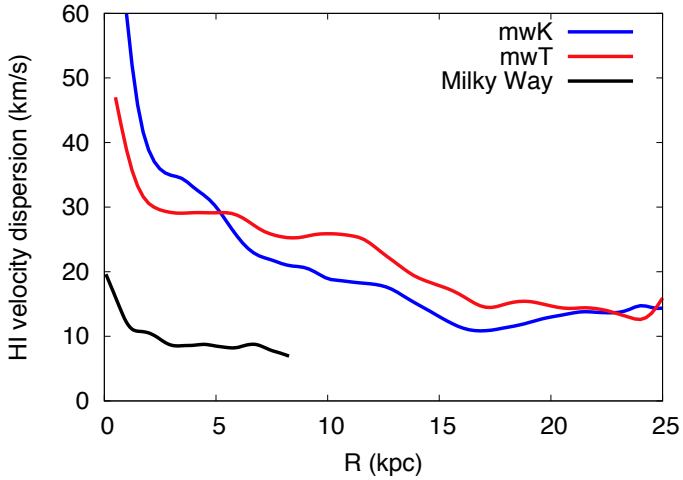

Figure 4.7: Velocity dispersion of H I as a function of radius for both the simulated galaxies and the Milky Way.

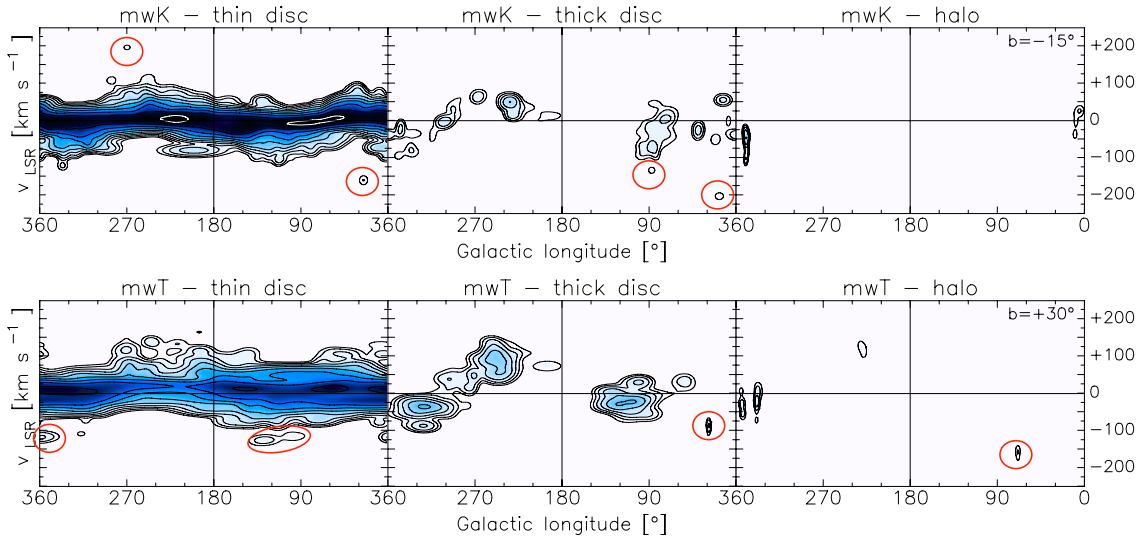

Figure 4.8: Longitude-velocity diagrams at $b=+15°$ (*top*) and $b=-15°$(*bottom*) for *mwK* and *mwT*, and those derived for the same galaxies by neglecting all the particles inside 4 scale-heights from the midplane.

Several discrete 'blobs' of H I emission are visible in the $l-v$ diagrams of Fig. 4.6 at anomalous velocities. Some of these blobs appear to 'swell' from the gas at lower

velocity, while others are completely detached from the disc kinematics and are qualitatively similar to the HVCs of the Milky Way. The location of this anomalous gas is marked with red circles in Fig. 4.6. Most of these features are located at $l<90^\circ$ and $l>270^\circ$, which suggests that their origin maybe related to star formation activities in the inner galaxy. To infer the spatial location of these features, for each simulated galaxy we built three modelcubes which account for the thin disc, the thick disc and the halo H I emission respectively. In the thin disc modelcube we consider only particles within 3 scaleheights from the midplane (i.e. $z \lesssim 1.2\,\mathrm{kpc}$), in the thick disc modelcube we consider particles between 3 and 10 scaleheights (i.e. $1.2 \lesssim z \lesssim 4.0\,\mathrm{kpc}$), and finally in the halo modelcube we take into account particles al larger distances. Fig. 4.8 compares the $l-v$ plots at $b=-15^\circ$ (for mwK) and at $b=+30^\circ$ (for mwT) derived in these three areas. Obviously, only a minor fraction of the total emission comes from regions outside the thin disc, and in particular H I features above 10 scaleheights are very rare. Red circles in Fig. 4.8 represent the location of the anomalous gas previously shown in Fig. 4.6. Half of the anomalous features shown in Fig. 4.8 originates in the thin disc. These features are likely to be produced by particles that have been accelerated by recent SN events. This is certainly not the case for the Galactic HVCs (van Woerden et al. 2004; Wakker et al. 2007, 2008).

Both simulations do not reproduce the asymmetry in H I emission between the positive and the negative velocities. In the Milky Way, H I emission is preferentially seen at $v_{\mathrm{LOS}}<0$, which can be interpreted as a global infall of the extraplanar gas onto the disc (Chapter 2). As explained in Chapter 3, this is likely due to the fact that the fountain clouds are ionised during the initial part of their orbits. The simulations instead do not show this pattern and as a consequence the global infall of H I towards the disc is negligible, as we discuss in Section 4.5.1.

4.4

Results for the cosmological runs

In this Section we show the results for the simulated galaxy evolved in a full ΛCDM framework down to redshift 0. The snapshot analysed is a high resolution simulated box of $\sim 3\,\mathrm{Mpc}$ of size extracted from the GIMIC simulations, which include gas cooling, photo-heating from a ionizing background, supernova feedback and galactic winds, but no AGN feedback. Further details on the GIMIC project can be found in Crain et al. (2009). We present the results for the kinetic and the thermal feedback runs separately.

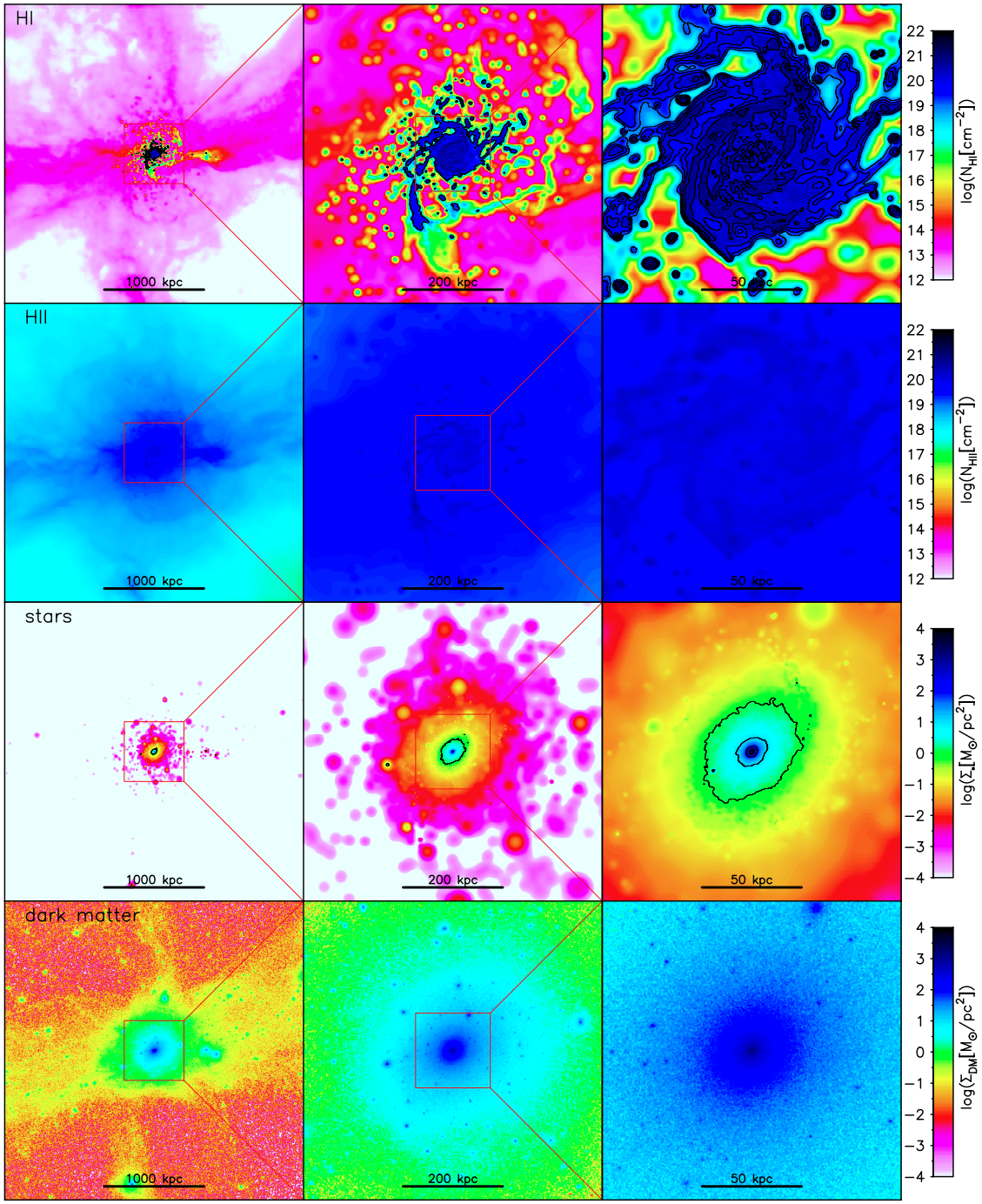

Figure 4.9: Surface density maps of H I (first row), H II (second raw), stars (third raw) and dark matter (last raw) for the simulation *cosmoK* obtained by collapsing all the particles on the (x, y) plane. Different columns show different area coverage. The first contour in the H I map is at $10^{19}\,\mathrm{cm}^{-2}$, the rightmost panel shows additional contours at $10^{19.5}$, 10^{20}, $10^{20.5}$ and $10^{21}\,\mathrm{cm}^{-2}$. The first contour in the star map is at $1\,\mathrm{M}_{\odot}\,\mathrm{pc}^{-2}$, the rightmost panel shows additional contours at 10, 10^2 and $10^3\,\mathrm{M}_{\odot}\,\mathrm{pc}^{-2}$. The maps are derived from the unrotated snapshot (the inclination of the galaxy disc with respect to the line of sight is $\sim 45°$).

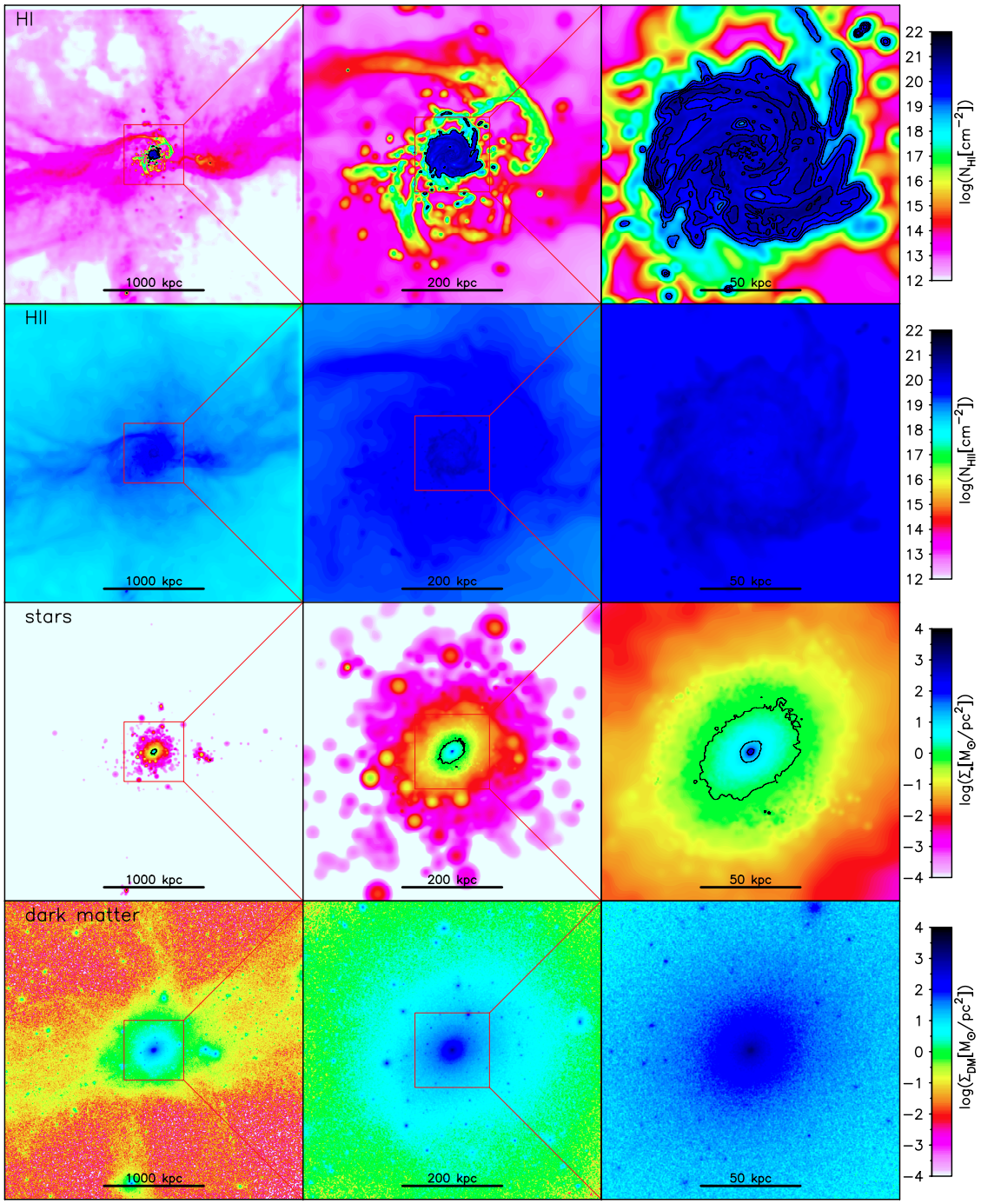

Figure 4.10: As figure 4.9, but for the simulation *cosmoT*. The maps are derived from the unrotated snapshot (inclination $i \simeq 47°$). The dark matter surface density map shown here is the same as for *cosmoK*, thus it must be considered indicative.

4.4.1 Morphology

Fig. 4.9 shows the total maps of H I, H II, stars and dark matter for the cosmological simulation with kinetic feedback using three different area coverages. The bottom left panel shows that the galaxy lies between two filaments of dark matter: a first larger filament extended horizontally, and a second thinner perpendicular to the first one. Globally, the gas distribution traces well the dark matter. The H I is concentrated in the central 300 kpc where its column density easily exceeds $10^{19}\,\mathrm{cm}^{-2}$ (first contour in the H I maps), while outside of this region it drops abruptly below $10^{13}\,\mathrm{cm}^{-2}$. The inclination of the galaxy disc with respect to the line of sight in this projection is about 45°. The H I disc is more than 100 kpc in diameter, and some well defined spiral arms are visible in the gas distribution. The H I scale-height is $1-2$ kpc, much larger than that of a typical disc galaxy. This is probably due to the low mass-resolution. Large filaments surround the main body of the galaxy, extending out to more than 100 kpc from the centre.

A striking feature of the H I distribution is the presence of a large number of H I clouds out to 200 kpc from the galaxy centre. The typical H I mass of these clouds is $\sim 5-10\times10^{6}\,\mathrm{M}_{\odot}$, while the total H I mass of this component is $2\times10^{8}\,\mathrm{M}_{\odot}$. Several of these clouds have column densities larger than $10^{19}\,\mathrm{cm}^{-2}$ and are thus - in principle - detectable in H I emission. However, deep H I observations reaching this detection limit do not show the presence of such a population of clouds at large distances from galaxies (Pisano et al. 2004, 2007; Oosterloo et al. 2007; Kovač et al. 2009). The presence of several extended gas filaments connecting the disc to the environment prevents us from distinguishing unambiguously between a thick disc and a halo. Assuming that the former is located between 3 and 10 scale-heights from the midplane, the H I mass of this component would be $\sim 10^{9}\,\mathrm{M}_{\odot}$. A similar mass has been found for the H I beyond 10 scale-heights, indicating that the above mentioned gas clumps do not constitute the main component of the extraplanar H I. The ionised gas is more diffuse and smooth than the H I. Although the H II density is larger in the region of the galaxy disc, the column density remains almost everywhere above $10^{18}\,\mathrm{cm}^{-2}$, forming a large and massive hot environment that surrounds the main body of the galaxy (see also Fig. 4.11). The stellar distribution shows the presence of a massive bulge, a smooth disc and a halo that extends for ~ 250 kpc in radius. The star density in the very centre of the bulge is almost $10^{4}\,\mathrm{M}_{\odot}\,\mathrm{pc}^{-2}$. A galaxy of this kind would be classified as an Sa, at least from its stellar properties.

Fig. 4.10 shows the same maps as Fig. 4.9 for the simulation with thermal feedback (inclination $i \simeq 47°$). Information on dark matter particles were not available for this run, but it is reasonable to assume that differences with respect to the previous case are minimal. The distribution of ionised gas is similar to that of *cosmoK*, but the total mass of this component is slightly smaller (see Table 4.1) and there is less H II in the inner regions of the simulated box. The H I map instead appears very different, since most of the filaments and the clouds that surrounded the disc in the

kinetic run have disappeared. Indeed, the total H I mass in the halo has decreased to $\sim 8 \times 10^7\,\mathrm{M}_\odot$ (a factor 13 smaller than *cosmoK*), equally distributed between clumps and filaments. Whether the massive H I halo visible in *cosmoK* comes from the disc (via stellar feedback) or from the cooling of the hot corona (via thermal instability), it is clear that thermal feedback is capable of quenching its formation very efficiently (see Section 4.5 for details). Also, thermal feedback prevents star formation in the very centre of the galaxy, and consequently the simulation *cosmoT* shows a less massive bulge. This has important consequences for the dynamics, as we see in Section 4.4.3.

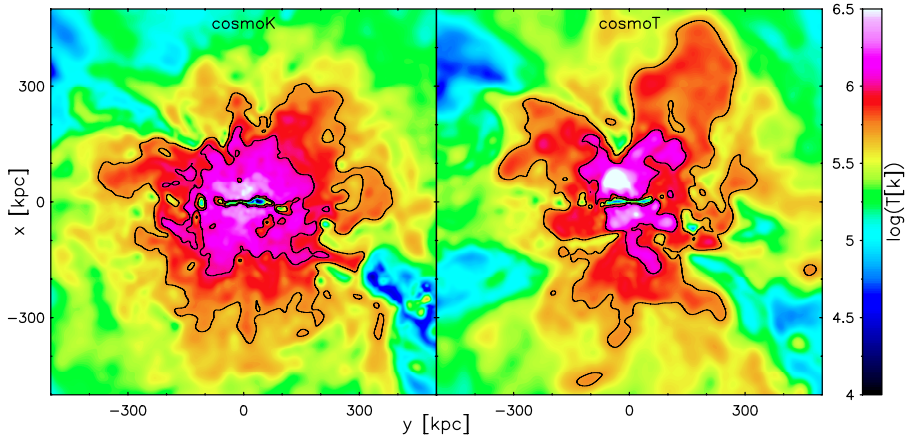

Figure 4.11: Temperature map for gas particles in *cosmoK* (*left panel*) and *cosmoT* (*right panel*) evaluated in a thin layer perpendicular to the midplane in a box of $1 \times 1\,\mathrm{Mpc}$ around the galactic centre. An edge-on projection of the disc has been adopted. Contours are at $5 \times 10^5\,\mathrm{K}$ (the outermost) and $10^6\,\mathrm{K}$ (the innermost).

Fig. 4.11 shows the temperature maps for *cosmoK* (left panel) and *cosmoT* (right panel) evaluated in a thin layer perpendicular to the galactic midplane. The discs are rotated edge-on. The gas temperature is larger than 10^6 K up to a distance of $\sim 150\,\mathrm{kpc}$ from the galactic centre, and remains above 5×10^5 K up to $\sim 300\,\mathrm{kpc}$. This hot gaseous halo appears rounder in the kinetic run, while in *cosmoT* it extends mainly in the direction perpendicular to the galaxy disc. The hottest ($T > 10^6\,\mathrm{K}$) component of this medium is probably built by a combination of pristine material coming from the intergalactic medium and high-metallicity gas expelled from the disc via stellar feedback. The relative importance of these two effects can be quantified considering the metallicity of the gas particles. This will be done in the next future. In Section 4.5.1 we show that the ionised gas in the innermost $\sim 150\,\mathrm{kpc}$ is mainly escaping from the disc, which suggests that supernova feedback must play an important role in building up this hot component.

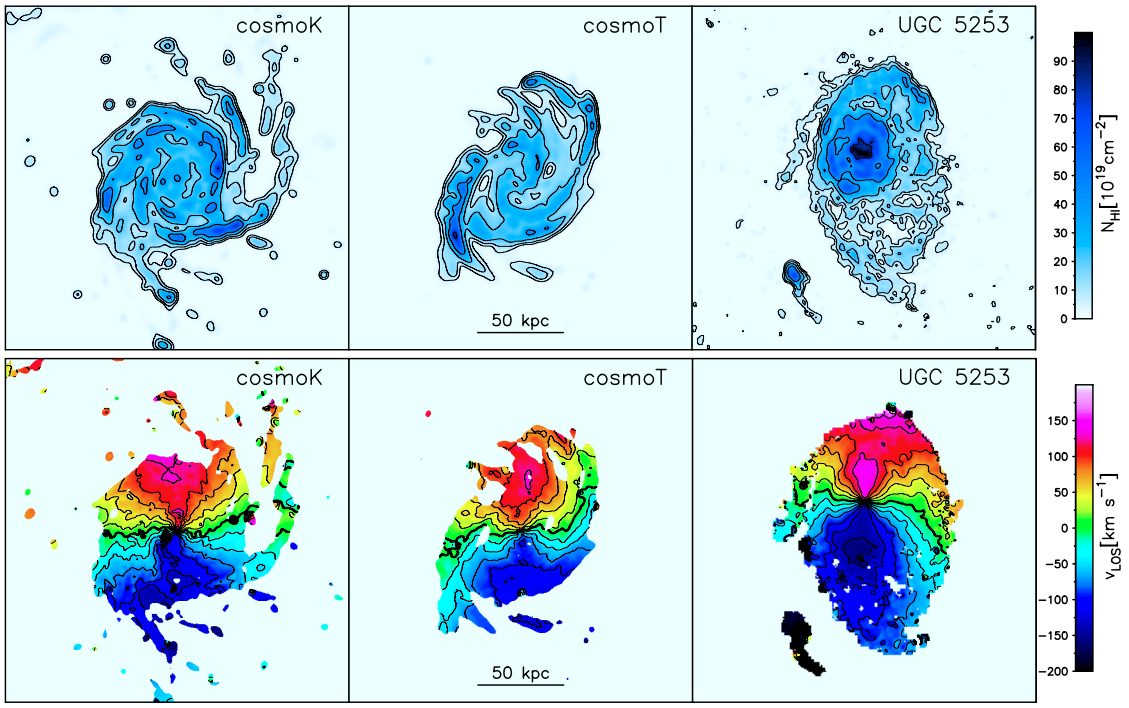

Figure 4.12: Comparison between the H I total maps (*top panles*) and the H I velocity fields (*bottom panels*) for *cosmoK* (*left*), *cosmoT* (*middle*) and for the spiral galaxy UGC 5253 (*right*). Inclination, position angle and resolution of the simulated galaxies have been set accordingly to those of UGC 5253. All maps are on the same scale. Contour levels at 5, 10, 20, 40, 80×10^{19} cm^{-2} in the total maps. Contours in the velocity field are spaced by 25 km s^{-1}, with the thick one representing the systemic velocity.

4.4.2 Total maps and velocity fields

In the case of simulations of isolated galaxies we have presented a full comparison with the position-velocity distribution of the H I in the Milky Way (Section 4.3.3). For *cosmoK* and *cosmoT*, however, a comparison with our Galaxy is not suitable because the gaseous discs of these simulated galaxies are much more extended than that of the Milky Way. Spiral galaxies of similar sizes are quite rare in the nearby Universe, which makes difficult a direct comparison with observations. In the Westerbork HI Survey of Irregular and Spiral Galaxies (WHISP; van der Hulst et al. 2001) we found a good candidate: UGC 5253, a large SAab galaxy with a well defined H I distribution and kinematics. In Fig. 4.12 we compare the H I total map and the velocity field of the simulated galaxies, derived using H I modelcubes (Section 4.2.4), with those of UGC 5253. The data have been taken from Noordermeer (2006), who analysed several early-type disc galaxies from the WHISP catalogue. Both *cosmoK* and *cosmoT* have been projected to the same inclination ($\sim 37°$) and position angle ($\sim 4°$) of UGC 5253, and have been smoothed to the same resolution of the observed galaxy ($37''$ at a distance of 21 Mpc, corresponding to ~ 3.8 kpc). The total H I maps show that the disc of UGC 5253 is roughly as extended as those of the simulated galaxies. The central H I density of UGC 5253 is much higher than that of *isoK* and

isoT (see also Fig. 4.13). The disc of this galaxy is lopsided, since in the southern part the H I distributes in a faint elongated structure, while it is more compact in the northern side. This is likely due to the interaction with a companion, visible in the south-western part of the map, that is disturbing the kinematics of the outer disc. The simulated galaxies instead show a quite regular disc in term of gas distribution. They also show spiral arms much more prominent that those of the real galaxy. The H I clumps surrounding the disc of *cosmoK* are clearly visible at column densities above $5 \times 10^{19}\,\mathrm{cm}^{-2}$, even if the resolution is now decreased by a factor ~ 2.2 with respect to the original value determined by the average smoothing length (1.7 kpc). Floating H I clouds are not visible in UGC 5253: the tiny features visible in the H I total map are due to noise. The velocity field of UGC 5253 is extremely regular, at least in the inner 30 kpc, while those of *cosmoT* and *cosmoK* (especially this latter) are somewhat more disturbed. The strong warp present in the simulated discs (see Fig. 4.1) can have a large impact on the H I velocity field. The kinematics of the H I clumps in *cosmoK* is similar to that of the disc: receding clumps are located around the receding half of the disc, and approaching clumps are on the other side. This may suggest an internal origin for these clouds. Instead, as we discuss in Section 4.5.2, most of these clumps have never been part of the disc during the evolution of the simulated galaxy.

4.4.3 Mass distribution and kinematics

The tilted ring fit applied to the simulated galaxies reveals the presence of a prominent warp in the H I distribution. Fig. 4.1 shows the mean displacement from the midplane for the cold gas of *cosmoK* (left panel) and compares it with the results of our tilted ring fit (right panel). Globally, the latter can nicely reproduce the features that are visible in the simulated galaxy. The extended H I filament close to the disc of *cosmoK* is located at $z \lesssim -5$ kpc and is considered external to the main disc, thus it is not reproduced by our tilted ring model. Note also that, since the model is axisymmetric, it can not account for local features.

The top panels in figure 4.13 show the surface density profiles for the gaseous, the stellar and the dark matter component for both the simulated galaxies, as well as those for the galaxy UGC 5253. The difference between the kinetic and the thermal run is visible mainly in the stellar surface density, that changes by an order of magnitude inside the inner 3 kpc. As a consequence, the effective radius changes dramatically between *cosmoK* and *cosmoT*, being 1.1 kpc for the former and 11.9 kpc for the latter. Both simulations - in particular the thermal one - show very little amount of molecular hydrogen (see table 4.1). Specifically, the percent ratio between the H_2 and the H I content is 1.2% for *cosmoK* and 0.16% for *cosmoT*. In contrast, observations of nearby disc galaxies show that neutral hydrogen very rarely exceeds the molecular one by more than one order of magnitude (e.g. Leroy et al. 2008). Dark matter is distributed similarly in both the simulated galaxies and UGC 5253.

It dominates the mass distribution beyond $R=3\,\mathrm{kpc}$ in *cosmoK*, and everywhere in *cosmoT*.

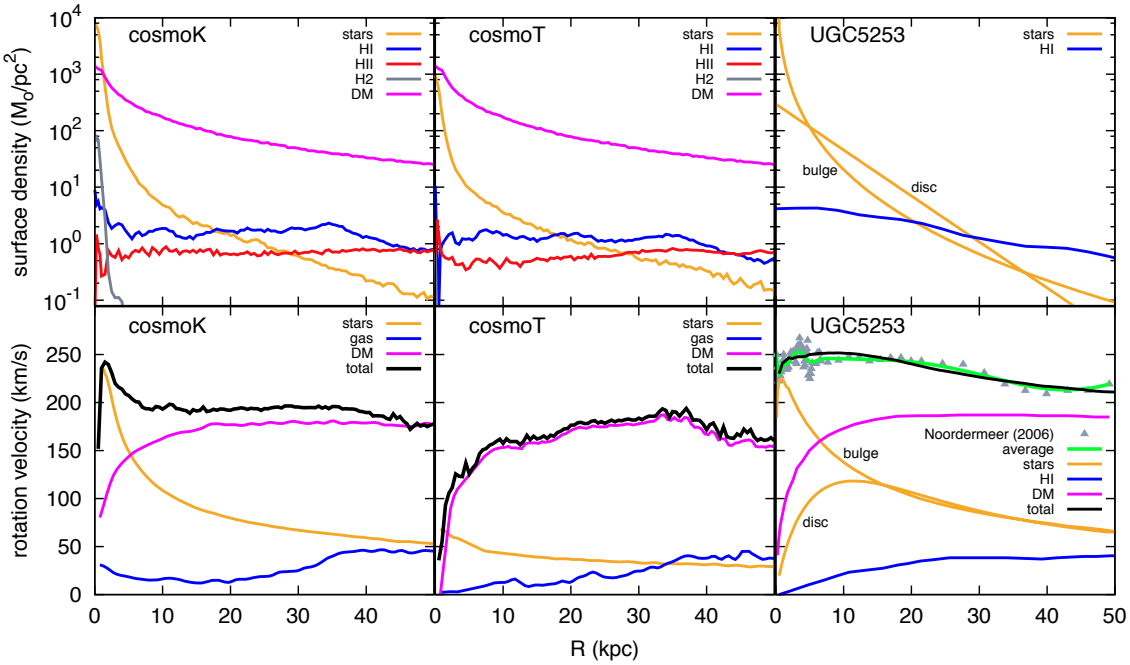

Figure 4.13: *Top panels:* surface density profiles of the various components for the simulated galaxies *cosmoK* (*left*) and *cosmoT* (*middle*), compared with that of UGC 5253 (*right*, from Noordermeer 2006). *Bottom panels*: H I rotation curve and contribution of the various component to the circular velocity for the same galaxies. The green line shows the average rotation curve of UGC 5253, obtained by approximating the data of Noordermeer (2006) with a Bezier curve.

The bottom panels of fig. 4.13 show the H I rotation curves for both the simulated galaxies and UGC 5253, as well as the contribute of the various components to the circular velocity. In the simulation *cosmoK*, the contribute of dark matter to the to the circular velocity has been determined using the actual particle distribution, while in *cosmoT* it has been set to match the total rotation curve. For UGC 5253 a standard mass decomposition has been performed by adopting a mass-to-light ratio of $2.7\,\mathrm{M_\odot/L_\odot}$ for the bulge and $4\,\mathrm{M_\odot/L_\odot}$ for the stellar disc (Noordermeer 2006) and by assuming a NFW dark matter profile. Since thermal feedback quenches star formation in the bulge, the rotation curves of the two simulated galaxies are completely different in the inner regions. The steep rise visible in *cosmoK* indicates that the dynamics of these regions is totally dominated by the baryonic matter (i.e. the bulge), while the shallow rise curve of the thermal run is a common feature of bulgeless galaxies. At large distance from the centre the two rotation speeds approach a similar value, consistently with these galaxies being hosted in similar dark matter potential wells. However, the dynamics of *cosmoK* is completely dominated by dark matter at every radius. While this can be a common feature in dwarf galaxies, it is widely accepted that the dynamics of large spirals is dominated by baryons, at least in the inner regions. In particular, recent studies on the mass distribution in late-type galaxies suggest that the ratio $\mathcal{R}_b$ between the circular

speed produced by baryonic matter alone and the total circular speed is $\gtrsim 0.8$ at the optical effective radius R_e (Dutton et al. 2011; Westfall et al. 2011). Note that UGC 5253 is not an exception: from the mass decompsition of Noordermeer (2006) we can infer $\mathcal{R}_b = 0.84$ at $R_e = 4.3$ kpc. For the simulated galaxy *cosmoK* we derived $\mathcal{R}_b \simeq 1$ at $R_e = 1.1$ kpc, while for *cosmoT* we found $\mathcal{R}_b \simeq 0.28$ at $R_e = 11.9$ kpc. It is clear that, in the simulations analysed, thermal feedback produces a very unrealistic distribution of baryons in the innermost regions of the galaxy. The kinematics of UGC 5253 is similar to that of *cosmoK*, with the exception that the rotation velocity is systematically $\sim 40\,\mathrm{km\,s^{-1}}$ above that of the simulated galaxy. This is possibly due to a larger amount of baryonic matter in UGC 5253, as the dark matter contribution to the rotation curve appears to be similar in this galaxy and in the simulated discs.

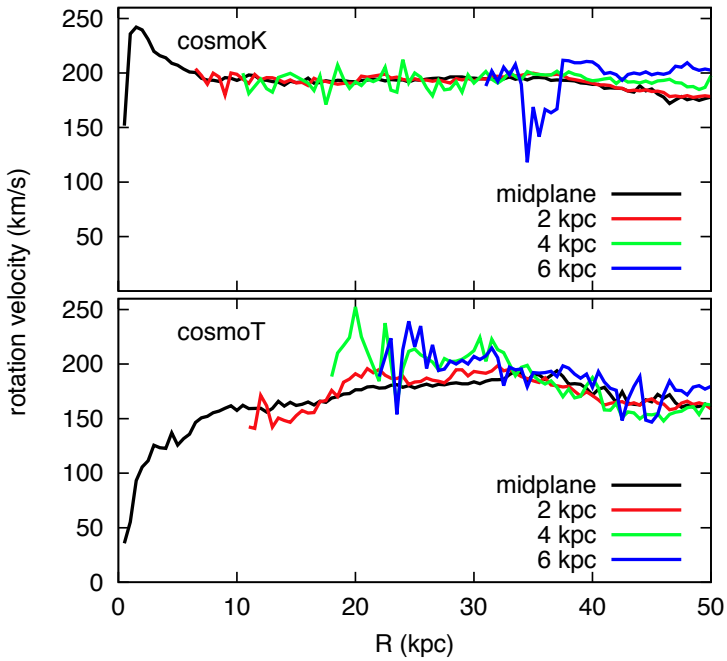

Figure 4.14: Rotation curves at different heights from the midplane for the simulated galaxies *cosmoK* (*top panel*) and *cosmoT* (*bottom panel*). Rings with less than 10 particles have been excluded.

Figure 4.14 shows the rotation curve of *cosmoK* (top) and *cosmoT* (bottom) at different heights from the midplane. In both models the rotation curves above the disc do not show the characteristic lag that is observed in nearby galaxies (Fraternali et al. 2002; Barbieri et al. 2005; Oosterloo et al. 2007). Instead, the H I at 2 and 4 kpc above the plane co-rotates with the disc. In the *cosmoT* run there are indications that at 6 kpc the gas is rotating even faster. It is possible that these rotation curves are not tracking the kinematics of the thick H I disc, but instead they are tracing the outer filaments that are merging with the galaxy. In Section 4.3 we showed that, in non-cosmological simulations, both thermal and kinetic feedback are able to build a lagging thick disc of H I whose kinematics is in fair agreement with observations. The lack of this medium in the cosmological simulations is probably connected to the different resolution, as we discuss in Section 4.5.

4.5 Discussion

In this Section we focus our analysis on the gaseous environment that surrounds the discs of the simulated galaxies, which is the subject more relevant for this Thesis. A proper, time-dependent analysis of this medium can not be done at the moment because, for each simulation, only the last snapshot has been used. However, since information on the gas particle velocities are available, it is possible to study the global motion of this component with respect to the disc (Section 4.5.1). The properties of the extraplanar H I in the simulated galaxies are discussed in Section 4.5.2.

4.5.1 Accretion and circulation of gas

Most of the gas particles in the halo region show a not negligible motion in the direction of the galaxy centre (gc). If d_i is the distance of the i-th particle from the gc, $v_{\mathrm{r},i}$ is the component of its velocity in the direction of the gc and $m_{\mathrm{HI},i}$ is its H I mass, then the cumulative radial flow of H I inside a sphere of radius d centered in the gc can be estimated as

$$\dot{M}_{\mathrm{HI}}(d) = \sum_{d_i<d} m_{\mathrm{HI},i}\,\frac{v_{\mathrm{r},i}}{d_i}\,. \tag{4.8}$$

Equation 4.8 assumes that the motion is straight and the velocity is constant. Obviously, an equivalent equation stands for $\dot{M}_{\mathrm{HII}}(d)$.

Figure 4.15 shows the cumulative radial flow of H I and H II as a function of the distance from the gc for both *cosmoK* (top panel) and *cosmoT* (bottom panel). In the kinetic run, the H I above the plane is globally infalling onto the disc at a rate of $\sim 2\,\mathrm{M}_\odot\,\mathrm{yr}^{-1}$ with an average velocity of $\sim 35\,\mathrm{km\,s}^{-1}$. Beyond $R = 200\,\mathrm{kpc}$ the cumulative flow of H I remains constant because cold gas is very rare at those distances. This suggest that the inflow of cold gas is produced mainly by the H I clumps that are visible in the total map of the *cosmoK* run in the inner 200 kpc. H I filaments visible at smaller distances can also play a role. The ionised gas instead is escaping the disc in the inner regions because of the feedback from the disc. At larger radii the inflow of H II start to be important, and beyond $\sim 200\,\mathrm{kpc}$ it dominates the gas accretion and keeps increasing out to the end of the box. This suggest that the entire hot corona that surrounds the galaxy (Fig. 4.11) is globally, slowly infalling. In Section 4.4 we have already seen that H I outside the disc is rare in the thermal run, thus it is not surprising that the H I flow is close to zero everywhere. It is instead remarkable that the inflow from H II is strongly mitigated at every distance from the main galaxy, suggesting that thermal feedback can heavily affect the whole environment in which the galaxy evolves.

Fernández et al. (2012) analysed an adaptive mesh refinement (AMR) cosmological simulation of a Milky-Way-like galaxy to study the cold gas accretion onto

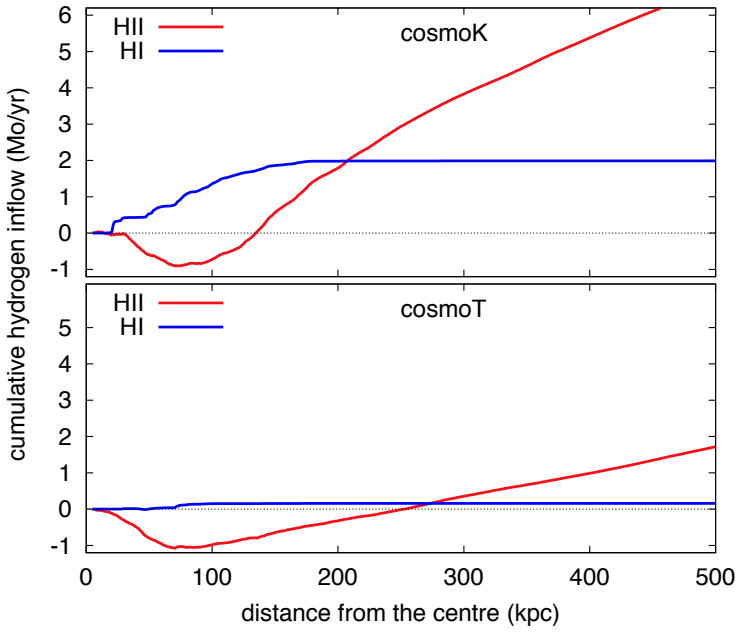

Figure 4.15: Cumulative H I and H II flow as a function of distance from the galactic centre for the simulated galaxies *cosmoK* (*top panel*) and *cosmoT* (*bottom panel*). Positive (negative) values represent inflow (outflow). Particles below 3 scale-heights from the midplane have been excluded.

this system in the redshift range $0 < z < 0.5$. They found that the main sources of H I inflow are two: gas stripped from satellites and cold filaments from the intergalactic medium. The combined accretion rate produced by these two sources is $0.2\,\mathrm{M_\odot\,yr^{-1}}$, a factor 10 smaller than what we found in the *cosmoK* run. Joung et al. (2012) analysed the gas at higher temperatures ($10^5 < T < 10^6\,\mathrm{K}$) in the simulation of Fernández et al. (2012), finding that most of this warm-hot component is organised in filamentary structures that inject material in the disc at a rate of $3-5\,\mathrm{M_\odot\,yr^{-1}}$. It is not clear whether in *cosmoK* and *cosmoT* the ionised gas is accreting onto the disc, because even though at large distances H II is globally moving inward, stellar feedback produces a powerful ionised outflow that dominates the gas flow in the inner regions.

Figure 4.16 is similar to Fig. 4.15, but for the galaxy evolved in isolation. In this case, the results for the kinetic and the thermal run are very similar. There is a strong outflow of H II from the disc of $\sim 10\,\mathrm{M_\odot\,yr^{-1}}$ that occurs in the inner 50 kpc from the centre. The typical velocity of the outflowing gas, evaluated as the median of the H II-weighted radial velocity distribution, is $78\,\mathrm{km\,s^{-1}}$ for *mwK* and $62\,\mathrm{km\,s^{-1}}$ for *mwT*. The net H I flow is instead close to zero, which is surprising since clouds of H I are visible around the disc (see Fig. 4.2 and Fig. 4.3) and the H I mass of the thick disc - especially in the thermal run - is not negligible. We checked the velocities of these clouds in the halo and found that approximately half of them is inflowing and half is outflowing, which would justify the above result. However, the interpretation of this result is not straightforward. In fact, it is unlikely that

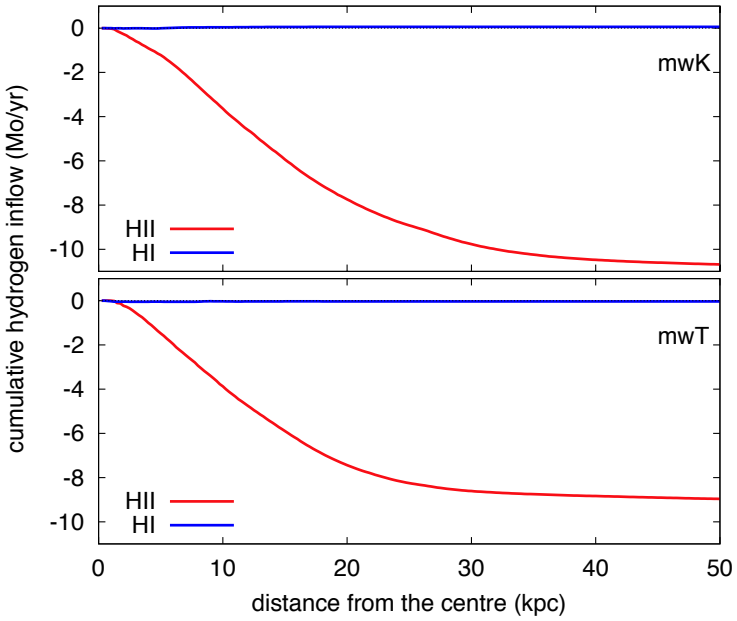

Figure 4.16: As figure 4.15, but for the isolated galaxy.

the outflowing clumps are directly ejected from the disc by stellar feedback, since the material escaping the disc is mostly ionised. The H I clumps probably form via condensation of this outflowing ionised layer. A possible explanation is that, when these H I clouds fall back onto the disc, their motion is not interrupted by the impact with the interstellar medium (ISM). A more accurate analysis would require a proper tracking of the particle trajectories.

4.5.2 Properties of extraplanar H I

It is commonly accepted that extraplanar H I in nearby disc galaxies originates mostly from supernova feedback that pushes part of the ISM outside the plane (Fraternali et al. 2002; Fraternali and Binney 2006), and it has also been argued that this layer may act as interface between the galaxy disc and the surrounding medium (galactic corona and intergalactic medium) by transferring mass and angular momentum between the two (Fraternali and Binney 2008; Marinacci et al. 2011, Chapters 3 and 5 of this Thesis). Therefore, it is interesting to check whether global N-body + SPH simulations with (realistic) stellar feedback do reproduce the fundamental properties of this layer.

Table 4.2 summarizes the gas distribution in the simulations analysed in this Chapter. We define the *thin disc* as the region within 3 scale-heights from the midplane, the *thick disc* as the region between 3 and 10 scale-heights, while the *halo* is the external area out to 300 kpc from the galaxy centre. Note that the H I content of the halo is made up by clumps in the isolated runs, and by a combinations of filaments and clumps in the cosmological runs. In nearby disc galaxies, the fraction of

H I embedded in thick discs is about 5−10% (Fraternali 2010). The more massive H I thick disc in the simulations considered is that of *cosmoK*, which contains about 8% of the total neutral hydrogen. However, most of this material is due to filamentary structures that connect the disc to the halo and are probably not related to stellar feedback. Filaments are almost absent in *cosmoT*, which shows an thick H I disc one order of magnitude less massive than that of *cosmoK*, although both simulated galaxies should have similar star formation rates according to their atomic and molecular gas content. The isolated run with thermal feedback has a significant amount of H I in its thick disc, $\sim 3\%$ of the total. Note that, in all the simulations analysed, the most massive component of the thick disc is ionised hydrogen. This is not in agreement with the prediction of our galactic fountain model (see Chapters 3 and 5).

Table 4.2: Gas content in the simulations analysed. Units are in solar masses.

Simulation		*mwK*	*mwT*	*cosmoK*	*cosmoT*
H I	thin disc	4.1×10^9	4.6×10^9	1.5×10^{10}	1.1×10^{10}
	thick disc	6.2×10^7	1.5×10^8	1.3×10^9	1.3×10^8
	halo	1.8×10^7	1.4×10^7	1.1×10^9	7.8×10^7
H II	thin disc	1.9×10^8	2.5×10^8	5.2×10^9	6.4×10^9
	thick disc	4.5×10^8	6.0×10^8	4.4×10^9	3.2×10^9
	halo	1.8×10^9	1.5×10^9	5.0×10^{10}	3.2×10^{10}
H_2	thin disc	4.1×10^9	3.7×10^9	2.1×10^8	1.9×10^7
	thick disc	2.0×10^5	2.0×10^6	1.9×10^6	-
	halo	1.1×10^5	3.2×10^4	2.6×10^6	-
Total	thin disc	1.1×10^{10}	1.1×10^{10}	2.7×10^{10}	2.4×10^{10}
	thick disc	6.8×10^8	1.0×10^9	7.6×10^9	4.5×10^9
	halo	2.5×10^9	2.0×10^9	6.8×10^{10}	4.3×10^{10}

Even though both cosmological and non-cosmological simulations analysed in this work implement the same recipe for stellar feedback, only the latter seems to predict a gaseous thick disc with kinematics consistent with the observations. The lack of this layer in the cosmological runs may be due to a couple of effects. The first is a numerical effect, i.e. the different mass resolution, which increases by a factor $\sim 3-4$ from the cosmological to the isolated runs. Dalla Vecchia and Schaye (2008) showed that a decrease in mass resolution implies a sensible increase in velocity and mass of the outflow, because the ejected particles experience a smaller net hydrodynamical drag. It is likely that the low mass resolution of the cosmological simulations prevents the formation of a smooth lagging thick disc, because particles are ejected too far away from the plane, producing a galactic wind rather than a galactic fountain. The second effect is more physical, and it is due to the global inflow of the hot corona onto the disc, which is present only in the cosmological simulations (see Section 4.5.1). It is possible that the pressure of this medium introduces a bias

in the particles ejected via stellar feedback, allowing only the fastest ones to escape the disc. Also in this case a galactic wind would prevail against the fountain.

Even though cosmological simulations do not produce a lagging extraplanar layer, H I clouds are present in a large (~ 200 kpc) region around the galaxy. We showed that *cosmoK* and *cosmoT* largely differ for the number of clouds and total H I mass of this component. To better understand the origin of this component, we followed the orbits of six particles representative of six different H I clouds in *cosmoK*, and five particles for five different clouds in *cosmoT*, from redshift 10 to redshift 0. We found that none of the particles in the thermal run have ever been part of the galactic disc, while in the kinetic run 2 particles out of 6 have been in the disc from redshift ~ 2 to ~ 0.8, before being ejected by stellar feedback. The poor statistics forbids robust conclusions, but we can speculate that most of these clouds are not produced by supernova feedback but likely come from the cooling of the hot corona via thermal instability. The differences between *cosmoK* and *cosmoT* can be explained if thermal feedback is able to mitigate efficiently the development of thermal instability up to large distances from the main galaxy. This could be a possibility given that, as discussed in Section 4.5.1, thermal feedback affects the gas circulation - in particular the inflow of H II - at very large distances. Floating clouds of H I masses above $10^6\,M_\odot$ are not observed in real data at distances larger than ~ 50 from galaxy discs (Pisano et al. 2007).

The isolated galaxies seem to reproduce much better the properties of the observed thick discs of neutral hydrogen. In particular, the lagging kinematics of the gas above the midplane is remarkably consistent with that of NGC 891 and the Milky Way, even though the H I mass of this component is a factor $2-5$ smaller than that of our Galaxy (Section 4.3.2 and Chapter 2). Above this layer, in the halo region, the H I emission is localized in some compact clouds similar to those present in *cosmoK*. Their H I masses are of a few $10^5\,M_\odot$, at least one order of magnitude smaller than those in the cosmological simulations. While this effect may be related to the different resolution, it is interesting to note that these masses are similar to those of the IVCs of the Milky Way (van Woerden et al. (2004)), which however are located at ~ 1 kpc from the disc of the Galaxy.

4.6 Conclusions

In this Chapter, we studied the properties of two simulated galaxies as resulting from recent N-body+SPH numerical simulations. The first galaxy is an isolated Milky-Way-like spiral that evolved for 250 Myr in a closed box. The second is a large early-type spiral, evolved for ~ 13.6 Gyr in a full ΛCDM cosmological framework. Two different realisations of each simulated galaxy were available, according to how stellar feedback was implemented (thermal or kinetic). We focussed mostly on the

properties of the neutral hydrogen, and in particular on those of the extraplanar H I. We compared these properties with those of the Milky Way (for the isolated simulation) and UGC 5253, an SAab galaxy from the WHISP sample (for the cosmological simulation).

The isolated Milky-Way-like galaxy shows a morphology and a kinematics similar to those of our Galaxy, but this is a consequence of the initial conditions. Only minor differences are visible between the kinetic and the thermal run. The H I velocity dispersion is about $2-3$ times larger than that normally observed in disc galaxies, probably due to numerical effects rather than an excessive heating by SN feedback. An H I thick disc is present in both runs, but that produced by thermal feedback is a factor $2-3$ more massive. This medium shows a vertical rotation-gradient, consistent with that measured in the H I thick discs of real galaxies like NGC 891 (Oosterloo et al. 2007) and the Milky Way itself (Chapter 2). There is a strong outflow of ionised gas, resembling a powerful galactic wind that removes $\sim 10\,\mathrm{M_\odot\,yr^{-1}}$ of gas from the disc. Obviously, this galaxy would consume all its gaseous content via star formation or expel it via the galactic wind in a few hundred Myr without accretion of material from the ambient medium. The disc is surrounded by a clumpy H I halo, probably produced by the cooling of the ejected ionised material. The position of the H I clumps is similar to that of the HVCs of the Milky Way.

The most striking feature of the galaxy simulated in the ΛCDM framework is how its morphology, kinematics and mass distribution depends dramatically on the feedback recipe used. The kinetic feedback produces an early-type disc with a massive bulge and a steeply rising rotation curve, similar to that of UGC 5253, our chosen comparison galaxy. Thermal feedback instead prevents star formation in the centre, producing a bulgeless spiral with a slowly rising rotation curve. In the thermal run the kinematics and the mass distribution are completely dominated by dark matter, while observations strongly suggest that, in large spiral galaxies, baryons should be dynamically important at least in the inner regions. In the kinetic run, H I clumps and filaments are visible up to large distances ($\sim 200\,\mathrm{kpc}$) from the disc. Most of these clumps are produced by the cooling of the corona via thermal instability. Each clump is very massive ($\sim 5-10\times10^6\,\mathrm{M_\odot}$), thus most of them should be visible in H I emission around real galaxies, which is definitely not the case. Thermal feedback completely prevents the formation of these clumps. It is surprising how SN feedback from the stellar disc can have such a large impact on the material located out to distances of 200 kpc from the galaxy. A lagging H I layer surrounding the thin disc is not present in these galaxies. This is probably due to the relatively low mass resolution.

The results of this Chapter indicate that understanding the physics of stellar feedback is of fundamental importance to carry out cosmological simulations which include baryons, since the final results may depend dramatically on the recipe used. Increasing the mass resolution of the simulations is certainly another important step, given that the same feedback recipe seems to produce different results depending on the resolution adopted. The presence of extraplanar gas in simulated galaxies is a

likely consequence.

We are grateful to Joop Schaye, Rob Crain and Alireza Rahmati (Leiden University) for kindly providing the simulations analysed in this Chapter and for fruitful suggestions and discussions. Most of the work presented here has been carried out at the Kapteyn Institute in Groningen (the Netherlands), which we thank for the hospitality.

Chapter 5

A dynamical model for the Galactic warm-hot halo

5.1 Introduction

The supernova-driven gas accretion model presented in Chapter 3 can explain how star-forming galaxies like the Milky Way are capable of replenishing the gas consumed by the process of star formation in the disc. In this model, fountain clouds are ejected from the disc by stellar feedback and interact with the lower corona of the Galaxy. Hot coronal material that mixes with the cold high-metallicity gas in the turbulent wakes of the fountain clouds cools and condenses. This process causes a modification of the H I kinematics that is visible in the LAB data and is successfully reproduced by our model, which predicts an accretion of pristine gas onto the disc at a rate of $\sim 2\,\mathrm{M}_\odot\,\mathrm{yr}^{-1}$. Here, we strengthen the results obtained in Chapter 3 by including in our dynamical model the ionised, warm-hot component of the material entrained by the wakes of the fountain clouds.

In the last years, the possibility that gas accretion manifests itself mostly as ionised gas has attracted a growing interest, as evidence for highly ionised material around the Galaxy disc have arisen. O VI absorption lines towards nearby AGNs have been observed with the Far Ultraviolet Spectroscopic Explorer (FUSE) by Wakker et al. (2003), Sembach et al. (2003) and Savage et al. (2003), showing that ionised material with temperatures of $2 - 5 \times 10^5\,\mathrm{K}$ is widespread in the sky. The distances of the absorbers are unknown, but the low standard-of-rest velocities of the lines ($|v_{\mathrm{LOS}}| < 400\,\mathrm{km\,s}^{-1}$) suggest that this this material is located within the Local Group. Ultraviolet spectra against bright AGNs obtained with the Space Telescope Imaging Spectrograph (STIS) and the Cosmic Origins Spectrograph (COS) on board of the Hubble Space Telescope (HST) have revealed a number of ionised species (C II, C III, C IV, Si II, Si III, and Si IV) at velocities incompatible with those of the gas in the Galactic disc (Collins et al. 2009; Shull et al. 2009). These ions probe material

at temperatures from a few times 10^4 K to 2×10^5 K (assuming collisional ionisation equilibrium). In a few cases, they have been identified in the spectra of halo stars, showing that at least a subsample of them lies at distances within about 10 kpc from the Galactic disc (Lehner and Howk 2011) and ruling out a formation in the distant corona or in the Local Group medium.

The nature of these features remains poorly understood. It is possible that the absorbers belongs to the extended, ionised envelope that surrounds the classical High-Velocity Clouds (HVCs), as proposed by Lehner et al. (2012). Recent cosmological simulations suggest that in Milky-Way-like galaxies gas inflow occurs mostly along filamentary structures of material at temperatures above 10^5 K (Joung et al. 2012); a small fraction of this gas can cool and form floating clouds, similar to the HVCs of the Milky Way, embedded in a diffuse ionised medium. Photoionisation of material ejected from the disc by stellar feedback may also play a role, although it seems unlikely that high-ions like O VI can be produced by this process (Sembach et al. 2003). An intriguing possibility is that this warm-hot material is instead produced by the cooling of the Galactic corona. Spontaneous cooling of coronal gas via thermal instability should not take place, as suggested by deep H I observations (Pisano et al. 2007), analytical calculations (Binney et al. 2009; Nipoti 2010; Nipoti and Posti 2012) and recent numerical simulations (Fernández et al. 2012; Joung et al. 2012; Hobbs et al. 2013).

As already discussed in Sections 1.4 and 3.2.3, Marinacci et al. (2010a, 2011, this latter hereafter M11) found that the interaction between fountain clouds and the hot corona triggers the cooling of the latter inside turbulent wakes lagging behind the clouds. Gas cooling in these wakes is expected to manifest itself in a wide range of temperatures between the virial one ($\sim 1-2 \times 10^6$ K) and 10^4 K. In this Chapter we investigate whether the material cooling in the wakes of the fountain clouds is responsible for the local ($|v_{\rm LOS}| < 400\,{\rm km\,s^{-1}}$) warm-hot absorptions of different ions (O VI, Si III, Si IV, C II, C IV) observed toward AGNs/QSOs and distant halo stars in the works of Lehner et al. (2012), Sembach et al. (2003) and Savage et al. (2003). For this purpose we make use of the dynamical model described in Chapter 3, but instead of studying the neutral hydrogen component of the cloud+wake systems, we focus on material at higher temperatures. In Section 5.2 we analyse the M11 simulations in order to include the dynamics of the warm-hot gas in the dynamical model of the galactic fountain described in Chapter 3. In Section 5.3 we compare the predictions of the resulting models with the available data of warm-hot absorptions. In Section 5.4 we discuss our results and in Section 5.5 we draw our conclusions.

The results of this Chapter have been submitted for publication to MNRAS.

5.2

The model

The framework adopted in this Chapter is based on the results of M11 for the hydrodynamical simulations of cloud-corona interaction, and on those derived in Chapter 3 for the dynamical model of the galactic fountain with condensation of the corona. We refer to Chapter 3 for further details.

The global picture that emerges from these works is sketched in Fig. 5.1. The gaseous halo of the Galaxy is populated by high metallicity fountain clouds, similar to the Intermediate-Velocity Clouds (IVCs), that interact with the metal poor coronal gas. This latter is entrained by the clouds' wakes and cools efficiently. The system cloud+wake is multiphase (see Section 5.2.1). In Chapter 3 we have shown that the cold phase of this medium can account for H I observations in the Galactic halo. Here, instead, we compare the warm-hot phase with the detections of different absorption lines of ionised material.

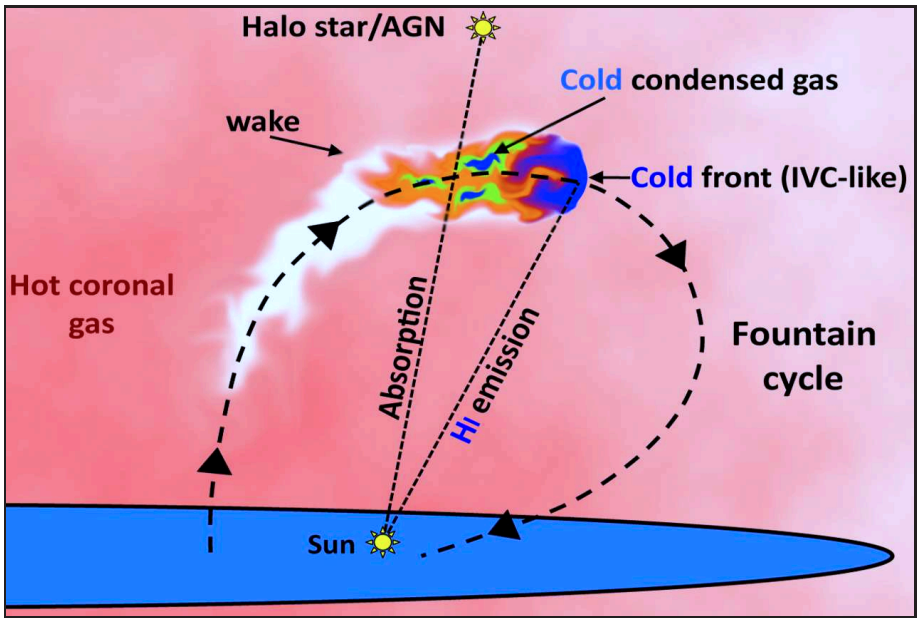

Figure 5.1: Scheme of the framework considered in this work. Fountain clouds, ejected form the disc by supernova feedback, travel through the halo and interact with the hot gas in the corona. The interaction creates a turbulent wake where coronal gas is entrained and mixed efficiently with high-metallicity disc material. This mixing produces a modification of the cold gas kinematics and triggers the cooling of some coronal material, which is then accreted onto the disc when the cloud falls back to it. An observer looking towards a background source intercepting the wake detects the absorption lines of the turbulent ionised material. An observer looking towards the cold front detects H I emission at velocities typical of intermediate-velocity clouds.

5.2.1 The wake of a fountain cloud

We use the simulations of M11 to quantify how the mass and the velocity of a fountain-cloud wake evolve with time for different ranges of temperature. The simulations include radiative cooling, and the relative velocity between the cold and the hot phase is fixed to $75\,\mathrm{km\,s^{-1}}$ for the reasons discussed in Section 3.2.3. The effects of different relative velocities are discussed in Section 5.4.2. We assume collisional ionisation equilibrium (CIE) to infer the ranges of temperature in which the considered ions are supposed to occur (Sutherland and Dopita 1993; Bregman 2007). We distinguish three ranges of temperature:

- *cold gas*: gas with $\log T < 4.3$, mainly H I;
- *warm gas*: gas with $4.3 < \log T < 5.3$, responsible for the absorptions in Si III, Si IV, C II, C III and C IV;
- *hot gas*: gas with $5.3 < \log T < 5.7$, responsible for the absorptions in O VI.

With the term *corona* instead we indicate the low density environment at the virial temperature ($\gtrsim 10^6\,\mathrm{K}$) that surrounds the Galaxy. Here, we assume that the ion abundances of a given atomic species in the gaseous halo depend only on the temperature of the medium, thus photoionisation from stellar disc and extragalactic sources is neglected. The influence of photoionisation on the O VI abundances should not be relevant (see Sembach et al. 2003), while it may have an impact on the other species considered (see Section 5.3.1). Fig. 5.2 shows a snapshot at time $t = 60\,\mathrm{Myr}$ taken from the simulation analysed. The different ranges of temperature considered are coded by three different colors. Clearly, the cold gas concentrates in the rightmost

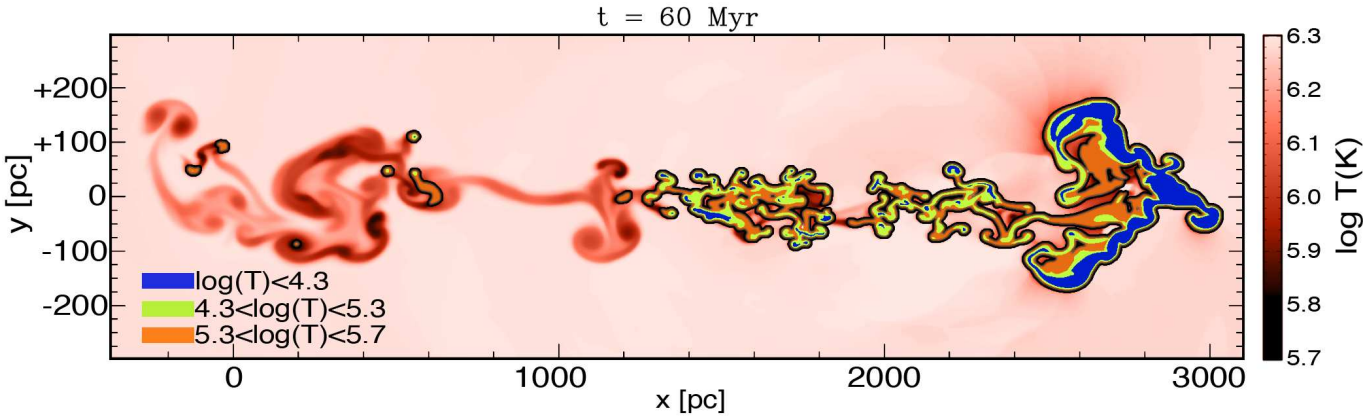

Figure 5.2: Snapshot at time $t = 60\,\mathrm{Myr}$ from the hydrodynamical simulation of M11. The initial relative velocity between the cloud and the hot environment is $75\,\mathrm{km\,s^{-1}}$. The colors code the different ranges of temperature defined in Section 5.2.1: *blue* regions represent the cold gas ($\log(T) < 4.3$), *green* regions represent the warm gas ($4.3 < \log(T) < 5.3$) and *orange* regions represent the hot gas ($5.3 < \log(T) < 5.7$). The black contour is at $log(T) = 5.7$. *Red* regions represent material at higher temperatures.

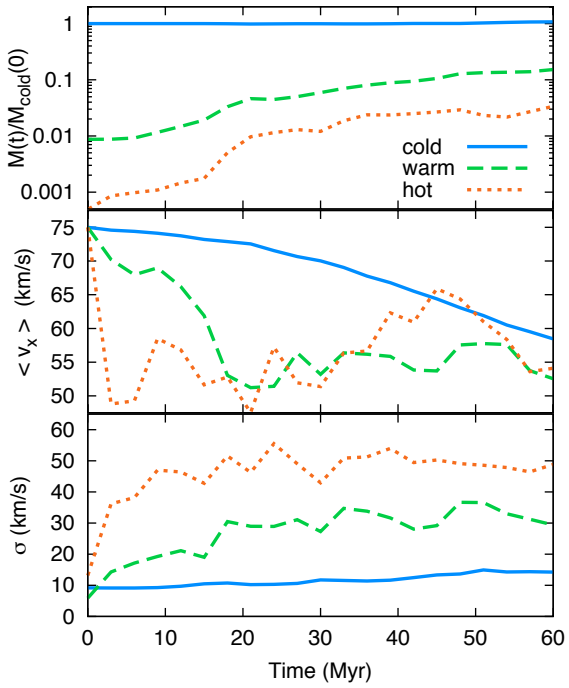

Figure 5.3: Time-evolution of different quantities in the hydrodynamical simulation of M11. Different lines show gas in different ranges of temperature, as indicated in the top panel (see also Section 5.2.1). *Top panel:* mass ratio between gas at a given temperature and the cold one at $t = 0$; *middle panel:* mass-weighted velocity along the x-axis; *bottom panel:* mass-weighted total (turbulent+thermal) velocity dispersion along the x-axis.

part of the system, but a few knots are present also in the wake due to coronal material cooling down to $\sim 10^4$ K. The warm and the hot gas are present both immediately behind the cold front and in the wake, which extends about 2 kpc.

For each snapshot of the simulation, we evaluate the mass $m(t)$, the mean velocity parallel to the motion of the cloud $\langle v_x(t) \rangle$ and the velocity dispersion $\sigma_{\rm turb}(t)$ for the gas in the above ranges of temperature. The latter, evaluated as the standard deviation of the v_x distribution, is assumed to be isotropic. The total one-dimensional velocity dispersion $\sigma(t)$ is computed as the quadratic sum of the turbulent and the thermal component:

$$\sigma(t) = \sqrt{\sigma^2_{\rm turb}(t) + \frac{k_B T(t)}{m_{\rm ion}}} \tag{5.1}$$

where $T(t)$ is the average temperature of the gas at a given time. Note that the thermal component depends on the mass of the ion considered. Fig. 5.3 shows the time evolution of the above-mentioned quantities. The panel on top clearly shows that the mass of the warm and the hot gas, negligible at the beginning of the simulation, increases by more than one order of magnitude in 60 Myr, while the mass of the cold gas increases only by a few percents with respect to the initial value. The velocity of the cold gas centroid smoothly decreases with time because of the combined effects of drag and condensation (see Section 3.5.1). The velocities

of the warm and the hot components remain below that of the cold material for the whole simulation, showing an irregular trend with time. As a consequence, the warm and the hot material falls further and further behind the cold front during the cloud's orbit. The total velocity dispersion, after the first 20 Myr, flattens to the values of $12\,\mathrm{km\,s^{-1}}$ for the cold gas, $31\,\mathrm{km\,s^{-1}}$ for the warm gas and $49\,\mathrm{km\,s^{-1}}$ for the hot gas. Since the thermal velocity dispersion is only $6\,\mathrm{km\,s^{-1}}$ for the warm gas (considering Carbon) and $14\,\mathrm{km\,s^{-1}}$ for the hot gas (considering Oxygen), the turbulent component always dominates over the thermal one in these cases. For the cold gas the two components are comparable.

5.2.2 From simulations to 'modelcubes'

In the previous Section we showed how the wake of a single fountain cloud develops and evolves with time. However, the halo of the Milky Way is supposed to be populated by thousands of these objects (Section 2.5.3), so we need a global 3D model to determine how the warm-hot gas of the fountain cloud wakes distributes in the sky. We take the axi-symmetric model built in Chapter 3 to reproduce the cold (H I) phase of the halo and we include the warm and the hot phases as follows.

We associate to each 'cold particle' that is ejected from the disc a 'warm-hot particle' that follows the orbit of the former. The cold particles represent the H I phase of the system cloud+wake, whose time evolution is already fixed in the model by the fit to the LAB H I Survey (Chapter 3). The mass and the velocity of the warm-hot particles are instead set accordingly to the trends shown in Fig. 5.3. Specifically, we focus on the mass ratio between the warm (or hot) and the cold gas, and on the velocity gap between them. We fit the first with a power law and the second with a linear function. We exclude from the fit all the points at $t < 25$ Myr, because the simulations begin with an unrealistic spherical cloud, as discussed in Section 3.5.1. In the dynamical model, at each timestep we set the masses of the warm-hot particles by multiplying the mass of the cold particle - which is known - by the mass ratio derived above, while the kinematics is obtained by subtracting the velocity gap from the velocity of the cold particle.

The dynamical model has a number of stochastic variables, like the ejection angles and velocities of the particles, which can produce fluctuations in the final synthetic datacube. To reduce their impact, we build an average synthetic datacube for the warm (and the hot) gas by combining the cubes resulting from 15 different runs. We apply a gaussian smoothing in the velocity direction to the average cube accordingly to the one-dimensional velocity dispersion associated to the warm and hot components (see Section 5.2.1). Finally, a spatial smoothing of 5° is applied in order to wash out the clumpyness due to the discrete nature of our model. The resulting synthetic datacube - or, simply, the 'modelcube' - contains the mass of the warm (or hot) gas as a function of sky position and line-of-sight velocity in the local standard of rest. We indicate with $I(l, b, v)$ the column density of the warm/hot gas

per velocity unit at the position (l, b) (typical units in $\mathrm{M}_\odot\,\mathrm{pc}^{-2}/\,\mathrm{km\,s}^{-1}$). We stress that this modelcube is not derived by fitting our model to the effective distribution of warm-hot gas in the Milky Way's halo, but it fully relies on our physical understanding of both the fountain dynamics and the disc-corona interaction. The only fit involved in the process is that of the parameters of the galactic fountain, which has been performed in Chapter 3 using the LAB H I Survey.

5.2.3 Comparison with the data

The absorption data analysed here are taken from the works of Lehner et al. (2012, warm absorbers with $|v_{\rm LOS}| > 90\,\mathrm{km\,s}^{-1}$), Sembach et al. (2003, O VI absorbers with $|v_{\rm LOS}| > 90\,\mathrm{km\,s}^{-1}$) and Savage et al. (2003, O VI absorbers with $|v_{\rm LOS}| < 90\,\mathrm{km\,s}^{-1}$). Each dataset is a list of observed lines of sight in the direction of several AGNs/QSOs and, in a few cases, halo stars. For each of them, if one or more absorptions are detected, the local standard-of-rest velocity centroids of each absorption line is reported. The O VI data contain also information on the line-width and on the O VI column density of the detections, or an upper limit to the column density in the case of non-detections. An all-sky velocity map of the O VI detections found by Sembach et al. (2003) is shown in Fig. 1.4. All together, 84 warm detections and 175 O VI detections are present in the datasets analysed. Using the approach that is discussed in Section 5.4.4 we identify 12 warm detections and 16 O VI detections that are likely to be related to the ionised gas surrounding the Magellanic Clouds/Stream (Bland-Hawthorn et al. 2007). These absorptions are not considered in our analysis, thus the effective number of detections decreases to 72 for the warm component and 159 for the O VI one. The inclusion of these features does not change our results significantly.

In order to compare our model with the data we must realise that the former represents an average, smooth, and axi-symmetric realization of the warm-hot gas distribution resulting from the fountain mechanism. This is because the number of particles that are ejected in our model is much larger than the number of clouds that effectively populate the Galactic halo. Hence, we can not compare our model with the details of the single detection, which depend on the chance of intercepting the wake of a specific fountain cloud. Instead, we adopt the following statistical approach. In our model, the intensity of the generic pixel $I(l, b, v)$ is proportional to the probability of finding an absorption at the position (l, b) in the sky and line-of-sight velocity v. We define the quantity

$$f(I_i) = \frac{F(I_i)}{F(0)} \tag{5.2}$$

where

$$F(I_i) = \Delta l\,\Delta b\,\Delta v \sum_{l,b,v} I(>I_i)(l, b, v)\cos(b)\,. \tag{5.3}$$

In the equation above, Δl, Δb and Δv are the pixel separations in the three directions, the factor $\cos(b)$ stands for the projection effects and the sum is extended to all the pixels with intensity larger than I_i. Note that since $F(0)$ is the total flux of the modelcube, we have $0 \leq f \leq 1$. Hence a fraction $f(I_i)$ of the total flux is contained in pixels with $I > I_i$. Using eq. (5.2) we define three confidence levels I_1, I_2 and I_3 as follows:

$$f(I_i) = \begin{cases} 0.6827 & \text{if } i = 1 \\ 0.9545 & \text{if } i = 2 \\ 0.9973 & \text{if } i = 3 \end{cases}$$

The meaning of these values is straightforward: if an absorption detected in (l, b, v) falls inside the first contour level (i.e. $I(l, b, v) > I_1$), then the model reproduces that detection with 1σ level of confidence (by analogy with a Gaussian statistics). If it falls inside the second one ($I_2 < I(l, b, v) < I_1$), the level of confidence is 2σ and so on.

We use these confidence levels to compare our models with the data in two ways. On the one hand, we show the confidence levels in a series of longitude-velocity (l–v) diagrams at different latitudes to visualise the probability of finding an absorption as a function of the position in the sky and the line-of-sight velocity. We overlay the detections on these diagrams to give a visual comparison between the two. On the other hand, we perform a statistical comparison between the predicted and the observed distribution of the absorptions in the (l, b, v) space. We interpret the discrepancy between the two distributions with the presence of a *different* population of absorbers, i.e. not produced by the fountain-cloud–corona interaction, that contaminates the data. We implement an algorithm based on the Kolmogorov-Smirnov (KS) test to determine the fraction of detections that must be discarded in order to have the two distributions consistent with each other. The algorithm is described in the next Section.

We point out that, with the method described, we can not predict the absolute probability that an absorption occurs at a given (l, b, v). Instead, our model gives the relative probability of an absorption to occur at a specific location (l, b, v) rather than a different one. Specifically, we discriminate the regions in the (l, b, v)-space where the warm-hot gas is present in a significant amount from those depleted of it, and we compare how the observed detections and the modelled warm-hot gas are distributed in that space (Section 5.3). In Section 5.3.2 we show that the density of hot gas predicted by our model in the regions where absorptions are observed is remarkably consistent with the measured column density of the absorbers.

5.2.4 Iterative KS algorithm

Given a modelcube of warm/hot gas and a list of n warm/O VI absorption features, we compute the fraction of detections that is consistent with the model using the following iterative procedure:

1. we evaluate the fraction and the cumulative fraction of detections observed and predicted as a function of the confidence level described in Section 5.2.3;

2. we use the numerical code of Marsaglia et al. (2003) to compute the KS critical value $K(n, d)$, where d is the largest absolute distance between the two cumulative fractions;

3. if $K(n, d) > 0.95$, i.e. if the model is rejected with a probability larger than 95%, we remove from the data a single detection. We choose it randomly within the confidence level with the largest (positive) difference between the fraction of detections observed and predicted.

This procedure is iterated until the probability of rejection drops below 95%. We consider the remaining detections consistent with the model. We evaluate an error bar on the fraction of detection to discard by considering different thresholds for the KS critical value: the lower limit is chosen at $K(n, d) = 0.99$, the upper limit at $K(n, d) = 0.90$. Note that in the calculation of the predicted fractions, only the observed lines of sight must be considered. This approach is mandatory because the background sources are not isotropically distributed in the sky (see Fig. 5.8), thus the ensemble of detections is not representative of the all-sky population of the absorbers.

5.3 Results

Fig. 5.4 shows different longitude-velocity diagrams for our model of galactic fountain wakes. Each panel represents a given latitude bin. Contour levels are derived with the approach described in Section 5.2.3, and both the warm and the O VI detections are overlayed on the diagrams. Detections that we consider related to the Magellanic system are represented by empty circles (see Section 5.4.4). The velocity range $|v_{\rm LSR}| < 90\,{\rm km\,s^{-1}}$ is excluded from the observations of Lehner et al. (2012), so the probability of finding a warm absorption at these velocities is set to zero by blanking all the pixels with $|v_{\rm LSR}| < 90\,{\rm km\,s^{-1}}$ in the modelcube of warm gas. Also, in both the modelcubes we blanked the pixels at $|b| < 20^\circ$ because these latitudes are systematically excluded from the observations in order to avoid overlapping with the Galactic disc. Globally, the warm absorptions concentrate at velocities $|v_{\rm LSR}| < 200\,{\rm km\,s^{-1}}$ while the O VI detections are much more spread over the whole velocity range. This is consistent with our models, which predict a larger velocity dispersion for the hot gas in the fountain wakes (Fig. 5.3). We have seen that this dispersion is almost completely due to turbulence (Section 5.2.1), which in turn depends on the physical mechanism of production, i.e. the fountain-cloud–corona interaction. Fig. 5.4 shows that most detections are inside 3σ level of confidence, especially in the case of the warm component, but the majority is not within 1σ. Our model predicts that most

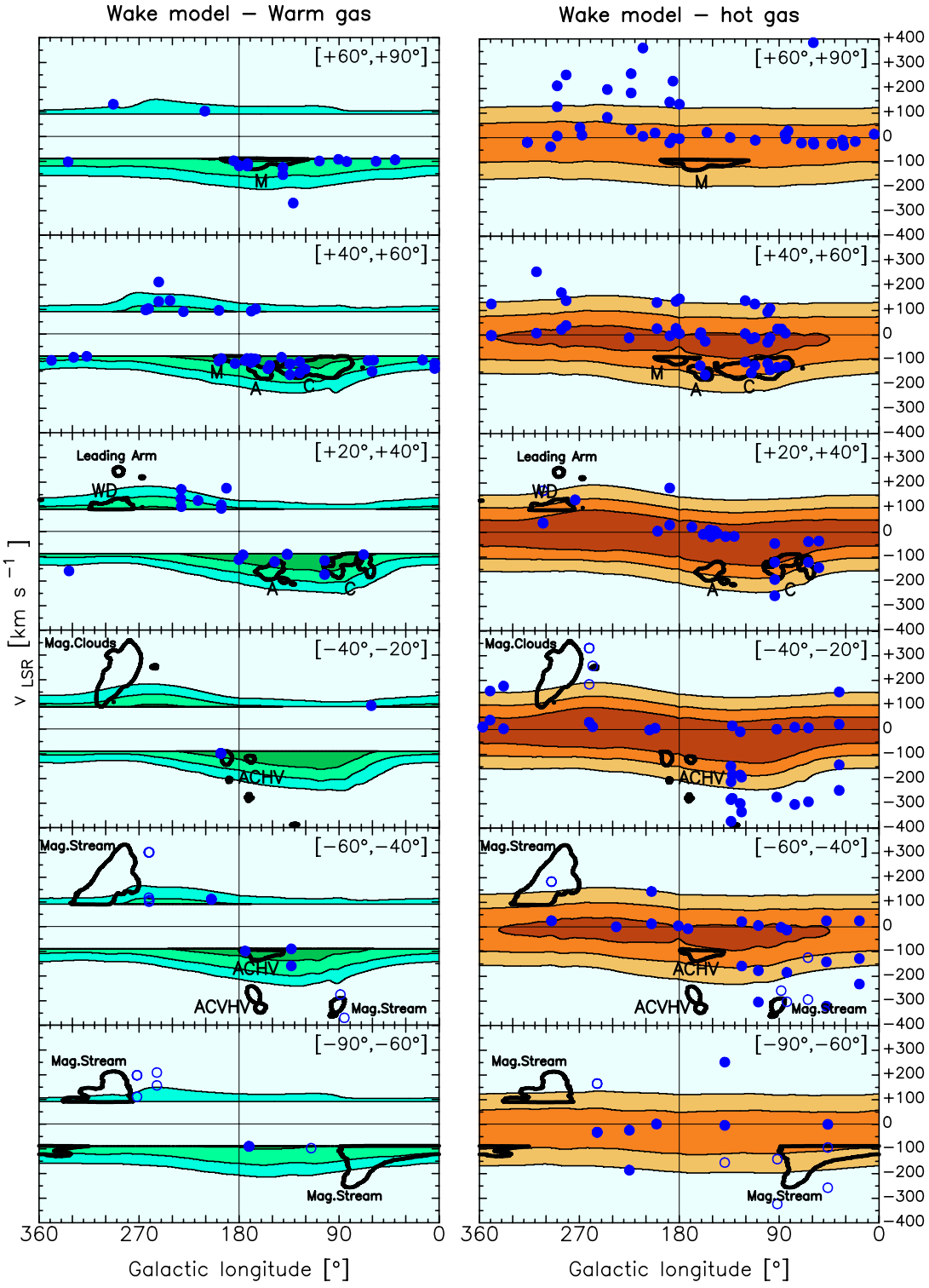

Figure 5.4: Longitude-velocity diagrams in 6 different latitude bins (indicated at the top right corner of each panel) showing the confidence contours of our model of fountain wakes. *Left panels:* warm phase of the fountain wakes. Circles represent warm detections from Lehner et al. (2012). *Right panels:* hot phase of the fountain wakes. Circles represent O VI detections from Sembach et al. (2003) and Savage et al. (2003). Empty circles represent detections considered related to the Magellanic Clouds/Stream. Contour levels are from the innermost to the outermost at 1σ, 2σ and 3σ (see Section 5.2.3). The H I emission of the classical HVCs is reported in the various panels in thick contours, labelled with the name of the respective complexes.

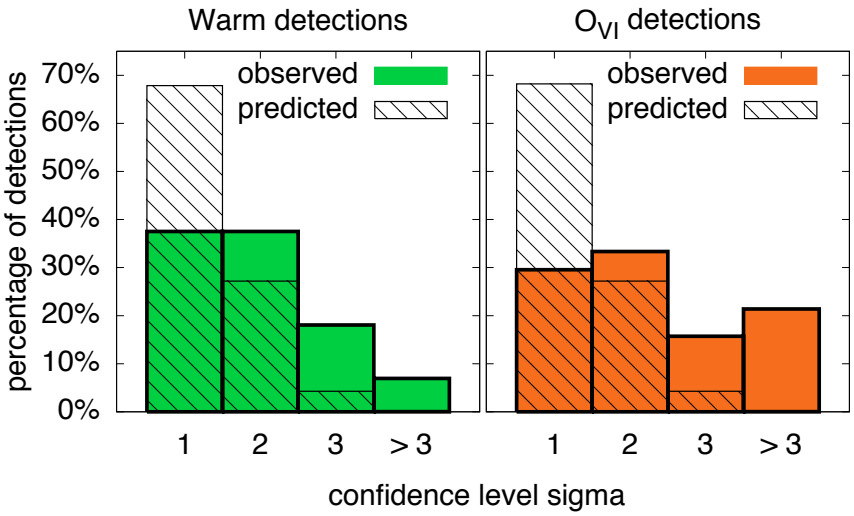

Figure 5.5: Comparison between the fractions of detections observed (*filled histograms*) and predicted (*hatched histograms*) within a given confidence level by our model of fountain wakes. Warm absorptions are shown in the left panel, O VI in the right panel.

of the warm-hot gas is produced in the descending part of the fountain orbits because of the increase in mass that the particles experience in time (Fig. 5.3), which implies that they are more massive when they are falling back to the disc. Since these massive infalling particles have $v_{\rm LOS} < 0$ by definition, the confidence contours are systematically shifted towards negative velocities. Consistently, detections occur more frequently at negative than positive velocities. However, note that the warm data at $+40^\circ \leq b \leq +60^\circ$ and the O VI data at $+60^\circ \leq b \leq +90^\circ$ show an overabundance of detections at positive velocities with respect to the prediction of our model. We discuss this point in Sections 5.3.1 and 5.4.4. In Fig. 5.4 we also show the H I emission of several classical High-Velocity complexes, which have been derived from the LAB Survey smoothed at 5° of resolution. Several warm and hot detections at negative velocities overlap with the H I emission of the complexes A, C and M (see also Fig. 5.8). The relation between the absorption features, the HVCs and the gas in the wakes of the fountain clouds is discussed in Section 5.4.3.

Fig. 5.5 compares the fractions of absorptions detected within a given confidence level (filled histogram) with those predicted by our model of fountain wakes (hatched histogram). The latter follows by definition a Gaussian distribution (see Section 5.2.3) and are obtained by considering only the observed lines of sight. We use the algorithm described in Section 5.2.4 to derive the fraction of detections that our model of fountain wakes reproduces, obtaining $73.5^{+4.8}_{-2.2}\%$ for the warm case and $54.2^{+2.6}_{-1.3}\%$ for the O VI case. Thus, even if most of the detections are consistent with our scheme, there is a significant fraction that is not in agreement. We discuss this further in Sections 5.3.1 and 5.4.4.

5.3.1 Fountain wakes + outflows

The standard picture of the galactic fountain states that the gas escaping from superbubble blowouts is ionised and it remains undetected in H I until it cools and recombines. This scenario is supported also by direct observations. A well-known case is that of the Ophiucus superbubble in the inner Galaxy, which shows large quantities of ionised gas visible in Hα (Pidopryhora et al. 2007). This outflowing ionised gas may largely contribute to the low and high-ion absorptions, thus it is important to include it in our model.

Since large uncertainties are present in the physics of the gas escaping from a superbubble, a rigorous treatment of this component is extremely difficult and it would be beyond the purposes of this work. Instead, we adopt a simple approach, based on the results found for the neutral gas. In Chapter 3 we have investigated what fraction of the fountain orbits must remain 'invisible' in order to reproduce the H I emission of the Galactic halo. We found that recombination should occur when gravity reduces the vertical speed of the ejected cloud by $\sim 30\%$ (Table 3.1), i.e. at about one-third of the ascending part of the orbit. Before that time, the gas is ionised and therefore it is not visible in H I. Here we assume that this ionised outflowing material, starting from the moment of the ejection and until the recombination, is in a *warm* phase and therefore it can be included in our modelcube of warm fountain gas. We have already mentioned (Section 5.2.1) that photoionisation from the disc can play an important role in shaping the distribution of the warm absorber material (see also Shull et al. 2009). Including the ionised outflowing component of the galactic fountain corresponds to consider the effect of the photoionisation in a region of few hundred parsecs above the Galactic disc.

In order to model the position-velocity distribution of these outflows, we use the best-fit model of Chapter 3 and consider only the first third of the ascending part of the fountain orbits. Also in this case, the modelcube related to this material is obtained by averaging 15 different runs and is smoothed to 5° of resolution. A critical ingredient to include in the model is the amount of velocity dispersion of the outflowing material, which depends on the turbulence of the gas escaping from the disc. For simplicity we set this value to $31\,\mathrm{km\,s^{-1}}$, the value derived for the warm material of the fountain wakes in the simulation analysed (Section 5.2.1). The resulting modelcube is then summed pixel by pixel to that obtained for the warm particles and is compared with the warm detections of Lehner et al. (2012) using the method described in Section 5.2.3.

Fig. 5.6 shows different longitude-velocity diagrams in 6 latitude bins for our models of fountain wakes (on the left), fountain outflows (in the middle) and fountain wakes+outflows (on the right) for the warm component. As expected, in the model of fountain outflows the gas occupies preferentially the positive velocities, where a consistent fraction of detections takes place. However, outflows alone can not explain the whole set of detections. The last model, obtained by combining the

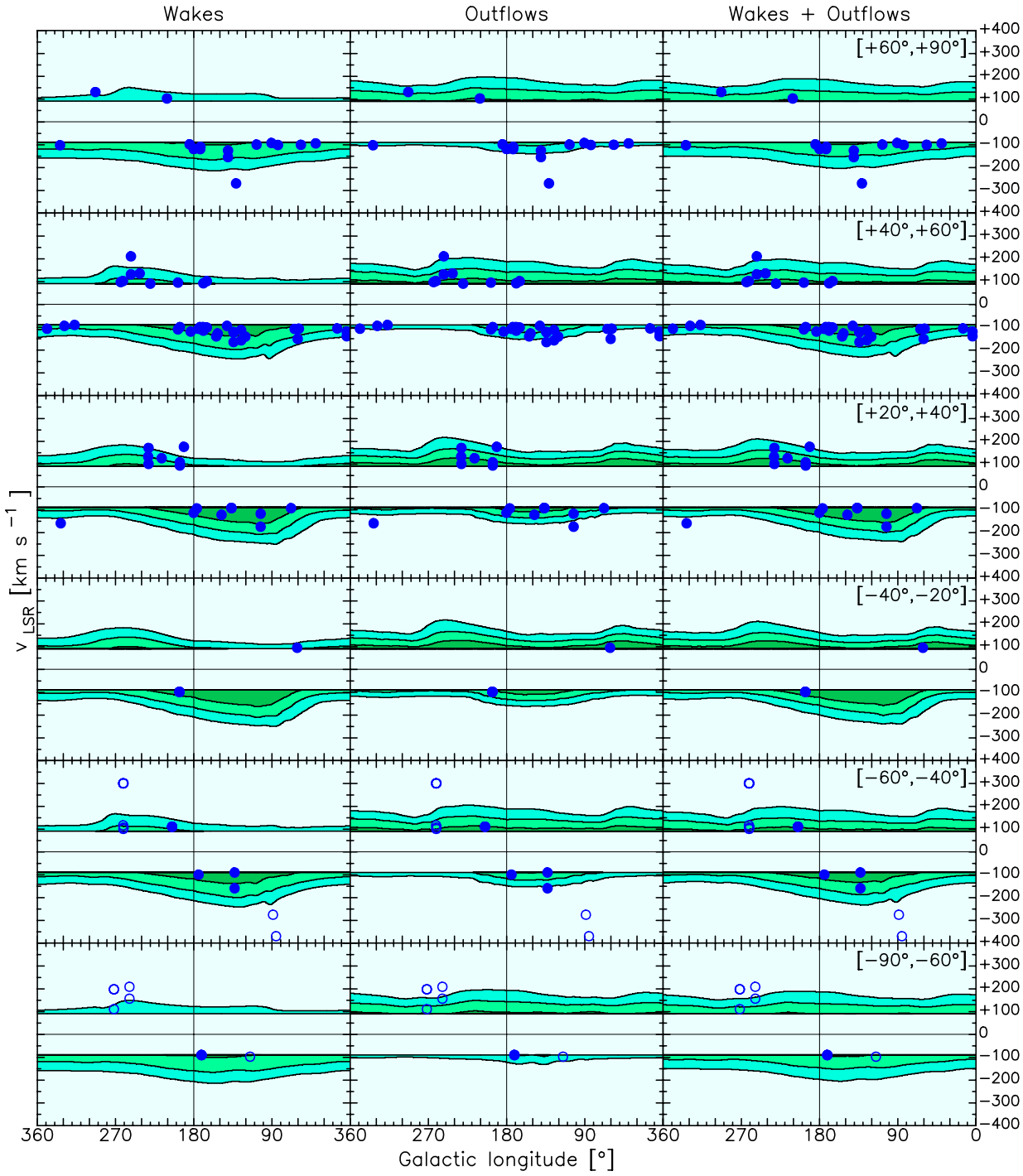

Figure 5.6: Longitude-velocity diagram in 6 different latitude bins (indicated at the top-right corner of the rightmost panels) for the warm gas component of our model of fountain wakes (*left panel*), fountain outflows (*middle panel*) and fountain wakes+outflows (*right panel*). The points represent the warm detections from Lehner et al. (2012). Empty circles indicate detections considered related to the Magellanic Clouds/Stream. Contour levels are from the innermost to the outermost at 1, 2 and 3σ (see Section 5.2.3).

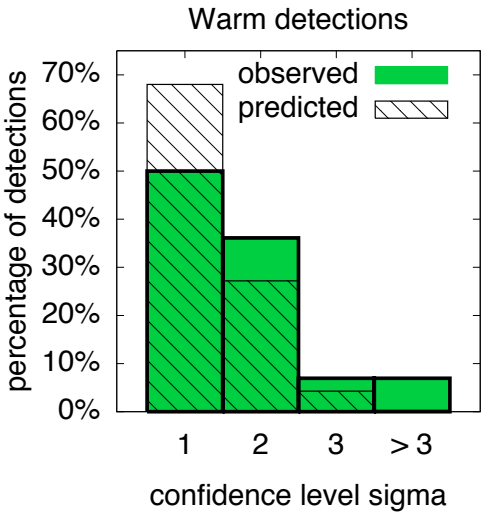

Figure 5.7: As in Fig. 5.5, but for a model of fountain wakes that include outflowing ionised gas. The comparison is with the warm detections from Lehner et al. (2012)

.

first two, provides a much better description of the space-velocity distribution of the warm dataset, as several detections at $v_{\rm LOS} > 0$ are now located in a higher confidence level with respect to the model without outflows. Fig. 5.7 compares the fractions of warm absorptions detected within a given confidence level with those predicted by our model of fountain wakes + outflows. The fraction of detections reproduced by the latter, inferred with our KS-based algorithm, is $94.4^{+5.6}_{-2.5}\%$. This fraction is significantly larger than that estimated for a model of fountain wakes alone ($73.5^{+4.8}_{-2.2}\%$, see Section 5.3), indicating that supernova-driven outflows from the disc play a significant role in populating the Galactic halo with ionised gas.

Fig. 5.8 offers an alternative way to compare this model with the data, giving an all-sky view of the velocity field predicted by our model compared to the velocity centroids (points) of the absorption lines detected by Lehner et al. (2012). Where there are multiple detections along a single line of sight, we have plotted the average velocity. The panel on top shows the median velocity field predicted, while in the bottom panel velocities are extracted randomly in cells of $2.5^\circ \times 2.5^\circ$ to give a measure of the turbulent motions in the wakes. In both cases, we excluded warm gas at velocities $|v_{\rm LOS}| < 90\,{\rm km\,s^{-1}}$, as was done in the observations. The detections are not distributed isotropically in the sky: the targeted background sources are located mostly at positive latitudes, and no targets are present for $|b| < 15^\circ$. Globally, the median velocity field predicts the correct dichotomy between detections at positive and negative velocities, indicating that the absorbing material is consistent with being part of a slowly rotating medium similar to that produced by the interaction between the galactic fountain and the corona. However, the data show large fluctuations around the predicted median value. The random velocity field (bottom panel) shows that fluctuations of similar amplitude are present also in our model. They

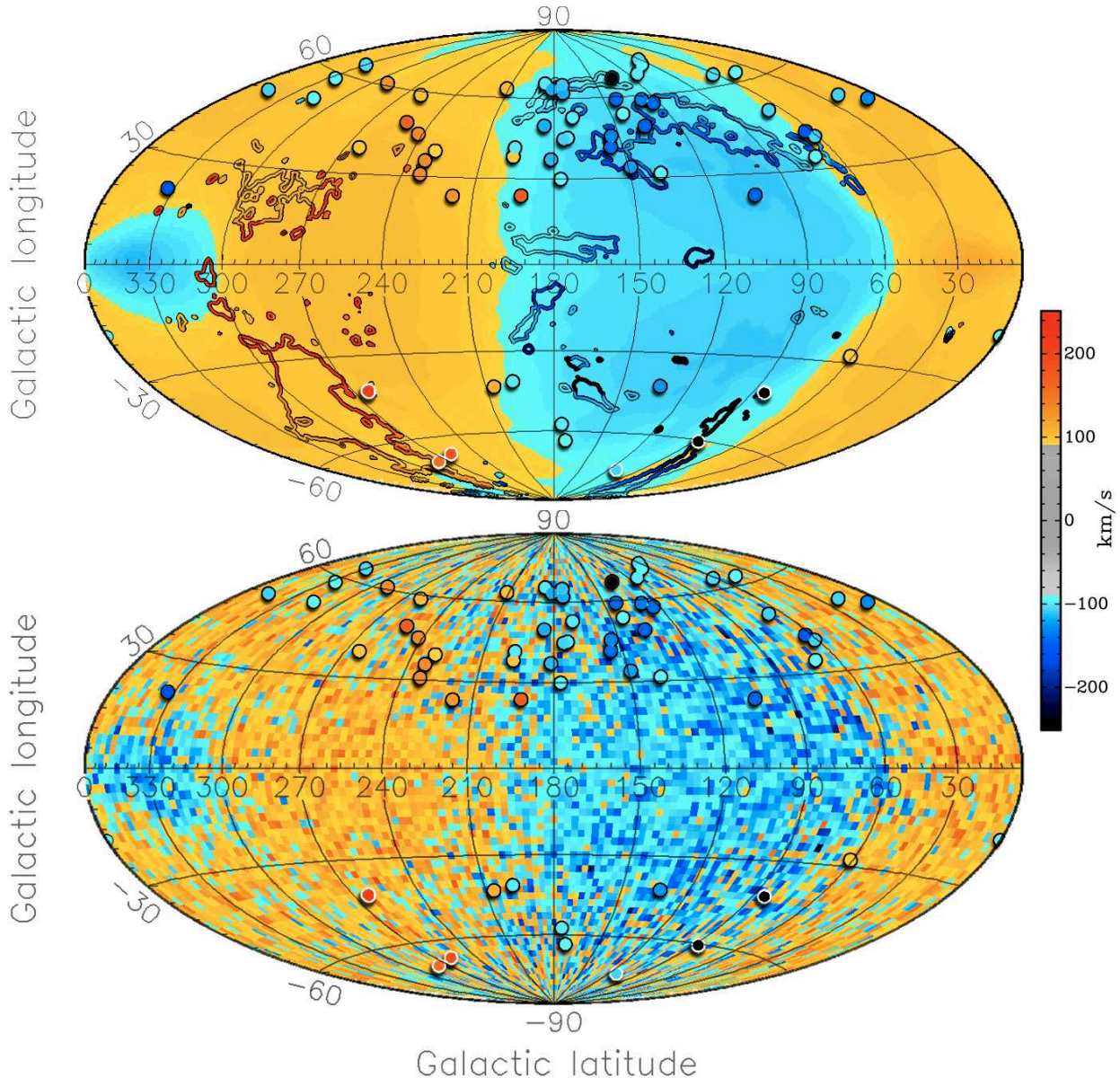

Figure 5.8: All-sky velocity maps comparing the absorption features detected by Lehner et al. (2012) (circles) with the prediction of our model of fountain wakes that include outflowing ionised gas (background color). Multiple detections along the same line of sight are averaged in velocity so the number of points (65) in these panels does not correspond to the total number of detections (84). Circles with white borders represent absorptions that we consider to be associated with the Magellanic Clouds/Stream. The top panel shows the median velocity field, while the bottom panel shows velocities extracted randomly from our model in cells of 2.5° × 2.5°. The contours in the top panel show the H I emission from the classical HVCs and the Magellanic Stream, color-coded accordingly to their mean line-of-sight velocities.

are caused by the large velocity dispersion ($\sigma \simeq 30\,\mathrm{km\,s^{-1}}$) of the warm material in the turbulent wakes of the fountain clouds.

5.3.2 Column density comparison

The amount of warm and hot gas present in the Galactic halo as a function of position and velocity is one of the most important predictions of our model. It is crucial to compare this prediction with the column densities observed for the warm and hot detections.

We first focus on the hot component, which we compare with the O VI column density measurements of Sembach et al. (2003) and Savage et al. (2003). In the case of a O VI detection at the position (l, b), with mean velocity v and line-width b_w, the O VI column density predicted by our model can be evaluated as

$$N_{\mathrm{O\,VI}} = \int_{v-2\sigma_w}^{v+2\sigma_w} \frac{n_{\mathrm{O}}}{n_{\mathrm{H}}}(Z)\, \frac{n_{\mathrm{O\,VI}}}{n_{\mathrm{O}}}(T)\, I(l, b, v)\, dv \tag{5.4}$$

where $\sigma_w = b_w/\sqrt{2}$ (Sembach et al. 2003), $\frac{n_{\mathrm{O}}}{n_{\mathrm{H}}}$ is the oxygen abundance, that depends on the metallicity Z as follows:

$$\log\left(\frac{n_{\mathrm{O}}}{n_{\mathrm{H}}}\right)(Z) = \log\left(\frac{n_{\mathrm{O}}}{n_{\mathrm{H}}}\right)_{\odot} + \log\left(\frac{Z}{Z_{\odot}}\right) \tag{5.5}$$

and $\frac{n_{\mathrm{O\,VI}}}{n_{\mathrm{O}}}$ is the O VI ion fraction, that for $\log(T) = 5.45$ is 0.22 if one assumes CIE (Sutherland & Dopita 1993). In eq. (5.5) we assume a constant value for $\log(Z/Z_{\odot})$ of -0.35 obtained as the mass-weighted metallicity of the hot gas in the simulations, while we fix $\log(n_{\mathrm{O}}/n_{\mathrm{H}})_{\odot}$ at -3.07 accordingly to Anders and Grevesse (1989). Note that we are assuming implicitly that the abundance ratio between different metals is solar-like. In the case of non-detections, we still use eq. (5.4) to give an upper limit to the O VI column density. In this case, the integral is extended to the velocity range $|v_{\mathrm{LOS}}| < 50\,\mathrm{km\,s^{-1}}$, consistently with the method used by Sembach et al. (2003) and Savage et al. (2003) to infer upper limits from the non-detections. This maximises the column density predicted, since in our model most of the gas occupies that range of velocities as shown in Fig. 5.4.

Fig. 5.9 compares the observed and the predicted O VI column densities for all those detections that are located inside the 3σ contour level of our all-sky model shown in Fig. 5.4. The absence of points in the leftmost part of the plot is due to the O VI detection limit, which is a few times $10^{13}\,\mathrm{cm^{-2}}$(Sembach et al. 2003). Error bars for the predicted column densities are derived by considering an average error of $\pm 5\,\mathrm{km\,s^{-1}}$ on the line-width b_w, while for the observed ones we assume a constant error of 0.13 dex. Both these errors are set accordingly to Sembach et al. (2003) and Savage et al. (2003). We point out that the error on the predicted column density is likely underestimated, since the integration limits in eq. (5.4) are fixed arbitrarily by analogy with a gaussian profile. For most detections the column densities predicted

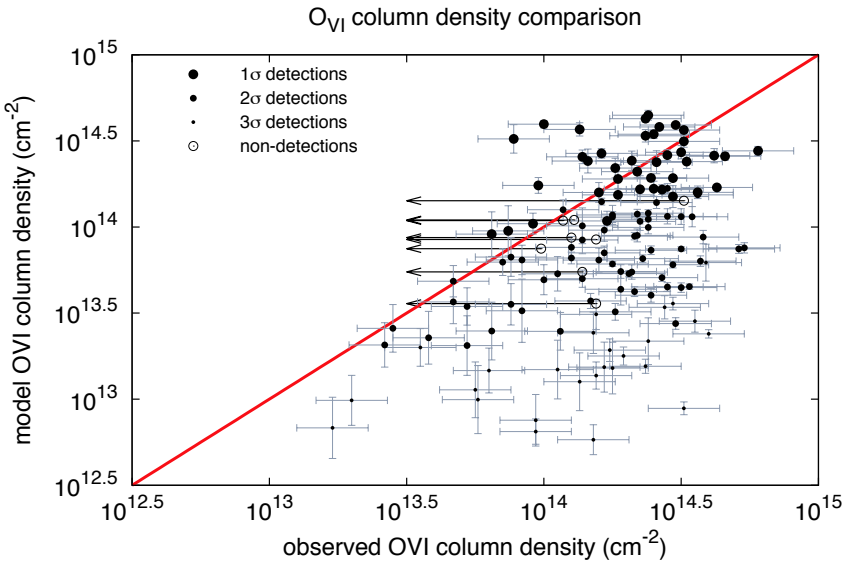

Figure 5.9: Comparison between the O VI column densities observed (x-axis) and those predicted by our model of fountain wakes (y-axis) for all those detections located inside the 3σ contour level shown in Fig. 5.4. Filled circles represent detections, different sizes are used to indicate different confidence levels. Empty circles represent non-detections. The straight line represents the function $y = x$.

are consistent with the observed ones within an order of magnitude, indicating that our model predicts the correct amount of hot gas in the Galactic halo. Interestingly, the O VI detections predicted with a higher confidence level (larger points in Fig. 5.9) are also those whose column densities are better reproduced by our model. This is a remarkable result, since detections are classified within a given confidence level only accordingly to their kinematics (see Section 5.2.3).

Considering together the datasets of Sembach et al. (2003) and Savage et al. (2003), the number of lines of sight where no O VI absorption is detected is small. Only 8 non-detections are found, with the respective upper limits on the column density. It is interesting that for all the non-detections our model predicts column densities smaller than those inferred by the upper limits (empty circles in Fig. 5.9). Note also that non-detection does not necessarily imply a lack of gas along a given line of sight. In fact, the warm-hot material in the turbulent wake of a fountain cloud is clumpy (see Fig. 5.2), and there is a chance that a pencil-beamed observation passes through different wakes without intercepting any of the cloudlets. This is possible given that the number of wakes intercepted by a generic line of sight is not too large (see Section 5.3.3).

Column density measurements for single warm detections are not reported in Lehner et al. (2012), so we consider the Si III average column density $\langle \log N_{\rm Si\,III} \rangle = 13.42 \pm 0.21$ obtained by Shull et al. (2009) as a representative case. The value predicted by our model can be derived using the same approach adopted for the O VI component. We consider the model of fountain wakes + outflows described in Section

5.3.1 and we assume $\frac{n_{\rm Si\,III}}{n_{\rm Si}} = 0.903$ (Sutherland and Dopita 1993, for $\log(T) = 4.45$), $\log[Z/Z_\odot] = -0.24$ (from the M11 simulation) and $\log(n_{\rm Si}/n_{\rm H})_\odot = -4.45$ (Anders and Grevesse 1989). The integral in eq. (5.4) is extended to $70\,{\rm km\,s^{-1}}$ around the velocity centroid of the line, consistently with the average line broadening found by Shull et al. (2009). The predicted Si III column density averaged over all the absorbers is $\langle \log N_{\rm Si\,III} \rangle = 13.44 \pm 0.36$, in remarkable agreement with the observed value.

We stress again that these column densities are not derived by fitting our model to the O VI or to the warm data, but they are instead fully determined by the fit to the H I data performed in Chapter 3 and by the physical connection between the H I phase and the warm-hot phase via the fountain-corona interaction. Thus, this comparison strongly reinforces the validity of our scheme for the origin of the absorbers.

5.3.3 The number of wakes per line of sight

A further test of the validity of our model comes from the number of warm and O VI absorptions observed for a given line of sight, which ranges from 0 (non-detections) up to 4 (some O VI detections shown in Fig. 5.4). If we average the number of O VI detections combining the data of Sembach et al. (2003) and Savage et al. (2003), we find a value of 1.6 detections per line of sight. For the warm absorptions, the data of Lehner et al. (2012) give 0.7 detections per line of sight, but this value is likely underestimated because the velocity range $|v_{\rm LOS}| < 90\,{\rm km\,s^{-1}}$ is excluded by the observations. To investigate whether these numbers are consistent with the considered scenario of fountain wakes, we proceed as follows.

Since the total gas mass of the Galactic halo is $\sim 3 \times 10^8\,{\rm M_\odot}$ (Table 3.1) and the H I mass of the clouds in the standard simulations of M11 is $2.4 \times 10^4\,{\rm M_\odot}$ (consistent with the typical H I mass of an IVC, e.g. van Woerden et al. 2004), we expect that the number of fountain clouds in the halo of the Milky Way is about 10^4. We consider the axi-symmetric H I density distribution $n_{\rm HI}(R,z)$ shown in Fig. 3.11, and we fit it with a formula similar to that used in Section 2.2.2 for our kinematic models of H I halo:

$$n_{\rm HI}(R,z) \propto \left(1 + \frac{R}{R_g}\right)^{\gamma} \exp\left(-\frac{R}{R_g}\right) \exp\left(-\frac{z}{h_g(R)}\right) \tag{5.6}$$

where

$$h_g(R) = h_0 + \left(\frac{R}{h_R}\right)^{\delta} \quad , \delta \geq 0. \tag{5.7}$$

The fit gives $R_g = 1.08\,{\rm kpc}$, $h_0 = 175\,{\rm pc}$, $h_R = 10.01\,{\rm kpc}$, $\gamma = 6.30$ and $\delta = 1.89$. Then, we consider a three-dimensional cartesian space (x, y, z), where the plane (x, y) represents the Galactic midplane and the axis z is the rotation axis of the Milky Way. In this space, we randomly generate 10^4 particles with space-density distribution set accordingly to eq. (5.6). Each particle represents both the warm

and the hot phase of a cloud's wake. In Section 5.4.2 we show that the relative velocity between the clouds and the corona $v_{\rm rel}$ can increase up to $100\,{\rm km\,s^{-1}}$ during the initial and the final part of the orbits. Since $v_{\rm rel}$ largely affects the size of the wake left behind the cloud's path, we evaluate the volume occupied by the warm and the hot gas by analyzing both simulations at $v_{\rm rel}=75\,{\rm km\,s^{-1}}$, shown in Fig. 5.2, and $v_{\rm rel}=100\,{\rm km\,s^{-1}}$. Typical volumes are calculated on the snapshot at $t=60\,{\rm Myr}$ by assuming a cylindrical symmetry along the major axis of the wake. For $v_{\rm rel}=75\,{\rm km\,s^{-1}}$, we find $3.8\times10^6\,{\rm pc^3}$ and $7.8\times10^6\,{\rm pc^3}$ for the warm and the hot component respectively. By increasing the velocity to $100\,{\rm km\,s^{-1}}$, the volume occupied by the warm (the hot) material increases by a factor 2.5 (9.5), which implies that the angular filling-factor grows by a factor 1.8 (4.5). Finally, we consider an observer at coordinates $(x=0, y=8.3\,{\rm kpc})$ scanning a large number of lines-of-sight in the simulated sky at $0^\circ\leq l<360^\circ$ and $20^\circ\leq|b|\leq80^\circ$, consistently with the region where real absorptions are observed, and we count the number of warm and hot particles intercepted by each line of sight.

We find that the average number of particles intercepted ranges from 0.5 to 1 particles per line of sight for the warm wakes, and from 0.8 to 4.0 per line of sight for the hot wakes, depending on the sizes considered and on the different stochastic realizations of the particle distribution. Despite the uncertainties, these values are fully consistent with the average numbers of warm and hot absorptions per line of sight found in the data.

5.4 Discussion

5.4.1 Limitations of the model

We have already pointed out that our model fully relies on the modelling of the Galactic H I halo made in Chapter 3 and on the simulations of cloud-corona interaction of M11. Both these works have their limitations, which in turn can affect the results presented in this Chapter.

Our dynamical model is symmetric with respect to both the rotation axis and the midplane, thus all the features related to asymmetries in the H I distribution or to specific H I clouds are not taken into account. Also, the parameters of the model (i.e. the mean kick velocities of the particles, the ionisation fraction and the coronal accretion rate) are kept constant in space. This implies that the model can account only for the global properties of the Galactic H I halo. The same is true for the warm-hot gas of our model of fountain wakes: non axisymmetries (e.g. spiral arms, Struck and Smith 2009) or isolated HVCs can not be reproduced (but see Section 5.4.3).

The main limitations of the M11's simulations are three: a) they are 2D; b) they

are evolved up to 60 Myr; c) gravity is not considered. Turbulence, which is an important ingredient for our models, can change significantly when passing from 2D to 3D. By increasing the amount of turbulence, the number of absorption features reproduced by our model increases accordingly. Also, the average orbital time for a particle in our dynamical model is ~ 80 Myr, while the cloud-corona interaction in the simulations is followed only for 60 Myr. Beyond that time, masses and velocities for the warm-hot particles are extrapolated from the simulation (see Section 5.2.1). Large deviations from this extrapolated behavior could produce differences in our modelcubes of warm-hot gas. Finally, the absence of gravity in the simulations implies that we must rely on our dynamical model to infer the orbits of the warm-hot gas in the wakes. However, it is possible that such material does not follow exactly the same orbit of the cold gas, or that the velocity gap between the different phases is larger than that determined in Section 5.2.1. This latter effect, if present, would produce a less rotating warm-hot medium that could help to reproduce some of the highest-velocity absorption features.

A further source of uncertainties is given by the initial conditions of the simulations: they start considering a spherical cloud of cold gas, while the gas ejected by a supershell/bubble would be already fragmented and (partially) ionised from the beginning (see Melioli et al. 2008). A way to solve this discrepancy is to include in the model the ionised outflowing part of the fountain clouds, as we did in Section 5.3.1. The warm particles escaping from the disc during the first $15-20$ Myr of the orbit, together with those associated with the fountain cloud wakes, provide a better description of the warm absorption dataset. All these uncertainties considered, it is remarkable that a simple, axi-symmetric model built specifically to fit the H I data reproduces both the kinematics and the column densities of such a large fraction of warm and hot absorption features in the halo of the Milky Way.

5.4.2 The effect of the cloud-corona relative motion

The outcome of the M11 simulations depends on the relative velocity $v_{\rm rel}$ between the cloud and the corona, which M11 found to spin with a given velocity lag with respect to the cold material. In our analysis we have fixed $v_{\rm rel}$ to $75\,{\rm km\,s^{-1}}$, which is a representative value of the lag in the azimuthal direction between the two media (see Section 3.2.3). However, because of the presence of non-circular (vertical+radial) motions during the beginning and the final part of the cloud's orbit, $v_{\rm rel}$ varies with time as:

$$v_{\rm rel}(t) = \sqrt{v_z^2(t) + \Delta v_\phi^2 + v_R^2(t)} \tag{5.8}$$

where $\Delta v_\phi = 75\,{\rm km\,s^{-1}}$ is the azimuthal lag, while v_z and v_R are respectively the vertical (i.e. perpendicular to the disc) and the radial (i.e. perpendicular to the rotation axis) component of the cloud's velocity. Since, on average, clouds are ejected from the disc with a vertical speed of $70\,{\rm km\,s^{-1}}$ (Table 3.1), v_z and v_R are not neg-

ligible during the initial and the final part of the orbits and $v_{\rm rel}$ can increase to a maximum value of $\sim 100\,{\rm km\,s^{-1}}$. We tested the impact of this larger speed by considering the extreme case of a constant lag between the clouds and the corona of $100\,{\rm km\,s^{-1}}$. For this purpose, we considered the hydrodynamical simulation of M11 at $v_{\rm rel} = 100\,{\rm km\,s^{-1}}$ and we repeated the analysis previously done for the case at $v_{\rm rel} = 75\,{\rm km\,s^{-1}}$. We found that the fraction of warm and O VI absorption reproduced by this new model is respectively $85.2^{+5.0}_{-2.4}\%$ (without considering outflows) and $48.0^{+2.5}_{-1.2}\%$, not very different from those found for the case at $v_{\rm rel} = 75\,{\rm km\,s^{-1}}$. This indicates that the change of $v_{\rm rel}$ during the orbit of the fountain clouds does not play a major role in shaping the position-velocity distribution of the warm-hot gas. The impact of a larger $v_{\rm rel}$ is instead particularly significant for the sizes of the fountain cloud wakes, as we discussed in Section 5.3.3.

5.4.3 Relation to the classical HVCs

Even though the low metallicity of the classical HVCs points firmly towards an extragalactic origin, there is no general consensus on how these systems are generated. The position-velocity plots of Fig. 5.4 show a significant overlapping between the HVCs and the gas of our model, thus one may wonder whether these complexes can be physically related to the warm-hot gas present in the fountain-cloud wakes. But can the galactic fountain produce the classical HVCs? In our scheme, a direct connection between the fountain mechanism and these systems seems quite unlikely, because the latter are located at distances above the plane that are hardly reached by the particles ejected from the disc, as already shown in Section 3.4.2. For instance, in order to bring cold particles at line-of-sight velocities, Galactocentric radii and heights consistent with those of the complex C, our model requires ejection velocities $\gtrsim 175\,{\rm km\,s^{-1}}$ occurring at the periphery of the stellar disc. Given that the H I mass of the complex C is $5 \times 10^6\,{\rm M_\odot}$ (Thom et al. 2008), the energy associated to the ejection would be $\gtrsim 3 \times 10^{54}$ erg, corresponding to ~ 30000 simultaneous supernova explosions (considering 10^{51} erg per SN and an efficiency of 10%) which is an extremely unlikely event.

Figs. 5.4 and 5.8 show also that the position-velocity locations of several warm and hot detections overlap with those of the HVCs. Lehner et al. (2012) have argued that all the detected warm absorption features originate in the ionised envelope that surround these complexes (e.g. Sembach et al. 1999). This would place the absorbers at typical distances of $\sim 3 - 9\,{\rm kpc}$ from the Galactic disc (Lehner and Howk 2011), while in our scheme the warm-hot gas is located mostly within a few kpc from the midplane (Section 3.4.2). Information on the metallicity cannot be used to discriminate between the two origins, given that a) the warm gas of our model has metallicities ranging from ~ 0.2 solar to solar; and b) the value that is commonly assumed for the high-velocity gas in the Galaxy ($0.2\,Z_\odot$) has been determined specifically for complex C (e.g. Wakker et al. 1999; Collins et al. 2003;

Tripp et al. 2003), and it is unclear to what extent this is representative of the whole population of absorbers. In the following, we check how our results change if we consider that some absorptions are related to the classical HVCs. We isolated the H I emission of these systems in the LAB datacube, and we excluded all those detections that are separated by less than 10° in the angular direction and by less than $60-100\,\mathrm{km\,s^{-1}}$ in the velocity direction - depending on whether we consider the warm or the O VI detections - from the $2\sigma_{\rm rms}$ contour of the H I datacube. The number of warm and O VI absorptions decreases respectively from 72 to 31 and from 159 to 138. We re-evaluated the fraction of absorptions reproduced by the model (without considering outflows), finding a modest increment to $60.1^{+3.0}_{-1.4}\%$ in the O VI case, while for the warm detections the fraction decreases to $37.8^{+6.4}_{-3.0}\%$. However, this value is biased by the fact that most HVCs are located at negative velocities, thus, after the cut, the warm dataset is dominated by detections at $v_{\rm LOS}>0$. Using the model with the outflows, all the warm absorptions are reproduced ($100^{+0}_{-4.1}\%$), consistently with the previous results (Section 5.3.1). Even though including or not these detections does not affect our results significantly, we can not exclude that a fraction of the warm absorptions of Lehner et al. (2012) is generated in the ionised envelope of the HVCs. The mechanism producing the warm-hot gas around these large complexes is likely to be the same as that producing the wakes of the fountain clouds (as already suggested by Fox et al. 2004), although the cooling of the corona may be less efficient given the low metallicity of the HVCs and the lower density of the corona at their typical distances. Photoionisation from both Galactic and extragalactic UV background can also play a role.

5.4.4 The high-velocity O VI *absorbers*

Our model of fountain wakes does not reproduce a significant fraction ($\sim 45\%$) of the O VI absorptions. Some of these features could be probably reproduced by tuning some parameters in our dynamical model and in the simulations of M11. However, most of them occur at velocities that are largely inconsistent with those predicted by our model (see, for instance, the top-right panel of Fig. 5.4). If we limit our analysis to the 68 high-velocity ($|v_{\rm LOS}|>90\,\mathrm{km\,s^{-1}}$) O VI detections of Sembach et al. (2003), the fraction reproduced by our model decreases down to $34.1^{+3.7}_{-1.8}\%$. Here, we discuss two possible different origins for these high-velocity O VI absorption features.

A first possibility is that these absorptions occur in the circumgalactic medium of the Milky Way, far beyond the regions where the galactic fountain takes place. Zsargó et al. (2003) studied the O VI absorption features towards a sample of 22 halo stars located between 3 and 5 kpc from the Galactic plane, finding that all the detections occur at $|v_{\rm LOS}|<100\,\mathrm{km\,s^{-1}}$. This would imply that the O VI absorbers at larger velocities found by Sembach et al. (2003) are likely to be located in the outskirt of the Galactic corona. O VI absorptions at large distances from the hosting galaxies are commonly observed up to redshift ~ 3 (Fox 2011). These detections have some

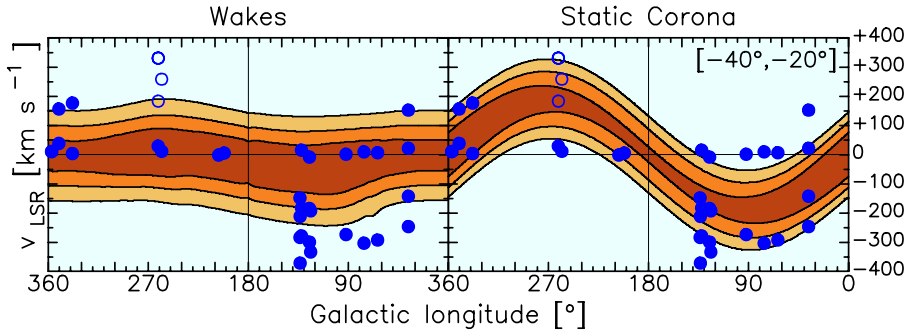

Figure 5.10: Longitude-velocity diagram at $-40° \leq b \leq -20°$ for the hot gas component of our model of fountain wakes (*left panel*) and for a static corona with density distribution $\propto r^{-3/2}$ (*right panel*). Filled circles represent O VI detections, empty circles represent detections related to the Magellanic system. Contour levels are from the innermost to the outermost at 1, 2 and 3σ (see Section 5.2.3).

peculiar properties: they are always located within half a Mpc of projected distance from a galaxy with luminosity $L > 0.25L_*$ (Wakker and Savage 2009), their column density is always around $10^{14}\,\mathrm{cm}^{-2}$ (Fox 2011), and to about half of them a Lyα absorption line can be associated within $50 - 200\,\mathrm{km\,s}^{-1}$ (Stocke et al. 2006). The origin of the absorber material is controversial: UV background photoionisation of cosmological filaments, strong outflows from the host galaxy and cooling flows from the circumgalactic medium are all viable possibilities. Thus, it is possible that a fraction of the high-velocity detections belongs to a second population of absorbers, placed in the outskirt of the Galactic corona and completely unrelated to the cooling mechanism proposed here. To test this hypothesis, we built a simple model of a *static* corona with density profile $\propto r^{-3/2}$ (Fukugita and Peebles 2006), and we compared the resulting modelcube with the O VI observations via the technique described in Section 5.2.3. We assumed for the coronal material a velocity dispersion similar to that of the hot gas in the wakes of the fountain clouds ($49\,\mathrm{km\,s}^{-1}$). Fig. 5.10 compares the l-v diagram around $b = -30°$ for our model of fountain wakes with that derived for this static coronal medium. Clearly, the latter allows to reproduce detections with a large v_{LOS}, even if it can not explain most of the O VI detections at $|v_{\mathrm{LOS}}| < 90\,\mathrm{km\,s}^{-1}$. The fraction of high-velocity O VI detections reproduced by this new model is $62.8^{+4.6}_{-2.2}\%$. This simple test suggests that a significant - but not dominant - fraction of O VI absorbers analysed in this work may take place in the outskirt of the Galactic corona, at tens or even hundreds of kpc from the gaseous thick disc of the Milky Way.

Another possibility is that part of the O VI detections are not related with the Milky Way, but they occur in the circumgalactic medium of external galaxies. As a test, we retrieved from the Nasa/Ipac Extragalactic Database a list of UGC and NGC galaxies with systemic velocity smaller than $600\,\mathrm{km\,s}^{-1}$. Then we used the HyperLeda catalogue (Paturel et al. 2003) to obtain distances (d), inclination angles (i) and rotation velocities (v_{rot}) for all the galaxies in our sample. When these data

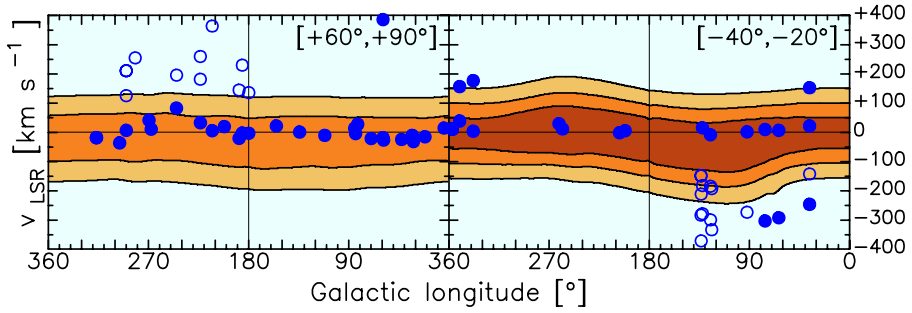

Figure 5.11: Longitude-velocity diagrams at $+60° \leq b \leq +90°$ (*left panel*) and $-40° \leq b \leq -20°$ (*right panel*) for the hot gas component of our model of fountain wakes. Filled circles represent O VI detections that we consider related to the Galactic halo, while empty circles represent O VI detections that can be related to nearby galaxies (see text). Detections related to the Magellanic system are not shown. Contour levels are from the innermost to the outermost at 1, 2 and 3σ (see Section 5.2.3).

were not available, we adopted average values based on the other galaxies in the sample. Assuming for the absorber material a velocity dispersion σ of 49 km s^{-1} and a typical distance to the galaxy centres $d_{\rm abs}$ of 500 kpc (Wakker and Savage 2009), we removed from the dataset of Sembach et al. (2003) all those detections located at angular separation smaller than $\tan^{-1}(d_{\rm abs}/d)$ and velocity separation smaller than $v_{\rm rot}\sin(i) + 2\sigma$ from the galaxies in our sample. After this cut, the number of high-velocity O VI features decreases significantly from 68 to 27. Fig. 5.11 shows that most of the O VI absorptions visible at positive velocities at $+60° \leq b \leq +90°$ are removed, as well as those located at $-40° \leq b \leq -20°$ and $l \simeq 130°$ in a stripe at negative velocities. These latter are absorptions related to M31. Our model of hot fountain wakes reproduces $65.2^{+8.3}_{-3.9}$% of the remaining 27 detections. When including also the detections at $|v_{\rm LOS}| < 90$ km s^{-1}, the fraction reproduced becomes $71.7^{+3.5}_{-1.7}$%, ~ 17% larger than that estimated in Section 5.3. It is interesting to note that if we assumed $d_{\rm abs} = 50$ kpc only 4 O VI features would be removed. This indicates that these absorption lines must be associated to extended media surrounding the nearby galaxies rather than to the galaxy discs. We conclude that some percentage of the O VI absorbers analysed in this work may be located outside the virial radius of the Milky Way and produced in the circumgalactic medium of nearby disc galaxies.

5.4.5 Relation to Shull et al. (2009)

Shull et al. (2009) found 83 high-velocity absorption features of Si II, Si III and Si IV in the spectra of 37 AGNs by combining data from STIS and FUSE. It is interesting to determine what fraction of these features are reproduced by our model of warm fountain wakes with outflows. Unlike Lehner et al. (2012), Shull et al. (2009) do not provide measurements of the line centroids but simply indicate a velocity range for each absorption feature, and we assumed that the centroids are located in the middle

of the ranges reported. After excluding 8 detections related to the Magellanic system, we found that our model reproduces merely $33.4^{+3.5}_{-1.6}\%$ of the remaining 75 detections. This fraction increases to $47.1^{+4.9}_{-2.2}\%$ when excluding further 22 detections that can be related to the external nearby galaxies (see Section 5.4.4). When combining the data of Shull et al. (2009) together with those of Lehner et al. (2012), the fraction reproduced increases to $63.2^{+3.2}_{-1.6}\%$ excluding only the detections related to the Magellanic system. This result is surprising as it seems to show that the two datasets are not fully compatible. The discrepancy can be caused by the different criteria used in selecting the absorption features (N. Lehner and C. Howk, private communications), and it is also possible that the uncertainties on the exact position of the line centroids may have biased our analysis. Most of the detections of the Shull et al. (2009) sample that are not reproduced by our model are located at high negative velocities at longitudes $20° < l < 120°$. Although this requires further investigation, it is possible that they originate in a very extended ionised envolope surrounding the Magellanic Stream, much larger than that we considered. Also, we noticed that some anomalous detections are located roughly at the edge of the X-ray bubble visible towards the inner Galaxy in the 0.75 keV band (Snowden et al. 1997). Therefore, we can speculate that some of these features may originate from the cooling of the hot gas ejected from the Galactic nucleus.

5.4.6 Gas accretion onto the disc

The ionised gas surrounding our Galaxy is regarded as one of the main candidates for replacing the material consumed by the process of star formation in the disc. Lehner and Howk (2011) used all the information available on their warm absorptions (e.g. upper limits on distances, sky covering fraction, ion column densities) to infer a mass accretion rate onto the disc of $0.8 - 1.4\,\mathrm{M_\odot\,yr^{-1}}$. This value was obtained by considering an average infall velocity of $90 - 150\,\mathrm{km\,s^{-1}}$. Using similar arguments but different absorption data, Shull et al. (2009) inferred an accretion rate onto the disc of $\sim 1\,\mathrm{M_\odot\,yr^{-1}}$. These values are derived regardless of the phase of the gas involved, and it is not clear whether the warm material cools during its infall or remains ionised.

In our model, because of the coronal condensation, the fountain cycle returns to the disc more material than what has ejected in the first place. A pristine, multi-phase gas accretion is thus 'hidden' in the fountain cycle. The cold phase of the accreting material can be inferred via the fitting of the H I kinematics: our dynamical model suggests a global accretion of neutral gas (H+He) onto the disc at a rate of $\sim 2\,\mathrm{M_\odot\,yr^{-1}}$ (Section 3.3.2). In addiction, a 'warm' accretion is provided by coronal material that, though entrained by the clouds' wakes, is not able to cool down to recombination temperatures before impacting with the disc. We used our dynamical model to infer the accretion rate of this warm gas, obtaining a value of $\sim 1\,\mathrm{M_\odot\,yr^{-1}}$ after correcting for the He abundance. This value is perfectly consistent

with that estimated in the works mentioned above for the ionised gas. What remains unclear is whether this ionised material can take part in the process of star formation in the Galactic disc.

5.5 Conclusions

Accretion of pristine gas from cosmological coronae seems to be required in order to explain the properties and the evolution of disc galaxies. Hydrodynamical simulations indicate that the cooling of the corona can be triggered by the passage of metal-rich gas clouds, like those ejected in star forming galaxies by stellar feedback (galactic fountains). The material cooling from the corona is expected to trail the cloud in an extended turbulent wake. In this framework, galaxy discs are surrounded by thick layers of multiphase gas at temperatures below the virial temperature produced by the interaction of the fountain with the coronal medium.

In this Chapter we tested the above scenario for the Milky Way. We studied whether the warm-hot gas present in the wakes of the fountain clouds is responsible for the ion absorption lines (O VI, Si III, Si IV, C II, C IV) that have been observed towards several background sources. We modelled the all-sky position-velocity distribution of this gas by combining the galactic fountain H I model described in Chapter 3 with the hydrodynamical simulations of M11. Our model does not have free parameters as it is fully determined by the fit on the H I component of the Galactic halo performed in Chapter 3. By comparing the properties of the absorptions detected by Sembach et al. (2003), Savage et al. (2003) and Lehner et al. (2012) with those predicted for the warm-hot gas by our model, we obtained the following results:

1. the great majority (75–95%) of the 'warm' absorptions (Si III, Si IV, C II, C IV) and about half of the O VI absorptions have a position-velocity distribution fully consistent with that predicted by our model;

2. the O VI and the Si III column densities of the absorbers agree with those predicted by our model;

3. the large velocity spread of the absorbers is consistent with the predictions of hydrodynamical simulations and it is due to the development of turbulence in the clouds' wakes;

4. the average number of absorptions detected per line of sight is consistent with the average number of wakes intercepted by the line of sight in our model;

5. excluding from our analysis all those absorptions that can be associated to the classical HVCs does not change significantly the above results.

We conclude that half of the O VI absorbers and virtually all the warm absorbers are likely to be produced within a few kiloparsecs above the disc, at the interface between the latter and the cosmological corona of the Milky Way. The material cooling from the corona provides an accretion of pristine gas onto the disc at a rate of $\sim 2{-}3\,\mathrm{M}_{\odot}\,\mathrm{yr}^{-1}$. This coronal accretion provides an adequate supply of material to maintain star formation in the Galaxy disc. We speculate that the high-velocity detections that are not reproduced by our model constitute a different population of absorbers, similar to those observed in extragalactic surveys. They are likely located in the circumgalactic medium of the Milky Way and/or of nearby disc galaxies at distances of tens or hundreds of kpc from the discs.

Chapter 6

Conclusions

In this Thesis we have studied the multiphase gaseous environment that surrounds the disc of the Milky Way. In this last Chapter, we summarise the results obtained and give some conclusive remarks. Section 6.1 contains a summary of the various Chapters of this Thesis. The global structure of the Galactic gaseous halo is sketched and discussed in Section 6.2, while in Section 6.3 we discuss the impact of the supernova-driven gas accretion mechanism presented in this work on the evolution of disc galaxies.

6.1 Thesis summary

We first focused on the neutral hydrogen component of the Galactic halo. In Chapter 2 we derived the global properties of this layer. We defined an axi-symmetric kinematic model of the Galaxy's H I halo and used it to reproduce the datacube of the Leiden-Argentine-Bonn (LAB) survey of Galactic H I emission (Kalberla et al. 2005). We found that the Milky Way has a thick H I disc with a mass of $\sim 3\times10^8\,\mathrm{M}_\odot$, about $5-10\%$ of the total H I content of the Galaxy, and a scale-height of 1.6 kpc (assuming a sech^2 vertical distribution). The kinematics of this layer is similar to that derived for the H I halos of nearby galaxies, showing both a vertical rotational gradient of about $-15\,\mathrm{km\,s^{-1}\ kpc^{-1}}$ and a global inflow motion of $\sim 20-30\,\mathrm{km\,s^{-1}}$. We concluded that the H I halo of the Milky Way is similar to that observed in other spirals. A galactic fountain origin is the most likely explanation for its origin. In this context, the Galactic H I halo would be made up of several thousands clouds with masses of $\sim 10^{4-5}\,\mathrm{M}_\odot$, of which the IVCs are the local counterpart.

The above kinematical models were derived without making any assumptions on the dynamical state of the halo. In Chapter 3, instead, we performed a full dynamical modelling of the H I halo of the Milky Way using an improved version of the galactic fountain model developed by Fraternali and Binney (2006, 2008). In this model, particles, representing fountain clouds, are ejected from the disc at a rate pro-

portional to the star formation rate density, and their orbits are followed until they return to the disc. Particles travel through a region where coronal gas is supposed to be significantly dense. Marinacci et al. (2010a, 2011) used 2D hydrodynamical simulations to show that the interaction between fountain clouds and the coronal material triggers the cooling of the latter inside the turbulent wakes that trail the clouds. Inspired by these works, we considered the possibility that gas particles, during their orbits, accrete gas from and exchange momentum with a spinning hot corona. The model has three free parameters: the average velocity at which particles are ejected from the disc, the percentage of the initial part of the orbits during which fountain clouds are ionised and therefore not visible in H I, and the coronal accretion rate. When fitted to the LAB data, this dynamical model provides a much better description of the observed H I emission with respect to the previous best-fit kinematic model. Gas particles that accrete gas from the corona must share their angular momentum with it. This produces a decrease in their rotational speed and an increase in their inward radial velocity, consistently with the global kinematic pattern found in Chapter 2. Fountain cloud particles return to the disc the material accreted at a rate of $\sim 2\,\mathrm{M}_\odot\,\mathrm{yr}^{-1}$, a value remarkably similar to the rate at which the Milky Way is forming stars. The model reproduces very well the H I emission of the Intermediate-Velocity Clouds (IVCs), but not that of the High-Velocity Clouds (HVCs), showing that these latter are likely to have an external origin.

In Chapter 4 we studied the gaseous halos of two synthetic disc galaxies as resulting from recent N-body + smoothed-particle hydrodynamics (SPH) simulations: a Milky-Way-like galaxy evolved in isolation for 250 Myr, and a large spiral evolved in a full cosmological ΛCDM framework down to redshift 0. Two different realisations for each simulation were available, depending on how stellar feedback was implemented ('kinetic' or 'thermal' method). The isolated galaxy shows a thick H I disc with a lagging kinematics similar to that found in our Galaxy, although this component is not as massive as that of the Milky Way. Stellar feedback produces a significant outflow of ionised material from the disc to the halo at a rate of $\sim 10\,\mathrm{M}_\odot\,\mathrm{yr}^{-1}$, which forms a diffuse atmosphere around the galaxy. This medium cools and forms clumps of cold gas up to distances of 10−15 kpc above the disc that are qualitatively similar to the Milky Way's HVCs, which however have probably an external origin. Only minor differences are visible between the thermal and the kinetic run. In contrast to the isolated galaxy, the outcome of the cosmological simulations is very different depending on the stellar-feedback recipe adopted. In the kinetic run, the galaxy shows prominent H I filaments around the disc and is surrounded by a system of massive cold clumps located out to 200 kpc from the centre, probably produced by the cooling of the coronal gas via thermal instability. Similar systems of clumps are not observed around real disc galaxies (Pisano et al. 2007). These clumps and most of the H I filaments disappear when thermal feedback is used. However, this recipe prevents star formation in the regions of the bulge, producing an extended, bulgeless spiral galaxy whose kinematics is completely dominated by the dark matter, which has no analogous in the real Universe. In both cases, an H I thick disc is

not present. The most likely explanation for the lack of this component is the lower resolution of these simulations with respect to that achieved in the isolated runs. We concluded that the H I gas distribution and kinematics of galaxies simulated in ΛCDM framework depend dramatically on the resolution adopted and on the recipe used to implement the supernova feedback.

In Chapter 5 we have investigated the possibility that the highly ionised atomic species (Si III, Si IV, C II, C IV, O VI) observed in absorptions towards several background targets at line-of-sight velocities $|v_{\rm LOS}| < 400\,{\rm km\,s^{-1}}$ are produced in the turbulent wakes created during the interaction between the fountain clouds and the corona of the Milky Way. For this purpose, we used the hydrodynamical simulations of Marinacci et al. (2011) to study how the warm ($4.3 < \log(T/\,{\rm K}) < 5.3$) and the hot ($5.3 < \log(T/\,{\rm K}) < 5.7$) gas in the wake of a typical fountain cloud evolve with respect to the cold component. The results of this analysis are included in the best-fit galactic fountain model of Chapter 3 in order to predict the all-sky position-velocity distribution of the warm-hot gas in the wakes of the fountain clouds. The resulting model has no free parameters, being it based only on the fit to the H I data performed in of Chapter 3 and on the physics of the fountain-clouds–corona interaction derived by Marinacci et al. (2011). We found that the vast majority of the warm absorption features (Si III, Si IV, C II, C IV) found by Lehner et al. (2012) and about half of the O VI absorption features found by Sembach et al. (2003) and Savage et al. (2003) have position-velocities and column densities in full agreement with those predicted by our model, and are therefore consistent with being located within a few kpc from the Galactic disc. Data show a large spread in velocities that is consistent with being produced by turbulence in the fountain cloud wakes. We speculate the the absorbers that are not reproduced by our models belong to a different populations, and are located at tens or hundreds of kpc from the disc of the Milky Way.

6.2
The structure of the gaseous halo of the Milky Way

Fig. 6.1 sketches the gaseous halo of the Milky Way as resulting from this Thesis. Different colors represent different gas phases: blue regions represent the cold gas ($\log(T/\,{\rm K}) < 4.3$), green regions represent the warm gas ($4.3 < \log(T/\,{\rm K}) < 5.3$), orange regions represent the hot gas ($5.3 < \log(T/\,{\rm K}) < 5.7$), and the red region surrounding the disc represents coronal gas at the Galaxy's virial temperature (a few $10^6\,{\rm K}$). Supernova explosions in the disc produce the onset of a galactic fountain, in which metal-rich gas is ejected from the disc, travels through the halo and falls back. The fountain clouds interact with the coronal gas: the Kelvin-Helmholtz instability develops and forms turbulent wakes that trail the clouds. In these wakes, the two media mix and produce material at intermediate temperatures and metallicities that

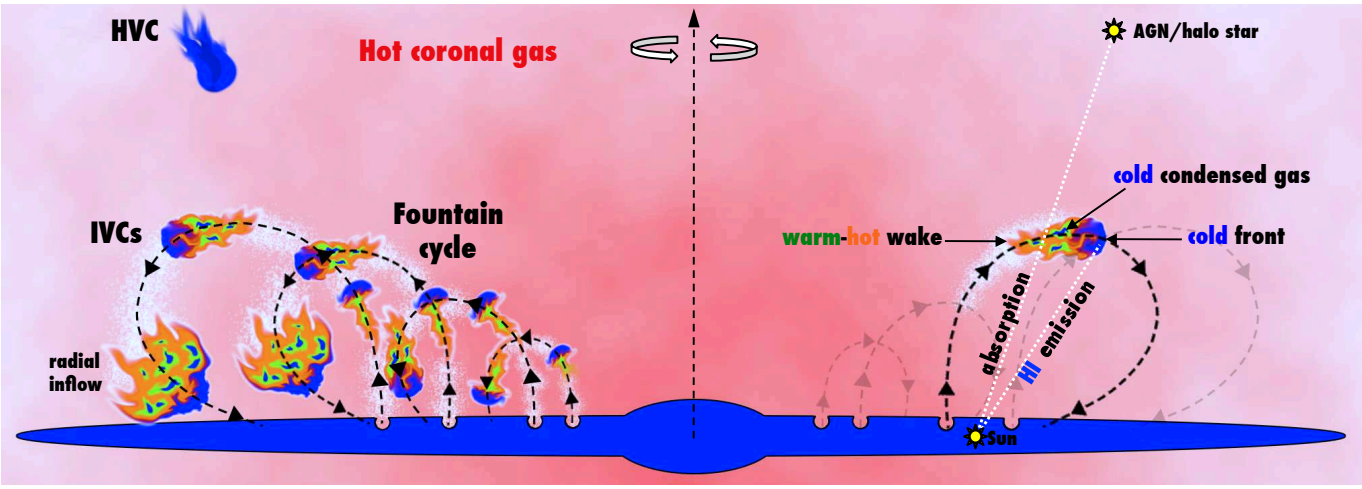

Figure 6.1: Scheme of the gaseous halo of the Milky Way emerging from this Thesis.

can cool efficiently. The interaction with the coronal gas modifies the kinematics of fountain clouds, which loose speed in the azimuthal direction (not shown in the figure) and acquire radial velocity directed inward. When the fountain clouds return to the disc, the material harvested from the corona is accreted into the Galactic interstellar medium.

This fountain cycle produces a multiphase gaseous halo located within a few kiloparsecs from the disc of the Galaxy. The vertical thickness of this medium increases from the inner to the outer regions, because the gravitational restoring force to the plane diminishes outwards. This halo is made up of thousands IVC-like clouds (Fig. 6.1). An observer looking towards a cold front of a fountain cloud would detect H I emission at (intermediate) anomalous velocity. An observer looking towards a background source and intercepting a turbulent warm-hot wake would detect broad (non-thermal) absorption lines of highly ionised material.

The classical H I HVCs do not fit in the picture described: they are too distant and massive to be produced by the Galactic fountain. Gas stripped from satellites or extragalactic accretion of pristine material (e.g. Joung et al. 2012) are more likely origins for these complexes.

6.3 Supernova-driven gas accretion and galaxy evolution

The main astrophysical problem addressed in this Thesis is how disc galaxies like the Milky Way accrete gas from the surrounding environment. Several pieces of evidence indicate that, in these galaxies, the gas consumed by the process of star formation in the disc gets continuously replenished. Observations in the local Universe indicate that cold gas accretion from minor mergers and floating clouds accounts only for $\sim$ 10% of the galaxy star formation rates (SFRs) (Sancisi et al. 2008; Fraternali

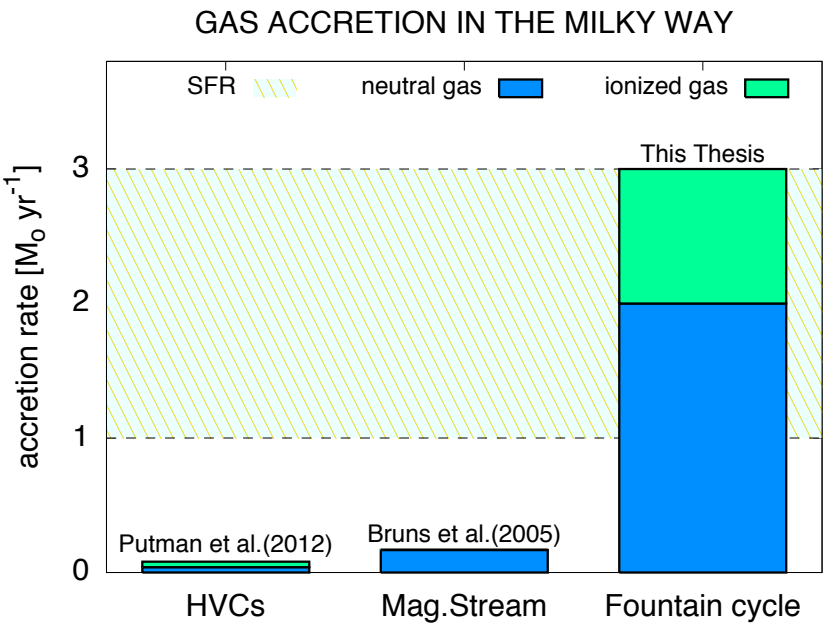

Figure 6.2: Comparison between different sources of gas accretion for the Milky Way.

2010), thus the vast majority of gas must be acquired in other forms.

In this Thesis, we have presented a mechanism by which the Milky Way - and similar star forming disc galaxies - can harvest material from the corona via their galactic fountain cycle. We called this mechanism 'supernova-driven gas accretion'. In Fig. 6.2 we compare the accretion rates onto the Galaxy that one can infer from the currently available gas sources. The classical HVCs contribute only $0.08\,\mathrm{M}_\odot\,\mathrm{yr}^{-1}$, and only half of this gas is in the neutral phase (Putman et al. 2012). Direct accretion of cold gas from satellites is only visible in the Magellanic Stream, which is a sporadic event and it is very unlikely to reach the Galactic disc before being ablated and thermalised. If the Magellanic Stream survives the journey, it will merge with the Galactic interstellar medium on a timescale likely larger than 1 Gyr (Putman et al. 2012). Given the H I mass of the Stream, $1.2 \times 10^8\,\mathrm{M}_\odot$ (Brüns et al. 2005), this gives an upper limit to the accretion rate of $0.16\,\mathrm{M}_\odot\,\mathrm{yr}^{-1}$. The supernova-driven gas accretion mechanism predicts instead an accretion rate of $\sim 3\,\mathrm{M}_\odot\,\mathrm{yr}^{-1}$, 2/3 of which is in a cold phase and can be directly used to form stars in the disc. This value is remarkably similar to the current SFR of the Milky Way, which lies in the range $1-3\,\mathrm{M}_\odot\,\mathrm{yr}^{-1}$ (Chomiuk and Povich 2011).

The results obtained in this Thesis can easily explain how a galaxy like the Milky Way can keep forming stars at a roughly constant rate on cosmological timescales: it is able to self-regulate its star formation. For this to happen, two requirements must be fulfilled: the galaxy must have developed a hot corona and it must retain its disc of gas. If this is the case, then the supernova-driven gas accretion can take care of the galaxy's gas demand. The higher the star formation, the larger is the stellar feedback. The more fountain clouds are ejected, the larger the amount of gas harvested from the corona is. Thus, this *positive* stellar feedback continuously

supplies low metallicity material to the disc at a rate similar to that at which the galaxy forms stars.

There are reasons to believe that this self-regulating mechanism fails in galaxies with exceptionally high star formation rates, like in starburst galaxies. In the first place, the coronal gas harvested by fountain clouds must be replaced by the upper layers of the corona, which should inflow towards the galaxy on dynamical timescales of the order of several tens or hundreds of Myrs (Binney et al. 2009). Galaxies that deplete their lower corona on timescales shorter than this will keep burning the gas stocked in their disc without any replacement. Supernova explosions in the disc produce also a *negative* feedback by injecting thermal energy into the surrounding gas. In a starburst galaxy this process can be particularly vigorous and can quench the cooling of the coronal material.

We speculate that supernova-driven gas accretion has been the way in which the cosmological hot-mode accretion has fed the star formation in the Milky Way and similar disc galaxies after the initial cold-mode phase. Models of galaxy evolution in ΛCDM framework aimed at reproducing the observed properties of nearby galaxies may wish to consider the novel accretion mechanism presented in this Thesis.

Appendix A

Modelling the inner Galactic HI disc

In this Appendix we present a novel approach, based on the tangent-point method (see Section 2.3.1), to derive the rotation curve, the velocity dispersion profile and the density profile for neutral hydrogen in the inner ($R \leq \mathrm{R}_\odot$) disc of the Milky Way.

A.1 The method

The rotation curve of the inner Milky Way is classically derived using the so-called *tangent-point* method, which is based on extracting the terminal-velocity from the H I line profiles (Shane and Bieger-Smith 1966; Malhotra 1995). This is usually done by assuming the velocity dispersion or the density of the gas to be constant for a wide range of line-of-sight velocities (Celnik et al. 1979; Rohlfs and Kreitschmann 1987). We developed an iterative method to fit the whole H I line profiles of the LAB 21-cm survey (Kalberla et al. 2005) at latitude $b = 0°$, assuming that the neutral gas in the inner Galaxy is distributed in coplanar rings in circular rotation, centered at the Galactic centre.

Our iterative method is sketched in Fig. A.1. The generic i-th ring at radius R_i is described by three parameters: the rotational velocity $v_{\phi,i}$, the velocity dispersion σ_i and the volume density n_i of the gas. At a given longitude l, the model H I column density integrated over the velocity range $[v,\, v + \Delta v]$, $N_{\mathrm{HI}}(v)$, can be obtained by summing the contributions (assumed Gaussian) of all rings with $0 \leq i \leq i_{\max}$ along the line of sight, where $R_0 = \mathrm{R}_\odot$ and $R_{i_{\max}} = \mathrm{R}_\odot \sin(l)$ is the tangent-point radius R_{tp}. Thus

$$N_{\mathrm{HI}}(v) = 2\,\Delta v \sum_{i=0}^{i_{\max}} n_i\, \delta_i(v, \sigma_i)\, \Delta d_i \tag{A.1}$$

where the factor 2 stands for axi-symmetry, $\delta_i(v, \sigma_i)$ is a normalized gaussian function centred at $v = \left(v_{\phi,i} \frac{\mathrm{R}_\odot}{R_i} - v_\odot\right) \sin(l)$ with dispersion equal to σ_i, and Δd_i is the

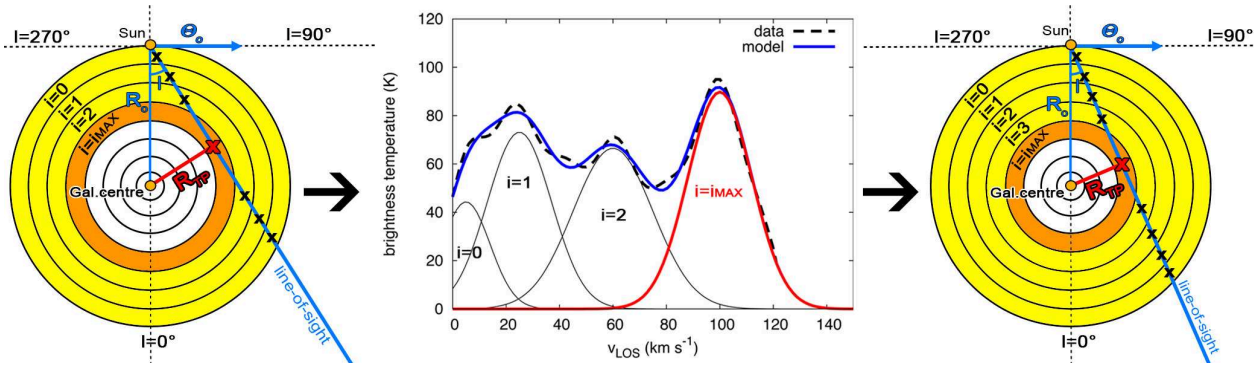

Figure A.1: Scheme of the recursive tangent-point method. The *first panel* sketches the inner Milky Way divided into rings. The H I line profile at longitude l is given by the sum of the contributions of all rings with $0 \leq i \leq i_{\max}$ (*second panel*), the parameters of the last ring can be found by fitting the last gaussian of the model profile (thick red curve) to the data (dashed curve). This procedure can be iterated by decreasing l (*third panel*).

separation along the line of sight between two consecutive rings and depends on the longitude considered. In order to fit our model to the H I line profiles of the LAB data, we must convert $N_{\rm HI}(v)$ to a brightness temperature $T_{\rm B}(v)$. For this purpose, we estimate the effect of the optical thickness by assuming the gas isothermal with a temperature of $T_{\rm LAB} = 152\,{\rm K}$, which is the maximum brightness temperature in the LAB dataset. Thus the model H I line profile can be obtained as:

$$T_{\rm B}(v)[\,{\rm K}] = T_{\rm LAB}\left(1 - \exp\left(-\frac{N_{\rm HI}(v)[\,{\rm cm}^{-2}]}{T_{\rm LAB}\,\Delta v\,1.82\times10^{18}}\right)\right) \qquad \text{(A.2)}$$

and therefore $T_{\rm B} \leq T_{\rm LAB}$, in agreement with the LAB data. Note that in the optically thin regime (i.e., $N_{\rm HI}(v) \ll T_{\rm LAB}\,\Delta v\,1.82\times10^{18}$), the brightness temperature is proportional to the column density.

For each new l we fix the values of $v_{\phi,i}$, σ_i and n_i for all the rings with $i < i_{\max}$ determined with the previous iterations, we evaluate $T_{\rm B}(v)$ via equations (A.1) and (A.2) and fit it to the observed H I line profile by varying only the values at $i = i_{\max}$. We apply this method to determine the values of the parameters for all rings recursively, starting from $R = {\rm R}_\odot$ (at $l = 90°$ for the receding region, or $l = 270°$ for the approaching one) down to the Galactic centre (at $l = 0°$). We assume ${\rm R}_\odot = 8.5\,{\rm kpc}$ and $v_\odot = 220\,{\rm km\,s^{-1}}$, and use $\Delta v = 2.061\,{\rm km\,s^{-1}}$ which is the channel separation in the LAB datacube.

A.2 Results

Fig. A.2 (top panels) shows $v_\phi(R)$, $\sigma(R)$ and the H I surface density $\Sigma(R)$ as derived with our method. Error bars on the average rotation curve take into account the differences between the approaching and the receding velocities, which are significant

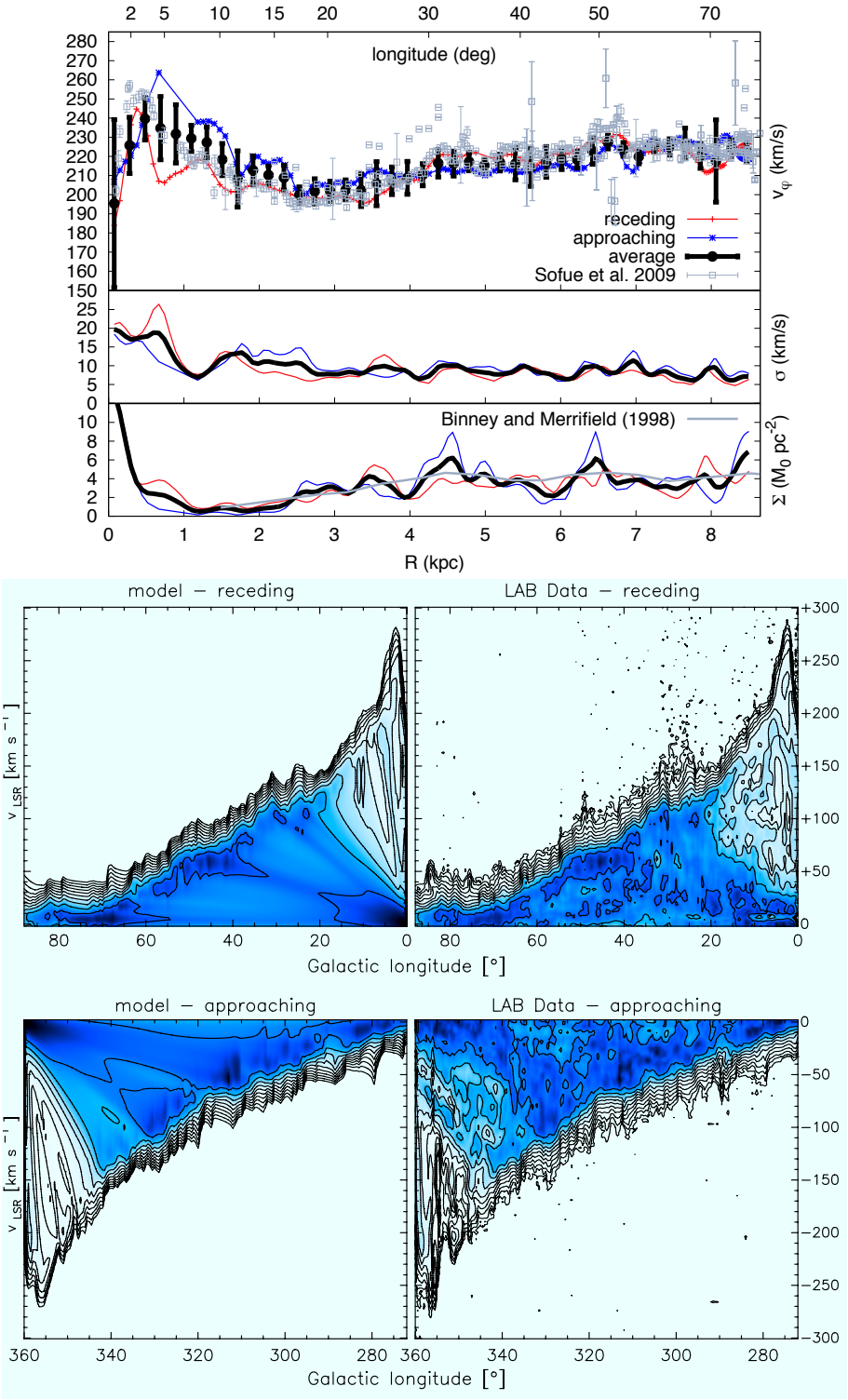

Figure A.2: Results of our axi-symmetric model for the inner Milky-Way disc. *Top panels*: rotation curve, dispersion and density profiles for the approching (blue) and receding (red) sides. *Bottom panels*: Comparison between our model and the LAB data, $l-v$ slices at $b=0°$. Contour levels range from 0.16 K to 81.92K scaling by a factor 2.

($\gtrsim 20\,\mathrm{km\,s^{-1}}$) only for $R \lesssim 2\,\mathrm{kpc}$ and are likely due to non-circular motions in the region of the bar. Our average rotation curve is consistent with that of Sofue et al. (2009). The velocity dispersion is rather high in the innermost regions decreasing to about $7-8\,\mathrm{km\,s^{-1}}$ for $R > 3\,\mathrm{kpc}$. Similar trends have been observed in external galaxies, like NGC 6946 (Boomsma et al. 2008). The surface density profile, derived by assuming a constant scale-height of 150 pc, is in excellent agreement with that found by Binney and Merrifield (1998). In addition, our fit shows a strong increase of the H I surface density in the innermost 500 pc, which is qualitatively similar to that observed in the molecular gas (Dame et al. 2001). We point out that neglecting the effects of the optical thickness would lower our esteem of the H I column density by $\sim 30\%$.

The bottom panels of Fig. A.2 compare the longitude-velocity ($l - v$) plots at $b = 0°$ predicted by our model with those of the data. It is remarkable that a fully axi-symmetric description reproduces the line profile in such detail including the emission far from the terminal velocities. This seems to indicate that the neutral gas in the inner Galaxy is not too much affected by the non-axisymmetry of the potential and its kinematics is dominated by rotation also in the region of the bar.

Bibliography

G. Altay, T. Theuns, J. Schaye, N. H. M. Crighton, and C. Dalla Vecchia. Through Thick and Thin H I Absorption in Cosmological Simulations. *ApJ*, 737:L37, August 2011. doi: 10.1088/2041-8205/737/2/L37.

E. Anders and N. Grevesse. Abundances of the elements - Meteoritic and solar. *Geochim. Cosmochim. Acta*, 53:197–214, January 1989. doi: 10.1016/0016-7037(89)90286-X.

M. E. Anderson and J. N. Bregman. Do Hot Halos Around Galaxies Contain the Missing Baryons? *ApJ*, 714:320–331, May 2010. doi: 10.1088/0004-637X/714/1/320.

M. E. Anderson and J. N. Bregman. Detection of a Hot Gaseous Halo around the Giant Spiral Galaxy NGC 1961. *ApJ*, 737:22–+, August 2011. doi: 10.1088/0004-637X/737/1/22.

M. Aumer and J. J. Binney. Kinematics and history of the solar neighbourhood revisited. *MNRAS*, 397:1286–1301, August 2009. doi: 10.1111/j.1365-2966.2009.15053.x.

E. Bajaja, R. Morras, and W. G. L. Pöppel. Solving asymmetries in the HVC's distribution. *Publications of the Astronomical Institute of the Czechoslovak Academy of Sciences*, 69:237–239, 1987.

C. V. Barbieri, F. Fraternali, T. Oosterloo, G. Bertin, R. Boomsma, and R. Sancisi. Extra-planar gas in the spiral galaxy NGC 4559. *A&A*, 439:947–956, September 2005. doi: 10.1051/0004-6361:20042395.

M. Barnabè, L. Ciotti, F. Fraternali, and R. Sancisi. Hydrostatic models for the rotation of extra-planar gas in disk galaxies. *A&A*, 446:61–69, January 2006. doi: 10.1051/0004-6361:20053386.

T. Bilitewski and R. Schönrich. Radial flows and angular momentum conservation in Galactic chemical evolution. *MNRAS*, 426:2266–2282, November 2012. doi: 10.1111/j.1365-2966.2012.21827.x.

J. Binney and M. Merrifield. *Galactic astronomy.* 1998.

J. Binney and S. Tremaine. *Galactic Dynamics: Second Edition.* Princeton University Press, 2008.

J. Binney, C. Nipoti, and F. Fraternali. Do high-velocity clouds form by thermal instability? *MNRAS*, 397:1804–1815, August 2009. doi: 10.1111/j.1365-2966.2009.15113.x.

J. Bland-Hawthorn, R. Sutherland, O. Agertz, and B. Moore. The Source of Ionization along the Magellanic Stream. *ApJ*, 670:L109–L112, December 2007. doi: 10.1086/524657.

L. Blitz and E. Rosolowsky. The Role of Pressure in GMC Formation II: The H_2-Pressure Relation. *ApJ*, 650:933–944, October 2006. doi: 10.1086/505417.

M. Bois, E. Emsellem, F. Bournaud, K. Alatalo, L. Blitz, M. Bureau, M. Cappellari, R. L. Davies, T. A. Davis, P. T. de Zeeuw, P.-A. Duc, S. Khochfar, D. Krajnović, H. Kuntschner, P.-Y. Lablanche, R. M. McDermid, R. Morganti, T. Naab, T. Oosterloo, M. Sarzi, N. Scott, P. Serra, A.-M. Weijmans, and L. M. Young. The ATLAS^{3D} project - VI. Simulations of binary galaxy mergers and the link with fast rotators, slow rotators and kinematically distinct cores. *MNRAS*, 416:1654–1679, September 2011. doi: 10.1111/j.1365-2966.2011.19113.x.

R. Boomsma, T. A. Oosterloo, F. Fraternali, J. M. van der Hulst, and R. Sancisi. Extra-planar H I in the starburst galaxy NGC 253. *A&A*, 431:65–72, February 2005. doi: 10.1051/0004-6361:20041715.

R. Boomsma, T. A. Oosterloo, F. Fraternali, J. M. van der Hulst, and R. Sancisi. HI holes and high-velocity clouds in the spiral galaxy NGC 6946. *A&A*, 490:555–570, November 2008. doi: 10.1051/0004-6361:200810120.

J. N. Bregman. The galactic fountain of high-velocity clouds. *ApJ*, 236:577–591, March 1980. doi: 10.1086/157776.

J. N. Bregman. The Search for the Missing Baryons at Low Redshift. *ARA&A*, 45:221–259, September 2007. doi: 10.1146/annurev.astro.45.051806.110619.

J. N. Bregman and E. J. Lloyd-Davies. X-Ray Absorption from the Milky Way Halo and the Local Group. *ApJ*, 669:990–1002, November 2007. doi: 10.1086/521321.

C. Brüns, J. Kerp, L. Staveley-Smith, U. Mebold, M. E. Putman, R. F. Haynes, P. M. W. Kalberla, E. Muller, and M. D. Filipovic. The Parkes H I Survey of the Magellanic System. *A&A*, 432:45–67, March 2005. doi: 10.1051/0004-6361:20040321.

W. Celnik, K. Rohlfs, and E. Braunsfurth. A new determination of the thickness of the galactic disk from H I-observations and a discussion of some consequences for galactic mass models. *A&A*, 76:24–34, June 1979.

C. Chiappini, F. Matteucci, and R. Gratton. The Chemical Evolution of the Galaxy: The Two-Infall Model. *ApJ*, 477:765–+, March 1997. doi: 10.1086/303726.

C. Chiappini, F. Matteucci, and D. Romano. Abundance Gradients and the Formation of the Milky Way. *ApJ*, 554:1044–1058, June 2001. doi: 10.1086/321427.

L. Chomiuk and M. S. Povich. Toward a Unification of Star Formation Rate Determinations in the Milky Way and Other Galaxies. *AJ*, 142:197, December 2011. doi: 10.1088/0004-6256/142/6/197.

K. M. Chynoweth, G. I. Langston, K. Holley-Bockelmann, and F. J. Lockman. A Search for Diffuse Neutral Hydrogen and H I Clouds in the NGC 2403 Group. *AJ*, 138:287–294, July 2009. doi: 10.1088/0004-6256/138/1/287.

J. A. Collins, R. A. Benjamin, and R. J. Rand. Kinematics of Diffuse Ionized Gas Halos: A Ballistic Model of Halo Rotation. *ApJ*, 578:98–108, October 2002. doi: 10.1086/342309.

J. A. Collins, J. M. Shull, and M. L. Giroux. A Survey of Far Ultraviolet Spectroscopic Explorer and Hubble Space Telescope Sight Lines through High-Velocity Cloud Complex C. *ApJ*, 585:336–354, March 2003. doi: 10.1086/345949.

J. A. Collins, J. M. Shull, and M. L. Giroux. Hubble Space Telescope Survey of Interstellar High-velocity Si III. *ApJ*, 705:962–977, November 2009. doi: 10.1088/0004-637X/705/1/962.

F. Combes. Secular Evolution of Disk Galaxies. In J. G. Funes and E. M. Corsini, editors, *Formation and Evolution of Galaxy Disks*, volume 396 of *Astronomical Society of the Pacific Conference Series*, page 325, October 2008.

R. A. Crain, T. Theuns, C. Dalla Vecchia, V. R. Eke, C. S. Frenk, A. Jenkins, S. T. Kay, J. A. Peacock, F. R. Pearce, J. Schaye, V. Springel, P. A. Thomas, S. D. M. White, and R. P. C. Wiersma. Galaxies-intergalactic medium interaction calculation - I. Galaxy formation as a function of large-scale environment. *MNRAS*, 399:1773–1794, November 2009. doi: 10.1111/j.1365-2966.2009.15402.x.

R. A. Crain, I. G. McCarthy, C. S. Frenk, T. Theuns, and J. Schaye. X-ray coronae in simulations of disc galaxy formation. *MNRAS*, 407:1403–1422, September 2010. doi: 10.1111/j.1365-2966.2010.16985.x.

X. Dai, M. E. Anderson, J. N. Bregman, and J. M. Miller. XMM-Newton Detects a Hot Gaseous Halo in the Fastest Rotating Spiral Galaxy UGC 12591. *ApJ*, 755:107, August 2012. doi: 10.1088/0004-637X/755/2/107.

C. Dalla Vecchia and J. Schaye. Simulating galactic outflows with kinetic supernova feedback. *MNRAS*, 387:1431–1444, July 2008. doi: 10.1111/j.1365-2966.2008.13322.x.

C. Dalla Vecchia and J. Schaye. Simulating galactic outflows with thermal supernova feedback. *MNRAS*, 426:140–158, October 2012. doi: 10.1111/j.1365-2966.2012.21704.x.

T. M. Dame, D. Hartmann, and P. Thaddeus. The Milky Way in Molecular Clouds: A New Complete CO Survey. *ApJ*, 547:792–813, February 2001. doi: 10.1086/318388.

V. P. Debattista, L. Mayer, C. M. Carollo, B. Moore, J. Wadsley, and T. Quinn. The Secular Evolution of Disk Structural Parameters. *ApJ*, 645:209–227, July 2006. doi: 10.1086/504147.

A. Dekel and Y. Birnboim. Galaxy bimodality due to cold flows and shock heating. *MNRAS*, 368:2–20, May 2006. doi: 10.1111/j.1365-2966.2006.10145.x.

A. A. Dutton, B. J. Brewer, P. J. Marshall, M. W. Auger, T. Treu, D. C. Koo, A. S. Bolton, B. P. Holden, and L. V. E. Koopmans. The SWELLS survey - II. Breaking the disc-halo degeneracy in the spiral galaxy gravitational lens SDSS J2141-0001. *MNRAS*, 417:1621–1642, November 2011. doi: 10.1111/j.1365-2966.2011.18706.x.

X. Fernández, M. R. Joung, and M. E. Putman. The Origin and Distribution of Cold Gas in the Halo of a Milky-Way-mass Galaxy. *ApJ*, 749:181, April 2012. doi: 10.1088/0004-637X/749/2/181.

H. A. Ford, N. M. McClure-Griffiths, F. J. Lockman, J. Bailin, M. R. Calabretta, P. M. W. Kalberla, T. Murphy, and D. J. Pisano. H I Clouds in the Lower Halo. I. The Galactic All-Sky Survey Pilot Region. *ApJ*, 688:290–305, November 2008. doi: 10.1086/592188.

H. A. Ford, F. J. Lockman, and N. M. McClure-Griffiths. Milky Way Disk-Halo Transition in H I: Properties of the Cloud Population. *ApJ*, 722:367–379, October 2010. doi: 10.1088/0004-637X/722/1/367.

A. J. Fox. The Surprisingly Constant Strength of O VI Absorbers Over Cosmic Time. *ApJ*, 730:58, March 2011. doi: 10.1088/0004-637X/730/1/58.

A. J. Fox, B. D. Savage, B. P. Wakker, P. Richter, K. R. Sembach, and T. M. Tripp. Highly Ionized Gas Surrounding High-Velocity Cloud Complex C. *ApJ*, 602:738–759, February 2004. doi: 10.1086/381024.

F. Fraternali. New evidence for halo gas accretion onto disk galaxies. In J. Andersen, J. Bland-Hawthorn, & B. Nordström, editor, *IAU Symp. 254,*, pages 255–262, March 2009. doi: 10.1017/S1743921308027671.

F. Fraternali. Gas Circulation and Galaxy Evolution. In V. P. Debattista and C. C. Popescu, editors, *American Institute of Physics Conference Series*, volume 1240 of *American Institute of Physics Conference Series*, pages 135–145, June 2010. doi: 10.1063/1.3458468.

F. Fraternali and J. J. Binney. A dynamical model for the extraplanar gas in spiral galaxies. *MNRAS*, 366:449–466, February 2006. doi: 10.1111/j.1365-2966.2005.09816.x.

F. Fraternali and J. J. Binney. Accretion of gas on to nearby spiral galaxies. *MNRAS*, 386:935–944, May 2008. doi: 10.1111/j.1365-2966.2008.13071.x.

F. Fraternali and M. Tomassetti. Estimating gas accretion in disc galaxies using the Kennicutt-Schmidt law. *ArXiv e-prints*, June 2012.

F. Fraternali, G. van Moorsel, R. Sancisi, and T. Oosterloo. Deep H I Survey of the Spiral Galaxy NGC 2403. *AJ*, 123:3124–3140, June 2002. doi: 10.1086/340358.

F. Fraternali, T. Oosterloo, and R. Sancisi. Kinematics of the ionised gas in the spiral galaxy NGC 2403. *A&A*, 424:485–495, September 2004. doi: 10.1051/0004-6361:20040529.

M. Fukugita and P. J. E. Peebles. Massive Coronae of Galaxies. *ApJ*, 639:590–599, March 2006. doi: 10.1086/499556.

J. Grcevich and M. E. Putman. H I in Local Group Dwarf Galaxies and Stripping by the Galactic Halo. *ApJ*, 696:385–395, May 2009. doi: 10.1088/0004-637X/696/1/385.

E. W. Greisen, K. Spekkens, and G. A. van Moorsel. Aperture Synthesis Observations of the Nearby Spiral NGC 6503: Modeling the Thin and Thick H I Disks. *AJ*, 137: 4718–4733, June 2009. doi: 10.1088/0004-6256/137/6/4718.

F. Haardt and P. Madau. Modelling the UV/X-ray cosmic background with CUBA. In D. M. Neumann and J. T. V. Tran, editors, *Clusters of Galaxies and the High Redshift Universe Observed in X-rays*, 2001.

H. J. Habing. High-velocity gas at intermediate latitudes and its relation to the outer part of the Galaxy. *Bull. Astron. Inst. Netherlands*, 18:323, 1966.

D. Hartmann and W. B. Burton. *Atlas of Galactic Neutral Hydrogen*. February 1997.

G. H. Heald, R. J. Rand, R. A. Benjamin, and M. A. Bershady. Integral Field Unit Observations of NGC 891: Kinematics of the Diffuse Ionized Gas Halo. *ApJ*, 647: 1018–1029, August 2006. doi: 10.1086/505464.

G. H. Heald, R. J. Rand, R. A. Benjamin, and M. A. Bershady. Integral Field Unit Observations of NGC 4302: Kinematics of the Diffuse Ionized Gas Halo. *ApJ*, 663: 933–947, July 2007. doi: 10.1086/518087.

F. Heitsch and M. E. Putman. The Fate of High-Velocity Clouds: Warm or Cold Cosmic Rain? *ApJ*, 698:1485–1496, June 2009. doi: 10.1088/0004-637X/698/2/1485.

K. M. Hess, D. J. Pisano, E. M. Wilcots, and J. N. Chengalur. Anomalous H I in NGC 2997. *ApJ*, 699:76–88, July 2009. doi: 10.1088/0004-637X/699/1/76.

A. Hobbs, J. Read, C. Power, and D. Cole. Thermal instabilities in cooling galactic coronae: fuelling star formation in galactic discs. *ArXiv e-prints*, July 2013.

E. J. Hodges-Kluck and J. N. Bregman. A Deep X-ray View of the Hot Halo in the Edge-on Spiral Galaxy NGC 891. *ArXiv e-prints*, November 2012.

C. G. Hoopes, R. A. M. Walterbos, and R. J. Rand. Diffuse Ionized Gas in Edge-on Spiral Galaxies: Extraplanar and Outer Disk Hα Emission. *ApJ*, 522:669–685, September 1999. doi: 10.1086/307670.

A. M. Hopkins, N. M. McClure-Griffiths, and B. M. Gaensler. Linked Evolution of Gas and Star Formation in Galaxies Over Cosmic History. *ApJ*, 682:L13–L16, July 2008. doi: 10.1086/590494.

A. N. M. Hulsbosch and B. P. Wakker. A deep, nearly complete, survey of northern high-velocity clouds. *A&AS*, 75:191–236, October 1988.

M. R. Joung, G. L. Bryan, and M. E. Putman. Gas Condensation in the Galactic Halo. *ApJ*, 745:148, February 2012. doi: 10.1088/0004-637X/745/2/148.

P. M. W. Kalberla and L. Dedes. Global properties of the H I distribution in the outer Milky Way. Planar and extra-planar gas. *A&A*, 487:951–963, September 2008. doi: 10.1051/0004-6361:20079240.

P. M. W. Kalberla, W. B. Burton, D. Hartmann, E. M. Arnal, E. Bajaja, R. Morras, and W. G. L. Pöppel. The Leiden/Argentine/Bonn (LAB) Survey of Galactic HI. Final data release of the combined LDS and IAR surveys with improved stray-radiation corrections. *A&A*, 440:775–782, September 2005. doi: 10.1051/0004-6361:20041864.

P. M. W. Kalberla, L. Dedes, J. Kerp, and U. Haud. Dark matter in the Milky Way. II. The HI gas distribution as a tracer of the gravitational potential. *A&A*, 469:511–527, July 2007. doi: 10.1051/0004-6361:20066362.

J. Kamphuis, R. Sancisi, and T. van der Hulst. An H I superbubble in the spiral galaxy M 101. *A&A*, 244:L29–L32, April 1991.

T. Kaufmann, L. Mayer, J. Wadsley, J. Stadel, and B. Moore. Cooling flows within galactic haloes: the kinematics and properties of infalling multiphase gas. *MNRAS*, 370:1612–1622, August 2006. doi: 10.1111/j.1365-2966.2006.10599.x.

T. Kaufmann, J. S. Bullock, A. H. Maller, T. Fang, and J. Wadsley. Redistributing hot gas around galaxies: do cool clouds signal a solution to the overcooling problem? *MNRAS*, 396:191–202, June 2009. doi: 10.1111/j.1365-2966.2009.14744.x.

R. C. Kennicutt, Jr. The Global Schmidt Law in Star-forming Galaxies. *ApJ*, 498:541–+, May 1998. doi: 10.1086/305588.

R. C. Kennicutt, Jr., D. Calzetti, F. Walter, G. Helou, D. J. Hollenbach, L. Armus, G. Bendo, D. A. Dale, B. T. Draine, C. W. Engelbracht, K. D. Gordon, M. K. M. Prescott, M. W. Regan, M. D. Thornley, C. Bot, and Brinks. Star Formation in NGC 5194 (M51a). II. The Spatially Resolved Star Formation Law. *ApJ*, 671:333–348, December 2007. doi: 10.1086/522300.

D. Kereš and L. Hernquist. Seeding the Formation of Cold Gaseous Clouds in Milky Way-Size Halos. *ApJ*, 700:L1–L5, July 2009. doi: 10.1088/0004-637X/700/1/L1.

D. Kereš, N. Katz, D. H. Weinberg, and R. Davé. How do galaxies get their gas? *MNRAS*, 363:2–28, October 2005. doi: 10.1111/j.1365-2966.2005.09451.x.

D. Kereš, N. Katz, R. Davé, M. Fardal, and D. H. Weinberg. Galaxies in a simulated ΛCDM universe - II. Observable properties and constraints on feedback. *MNRAS*, 396: 2332–2344, July 2009a. doi: 10.1111/j.1365-2966.2009.14924.x.

D. Kereš, N. Katz, M. Fardal, R. Davé, and D. H. Weinberg. Galaxies in a simulated ΛCDM Universe - I. Cold mode and hot cores. *MNRAS*, 395:160–179, May 2009b. doi: 10.1111/j.1365-2966.2009.14541.x.

F. J. Kerr. Galactic velocity models and the interpretation of 21-cm surveys. *MNRAS*, 123:327, 1962.

F. J. Kerr, editor. *The galaxy and the Magellancic clouds, proceedings of the International Astronomical Union Symposium no. 20 Held in Canberra March 18-28, 1963.*, volume 20 of *IAU Symposium*, 1964.

K. Kovač, T. A. Oosterloo, and J. M. van der Hulst. A blind HI survey in the Canes Venatici region. *MNRAS*, 400:743–765, December 2009. doi: 10.1111/j.1365-2966.2009.14662.x.

M. R. Krumholz, A. K. Leroy, and C. F. McKee. What Phase of the Interstellar Medium Correlates with the Star Formation Rate? *ArXiv e-prints*, January 2011.

N. Lehner and J. C. Howk. A Reservoir of Ionized Gas in the Galactic Halo to Sustain Star Formation in the Milky Way. *Science*, 334:955–, November 2011. doi: 10.1126/science.1209069.

N. Lehner, J. C. Howk, C. Thom, A. J. Fox, J. Tumlinson, T. M. Tripp, and J. D. Meiring. High-velocity clouds as streams of ionized and neutral gas in the halo of the Milky Way. *MNRAS*, page 3333, July 2012. doi: 10.1111/j.1365-2966.2012.21428.x.

A. K. Leroy, F. Walter, E. Brinks, F. Bigiel, W. J. G. de Blok, B. Madore, and M. D. Thornley. The Star Formation Efficiency in Nearby Galaxies: Measuring Where Gas Forms Stars Effectively. *AJ*, 136:2782–2845, December 2008. doi: 10.1088/0004-6256/136/6/2782.

E. S. Levine, L. Blitz, C. Heiles, and M. Weinberg. The Warp and Spiral Arms of the Milky Way. *ArXiv Astrophysics e-prints*, September 2006.

E. S. Levine, C. Heiles, and L. Blitz. The Milky Way Rotation Curve and Its Vertical Derivatives: Inside the Solar Circle. *ApJ*, 679:1288–1298, June 2008. doi: 10.1086/587444.

F. J. Lockman. The H I halo in the inner galaxy. *ApJ*, 283:90–97, August 1984. doi: 10.1086/162277.

F. J. Lockman. Discovery of a Population of H I Clouds in the Galactic Halo. *ApJ*, 580: L47–L50, November 2002. doi: 10.1086/345495.

F. J. Lockman, R. A. Benjamin, A. J. Heroux, and G. I. Langston. The Smith Cloud: A High-Velocity Cloud Colliding with the Milky Way. *ApJ*, 679:L21–L24, May 2008. doi: 10.1086/588838.

M.-M. Mac Low, R. McCray, and M. L. Norman. Superbubble blowout dynamics. *ApJ*, 337:141–154, February 1989. doi: 10.1086/167094.

S. Malhotra. The Vertical Distribution and Kinematics of H i and Mass Models of the Galactic Disk. *ApJ*, 448:138, July 1995. doi: 10.1086/175946.

A. H. Maller and J. S. Bullock. Multiphase galaxy formation: high-velocity clouds and the missing baryon problem. *MNRAS*, 355:694–712, December 2004. doi: 10.1111/j.1365-2966.2004.08349.x.

A. Marasco and F. Fraternali. Modelling the H I halo of the Milky Way. *A&A*, 525:A134+, January 2011. doi: 10.1051/0004-6361/201015508.

A. Marasco, F. Fraternali, and J. J. Binney. Supernova-driven gas accretion in the Milky Way. *MNRAS*, 419:1107–1120, January 2012. doi: 10.1111/j.1365-2966.2011.19771.x.

F. Marinacci, J. Binney, F. Fraternali, C. Nipoti, L. Ciotti, and P. Londrillo. The mode of gas accretion on to star-forming galaxies. *MNRAS*, 404:1464–1474, May 2010a. doi: 10.1111/j.1365-2966.2010.16352.x.

F. Marinacci, F. Fraternali, L. Ciotti, and C. Nipoti. Stationary models for the extraplanar gas in disc galaxies. *MNRAS*, 401:2451–2462, February 2010b. doi: 10.1111/j.1365-2966.2009.15821.x.

F. Marinacci, F. Fraternali, C. Nipoti, J. Binney, L. Ciotti, and P. Londrillo. Galactic fountains and the rotation of disc-galaxy coronae. *MNRAS*, pages 855–+, June 2011. doi: 10.1111/j.1365-2966.2011.18810.x.

F. Marinacci, F. Fraternali, J. Binney, C. Nipoti, L. Ciotti, and P. Londrillo. Fountain-driven gas accretion by the Milky Way. In *European Physical Journal Web of Conferences*, volume 19 of *European Physical Journal Web of Conferences*, page 8008, February 2012. doi: 10.1051/epjconf/20121908008.

George Marsaglia, Wai Wan Tsang, and Jingbo Wang. Evaluating kolmogorov's distribution. *Journal of Statistical Software*, 8(18):1–4, 11 2003. ISSN 1548-7660. URL `http://www.jstatsoft.org/v08/i18`.

C. Mastropietro, B. Moore, L. Mayer, J. Wadsley, and J. Stadel. The gravitational and hydrodynamical interaction between the Large Magellanic Cloud and the Galaxy. *MNRAS*, 363:509–520, October 2005. doi: 10.1111/j.1365-2966.2005.09435.x.

N. M. McClure-Griffiths, J. M. Dickey, B. M. Gaensler, A. J. Green, M. Haverkorn, and S. Strasser. The Southern Galactic Plane Survey: H I Observations and Analysis. *ApJS*, 158:178–187, June 2005. doi: 10.1086/430114.

P. J. McMillan. Mass models of the Milky Way. *MNRAS*, 414:2446–2457, July 2011. doi: 10.1111/j.1365-2966.2011.18564.x.

C. Melioli, F. Brighenti, A. D'Ercole, and E. M. de Gouveia Dal Pino. Hydrodynamical simulations of Galactic fountains - I. Evolution of single fountains. *MNRAS*, 388:573–586, August 2008. doi: 10.1111/j.1365-2966.2008.13446.x.

C. Melioli, F. Brighenti, A. D'Ercole, and E. M. de Gouveia Dal Pino. Hydrodynamical simulations of Galactic fountains - II. Evolution of multiple fountains. *MNRAS*, 399: 1089–1105, November 2009. doi: 10.1111/j.1365-2966.2009.14725.x.

R. Morras, E. Bajaja, E. M. Arnal, and W. G. L. Pöppel. A new survey for high velocity HI detections in the Southern Hemisphere. *A&AS*, 142:25–30, February 2000. doi: 10.1051/aas:2000132.

C. Nipoti. Thermal instability in rotating galactic coronae. *MNRAS*, 406:247–263, July 2010. doi: 10.1111/j.1365-2966.2010.16705.x.

C. Nipoti and L. Posti. Thermal stability of a weakly magnetized rotating plasma. *MNRAS*, page 53, September 2012. doi: 10.1093/mnras/sts070.

E. Noordermeer. *The distribution of gas, stars and dark matter in early-type disk galaxies*. PhD thesis, Groningen: Rijksuniversiteit, 2006.

J. H. Oort. Possible Interpretations of the High-Velocity Clouds. *Bull. Astron. Inst. Netherlands*, 18:421–438, 1966.

J. H. Oort. The formation of galaxies and the origin of the high-velocity hydrogen. *A&A*, 7:381–404, September 1970.

T. Oosterloo, F. Fraternali, and R. Sancisi. The Cold Gaseous Halo of NGC 891. *AJ*, 134: 1019–1036, September 2007. doi: 10.1086/520332.

B. E. J. Pagel. *Nucleosynthesis and Chemical Evolution of Galaxies*. Cambridge University Press, October 1997.

G. Paturel, C. Petit, P. Prugniel, G. Theureau, J. Rousseau, M. Brouty, P. Dubois, and L. Cambrésy. HYPERLEDA. I. Identification and designation of galaxies. *A&A*, 412: 45–55, December 2003. doi: 10.1051/0004-6361:20031411.

A. H. Pawlik and J. Schaye. TRAPHIC - radiative transfer for smoothed particle hydrodynamics simulations. *MNRAS*, 389:651–677, September 2008. doi: 10.1111/j.1365-2966.2008.13601.x.

J. E. G. Peek, M. E. Putman, and J. Sommer-Larsen. Ongoing Galactic Accretion: Simulations and Observations of Condensed Gas in Hot Halos. *ApJ*, 674:227–236, February 2008. doi: 10.1086/524374.

S. V. Penton, J. T. Stocke, and J. M. Shull. The Local Lyα Forest. IV. Space Telescope Imaging Spectrograph G140M Spectra and Results on the Distribution and Baryon Content of H I Absorbers. *ApJS*, 152:29–62, May 2004. doi: 10.1086/382877.

Y. Pidopryhora, F. J. Lockman, and J. C. Shields. The Ophiuchus Superbubble: A Gigantic Eruption from the Inner Disk of the Milky Way. *ApJ*, 656:928–942, February 2007. doi: 10.1086/510521.

D. J. Pisano, D. G. Barnes, B. K. Gibson, L. Staveley-Smith, K. C. Freeman, and V. A. Kilborn. Where Are the High-Velocity Clouds in Local Group Analogs? *ApJ*, 610: L17–L20, July 2004. doi: 10.1086/423239.

D. J. Pisano, D. G. Barnes, B. K. Gibson, L. Staveley-Smith, K. C. Freeman, and V. A. Kilborn. An H I Survey of Six Local Group Analogs. I. Survey Description and the Search for High-Velocity Clouds. *ApJ*, 662:959–968, June 2007. doi: 10.1086/517986.

M. E. Putman, J. Bland-Hawthorn, S. Veilleux, B. K. Gibson, K. C. Freeman, and P. R. Maloney. Hα Emission from High-Velocity Clouds and Their Distances. *ApJ*, 597: 948–956, November 2003. doi: 10.1086/378555.

M. E. Putman, C. Thom, B. K. Gibson, and L. Staveley-Smith. The Gaseous Trail of the Sagittarius Dwarf Galaxy. *ApJ*, 603:L77–L80, March 2004. doi: 10.1086/382728.

M. E. Putman, D. R. Saul, and E. Mets. Head-tail clouds: drops to probe the diffuse Galactic halo. *MNRAS*, 418:1575–1586, December 2011. doi: 10.1111/j.1365-2966.2011.19524.x.

M. E. Putman, J. E. G. Peek, and M. R. Joung. Gaseous Galaxy Halos. *ArXiv e-prints*, July 2012.

A. Rahmati, A. P. Pawlik, M. Raičević, and J. Schaye. On the evolution of the HI column density distribution in cosmological simulations. *ArXiv e-prints*, October 2012.

J. Rasmussen, J. Sommer-Larsen, K. Pedersen, S. Toft, A. Benson, R. G. Bower, and L. F. Grove. Hot Gas Halos Around Disk Galaxies: Confronting Cosmological Simulations with Observations. *ApJ*, 697:79–93, May 2009. doi: 10.1088/0004-637X/697/1/79.

M. J. Reid, K. M. Menten, X. W. Zheng, A. Brunthaler, L. Moscadelli, Y. Xu, B. Zhang, M. Sato, M. Honma, T. Hirota, K. Hachisuka, Y. K. Choi, G. A. Moellenbrock, and A. Bartkiewicz. Trigonometric Parallaxes of Massive Star-Forming Regions. VI. Galactic Structure, Fundamental Parameters, and Noncircular Motions. *ApJ*, 700:137–148, July 2009. doi: 10.1088/0004-637X/700/1/137.

R. J. Reynolds. Ionized disk/halo gas - Insight from optical emission lines and pulsar dispersion measures. In H. Bloemen, editor, *The Interstellar Disk-Halo Connection in Galaxies*, volume 144 of *IAU Symposium*, pages 67–76, 1991.

R. J. Reynolds, F. Scherb, and F. L. Roesler. Observations of Diffuse Galactic HA and [n II] Emission. *ApJ*, 185:869–876, November 1973. doi: 10.1086/152461.

R. J. Reynolds, N. C. Sterling, and L. M. Haffner. Detection of a Large Arc of Ionized Hydrogen Far above the Cassiopeia OB6 Association: A Superbubble Blowout into the Galactic Halo? *ApJ*, 558:L101–L104, September 2001. doi: 10.1086/323638.

K. Rohlfs and J. Kreitschmann. Kinematics and physical parameters of neutral hydrogen in the inner Galaxy. *A&A*, 178:95–105, July 1987.

J. Rossa and R.-J. Dettmar. An Hα survey aiming at the detection of extraplanar diffuse ionized gas in halos of edge-on spiral galaxies. II. The Hα survey atlas and catalog. *A&A*, 406:505–525, August 2003. doi: 10.1051/0004-6361:20030698.

R. Sancisi, F. Fraternali, T. Oosterloo, and T. van der Hulst. Cold gas accretion in galaxies. *A&AR*, 15:189–223, June 2008. doi: 10.1007/s00159-008-0010-0.

C. L. Sarazin. *X-Ray Emission from Clusters of Galaxies*. June 2009.

B. D. Savage, K. R. Sembach, B. P. Wakker, P. Richter, M. Meade, E. B. Jenkins, J. M. Shull, H. W. Moos, and G. Sonneborn. Distribution and Kinematics of O VI in the Galactic Halo. *ApJS*, 146:125–164, May 2003. doi: 10.1086/346229.

J. Schaye, C. Dalla Vecchia, C. M. Booth, R. P. C. Wiersma, T. Theuns, M. R. Haas, S. Bertone, A. R. Duffy, I. G. McCarthy, and F. van de Voort. The physics driving the cosmic star formation history. *MNRAS*, 402:1536–1560, March 2010. doi: 10.1111/j.1365-2966.2009.16029.x.

M. Schmidt. The Rate of Star Formation. *ApJ*, 129:243–+, March 1959. doi: 10.1086/146614.

R. Schönrich and J. Binney. Chemical evolution with radial mixing. *MNRAS*, 396:203–222, June 2009. doi: 10.1111/j.1365-2966.2009.14750.x.

K. R. Sembach, B. D. Savage, L. Lu, and E. M. Murphy. Highly Ionized High-Velocity Clouds: Intergalactic Gas in the Local Group or Distant Gas in the Galactic Halo? *ApJ*, 515:108–127, April 1999. doi: 10.1086/306999.

K. R. Sembach, B. P. Wakker, B. D. Savage, P. Richter, M. Meade, J. M. Shull, E. B. Jenkins, G. Sonneborn, and H. W. Moos. Highly Ionized High-Velocity Gas in the Vicinity of the Galaxy. *ApJS*, 146:165–208, May 2003. doi: 10.1086/346231.

W. W. Shane and G. P. Bieger-Smith. The galactic rotation curve derived from observations of neutral hydrogen. *Bull. Astron. Inst. Netherlands*, 18:263, 1966.

P. R. Shapiro and G. B. Field. Consequences of a New Hot Component of the Interstellar Medium. *ApJ*, 205:762–765, May 1976. doi: 10.1086/154332.

J. M. Shull, J. R. Jones, C. W. Danforth, and J. A. Collins. A Large Reservoir of Ionized Gas in the Galactic Halo: Ionized Silicon in High-velocity and Intermediate-velocity Clouds. *ApJ*, 699:754–767, July 2009. doi: 10.1088/0004-637X/699/1/754.

G. P. Smith. A peculiar feature at $l^{II} = 40°.5$, $b^{II} = -15°.0$. *Bull. Astron. Inst. Netherlands*, 17:203, March 1963.

S. L. Snowden, R. Egger, M. J. Freyberg, D. McCammon, P. P. Plucinsky, W. T. Sanders, J. H. M. M. Schmitt, J. Truemper, and W. Voges. ROSAT Survey Diffuse X-Ray Background Maps. II. *ApJ*, 485:125, August 1997. doi: 10.1086/304399.

Y. Sofue, M. Honma, and T. Omodaka. Unified Rotation Curve of the Galaxy – Decomposition into de Vaucouleurs Bulge, Disk, Dark Halo, and the 9-kpc Rotation Dip –. *PASJ*, 61:227–, February 2009.

D. N. Spergel, R. Bean, O. Doré, M. R. Nolta, C. L. Bennett, J. Dunkley, G. Hinshaw, N. Jarosik, E. Komatsu, L. Page, H. V. Peiris, L. Verde, M. Halpern, R. S. Hill, A. Kogut, M. Limon, S. S. Meyer, N. Odegard, and G. S. Tucker. Three-Year Wilkinson Microwave Anisotropy Probe (WMAP) Observations: Implications for Cosmology. *ApJS*, 170:377–408, June 2007. doi: 10.1086/513700.

E. Spitoni and F. Matteucci. Effects of radial flows on the chemical evolution of the Milky Way disk. *ArXiv e-prints*, April 2011.

E. Spitoni, S. Recchi, and F. Matteucci. Galactic fountains and their connection with high and intermediate velocity clouds. *A&A*, 484:743–753, June 2008. doi: 10.1051/0004-6361:200809403.

L. Spitzer, Jr. On a Possible Interstellar Galactic Corona. *ApJ*, 124:20, July 1956. doi: 10.1086/146200.

V. Springel. The cosmological simulation code GADGET-2. *MNRAS*, 364:1105–1134, December 2005. doi: 10.1111/j.1365-2966.2005.09655.x.

V. Springel, N. Yoshida, and S. D. M. White. GADGET: a code for collisionless and gas-dynamical cosmological simulations. *New A*, 6:79–117, April 2001. doi: 10.1016/S1384-1076(01)00042-2.

V. Springel, S. D. M. White, A. Jenkins, C. S. Frenk, N. Yoshida, L. Gao, J. Navarro, R. Thacker, D. Croton, J. Helly, J. A. Peacock, S. Cole, P. Thomas, H. Couchman, A. Evrard, J. Colberg, and F. Pearce. Simulations of the formation, evolution and clustering of galaxies and quasars. *Nature*, 435:629–636, June 2005. doi: 10.1038/nature03597.

J. M. Stil, A. R. Taylor, J. M. Dickey, D. W. Kavars, P. G. Martin, T. A. Rothwell, A. I. Boothroyd, F. J. Lockman, and N. M. McClure-Griffiths. The VLA Galactic Plane Survey. *AJ*, 132:1158–1176, September 2006. doi: 10.1086/505940.

G. Stinson, A. Seth, N. Katz, J. Wadsley, F. Governato, and T. Quinn. Star formation and feedback in smoothed particle hydrodynamic simulations - I. Isolated galaxies. *MNRAS*, 373:1074–1090, December 2006. doi: 10.1111/j.1365-2966.2006.11097.x.

J. T. Stocke, S. V. Penton, C. W. Danforth, J. M. Shull, J. Tumlinson, and K. M. McLin. The Galaxy Environment of O VI Absorption Systems. *ApJ*, 641:217–228, April 2006. doi: 10.1086/500386.

C. Struck and D. C. Smith. Storm fronts over galaxy discs: models of how waves generate extraplanar gas and its anomalous kinematics. *MNRAS*, 398:1069–1081, September 2009. doi: 10.1111/j.1365-2966.2009.15035.x.

R. S. Sutherland and M. A. Dopita. Cooling functions for low-density astrophysical plasmas. *ApJS*, 88:253–327, September 1993. doi: 10.1086/191823.

D. A. Thilker, R. Braun, R. A. M. Walterbos, E. Corbelli, F. J. Lockman, E. Murphy, and R. Maddalena. On the Continuing Formation of the Andromeda Galaxy: Detection of H I Clouds in the M31 Halo. *ApJ*, 601:L39–L42, January 2004. doi: 10.1086/381703.

C. Thom, J. E. G. Peek, M. E. Putman, C. Heiles, K. M. G. Peek, and R. Wilhelm. An Accurate Distance to High-Velocity Cloud Complex C. *ApJ*, 684:364–372, September 2008. doi: 10.1086/589960.

T. M. Tripp, B. P. Wakker, E. B. Jenkins, C. W. Bowers, A. C. Danks, R. F. Green, S. R. Heap, C. L. Joseph, M. E. Kaiser, J. L. Linsky, and B. E. Woodgate. Complex C: A Low-Metallicity, High-Velocity Cloud Plunging into the Milky Way. *AJ*, 125:3122–3144, June 2003. doi: 10.1086/374995.

J. Tumlinson, J. M. Shull, M. L. Giroux, and J. T. Stocke. The Hot Intergalactic Medium-Galaxy Connection: Two Strong O VI Absorbers in the Sight Line toward PG 1211+143. *ApJ*, 620:95–112, February 2005. doi: 10.1086/426961.

B. A. Twarog. The chemical evolution of the solar neighborhood. II - The age-metallicity relation and the history of star formation in the galactic disk. *ApJ*, 242:242–259, November 1980. doi: 10.1086/158460.

J. M. van der Hulst, T. S. van Albada, and R. Sancisi. The Westerbork HI Survey of Irregular and Spiral Galaxies, WHISP. In J. E. Hibbard, M. Rupen, and J. H. van Gorkom, editors, *Gas and Galaxy Evolution*, volume 240 of *Astronomical Society of the Pacific Conference Series*, page 451, 2001.

H. van Woerden, U. J. Schwarz, and A. N. M. Hulsbosch. Highlights of High-Velocity Clouds. In H. van Woerden, R. J. Allen, & W. B. Burton, editor, *The Milky Way Galaxy*, volume 106 of *IAU Symposium*, pages 387–407, 1985.

H. van Woerden, B. P. Wakker, U. J. Schwarz, and K. S. de Boer, editors. *High Velocity Clouds*, volume 312 of *Astrophysics and Space Science Library*, January 2004.

Á. Villalobos and A. Helmi. Simulations of minor mergers - II. The phase-space structure of thick discs. *MNRAS*, 399:166–176, October 2009. doi: 10.1111/j.1365-2966.2009.15085.x.

B. P. Wakker. Distribution and origin of high-velocity clouds. II - Statistical analysis of the whole-sky survey. *A&A*, 250:499–508, October 1991.

B. P. Wakker. Distances and Metallicities of High- and Intermediate-Velocity Clouds. *ApJS*, 136:463–535, October 2001. doi: 10.1086/321783.

B. P. Wakker and B. D. Savage. The Relationship Between Intergalactic H I/O VI and Nearby ($z < 0.017$) Galaxies. *ApJS*, 182:378–467, May 2009. doi: 10.1088/0067-0049/182/1/378.

B. P. Wakker and H. van Woerden. High-Velocity Clouds. *ARA&A*, 35:217–266, 1997. doi: 10.1146/annurev.astro.35.1.217.

B. P. Wakker, J. C. Howk, B. D. Savage, S. L. Tufte, R. J. Reynolds, H. van Woerden, U. J. Schwarz, and R. F. Peletier. Observational Evidence for the Accretion of Low-metallicity Gas onto the Milky Way: Metallicity, Physical Conditions and Distance Limit for HVC Complex C. In B. K. Gibson & M. E. Putman, editor, *Stromlo Workshop on High-Velocity Clouds*, volume 166 of *Astronomical Society of the Pacific Conference Series*, pages 26–+, 1999.

B. P. Wakker, B. D. Savage, K. R. Sembach, P. Richter, M. Meade, E. B. Jenkins, J. M. Shull, T. B. Ake, W. P. Blair, W. V. Dixon, S. D. Friedman, J. C. Green, R. F. Green, J. W. Kruk, H. W. Moos, E. M. Murphy, W. R. Oegerle, D. J. Sahnow, G. Sonneborn, E. Wilkinson, and D. G. York. The Far Ultraviolet Spectroscopic Explorer Survey of O VI Absorption in and near the Galaxy. *ApJS*, 146:1–123, May 2003. doi: 10.1086/346230.

B. P. Wakker, D. G. York, J. C. Howk, J. C. Barentine, R. Wilhelm, R. F. Peletier, H. van Woerden, T. C. Beers, Ž. Ivezić, P. Richter, and U. J. Schwarz. Distances to Galactic High-Velocity Clouds: Complex C. *ApJL*, 670:L113–L116, December 2007. doi: 10.1086/524222.

B. P. Wakker, D. G. York, R. Wilhelm, J. C. Barentine, P. Richter, T. C. Beers, Ž. Ivezić, and J. C. Howk. Distances to Galactic High-Velocity Clouds. I. Cohen Stream, Complex GCP, Cloud g1. *ApJ*, 672:298–319, January 2008. doi: 10.1086/523845.

K. B. Westfall, M. A. Bershady, M. A. W. Verheijen, D. R. Andersen, T. P. K. Martinsson, R. A. Swaters, and A. Schechtman-Rook. The DiskMass Survey. IV. The Dark-matter-dominated Galaxy UGC 463. *ApJ*, 742:18, November 2011. doi: 10.1088/0004-637X/742/1/18.

S. D. M. White and M. J. Rees. Core condensation in heavy halos - A two-stage theory for galaxy formation and clustering. *MNRAS*, 183:341–358, May 1978.

Y. Yao, M. A. Nowak, Q. D. Wang, N. S. Schulz, and C. R. Canizares. Limits on Hot Galactic Halo Gas from X-Ray Absorption Lines. *ApJL*, 672:L21–L24, January 2008. doi: 10.1086/526767.

J. Zsargó, K. R. Sembach, J. C. Howk, and B. D. Savage. Highly Ionized Gas in the Galactic Halo: A FUSE Survey of O VI Absorption toward 22 Halo Stars. *ApJ*, 586: 1019–1049, April 2003. doi: 10.1086/367766.